LANCASTER UNIVERSITY

DEPARTMENT OF PHYSICS

THESIS FOR QUALIFICATION OF DOCTOR OF PHILOSOPHY (PH.D.)

Illuminating the Dark: Laboratory-Based Dark Matter Production

Author:

John David Edward SCOTT,
MPhys

Supervisors:

Dr. David BURTON

Dr. Ian BAILEY

November, 2021

Declaration

I, John David Edward Scott, do hereby declare that all content contained within this thesis is original, of my own composition, and has not been submitted, in whole or in part, in relation to any other degree or professional qualification. Furthermore, I grant Lancaster University the right to make available this thesis and the works contained herein.

For my loving and supportive wife, Heather.

Ah! if you prize my subdued soul above

The poor, the fading, brief pride of an hour:

Let none profane my Holy See of Love,

Or with a rude hand break

The sacramental cake:

Let none else touch the just new-budded flower;

If not – may my eyes close,

Love, on their last repose!

— John Keats

Acknowledgements

Academic

First and foremost, I wish to thank my primary supervisor, Dr. David Burton. His diligent approaches to problem-solving have undeniably made me a better physicist and more rigorous mathematician. Further, his patience and compassion have seen me through what have undoubtedly been the hardest years of my life to date.

I would also like to acknowledge and thank my secondary supervisor, Dr. Ian Bailey. His feedback and oversight have kept my studies grounded in the realms of experimental applicability. Our conversations have proved invaluable in facilitating my research.

The final months of my studies was made possible through the funding provided by a postdoctoral research associate position. For this opportunity I am eternally grateful to Dr. Elisabetta Boella, with whom I greatly look forward to conducting research in coming months.

On a final academic note, I owe my sincerest gratitude to Prof. Alec Thomas and Dr. Louise Willingale, without whom I would not have been granted the initial opportunity to undertake my PhD.

Personal

I wish to thank my family for their continued support throughout my academic journey. In particular, I wish to thank my brother-in-law, Tom Maxwell-Hodkinson, whose invaluable insights made him a fantastic debugging partner.

Funding and Facilities

Contents

List of Figures

List of Tables

Nomenclature

ALP   Axion-Like Particle
CGS   Centimetre-Gramme-Second
DLP   Dilaton-like particle
DMC   Dark Matter Candidate
EM   Electromagnetism
HSP   Hidden Sector Photon
LHC   Large Hadron Collider
LSW   Light-shining-through-wall
LWFA   Laser Wakefield Acceleration
PBG   Photonic BandGap
QCD   Quantum ChromoDynamics
QED   Quantum ElectroDynamics
SI   Systéme Internationale
SM   Standard Model
WISP   Weakly-Interacting Slim Particle

&c   Et cetera
c.   Circa
viz.   Videlicet

Notation

Constants

Symbol	Value	Units	Description
ϵ_0	8.854×10^{-12}	$\mathrm{F\,m^{-1}}$	Vacuum permittivity
c	2.998×10^{8}	$\mathrm{m\,s^{-1}}$	Speed of light in free space
e	1.602×10^{-19}	C	Elementary charge
m_e	9.109×10^{-31}	kg	Electron mass

Variables

Scalar Quantities

Symbol	Units	Description
η	—	Refractive index
λ_p	m	Plasma wavelength
ϱ	$\mathrm{m^{-3}}$	Source density
ρ	$\mathrm{C\,m^{-3}}$	Charge density
ω_p	$\mathrm{rad\,s^{-1}}$	Plasma frequency
a_0	—	Normalised laser amplitude
E	J	Energy
k_p	$\mathrm{m^{-1}}$	Plasma wavenumber
$\mathscr{L}$	$\mathrm{J\,m^{-3}}$	Lagrangian density
M, m	kg	Mass
n_0	$\mathrm{m^{-3}}$	Ambient plasma number density
q	C	Charge
r	m	Radius
t	s	Time
V	$\mathrm{m^3}$	Volume

Vector Quantities

a	$\mathrm{m\,s^{-2}}$	Acceleration
B	T	Magnetic field
E	$\mathrm{eV\,m^{-1}}$	Electric field/Acceleration gradient
F	N	Force
v	$\mathrm{m\,s^{-1}}$	Velocity

Conventions

- Unless stated otherwise, calculations are conducted using Heaviside-Lorentz units in which $\hbar = c = 1$.

- Vectors are denoted in mathematical expressions using bold typeface, e.g. the position vector in three-dimensional space is written $\mathbf{x} = (x, y, z)$.

- Three similar but distinct equality symbols are utilised throughout this thesis: $=$, $\equiv$ and $\coloneqq$. The canonical "$=$" symbol denotes a computational equality relation and serves as an assignment operator. The "$\equiv$" symbol indicates an equivalence relationship between two quantities; within this thesis, one may verbalise the symbol as "are equal *from* definition". Finally, "$\coloneqq$" is used to symbolise the construction of recognised definitions; consequently, one can mentally regard the symbol as replacing the phrase "are equal *as* definition".

- Separate notations are used in the demarcations of absolute-value and L^2 norms. The absolute value of a variable is denoted with single vertical bar, i.e. $|a| = +\sqrt{a^2}$, whereas norms on Euclidean space are denoted using double vertical bars, i.e. for a vector $\mathbf{x} = (x_1, \ldots x_n)$ the L^2 norm is defined as $\|\mathbf{x}\| \coloneqq \sqrt{x_1^2 + \ldots + x_n^2}$.

- Fourier transforms:

$$f(t, \mathbf{x}) = \frac{1}{(2\pi)^3} \int_{-\infty}^{\infty} e^{-i\mathbf{k}\cdot\mathbf{x}} \widetilde{f}_{\mathbf{k}}(t) \, \mathrm{d}^3\mathbf{k}$$

$$\widetilde{f}_{\mathbf{k}}(t) = \int_{-\infty}^{\infty} e^{i\mathbf{k}\cdot\mathbf{x}} f(t, \mathbf{x})(t) \, \mathrm{d}^3\mathbf{x}.$$

- Heaviside step function:

$$\Theta(x - y) = \begin{cases} 1 & x > y \\ \frac{1}{2} & x = y \\ 0 & x < y. \end{cases}$$

Abstract

The focus of this thesis is the exploration of novel theoretical approaches to the production and detection of dark matter candidates using laboratory-based electromagnetic sources. The pursuit of these investigations culminated in the development and application of a post-process numeric analysis software, **Run:DMC**. This code was applied to the output data of two accelerator simulation packages, namely EPOCH and MEEP, to calculate the field strengths of particular dark matter candidates – axion-like particles, dilaton-like particles and dark photons – within these systems. The conclusion of these analyses found that dark matter candidates can be produced in a variety of experimental systems within modern laboratories with relatively modest equipment.

Chapter 1 chronicles the amassing of observational evidence supporting the existence of dark matter, along with the developments of the dark matter candidates of concern for this thesis and the proposed investigational approaches. Chapter 2 derives and discusses the theoretical underpinnings and developments of particular dark matter candidates. Similarly, Chapters 3, 4 and 5 cover the theory of the methodologies and techniques utilised within this thesis. Chapter 6 presents **Run:DMC**, the computational code designed and developed for the purpose of post-process analysing data produced by simulations to calculate the corresponding dark matter fields. Within this chapter, relevant theory is derived and the code is applied to several test cases, the results of which are used to infer its strengths and weaknesses. Chapter 7 focusses on axion-like particle (ALP) and dilaton-like particle (DLP) production within laser-driven plasma wake field acceleration. It was found that magnetised plasma wakes are capable of producing both ALPs and DLPs, however it was also found that the dominant field contributions for both dark matter candidates derive from the laser pulse driving the wake. Trends across system parameters were then investigated: ALP production was found to be maximised when the system is exposed to high strength external magnetic fields which are parallel to the direction of laser propagation; in contrast, DLPs are relatively unaffected by

magnetic field strength or angle. Chapter 8 presents and discusses results of the second method of dark matter production, namely ALPs and hidden sector photons (HSPs) from a photonic bandgap lattice (PBL) located within a microwave resonant cavity (MRC). It was found that magnetised MRCs are suitable mechanisms of laboratory-based dark matter production, which is capable of being coupled with a PBG to effectively restrict the applied electric field to a much more localised region than ordinarily possible. Lastly, Chapter 9 concludes the thesis by uniting all concepts theretofore discussed, summarising results and suggesting further developments of the presented ideas.

Chapter 1

Introduction

*"The story so far: In the beginning the Universe
was created. This has made a lot of people very
angry and been widely regarded as a bad move."*
— Douglas Adams, *The Restaurant at the End of
the Universe*

The focus of this thesis is the exploration of two novel schemes of laboratory-based production and detection of particular *dark matter candidates*, namely *axion-like particles*, *dilaton-like particles* and *dark photons*. Both of these schemes propose the utilisation of *light shining through wall* methodology as the means of efficient particle detection from different physical systems, specifically *laser wake field acceleration* and *photonic bandgap lattices*. To date, the main application of particle accelerators to particle physics research has been in high energy physics, which has proved successful in the discoveries of a plethora of subatomic particles. However, the methods explored within this thesis open the possibility for accelerator-based low energy particle physics research, a relatively unexplored area of research which potentially holds epochal outcomes. This introductory chapter considers the above italicised terms with the intention of granting the reader an understanding of their definitions, conceptual developments and their advancing of fundamental physics.

1.1 Dark Matter

In his 1922 paper, the Dutch astronomer Jacobus Kapteyn outlined a preliminary "general theory of the distribution of masses, forces and velocities" in the Milky Way based on observations of stellar luminosities [1]. Presented in this paper was one of the first

models envisaging our galaxy as a flattened distribution of stars rotating about a common axis; along with an allusion to the potential existence of invisible matter. This substance could interact gravitationally but would be incapable of emitting, reflecting or absorbing electromagnetic radiation, coining the term "Dark Matter".

In modern physics, dark matter is hypothetical additional matter of unknown composition in galaxies and the wider Universe whose existence has been inferred by various astrophysical observations which will be later explained. Characteristically, dark matter is non-luminous and non-absorbing; the combination of which has made detection onerous. However, its existence has been inferred through a number of astrophysical observations and according to recent data, dark matter is thought to comprise 84% of the mass in the Universe [2, p. 396]. The following outlines the theoretical development and accumulating observational evidence supporting the existence of dark matter. For a more complete history, see Jaan Einasto's *Dark Matter* or Gianfranco Bertone and Dan Hooper's *History of dark matter* [3,4].

Some terminology will now be briefly introduced for later use. The rotational velocity v for a body following a stable Keplerian orbit at radius r is given by $v \propto \sqrt{\frac{M(r)}{r}}$, where $M(r)$ is the total mass encompassed by the orbit. The *nucleus* of a galaxy is a compact central region of high luminosity.

1.1.1   Galaxy Clusters

1.1.1.1   Fritz Zwicky and the Coma Cluster

Arguably the most famous pioneer in the field of dark matter research is the Bulgarian-born Swiss-American astronomer Fritz Zwicky. In 1933, Zwicky published a paper on his investigations into the velocity dispersion of galaxies within the Coma cluster [5]. By using the virial theorem, which relates a system's time-averaged kinetic energy to its total potential energy, it was possible to calculate the gravitational mass of the cluster. Notably, this was significantly greater than that observed in the luminosity of ordinary *leuchtende Materie* ("glowing matter"); Zwicky attributed the discrepancy to an unseen *dunkle Materie* ("dark matter"). Further calculation revealed that the Coma cluster would be torn apart into 800 individual galaxies without this additional matter [5, p. 125].

Despite his major discovery, Zwicky's work garnered little interest by his peers and

dark matter in galaxy clusters was largely overlooked. Undoubtedly, his work was ignored by many due to his abrasive nature [6].

1.1.1.2   The Bullet Cluster

Situated in the Carina constellation, 3.7 billion lightyears from Earth, 1E 0657-56 is an astrophysical system formed by the collision of two large galaxy clusters [7, 8]. During the relatively recent merger, the intergalactic gases within each cluster interspersed, the interactions from which slowed and heated the gases to the point of X-radiation emission.

In 2002, the Chandra X-ray Observatory measured the X-radiation produced within 1E 0657-56 [9]. From this, they detected the first ever clear evidence of a bow shock in a galaxy cluster – a nearly discontinuous boundary between regions of different intracluster medium pressures. However, in the annals of time this would fall secondary to another observation of the same paper. What they noted was that the shape of the gas cloud exiting the cluster core resembled that of a bullet, resulting in the coinage of its more common name, the Bullet Cluster (though technically the Bullet Cluster specifically refers to the smaller of the clusters).

Two years thereafter, in 2004, the mass distribution of the Bullet Cluster was measured using weak gravitational lensing [10]. It transpired that the majority of the cluster's mass was optically non-luminous and located within the intergalactic regions. Further, the majority of the mass was found to be situated between the gas – which was concentrated in the galactic centroid – and the visible galactic matter, as shown in Figure 1.1. This observed offset was concluded to be clear, direct evidence for the existence of dark matter. Shortly thereafter, the Chandra Observatory combined their 2002 X-ray data with the optical and new gravitational lensing observations to place constraints on dark matter self-interaction [11]. The conclusion of this was that the cross sections of dark matter self-interaction are very small. From this, they were able to explain their observation as the dark matter having interpassed relatively unhindered while the intergalactic gases were heated, thus explaining the spatial offset of observable baryonic matter and gravitational lensing. A 2006 analysis of additional data found an 8σ significance of the spatial offset between the centres of total and baryonic mass [12].

One should note that the Bullet Cluster is not an anomaly, with other clusters such as MACS J0025.4-1222 providing additional support for the existence of dark matter [13]. The reason for the Bullet Cluster being so dominant a discovery lies in its orientation
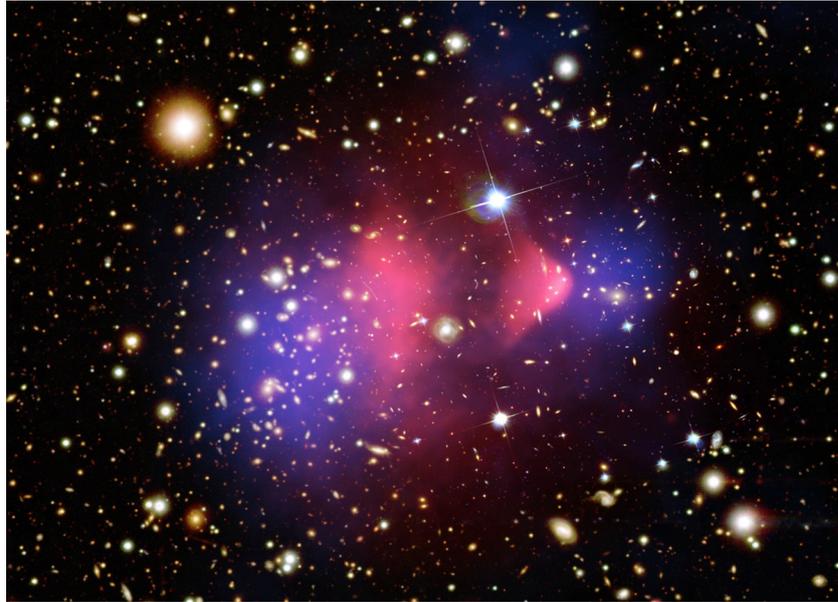
Figure 1.1: NASA composite image of the Bullet Cluster from
X-ray, optical and gravitational lensing data. Non-luminous
baryonic mass is in pink and the putative dark matter in blue.
Image credit: X-ray: NASA/CXC/CfA/M.Markevitch et al.;
Optical: NASA/STScI; Magellan/U.Arizona/D.Clowe et al.;
Lensing Map: NASA/STScI; ESO WFI;
Magellan/U.Arizona/D.Clowe et al.

being planar relative to Earth, thus is easier to observe.

1.1.2   The Galaxy Rotation Problem

In his 1939 doctoral thesis, the American astronomer Horace Babcock reported various
measurements of the galaxy Messier 31 (also known as M31 or Andromeda) [14]. Among
his observations, Babcock noted that the mass-luminosity ratio increased with radial dis-
tance, from 0.001 at 0 arcminutes to 62 at 80 arcminutes, suggesting either additional
mass or reduced luminosity toward the outer reaches. However, he did not regard the
existence of unseen massive matter a possibility, instead attributing the behaviour to ab-
sorption of light by interstellar media or modified dynamics – which he termed "internal
gravitational viscosity" – in the farther extents of the galaxy. Babcock also reported a
plateauing of the angular velocity with radial distance, as shown in Figure 1.2, running
counter to the expected radial drop-off.

On the discovery of this deviation from theory, Babcock concluded that a significant
mass must be present in the galaxy's exterior, writing:

"[T]he obvious interpretation of the nearly constant angular velocity from a

radius of 20 minutes of arc outward is that a very great proportion of the mass of the nebula must lie in the outer regions."

Fig. 5. Angular velocity, ω, in units of 10^{-15} radians per second, plotted against radius.
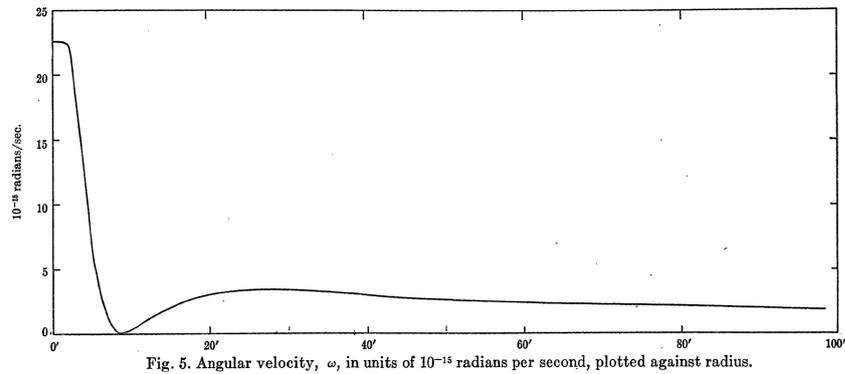
Figure 1.2: Babcock's plot of stellar angular velocity vs. radial distance from the galaxy centre of M31 [14].

During the late 1960s and throughout the 1970s, the astronomers Vera Rubin and Kent Ford measured the rotation curves of stars within spiral galaxies [15]. In a 1970 paper they published results of rotational velocity vs. radial distance from the centre of the M31 galaxy, indicating a similar trend to Babcock, as can be seen in Figure 1.3.
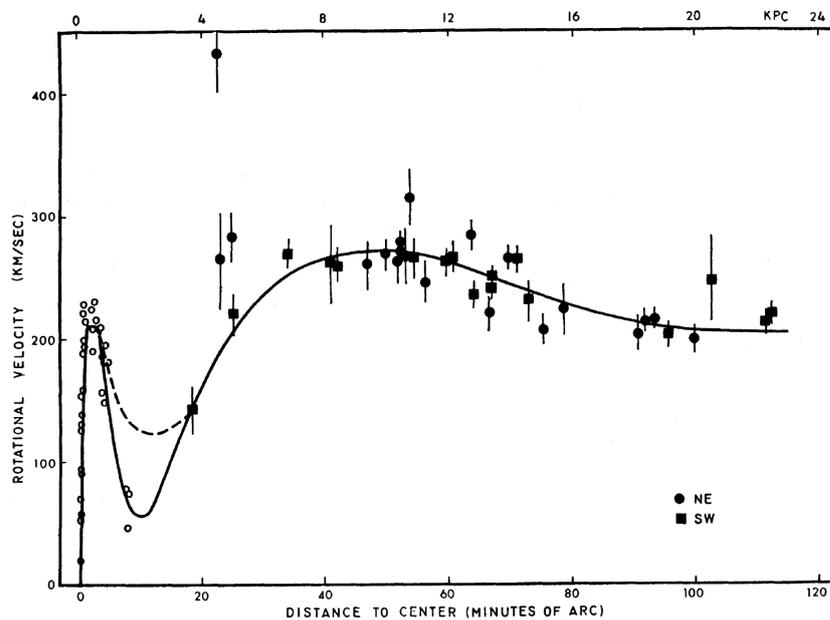
Figure 1.3: Rubin and Ford's plot of stellar orbital speed vs. radial distance from the galaxy centre of M31 [15].

Ten years later, Rubin and Ford, along with their colleague Norbert Thonnard, published a paper of galaxy rotation curves for 21 Sc classification galaxies; those with small nuclei, spiral arms and large pitch angles [16]. The conclusion of this research was that, regardless of the luminosity or size of the galaxy, all showed rotation curves which

19

did not fall over radial distance, in contradiction with all gravitational models. From this, they deduced the existence of significant mass from non-luminous matter at larger radii, providing further evidence for dark matter.

Collectively, the works by Babcock, Rubin, Ford and Thonnard became known as the *galaxy rotation problem*. This problem encompasses the observed discrepancy in mass profiles between those measured from mass-to-luminosity ratios and those calculated from rotation curves and the theory of gravity as it was understood.

In 1970, the Australian astronomer and astrophysicist Ken Freeman proposed a solution to the galaxy rotation problem [17]. Freeman posited that the rotation curve could be explained through a two-component mass model; galaxies could be composed of a centrally-concentrated spheroid and an invisible contribution that is distributed exponentially throughout the galaxy – a phenomenon which would later become known as the *dark matter halo*. When commenting on the flattened rotational curve of the spiral galaxy NGC 300, Freeman remarked:

> "If the [rotation curve] is correct, then there must be undetected matter beyond the optical extent of NGC 300; its mass must be at least of the same order as the mass of the detected galaxy."

Later, in 1985, the cumulative dark matter halo mass of the galaxy NGC 3198 was calculated using the observed rotation curve with surface photometry, as shown in Figure 1.4 [18]. From the result of this they estimated a galactic dark matter composition at upwards of 83%, concluding:

> "Using this curve, we find that the minimum amount of dark matter associated with NGC 3198 inside 50 kpc is probably at least 6 times larger than the amount of visible matter; thus, for the galaxy as a whole."

However, one should note that this dark matter halo is not a necessity for galactogenesis. In April 2019, a team led by Pieter van Dokkum of Yale University published a paper on the velocity dispersion of NGC1052-DF2, an ultra diffuse galaxy [19]. They noted that there was little to no dark matter present within the galaxy.
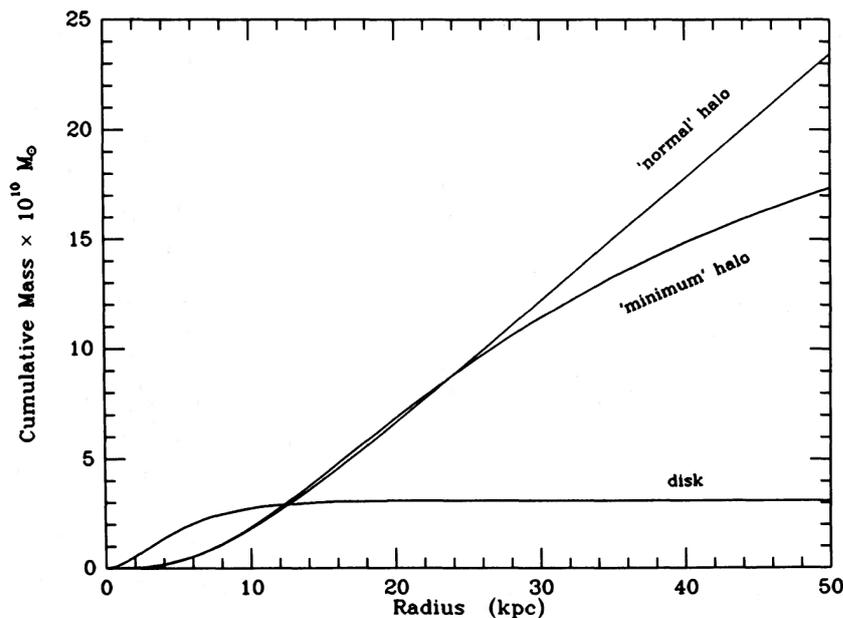
Figure 1.4: Cumulative mass distributions of galactic components with radius. The curve labelled "disk" indicates measured quantities of mass in the observable galactic disk and the curves labelled "'normal' halo" and "'minimum' halo" are estimates of dark matter distribution according to different theoretical models [18].

1.1.3   The Cosmic Microwave Background

The Wilkinson Microwave Anisotropy Probe (WMAP) was a satellite which was operated by NASA and Princeton University between 2001 and 2010 [20]. Its purpose was to measure regional temperature differences in the remnant heat of the Big Bang in the form of the Cosmic Microwave Background (CMB). The final results of the nine year data collection period found a baryonic matter density of $\Omega_b h^2 = 0.02223$, where h is Planck's constant, and a dark matter density of $\Omega_c h^2 = 0.1153$, indicating that 83.8% of all matter is dark [21].

The successor to WMAP, the European Space Agency's Planck spacecraft, was launched in 2010 with a number of objectives, including improving the resolution of measurements by its predecessor [22]. By combining the data of multiple measurements, Planck calculated a baronyic matter density of $\Omega_b h^2 = 0.02227$ and a dark matter density of $\Omega_c h^2 = 0.1184$, increasing the dark matter abundance ratio inferred by WMAP to 84.2% [2, p. 388].

1.1.4   Summary

Combining the considerable evidence presented, over the past century physicists have not only inferred the existence of dark matter, but also deduced a number of its properties.

Firstly and fundamentally, dark matter must be "dark", which is to say that it emits and absorbs negligible levels of electromagnetic radiation. The justification for this conclusion is elementary: if this were not the case then dark matter would already have been observed. However, dark matter is not inert to all fundamental forces since it must be able to interact gravitationally due to those being the methods by which its existence was inferred.

Since the effects of dark matter were observed in the CMB, one concludes that it must have been produced during the big bang. Furthermore, dark matter must be stable, since its effects are still observable, nearly 14 billion years later. Finally, for dark matter to exist in stable orbit throughout galaxies, its speed must be relatively slow, thus ruling out the prospect of it being massless. However, this orbital stability is not the only consideration when discussing the mass ranges of dark matter candidates; depending on the models used in theorising their existences, these masses can vary by dozens of orders of magnitude. For example, some dark matter models posit sub-electronvolt hypothetical elementary particles as their primary candidates, while others prefer much larger objects which can range from small planets to supermassive black holes.

1.2   The Dark Matter Candidate Menagerie

Since the first evidence hinting the existence of dark matter, a plethora of theories have arisen in attempts to account for the observations. This section will outline the three dark matter candidates (DMCs) of interest in this thesis, namely axions, dilatons and dark photons.

1.2.1   Axions

The axion is a well motivated hypothetical particle which was originally theorised to explain one of the foremost unanswered questions of modern fundamental physics – the Strong CP Problem – and has been hailed as a suitable candidate for dark matter.

1.2.1.1   The Strong CP Problem

Quantum ChromoDynamics (QCD) is the theoretical framework which governs our understanding of the strong interaction. Within the QCD Lagrangian there exists a term, colloquially referred to as the "θ term" owing to its leading dimensionless parameter;

$$\mathscr{L}_\theta = \theta \frac{1}{32\pi^2} G_{a\mu\nu} \widetilde{G}_a^{\mu\nu},$$

where G is the gauge field tensor and $\widetilde{G}_{a\mu\nu} = \frac{1}{2}\epsilon_{\mu\nu\rho\sigma} G_a^{\rho\sigma}$ its dual. Whilst this term conserves charge conjugation, it violates both parity and time inversions, the latter of which being equivalent to CP violation by the CPT theorem, the latter of which was initially recognised and formulated by Gerhart Lüders and Wolfgang Pauli, and further developed by Res Jost [23–26]. Since there is no reason to assume that θ takes any particular value, one deduces that QCD theory predicts a manifestly observable violation of CP symmetry. This is a problematic conclusion because there exists no experimental evidence supporting such a conclusion from any interactions mediated by the strong force; this apparent contradiction between theory and observation is the *Strong CP Problem*. Since the value of θ is a priori unknown, one may naïvely argue that by naturalness it should take a value of order unity. However, measurement of the neutron electric dipole moment – which is non-zero by the Strong CP Problem – has set a stringent constraint on this parameter, narrowing it down to $|\theta| \lesssim 10^{-10}$ [27]. The Strong CP Problem may hence be reformulated as a fine-tuning problem: Why should θ be so small instead of order unity, as expected by arguments of naturalness?

Among the solutions to this problem include massless quarks and argumentation by fine tuning i.e. it is what it is because it must be. However, arguably the best motivated solution is the introduction of a new particle which necessarily solves the Strong CP Problem: the axion.

1.2.1.2   The Axion Solution

In 1977, the physicists Roberto Peccei and Helen Quinn proposed a new anomalous global chiral U(1) symmetry on the Standard Model, the eponymic Peccei-Quinn symmetry [28, 29]. This would necessarily be spontaneously broken, in such a manner that it exactly counters the CP violation from QCD, such that the CP symmetry is automatically restored. In the following year, Steven Weinberg and Frank Wilczek noted that this symmetry breaking was tantamount to promoting the θ parameter to a dynamical field, thus introducing a new pseudo-Nambu-Goldstone boson, which Wilczek coined the

axion [30, 31]. During his 2004 Nobel lecture, Frank Wilczek spoke of this coinage; "I named them after a laundry detergent, since they clean up a problem with an axial current" [32]. In the same paper in which he coined the axion, Wilczek also calculated its expected mass to be of order $100\,\mathrm{keV}\,\mathrm{c}^{-2}$.

1.2.1.3   Searches

Over four decades since its original theorisation, the axion yet remains elusive. Initial axion searches during the late 1970s and early 80s used accelerator- and reactor-based facilities to explore the predicted mass regions, see e.g. [33–37]. These experiments had quickly and definitively ruled out the original Peccei-Quinn-Weinberg-Wilczek axion.

However, hope was not lost for the existence of the axion, merely its original formulation. First posited in 1979 by the South Korean physicist Kim Jihn-eui, so-called *invisible axions* are still able to resolve the Strong CP problem while instead taking masses of order electronvolt to sub-electronvolt [38]. Kim's theory would be incorporated with a 1980 paper by Mikhail Shifman, Arkady Vainshtein and Valentin Zakharov, to form the eponymous KSVZ model [39]. Shortly thereafter, a second invisible axion model came to fruition, the Dine–Fischler–Srednicki–Zhitnitsky (DFSZ) model [40, 41]. The coupling constant of members of the axion family – more often referred to as axion-like particles (ALPs) – to two photons is given by $g_{a\gamma\gamma} = \frac{\alpha}{2\pi f_a}\left(\frac{E}{N} - 1.92(4)\right)$, where α is the fine structure constant, f_a denotes the axion decay constant, and $\frac{E}{N}$ denotes the ratio of the electromagnetic and colour anomalies of the axial current associated with the axion [42, §91.2.2]. The KSVZ and DFSZ formulations, which respectively have $\frac{E}{N}$ values of 0 and $\frac{8}{3}$, are the current contending axion models of concern for this thesis. Not only do they solve the Strong CP Problem, but they may also account for dark matter in the Universe [43–45]. Specifically, cosmological invisible axions are theorised to be charge-neutral, non-relativistic and collisionless, and exist in sufficient quantity to exhibit observed behaviours [46].

Axion searches can be broadly generalised into three categories: haloscopes, helioscopes and laboratory-based optical. Invented for axion detection by Pierre Sikivie in 1983, haloscopes search galactic dark matter halos for signature signals which would indicate the existence of axions [47]. Within the same paper, Sikivie also proposed helioscopes for axion detection, which look to detect axions produced in stars, most commonly within the solar core. Finally, laboratory-based optical experiments direct laser pulses

through inhomogeneous magnetic fields which polarise the beam – a non-vanishing result would indicate the existence of a background axionic field. An example from each of these categories will now be presented, however readers should note that these are by no means isolated instances of their respective experimental classes.

ADMX

The Axion Dark Matter eXperiment (ADMX) is a haloscope searching the local galactic dark matter halo for signals of axionic matter [48]. The operation of haloscopes uses the theorised behaviour that axions are able to couple to two photons. Through interacting an axion with an external magnetic field, one is able to stimulate the decay of axions into photons of frequency corresponding to that of the magnetic field (later covered in Section 1.3.1), which would result in an observable increase in the cavity's magnetic field strength. The ADMX haloscope utilises a narrowband microwave resonant cavity which is capable of surveying the microwave sector of the electromagnetic spectrum, bandwidth by bandwidth. By iteratively scanning frequency ranges, ADMX is able to either exclude axion mass regions or infer their existence through the detection of a signal at a characteristic frequency. In the words of ADMX co-spokesman Gray Rybka [49], "If you think of an AM radio, it's exactly like that [...] We've built a radio that looks for a radio station, but we don't know its frequency. We turn the knob slowly while listening. Ideally we will hear a tone when the frequency is right."

CAST

Situated in Geneva, Switzerland, the CERN Axion Solar Telescope (CAST) [50] is a modern example of a helioscope which is designed to detect axions streaming from the Sun. The CAST experiment repurposes a decommissioned test magnet from the Large Hadron Collider (LHC) to stimulate the decay of solar axions into detectable photons through the same process as ADMX. The thermal spectrum of solar axions has an average energy of $4.2\,\mathrm{keV}$, thus placing their decay photons firmly within the X-ray region of the electromagnetic spectrum [51]. In 2017 the CAST collaboration published results constraining the mass coupling to $g_{a\gamma\gamma} \lesssim 0.66 \times 10^{-10}\,\mathrm{GeV}^{-1}$, and $m_a \lesssim 10^{-1}\,\mathrm{eV}$ [52].

PVLAS

Initially proposed in 1991 as a means of measuring quantum electrodynamical effects, the Polarizzazione del Vuoto con LASer (PVLAS) experiment is a laboratory-based axion search located in Ferrara University, Italy [53]. The experiment uses a high finesse Fabry-Perot etalon to investigate a background axion field through measuring the induced

polarisation of a laser beam directed through a strong inhomogeneous magnetic field under vacuum. The interaction between the laser and magnetic field photons should produce axions, which within the KSVZ and DFSZ models are known massive, hence travel at subluminal speeds in vacuo. As such, once the axion decays back into photons, one would expect to observe a phase difference in the measured electric field which would mimic ellipticity. In 2006, the PVLAS collaboration reported a non-vanishing rotation in the polarisation of their laser beam following 44,000 passes of the magnetic field [54]. From this observation, they deduced the existence of a light, neutral, spin-zero particle – alluding to the axion – however, they excluded this conclusion two years thereafter when they failed to replicate the outcome, citing instrumental artefacts as the source of the original signal [55].

Over the last forty years, numerous experiments have explored various axion models and decay modes, however – due to the specifics of the equipment – each setup can only be sensitive to specific domains of mass and coupling. For example, the Compton wavelength of a particle is inversely proportional to its mass, thus larger detectors are required to measure smaller particle masses. Further considerations when discussing the sensitivity of experimental particle physics detection include, but are not limited to, the effective quality factor of the detector, the types of signal amplifiers and the system temperature. The experimentally excluded areas in ALP mass-di-photon-coupling parameter space are shown in Figure 1.5. In general, ALP masses and di-photon coupling constants are free parameters, thus their pairing may reside anywhere within the parameter space. However, QCD axion theoretical models (including "invisible" axions) scale one parameter relative to the other, resulting in the diagonal yellow band, which incorporates a typical range of $\frac{E}{N}$ values.

Highly sensitive haloscopes, such as ADMX, are able to fine tune their electromagnetic frequencies for precision measurements over small mass regions, resulting in thin mass ranges extended over many orders of magnitude of coupling. Meanwhile, less attuned helioscopes, such as CAST, are able to probe much broader mass regions at lower coupling resolutions.

1.2.2 Dilatons

Generically, the *dilaton* (also known as the *radion*) refers to both the scalar field and its associated hypothetical particle which arise in $n > 4$-dimensional theories. Mathemat-
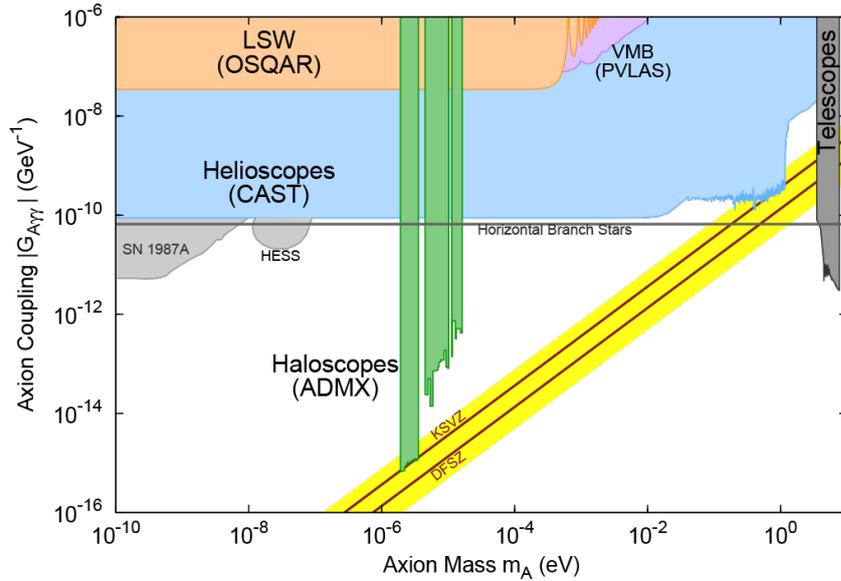
Figure 1.5: Axion exclusion plot in mass-coupling parameter space [2, p. 822]. QCD axions are constrained to within the diagonal yellow band. The vertical green columns indicate the parameter space regions investigated by haloscopes, including ADMX. The horizontal blue region denotes the cumulative parameter space volume for helioscope experiments such as CAST. Further coloured regions illustrate investigation areas for specific experiments.

ically, the dilaton is the result of redefining a theory from a higher-dimensional space onto four-dimensional spacetime through a process known as compactification, in the process generating a pseudo-Nambu-Goldstone boson [56].

1.2.2.1   Searches

From the perspective of particle physics, dedicated experimental dilaton searches are non-existent and those non-dedicated are scarce afterthoughts. With that said, in 2015 an Israeli team constrained the parameter space in which the dilaton may reside based upon LHC data and cosmological observations, ultimately concluding that current collider experiments are not yet sensitive enough to directly measure them [57]. However, there exist recent experimental proposals for dedicated dilaton searches.

A 2015 paper headed by Greek theoretical physicist Asimina Arvanitaki outlined the potential for atomic clocks to be used in detecting dilatons [58]. According to this paper, fundamental constants undergo coherent oscillations caused by scalar couplings between dark matter and the Standard Model at a frequency determined by the mass of the dark matter candidate. As such, atomic energy levels – which are proportional to the fine structure constant – would oscillate. Therefore, atomic clocks, with their extremely high

precisions, could be utilised to search for signature dilatonic signals in these oscillations.

1.2.3 Dark Photons

Since the discovery of the Z boson by the UA2 experiment in 1983, particle physicists have been interested in the possibility of finding other massive neutral vector bosons, generally denoted A' [59]. Located in the *dark sector* of particle physics – a collection of yet unobserved hypothetical quantum fields and associated particles – the *dark photon* (also called the *para-*, *secluded*, *heavy* or *hidden sector* photon) is the hypothetical particle resulting from an additional Abelian U(1) gauge symmetry on the Standard Model.

The dark photon, denoted γ', is able to couple to the Standard Model photon at arbitrarily high energies through the exchange of messenger particles [60]. Furthermore, the dark photon is able to very feebly couple to other Standard Model particles through this kinetic mixing, consequently inducing minor shifts in charge $e' = \epsilon e$, where ϵ is a small dimensionless parameter, akin to a coupling constant, and e is the elementary charge. The dark photon – unlike its Standard Model counterpart – assumes an arbitrary mass [61], with the current favoured region of experimental interest being 10 to 1000 MeV, as evidenced by the exclusion plot in Figure 1.6.

1.2.3.1 Searches

As with ALP searches outlined in Section 1.2.1.3, the particulars of each experiment are dependent on several factors which are specific to each setup. Laboratory-based searches for dark photons generally utilise particle accelerator beams to explore a variety of production and decay modes. The following outlines two such experiments.

BaBar

Initially designed for the detection of CP violation in the B meson system, the BaBar experiment – named for the B meson and its antiparticle ($\bar{B}$, pronounced B-bar) – is based at the Stanford Linear Accelerator Center National Accelerator Laboratory (SLAC), California, USA [66]. Utilising the SLAC linear electron accelerator and PEP-II electron storage ring facilities, the BaBar detector houses the collider interaction point, from which location by-products originate. The collision energy in the centre-of-mass frame is such that $\Upsilon(4S)$ and B mesons are produced at a very high rate with little momentum in the laboratory frame, resulting in a short travel distance prior to decay,
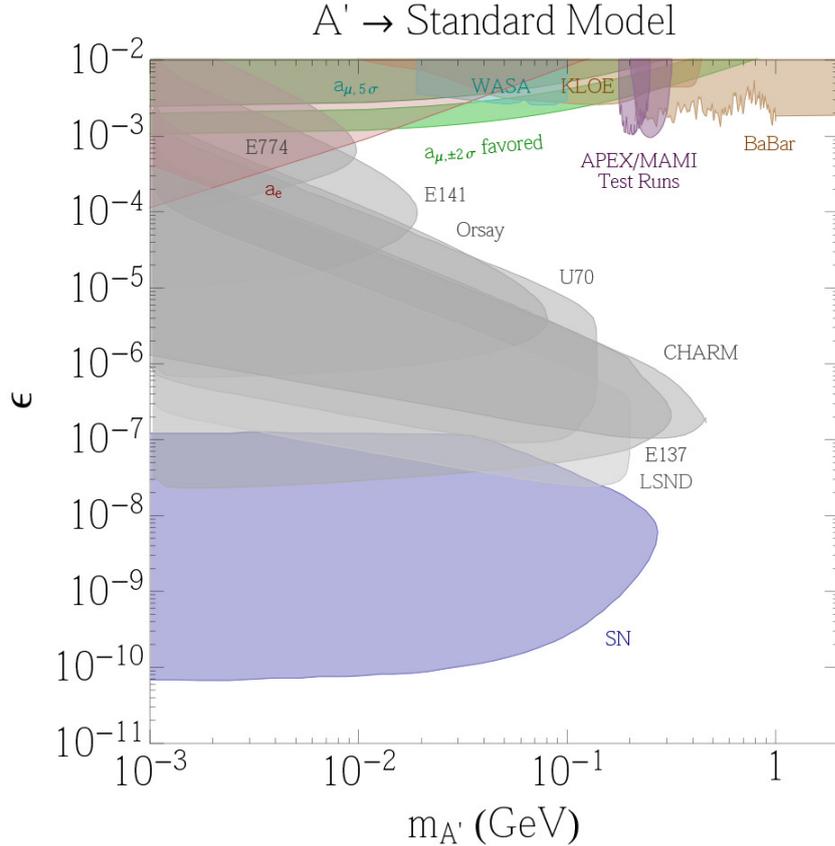
Figure 1.6: Exclusion plot of the hidden sector gauge boson (A') in $m_{A'}$-ϵ space [62]. The large blue-purple region labelled "SN" denotes the cumulative exclusion zones of supernovae observations, see e.g. [63, 64]. The grey E137, E141 and E774 zones indicate accelerator beam dump experiments at SLAC and FermiLab [63, 65]. Smaller, more colourful, regions demonstrate specific experimental investigations.

thus affording high precision measurements. A 2017 paper from the BaBar Collaboration analysed the four-momenta of by-products from e^+e^- collisions, in search of events with missing energy and momentum congruent with the production of an undetected spin-1 particle [67]. The result of this found no evidence for its existence in the mass range $0 \lesssim m_{\gamma'} \lesssim 8\,\mathrm{GeV}$ for $\epsilon \gtrsim 10^{-3}$.

APEX

The A' EXperiment (APEX), based in the Thomas Jefferson National Accelerator Facility (JLab), Virginia, USA, is a contemporary experiment dedicated to the search for new vector bosons [68]. The search for these particles utilises the Continuous Electron Beam Accelerator Facility's beam to measure various modes of dark photon production and decay in the electron system, e.g. $\gamma' \to e^+e^-$ [69].

1.3   Light Shining Through Walls

In name, light shining through wall (LSW) methodology appears rather paradoxical: How does one shine a light through a wall? The underlying premise of this experimental approach lies with the ability of feebly interacting particles to traverse an absorbing medium. Once the absorber has been navigated, these particles may decay naturally or through stimulation, the by-products of which being more readily detected, e.g. photons. As such, one is able to measure "light" which has originated outside the confines of a chamber, thus coining the methodology's moniker.

Since it is known a priori that dark matter candidates must have very slight interactions with ordinary matter, otherwise they would already have been detected, the LSW technique befits dark matter searches. The basis for these pivots on the dark matter candidate having the ability to traverse an otherwise impenetrable absorbing medium, e.g. the Earth, relatively unimpeded. A number of existing experiments attempt to stimulate dark matter candidates to decay into photons through the *Primakoff effect*. For further information on LSW methodology, see Javier Redondo and Andreas Ringwald's 2011 paper [70].

1.3.1   The Primakoff Effect

In 1951, the Russian theoretical physicist Henry Primakoff proposed a method of measuring a lower bound for the lifetime of the π^0 meson [71]. This method used the fact that the cross-section for photoproduction of a decaying neutral meson in the Coulombic field of a heavy nucleus is inversely proportional to its lifetime, illustrated in Figure 1.7, a process now known as the *Primakoff effect.*
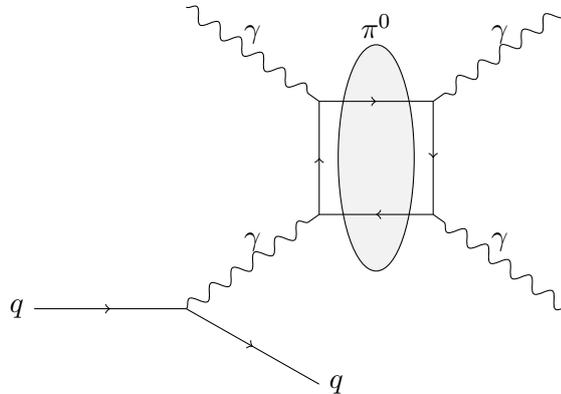
Figure 1.7: Schematic of the Primakoff effect.

Through this phenomenon one can also prompt particles to decay into products which are potentially easier to detect, e.g. ALPs can be stimulated to decay through coupling to a virtual photon via a powerful transverse magnetic field, resulting in a single photon carrying the same four-momentum as the original axion, as shown in Figure 1.8. Since, classically, magnetic fields are unable to do work, energy is conserved when $m_a c^2 \sim \hbar \omega$ (excluding kinetic energy), thus the resultant photon's frequency can be used to calculate the ALP mass.
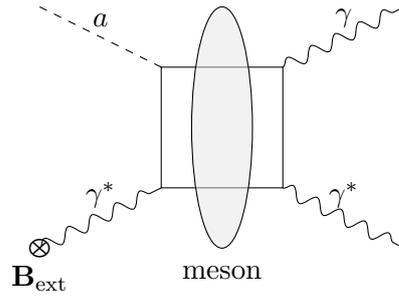
Figure 1.8: Axionic reverse Primakoff effect. A strong external magnetic field is able to stimulate axion decay into photons.

1.4   Physical Systems and Tools

With the purpose of this thesis being the exploration of novel laboratory-based searches for dark matter candidates, attention must now turn to the physical systems of interest and tools to be utilised.

1.4.1   Laser Wake Field Acceleration

Canonically, the inception of Laser Wake Field Acceleration (LWFA) is taken to be John Dawson and Toshiki Tajima's 1979 paper in which they proposed a novel method of accelerating electrons through the exposing an electron-ion plasma to intense electromagnetic pulses [72]. However, the idea of utilising a plasma as the medium of acceleration predated Tajima and Dawson; in his 1956 paper the Soviet experimental physicist Vladimir Veksler qualitatively described a novel principle of particle acceleration [73].

When an electromagnetically-interacting beam is directed through a plasma, one transversely drives the plasma electrons outward from the centre through a ponderomotive ("mass moving") force while leaving the much heavier ions relatively unperturbed, thus establishing a space-charge separation. The central region of positive charge strongly attracts the peripheral electrons back inward, whereupon they overshoot their

original positions, pass one another to then reach the opposite extremity to then be drawn back, repetitio ad nauseam, forming a density perturbation known as a *wake field.* Veksler noted that these oscillations within the plasma – a phenomenon first observed by Lewi Tonks and Irving Langmuir in the late 1920s [74] – held the capacity to generate electric fields orders of magnitude greater than those available through traditional resonance accelerators. However, despite the potential of his acceleration methodology, Veksler recognised that he had not sufficiently developed the theory for experimental application, writing:

> "Although the practical development of the ideas set forth below is still far from clear in all its details, the author assumes it is possible, by this means, to approach the problem of constructing accelerators for very high currents and super-high energies of the order 10^{12} eV and even more."

Four years thereafter, the Ukrainian physicist Ya Faĭnberg explicitly outlined [75] a mechanism by which one could accelerate charged particles via plasma oscillations building upon Veksler's principle, commenting:

> "Veksler very quickly realized the possibilities that might be made available by the use of an electron-ion plasma for the acceleration of charged particles."

The combined works of Veksler and Faĭnberg set up the foundations of wake field acceleration, however they both envisioned plasma oscillations being driven by a particle beam. In contrast, Tajima and Dawson proposed a laser-driven wake field accelerator. By directing an intense short laser pulse at a gas jet, the photons are able to ionise the constituent atoms, forming a quasi-neutral plasma while simultaneously exciting oscillations. Correctly phased plasma electrons can then become trapped within this wake, greatly accelerating them within a short distance, as shown in Figure 1.9.

The intensity of the laser in relation to the plasma discriminates two schemes of LWFA: either the electrons in the wake field undergo periodic sinusoidal oscillations (linear regime) or are fully expelled to form a cavity following the pulse (non-linear or bubble regime). The standing oscillations of the electrons produce a transverse electric field, whereas their collective oscillatory movements create a longitudinal electric field. These acceleration gradients are capable of reaching levels of order TeV m^{-1},
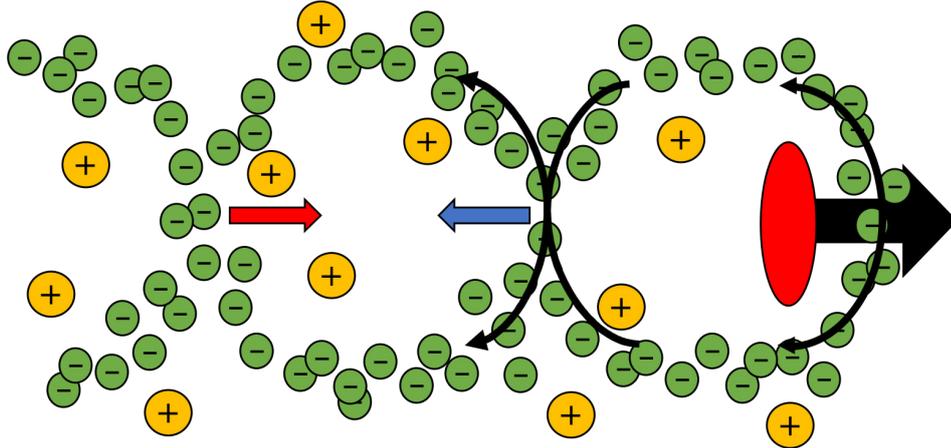
Figure 1.9: Graphical representation of laser wake field acceleration. The laser pulse (red ellipse) expels plasma electrons (green circles) transversely outward, leaving regions of excess positive charge due to significantly heavier ions (orange circles) being moved less by the laser. This space charge density imbalance results in the electrons being attracted back inward, overshooting equilibrium and forming a stationary wave comprised of "bubbles" following the laser. Within these bubbles are powerful alternating electric fields (red and blue arrows) which can be used for particle acceleration.

with currently realisable strengths of order $100\,\mathrm{GeV\,m^{-1}}$. An introduction to the theory underpinning LWFA is outlined in Chapter 3.

1.4.2   Photonic Band Gap Lattices

A *photonic band gap* (PBG) structure is a periodic and/or disordered structure comprised of dielectric materials [76]. These dielectric ensembles can be arranged in such a manner that the flow of electromagnetic radiation within the structure can be controlled. These manipulations include the localisation of photons to a region and the limitation of propagation to specific frequency ranges.

The phenomenon of photonic band gaps was first written about in 1887, when Lord Rayleigh discussed the interesting vibrational properties of one-dimensional periodic structures [77]. However, the foundational works on modern photonic band gap structures were two separate 1987 papers by Eli Yablonovitch and Sajeev John [78, 79]. In both papers the authors drew direct analogies to electronic behaviours in solid state matter in order to discuss similar phenomena exhibited by photons in dielectric structures. The generic term for the class of materials to which photonic band gap structures belong, *photonic crystals*, was coined by Yablonovitch and Thomas Gmitter in 1989 [80]. The relevant theoretical aspects of photonic band gap lattices are derived in Chapter 4.
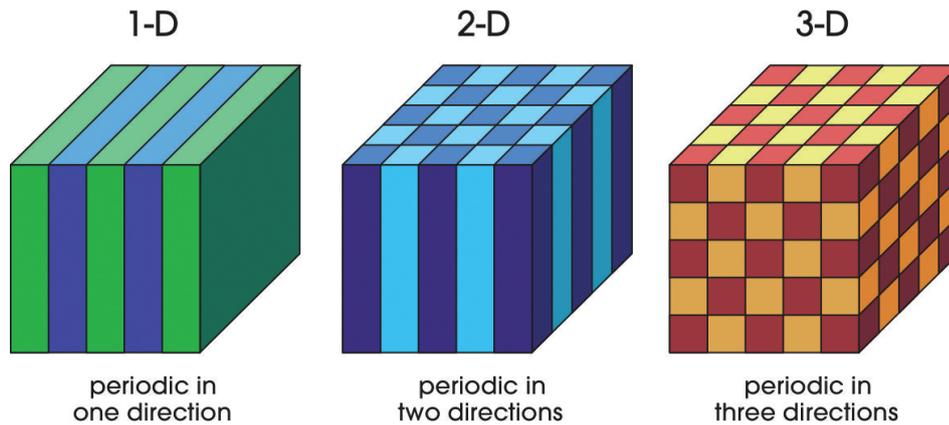
Figure 1.10: Periodic structures in one, two and three dimensions [81, §1].

1.4.3   Physical Simulation Codes

Until the early twentieth century, the foundations underpinning all physics revolved around the idea that every physical system can be fully described through deterministic equations, provided a set of initial conditions. In 1814, the French polymath Pierre-Simon Laplace articulated this idea through the eponymous *Laplace's demon*, writing [82, p. 4]:

> "We ought then to regard the present state of the universe as the effect of its anterior state and as the cause of the one which is to follow. Given for one instant an intelligence which could comprehend all the forces by which nature is animated and the respective situation of the beings who compose it – an intelligence sufficiently vast to submit these data to analysis – it would embrace in the same formula the movements of the greatest bodies in the universe and those of the lightest atom; for it, nothing would be uncertain and the future, as the past, would be present in its eyes."

Despite generations of efforts by theorists and mathematicians alike, the complete description of some physical systems appeared impervious to analytic calculation techniques. Whilst initially obeying deterministic equations, over a sufficiently long duration these systems diverged in behaviours subject to minute differences in initial conditions. The time-evolution of these systems were characteristically irregular and non-repeating, resulting in their being completely unpredictable on a long enough time scale. The French polymath Henri Poincaré was the first to note this behaviour, remarking [83, p. 397]:

"[I]t may happen that slight differences in the initial conditions produce very great differences in the final phenomena; a slight error in the former would make an erroneous error in the latter. Prediction becomes impossible and we have the fortuitous phenomenon."

Despite this, one is able to approximately model complex systems by discretising the deterministic equations and iteratively evolving the system in time. This algorithmic approach makes the application of computers in the simulation of these systems ideal. The two numerical techniques of note in this thesis are those of Finite Difference and Particle-in-Cell methodologies, which will be discussed in Chapter 5.

1.5   Recapitulation and Hypotheses

1.5.1   Recapitulation

Nearly a century has passed since initial observations predicated the advent of dark matter. The models theorised to explain this have been plenty, including such particles as the axion and dark photon, and despite decades of dedicated searches they have all either been discredited or remain elusive. These searches often employ light shining through wall methodology, in which the dark matter candidates traverse an impenetrable absorber, as a means of suppressing ambient signal.

1.5.2   Hypotheses

The purpose of this thesis is the exploration of two novel schemes of producing and detecting electromagnetically-interacting dark matter candidates through the application of light shining through wall methodology. The hypotheses in both cases are that the candidates of interest (a) can be produced, and (b) are able to arrive at the detector with a flux comparable to that of current best known sources, terrestrial or otherwise.

1.5.2.1   Axions from LWFA

The first proposition comes as an extension to David Burton and Adam Noble's 2018 paper [84]. The large acceleration gradients found in the wakes of plasma-based accelerators appear to offer passage to the laboratory-based production of axion-like particles since they are theorised to couple to electric and magnetic fields. As such, by subjecting the plasma channel to a powerful external magnetic field, one should be able to produce

these dark matter candidates. By generating these DMCs with a forward momentum, it is expected that their weakly interacting natures would allow them to negotiate an otherwise impenetrable barrier. Once traversed, the candidate could then be stimulated to decay back into photons through the reverse Primakoff effect, as shown in Figure 1.8, whereupon they could be detected, inferring the particle's existence as an intermediary. A proposed experimental schematic is shown in Figure 1.11.
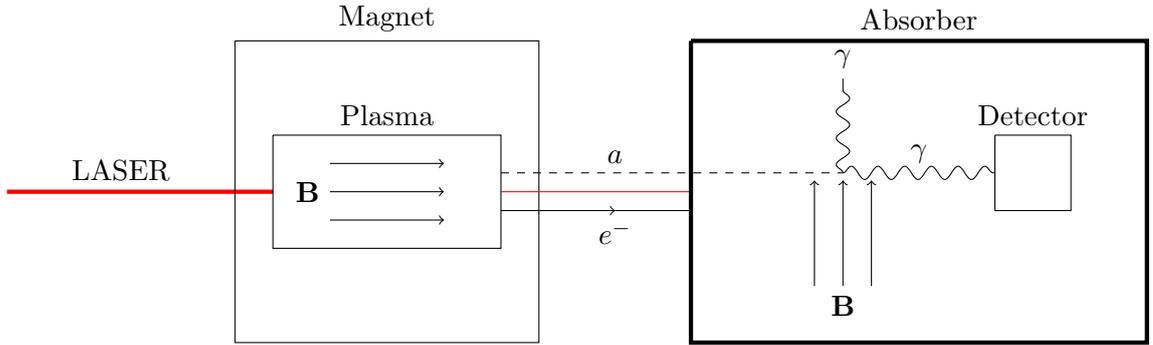
Figure 1.11: Schematic of proposed experimental setup using a plasma-based accelerator with light shining through wall methodology for the production and detection of ALPs.

1.5.2.2   Dark Photons from PBG Lattices

The second proposition is the application of a microwave resonant cavity for dark photon production and a photonic band gap lattice for detection optimisation.

One is able to effectively confine the region in which photons of a particular frequency can reside by periodically spacing a lattice of dielectric resonators. An example of suitable dielectric resonators are sapphire rods with relative permittivity $\epsilon_r \sim 9$ at room temperature for perpendicularly-polarised electromagnetic radiation in the low-frequency (~ 0 to 10^{13} Hz) limit [85], such that the traversal of specific wavelength bands are disallowed.

In the proposed experimental setup, one would situate a PBG lattice within a microwave resonant cavity. By introducing a defect to the system through the removal of rods, one enables the disallowed electromagnetic frequencies to inhabit these enclosed regions. Consequently, one can apply an electric field at these frequencies to one of the defects and it will be constrained to a significantly smaller radius than normally. As earlier mentioned, theory suggests that baryonic photons can kinetically mix into dark photons, which are feebly interacting. As such, these are able to traverse the band gap lattice, whereupon reverse mixing can occur. Consequently, by placing an antenna in

another defect sufficiently distanced from the origin, one would expect to measure the electric field in excess of that for a system in which the dark photon was not present, thus inferring its existence as an intermediary. One of the strengths of this methodology is that the detection of these signals provides unambiguous confirmation of the particle with a relatively small range of mass values. A schematic of this system is shown in Figure 1.12.
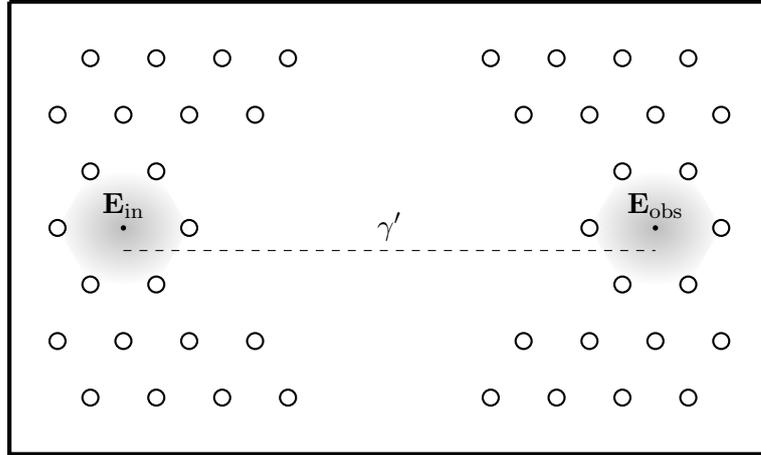
Figure 1.12: Schematic of proposed experimental setup using a photonic band gap lattice with light shining through wall methodology for the production and detection of HSPs. Circular nodes indicate dielectric rods. The central region devoid of rods denotes a continuation of the dielectric lattice of arbitrary distance. The intermediary rods between the defects of emission and detection provide effective shielding to prevent photons of particular frequencies from traversing the lattice.

Chapter 2

Theory: Particles

"Il apparut que, entre deux vérités du domaine réel,
le chemin le plus facile et le plus court passe bien
souvent par le domaine complexe."

— Paul Painlevé[1] [86]

2.1   Axions

2.1.1   The $U(1)_A$ Problem

Despite the early success of quantum chromodynamics (QCD) during its development in the 1960s and early 1970s, in 1975 Steven Weinberg noted a major failure of the model [88]. In the massless limit, the quark sector of the standard model bisects into chiral components, those for which the spin vector is aligned with the momentum vector (right-handed) and those for which these are anti-aligned (left-handed). Under this assumption of small up-, down- and strange-quark masses, i.e. much lower than the QCD energy scale $m_{u,d,s} \ll \Lambda_{\text{QCD}}$, the QCD Lagrangian has a global unitary chiral symmetry, the axial $U(1)$ symmetry given by the rotations

$$q_k \mapsto e^{i\gamma_5\theta} q_k,$$

where $\gamma_5 \equiv i\gamma_0\gamma_1\gamma_2\gamma_3$ is the "fifth" Dirac gamma matrix and θ is a parameter which takes the same value for all "massless" quark flavours $q_k \in \{u, d, s\}$. This transformation introduces a phase $e^{i\theta}$ in the right-handed quarks and a phase $e^{-i\theta}$ in the left-handed quarks. If this symmetry is conserved then one expects to observe a hadronic parity doubling, i.e.

---

[1] "It appeared that, between two truths of the real domain, the easiest and shortest path quite often passes through the complex domain". A similar later quote is attributed to Jacques Hadamard [87].

the existence of opposite parity states with equal spin values, but to this end no evidence exists. If instead this symmetry were violated, the result would be the addition of two new isoscalar 0^- bosons. The first of these Weinberg identified as being the π^0 meson, whereas the second was calculated to have an upper mass limit $\sqrt{3}\,m_{\pi^0} \approx 240\,\mathrm{MeV\,c^{-2}}$. However, by that time this region had already been thoroughly investigated and the closest suitable candidate was the η meson, of mass $m_\eta \approx 548\,\mathrm{MeV\,c^{-2}}$ – twice that of the theoretical maximum. This prediction, but apparent non-existence, of either a hadronic parity doubling or an appropriate η particle was dubbed the $U(1)_A$ *Problem*.

2.1.2 The Strong CP Problem

An initial solution to the problem appeared to lie in the axial symmetry's associated *anomaly* (a classical symmetry that is broken within quantum theory) [89–91]. The divergence of the U (1)-associated axial current J_5^μ receives quantum corrections from two gluons, connected to it via a quark triangle loop, as illustrated in Figure 2.1.
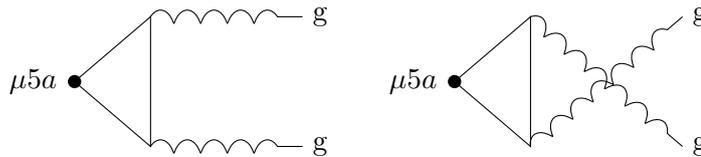
Figure 2.1: Graphs resulting in an axial anomaly in the QCD chiral current. Reproduced from Peskin and Schroeder [92, §19.3].

The result of these graphs is that the QCD chiral current receives a non-zero divergence [93, §1.1]:

$$\partial_\mu J_5^\mu = \frac{g_s^2 N}{32\pi^2} G_a^{\mu\nu} \widetilde{G}_{a\mu\nu},$$

where N is the number of quark flavours, g_s is the strong coupling strength, G is the gauge field tensor and $\widetilde{G}_{a\mu\nu} = \frac{1}{2}\epsilon_{\mu\nu\alpha\beta}G_a^{\alpha\beta}$ its dual. From this, one sees that in the massless quark limit under U $(1)_A$ transformations $q_k \mapsto e^{i\alpha_s \gamma_5/2}q_k$, the current is invariant. However, under the same transformation the chiral anomaly also affects the action, $\mathscr{S}$, in a non-vanishing manner as

$$\delta\mathscr{S} = \alpha_s \int \mathrm{d}^4x \, \partial_\mu J_5^\mu = \alpha_s \frac{g_s^2 N}{32\pi^2} \int \mathrm{d}^4x \, G_a^{\mu\nu} \widetilde{G}_{a\mu\nu}.$$

Noting that the new pseudoscalar density can be written as the total divergence of some current, i.e.

$$G_a^{\mu\nu} \widetilde{G}_{a\mu\nu} = \partial_\mu K^\mu,$$

with [94]

$$K^\mu = \epsilon^{\mu\alpha\beta\gamma} A_{a\alpha} \left(G_{a\beta\gamma} - \frac{g_s}{3} f_{abc} A_{b\beta} A_{c\gamma} \right),$$

then by Gauss' theorem one may integrate the term to remove all terms excepting those located on surface boundaries.

In the year following Weinberg's outlining of the $U(1)_A$ problem, Gerard 't Hooft proposed that, in the presence of *instantons*[2], one is able to preserve the axial symmetry without the necessity of a new boson, thus solving Weinberg's $U(1)_A$ problem [96–98]. This effectively made the axial rotation not a true symmetry of QCD, despite apparently holding for the Lagrangian under the limit of massless quarks.

Noting that QCD has a non-trivial vacuum state which is comprised of a superposition of vacua of winding numbers ν, each belonging to its own homotopy class [99];

$$|\theta\rangle = \sum_\nu e^{-i\nu\theta} |\nu\rangle,$$

then one is able to show through path integral methodology that the vacuum-to-vacuum transition amplitude is given by

$$_+\langle\theta|\theta\rangle_- = \sum_\nu \int \mathscr{D}A \, e^{i\mathscr{S}_{\text{eff}}[A]} \delta\left(\nu - \frac{g_s^2}{32\pi^2} \int \mathrm{d}^4x \, G_a^{\mu\nu} \widetilde{G}_{a\mu\nu} \right),$$

where $\mathscr{D}A$ is the integral measure and $\mathscr{S}_{\text{eff}}[A] = \mathscr{S}_{\text{QCD}}[A] + \theta \frac{g_s^2}{32\pi^2} \int \mathrm{d}^4x \, G_a^{\mu\nu} \widetilde{G}_{a\mu\nu}$ is the effective action [93]. The QCD Lagrangian hence gains a non-vanishing term as a result of the vacuum topology:

$$\mathscr{L}_\theta = \theta \frac{g^2}{32\pi^2} G_a^{\mu\nu} \widetilde{G}_{a\mu\nu},$$

the addition of which begot its own issue. One should note that $G_a^{\mu\nu} \widetilde{G}_{a\mu\nu}$ can be similarly replaced by $F^{\mu\nu} \widetilde{F}_{\mu\nu}$, where $F^{\mu\nu}$ is the electromagnetic field tensor, which then describes additional interactions.

Under parity transformations, i.e. spatial coordinate inversion $\mathbf{x} \mapsto -\mathbf{x}$, the electric and magnetic fields transform as

$$\mathbf{E} \mapsto -\mathbf{E}; \qquad \mathbf{B} \mapsto \mathbf{B}.$$

Similarly, under time inversion transformations, i.e. temporal reversal $t \mapsto -t$, the electromagnetic fields transform as

$$\mathbf{E} \mapsto \mathbf{E}; \qquad \mathbf{B} \mapsto -\mathbf{B}.$$

---

[2]First proposed in 1975 by Alexander Belavin, Alexander Polyakov, Albert Schwartz and Yu Tyupkin as a means of minimising local actions of Yang-Mills theories, instantons describe the tunnelling between different degenerate vacua at spatial infinity [95].

Hence, by the CPT theorem, one sees that the additional θ term of the Lagrangian violates both spatial inversion and temporal reversal (consequently also charge-parity inversion by the CPT theorem) symmetries, a result which comes in stark contrast with the universal evidence that strong interactions conserve these symmetries to extremely high accuracy [100]. This blatant contradiction between theory and observation is known as the *Strong CP Problem*.

The Strong CP Problem is exacerbated when considering the effects of the chiral symmetry on the θ vacuum, which changes as

$$e^{i\alpha Q_5} \left| \theta \right\rangle = \left| \theta + \alpha \right\rangle,$$

where Q_5 is the associated axial charge [101]. Additionally, when expanding the theory to include weak interactions one gains a further Lagrangian term

$$\mathscr{L}_{\text{mass}} = \overline{q}_{iR} M_{ij} q_{jL} + \text{h.c.},$$

where $q_{i,j}$ are the quark fields with left- or right-handedness and M_{ij} is the quark Yukawa matrix, which in general may be complex. Consequently, in the full theory the effective θ parameter shifts as

$$\theta \mapsto \theta + \arg \det M.$$

2.1.3   The Axion Solution

In 1977, when faced with the Strong CP Problem, Roberto Peccei and Helen Quinn proposed a theory in which the θ parameter became a dynamical variable through an additional global U(1) chiral symmetry which is spontaneously broken at an unknown energy scale, the Peccei-Quinn or PQ symmetry [28,29]. The PQ mechanism causes this θ variable to relax such that its expectation value could take arbitrarily small values, effectively eliminating $\mathscr{L}_\theta$ and hence conserving CP symmetry in QCD. In the year following, Steven Weinberg and Frank Wilczek noted that the breaking of the PQ symmetry introduced a new Nambu-Goldstone boson which Wilczek coined the axion [30,31].

To illustrate how this mechanism resolves the Strong CP Problem, consider the introduction of a new field which couples to the quark Yukawa matrix via a phase term, a, to the overall Lagrangian [102, §16.6]:

$$\mathscr{L}_a = \overline{q} M e^{-ia} q + \frac{1}{2} \partial_\mu a \partial^\mu a.$$

Through performing an additional $U(1)_A$ transformation on the quark fields, the mass terms multiply to combine the various phase factors:

$$\mathscr{L}_a = \overline{q}\left(M e^{i(\theta + \arg\det M - a)}\right)q + \frac{1}{2}\partial_\mu a \partial^\mu a.$$

One can therefore encapsulate all CP violating contributions into the axion field through a shift

$$a \mapsto a + \theta + \arg\det M.$$

Due to the inclusion of mass terms in higher order perturbations, the axion is no longer theorised to be a Goldstone boson, but instead a pseudo-Nambu-Goldstone boson. The original Peccei-Quinn-Weinberg-Wilczek formulation of the axion was predicted to have a mass of order [30]

$$m_a \approx \frac{N_f m_\pi F_\pi}{2\sqrt{m_u + m_d}}\sqrt{\frac{m_u m_d m_s}{m_u m_d + m_d m_s + m_s m_u}}\frac{\sqrt[4]{2}\sqrt{G_F}}{\sin(2\alpha)} \approx 100\,\mathrm{keV\,c^{-2}},$$

where N_f is the number of "massless" quark flavours, $m_{u,d,s}$ are respectively the masses of the up, down and strange quarks, m_π is the pion mass, $F_\pi \approx 190\,\mathrm{MeV}$, G_F is the Fermi coupling constant and α is an unknown angle. If the axion were to exist with the mass calculated through Peccei-Quinn theory then it should have been discovered shortly following its prediction. However, more recent models predict the existence of axion-like particles with sub-electronvolt masses [38–41].

Below the scale of QCD chiral symmetry breaking, axions are able to minimally couple to two photons as illustrated in Figure 2.2, the Lagrangian for which is [100]

$$\mathscr{L} \supset -\frac{1}{4}g_{a\gamma\gamma}F_{\mu\nu}\widetilde{F}^{\mu\nu}a = g_{a\gamma\gamma}\mathbf{E}\cdot\mathbf{B}a,$$

where $g_{a\gamma\gamma}$ is the axion-photon coupling constant, F is the electromagnetic field tensor and $\widetilde{F}$ its dual.
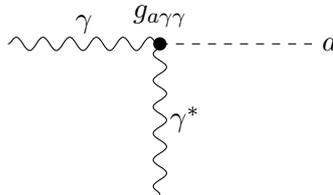
Figure 2.2: Axion-photon vertex for theories in which $g_{a\gamma\gamma} \neq 0$.

From this, the overall axion Lagrangian is

$$\mathscr{L} = \frac{1}{2}\partial_\mu a \partial^\mu a - \frac{1}{2}m_a^2 a^2 - \frac{1}{4}g_{a\gamma\gamma}F_{\mu\nu}\tilde{F}^{\mu\nu}a.$$

The Euler-Lagrange equation of motion of the axion is hence given by

$$\left(\partial_\mu \partial^\mu + m^2\right) a = -g_{a\gamma\gamma} \mathbf{E} \cdot \mathbf{B},$$

which one recognises as the inhomogeneous *Klein-Gordon equation.*

2.2   Dilatons

The dilaton is the particle of a scalar field which derives from $n > 4$-dimensional theories. For example, Kaluza-Klein theory was formulated in the first half of the twentieth century as a means of unifying general relativity and electrodynamics. In order to achieve this unification, Theodor Kaluza extended general relativity to five dimensions. The resulting metric tensor of this five-dimensional spacetime, $\tilde{g}_{ab}$, is given by

$$\tilde{g}_{ab} = \begin{pmatrix} g_{\mu\nu} + \phi^2 A_\mu A_\nu & \phi^2 A_\mu \\ \phi^2 A_\nu & \phi^2 \end{pmatrix},$$

where $g_{\mu\nu}$ is the standard four-dimensional metric tensor, A_μ is the canonical electromagnetic four-potential and ϕ is a scalar field which can be identified as the dilaton. Kaluza made a further ansatz to the fifth dimension, which he coined the cylinder condition. This condition stated that no field is dependent upon the fifth dimension, i.e. $\partial_5 \tilde{g}_{ab} = 0$, where ∂_5 denotes the partial derivative with respect to the fifth dimension. As a result of the cylinder condition, the additional scalar field ϕ, can be shown to obey a non-linear wave equation.

The Einstein-Hilbert action for pure gravity in 5 dimensions reduces, following a Weyl transformation of $g_{\mu\nu}$, to the Einstein-Hilbert-Maxwell [103, §X.1]:

$$S = \int \mathrm{d}^4 x \sqrt{-g} \left(M_p^2 R - \frac{1}{4} e^{\sqrt{3}\ell_p \varphi} F_{\mu\nu} F^{\mu\nu} - \frac{1}{2} g^{\mu\nu} \partial_\mu \varphi \partial_\nu \varphi \right),$$

where φ is a scalar field which can be identified as the dilaton, M_p is the Planck mass, R is the Ricci scalar, ℓ_p is the Planck length, and $F_{\mu\nu}$ is the canonical electromagnetic field tensor. Since the integrand is equal to the system Lagrangian, then the Euler-Lagrange equation of motion for ϕ becomes

$$\Box \varphi = \frac{\sqrt{3}}{4} \ell_p e^{\sqrt{3}\ell_p \varphi} F_{\mu\nu} F^{\mu\nu},$$

where $\Box \equiv g^{\mu\nu} \nabla_\mu \nabla_\nu$, with covariant derivative ∇_μ. Defining $\Phi = e^{\sqrt{3}\ell_p \varphi}$, then

$$\Box \varphi = \frac{\sqrt{3}}{4} \ell_p \Phi F_{\mu\nu} F^{\mu\nu}.$$

Noting that $\Phi \sim 1$ – but the same cannot necessarily be said for its derivatives – then

$$\Box\varphi = \frac{\sqrt{3}}{4}\ell_p F_{\mu\nu}F^{\mu\nu} \propto |\mathbf{E}|^2 - |\mathbf{B}|^2 \,,$$

from which one concludes the coupling of dilaton-like particles to electromagnetic fields. It should be noted that mass can be added within the theory through a variety of mechanisms, which would lead to an inhomogeneous Klein-Gordon formulation.

2.3   The Klein-Gordon Equation

2.3.1   Exposition

The eponymous Klein-Gordon equation is a relativistic second-order wave equation which was formulated by its namesakes Oskar Klein and Walter Gordon during the mid-1920s. The equation was initially proposed to describe the dynamics of relativistic electrons, however it did not account for spin, resulting in its modern interpretation as the equation of motion for massive spin-0 fields. In its most general form one, the inhomogeneous (sourced) Klein-Gordon equation for an interacting scalar or pseudoscalar field Ψ of mass m is given by

$$\left(\Box + m^2\right)\Psi\left(x\right) = \varrho\left(x\right),$$

where $\Box \equiv \partial^\mu\partial_\mu$ denotes the d'Alembertian differential operator, ϱ is the source, and x indicates the spacetime coordinate. In the cases of the ALPs and DLPs, the source term derives from the $\mathbf{E} \cdot \mathbf{B}$ and $\mathbf{E}^2 - \mathbf{B}^2$ couplings.

2.3.2   Solution to the Inhomogeneous Klein-Gordon equation

One is able to obtain a form of the field Ψ through Green's function methodology because the inhomogeneous Klein-Gordon equation is of the form $Lu\left(x\right) = f\left(x\right)$, where $L = L\left(x\right)$ is a linear differential operator acting on a solution $u\left(x\right)$, as the result of a source $f\left(x\right)$. The field can hence be written

$$\Psi\left(t_f, \mathbf{x}_f\right) = \int_\Omega G\left(t_f, \mathbf{x}_f \middle| t_s, \mathbf{x}_s\right)\varrho\left(t_s, \mathbf{x}_s\right)\mathrm{d}^4 x_s, \tag{2.1}$$

where the source has compact support Ω, i.e. it is closed and bounded.

The $\mathbf{x} \mapsto \mathbf{k}$ space Fourier transformed inhomogeneous Klein-Gordon equation is written

$$\ddot{\widetilde{\Psi}}_{\mathbf{k}} + k^2\widetilde{\Psi}_{\mathbf{k}} + m^2\widetilde{\Psi}_{\mathbf{k}} = \widetilde{\varrho}_{\mathbf{k}},$$

where $k \equiv \sqrt{\mathbf{k} \cdot \mathbf{k}}$ and $\widetilde{\varrho} = \int_{-\infty}^{\infty} e^{i\mathbf{k}\cdot\mathbf{x}} \varrho \, \mathrm{d}^3\mathbf{x}$. The dispersion relation for this can then be defined by $\omega := \sqrt{k^2 + m^2}$ such that the inhomogeneous Klein-Gordon equation can be written as a driven simple harmonic oscillator in k-space;

$$\ddot{\widetilde{\Psi}}_{\mathbf{k}} + \omega^2 \widetilde{\Psi}_{\mathbf{k}} = \widetilde{\varrho}_{\mathbf{k}},$$

the solution to which is known to be (see Appendix C)

$$\widetilde{\Psi}_{\mathbf{k}}\left(t_f\right) = \int_{-\infty}^{t_f} \frac{\sin\left(\omega\left(t_f - t_s\right)\right)}{\omega} \widetilde{\varrho}_{\mathbf{k}}\left(t_s\right) \, \mathrm{d}t_s.$$

Inverse Fourier transforming this gives the value at each field point in x-space as

$$\Psi\left(t_f, \mathbf{x}_f\right) = \int_{-\infty}^{\infty} \int_{-\infty}^{\infty} \left[\frac{\Theta\left(t_f - t_s\right)}{(2\pi)^3} \right.$$
$$\left. \times \int_{-\infty}^{\infty} e^{-i\mathbf{k}\cdot\left(\mathbf{x}_f - \mathbf{x}_s\right)} \frac{\sin\left(\omega\left(t_f - t_s\right)\right)}{\omega} \, \mathrm{d}^3\mathbf{k} \right] \varrho\left(t_s, \mathbf{x}_s\right) \, \mathrm{d}t_s \, \mathrm{d}^3\mathbf{x}_s, \quad (2.2)$$

where $\Theta\left(\cdot\right)$ is the Heaviside step function. Comparing this with Equation (2.1), one concludes that the bracketed term is the retarded Green's function solution to the inhomogeneous Klein-Gordon equation $G\left(t_f, \mathbf{x}_f \mid t_s, \mathbf{x}_s\right)$, which can be calculated exactly.

For notational brevity, the spatiotemporal differences will be defined as follows:

$$T = t_f - t_s;$$
$$\mathbf{X} = \mathbf{x}_f - \mathbf{x}_s.$$

Further, to aid in the simplicity of the calculation, the $\mathbf{k}$ space coordinate system will be transformed to spherical polars (k, θ, ϕ) orientated in such a manner that $\mathbf{k} \cdot \mathbf{X} = |\mathbf{k}| \, |\mathbf{X}| \cos\left(\theta\right)$, then the differential becomes $\mathrm{d}^3\mathbf{k} = k^2 \sin\left(\theta\right) \, \mathrm{d}k \, \mathrm{d}\theta \, \mathrm{d}\phi$ over intervals

$$\begin{cases} k \in [0, \infty); \\ \theta \in [0, \pi); \\ \phi \in [0, 2\pi). \end{cases}$$

Using these conventions, the Green's function can be shown to be

$$G\left(t_f, \mathbf{x}_f \mid t_s, \mathbf{x}_s\right) = \frac{\Theta\left(T\right)}{(2\pi)^2 X} \int_0^{\infty} 2k \sin\left(kX\right) \frac{\sin\left(\omega T\right)}{\omega} \, \mathrm{d}k,$$

where $X \equiv \sqrt{\mathbf{X} \cdot \mathbf{X}}$. Denoting the integral component $I\left(T, X\right)$, then by writing this so as to absorb the factor of k through the inclusion of a derivative, and exploiting the

symmetric behaviour of even functions to double the integration interval by introducing a factor of $\frac{1}{2}$, then

$$I\left(T, X\right) = -\frac{\partial}{\partial X} \int_{-\infty}^{\infty} \frac{\sin\left(\omega T + kX\right) + \sin\left(\omega T - kX\right)}{2\omega}\, \mathrm{d}k, \qquad (2.3)$$

where the trigonometric identity $\sin\left(\alpha \pm \beta\right) = \sin\left(\alpha\right)\cos\left(\beta\right) \pm \cos\left(\alpha\right)\sin\left(\beta\right)$ has been used. $I\left(T, X\right)$ will now be calculated for the regimes $T > X$ and $T < X$ separately. However, it should be noted that only $T > 0$ is necessary for the latter regime due to the Heaviside function present in Equation (2.2).

2.3.3 $\mathbf{T > X}$

Define T and X in terms of variables such that $T > X$:

$$\begin{cases} T = \lambda \cosh\left(\zeta\right) \\ X = \lambda \sinh\left(\zeta\right) \end{cases}$$

with $\lambda > 0$ and $0 < \zeta < \infty$ to avoid negative values of X. Further, as a result of these definitions, $\lambda = \sqrt{T^2 - X^2}$.

Writing $k = m\sinh\left(\xi\right)$, then $\mathrm{d}k = m\cosh\left(\xi\right)\mathrm{d}\xi$. Furthermore, by the earlier dispersion relation, then $\omega \equiv \sqrt{k^2 + m^2} = m\cosh\left(\xi\right)$ and thus $k = \omega\,\mathrm{d}\xi$. Therefore

$$\omega T + kX = m\lambda \cosh\left(\xi + \zeta\right),$$

from the trigonometric identity $\cosh\left(\alpha \pm \beta\right) = \cosh\left(\alpha\right)\cosh\left(\beta\right) \pm \sinh\left(\alpha\right)\sinh\left(\beta\right)$.

The Mehler-Sonine representation of the Bessel function of the first kind [104, §10.9.8] is

$$J_{\nu}\left(x\right) = \frac{2}{\pi} \int_{0}^{\infty} \sin\left(x\cosh\left(y\right) - \frac{1}{2}\nu\pi\right)\cosh\left(\nu y\right)\,\mathrm{d}y.$$

Using this identity, separately the terms of $I\left(T, X\right)$ are hence calculated to be

$$\int_{-\infty}^{\infty} \frac{\sin\left(\omega T + kX\right)}{\omega}\,\mathrm{d}k = \pi J_0\left(m\lambda\right);$$
$$\int_{-\infty}^{\infty} \frac{\sin\left(\omega T - kX\right)}{\omega}\,\mathrm{d}k = \pi J_0\left(m\lambda\right).$$

2.3.4 $\mathbf{T < X}$

As before, define T and X in terms of variables but this time such that $T < X$:

$$\begin{cases} T = \lambda \sinh\left(\zeta\right) \\ X = \lambda \cosh\left(\zeta\right). \end{cases}$$

46

Following the same procedure as previously, the first term

$$\int_{-\infty}^{\infty} \frac{\sin(\omega T + kX)}{\omega}\, \mathrm{d}k = \int_{-\infty}^{\infty} \sin\left(m\lambda \sinh\left(\xi'\right)\right)\, \mathrm{d}\xi'$$

where $\xi' = \xi + \zeta$. Since this is an integral over all space of an odd function, one is immediately able to conclude that it evaluates to zero, with the same applying for the second term of the integral.

2.3.5   Evaluating the Integral and Assigning Physical Interpretation

Combining the $T > X$ and $T < X$ cases;

$$\int_{-\infty}^{\infty} \frac{\sin(\omega T + kX) + \sin(\omega T - kX)}{2\omega}\, \mathrm{d}k = \begin{cases} \pi J_0(m\lambda) & T > X; \\ 0 & T < X \end{cases}$$

$$\equiv \Theta(T - X)\,\pi J_0(m\lambda),$$

then one sees that the integral $I(T, X)$ defined in Equation (2.3) evaluates to

$$I(T, X) = -\frac{\partial}{\partial X}\left(\Theta(T - X)\,\pi J_0(m\lambda)\right).$$

Using the differentiation identities [105, §13.1, §18.5]

$$\begin{cases} \dfrac{\mathrm{d}}{\mathrm{d}x}\,\Theta(x) = \delta(x); \\[2mm] \dfrac{\mathrm{d}}{\mathrm{d}x}\,J_0(x) = -J_1(x), \end{cases}$$

then the Green's function becomes

$$G\left(t_f, \mathbf{x}_f \,|\, t_s, \mathbf{x}_s\right) = \frac{\Theta(T)}{4\pi X}\left[\delta(T - X)\, J_0\left(m\sqrt{T^2 - X^2}\right)\right.$$
$$\left. -\Theta(T - X)\frac{mX}{\sqrt{T^2 - X^2}} J_1\left(m\sqrt{T^2 - X^2}\right)\right].$$

Since $J_0(0) = 1$, when $\delta(T - X) \neq 0$ the first term simplifies, and since $X \geq 0$ then $\Theta(T - X)$ subsumes $\Theta(T)$, thus

$$G\left(t_f, \mathbf{x}_f \,|\, t_s, \mathbf{x}_s\right) = \frac{\Theta(T)\,\delta(T - X)}{4\pi X} - \frac{m}{4\pi}\frac{\Theta(T - X)}{\sqrt{T^2 - X^2}} J_1\left(m\sqrt{T^2 - X^2}\right).$$

Hence, according to Equation (2.2) the field can be written

$$\Psi\left(t_f, \mathbf{x}_f\right) = \int_{-\infty}^{\infty} \mathrm{d}^4 x_s \left(\frac{\Theta(T)\,\delta(T - X)}{4\pi X}\right.$$
$$\left. -\frac{m}{4\pi}\frac{\Theta(T - X)}{\sqrt{T^2 - X^2}} J_1\left(m\sqrt{T^2 - X^2}\right)\right)\varrho\left(t_s, \mathbf{x}_s\right). \quad (2.4)$$

47

One might now query the physical interpretation of this mathematical result. The first term of the integral indicates that the contributing source points at spacetime coordinate $(t_s, \mathbf{x}_s)$ to a field point at $(t_f, \mathbf{x}_f)$ are those that are light-like separated, i.e. $t_f - t_s = |\mathbf{x}_f - \mathbf{x}_s|$; as such, one is able to designate these as "massless" contributions, i.e. $m = 0$. The second term, however, finds that all source points located within the past lightcone, i.e. $t_f - t_s > |\mathbf{x}_f - \mathbf{x}_s|$, contribute and consequently these are the "massive" contributions, i.e. $m > 0$. A spacetime diagram illustrating the contributing regions with corresponding demarcations is shown in Figure 2.3.
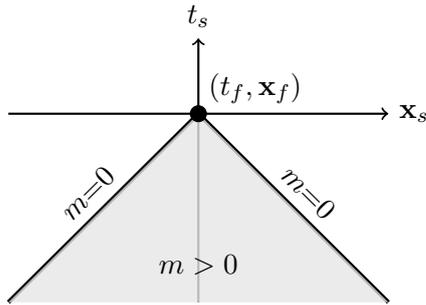
Figure 2.3: Spacetime diagrammatical representation of source point contribution regimes for a field point at spacetime coordinate $(t_f, \mathbf{x}_f)$.

2.4   The Dark Photon

The introduction of a second $\mathrm{U}(1)$ gauge group to the standard model establishes a mechanism by which the visible gauge sector may mix with some "dark", or "hidden", gauge sector. One postulates that these sectors are able to communicate with one another through the exchange of messenger particles – often called *portal matter fields* – which are charged under both gauge groups.

Figure 2.4: Mass hierarchy of toy model.

Consider a toy model composed of two heavy messengers, denoted Φ and Φ', which are charged under both gauge groups. An arbitrary number of fields reside solely either in the visible sector (φ) or the dark sector (ϕ), such that their masses are related by $m_{\Phi'} > m_\Phi \gg m_\varphi \sim m_\phi$, as shown in Figure 2.4. At a sufficiently high energy scale $\Lambda \gg m_{\Phi,\Phi'}$, these heavy messenger particles are able to mediate the two gauge sectors through their exchange, as shown in Figure 2.5. At this scale, the mixing provides kinetic contributions

to the Lagrangian of the canonical form [61]:

$$\mathscr{L}_{\text{kin}} = -\frac{1}{4} \begin{pmatrix} F_{\mu\nu} & B_{\mu\nu} \end{pmatrix} \begin{pmatrix} F^{\mu\nu} \\ B^{\mu\nu} \end{pmatrix},$$

where $F_{\mu\nu} \equiv \partial_\mu A_\nu - \partial_\nu A_\mu$ is the visible gauge field tensor with visible sector gauge field A_μ and $B_{\mu\nu} \equiv \partial_\mu A'_\nu - \partial_\nu A'_\mu$ is the dark sector gauge field tensor with dark sector gauge field A'_μ.

Dark sector fermion, ϕ

A'^μ

$\Phi^{(\prime)}$

A^μ

Visible sector fermion, φ
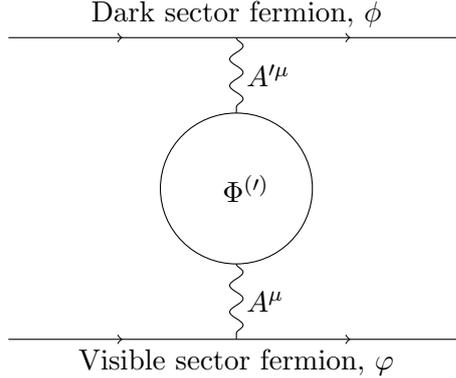
Figure 2.5: Heavy messenger particles mediating interactions between the visible and dark gauge sectors.

In the low-energy scale, i.e. $\Lambda \ll m_\Phi, m_{\Phi'}$, one sees that the mixing of the visible and dark sectors can no longer be mediated by the exchange of these messenger particles at the tree level. Instead, they exist as virtual particles mediating the visible and dark gauge sectors through 1-loop vacuum polarisation, as shown in Figure 2.6, a process known as *kinetic mixing*. The mixing within this regime can be formalised as an effective interaction extension to the model's Lagrangian [60]:

$$\mathscr{L}_{\text{int}} = -\frac{1}{4} \begin{pmatrix} F_{\mu\nu} & B_{\mu\nu} \end{pmatrix} \begin{pmatrix} \chi_{11} & \chi_{12} \\ \chi_{21} & \chi_{22} \end{pmatrix} \begin{pmatrix} F^{\mu\nu} \\ B^{\mu\nu} \end{pmatrix},$$

where χ_{11}, χ_{12}, χ_{21} and χ_{22} are real gauge coupling parameters, which characterise the strength of this messenger exchange within and across sectors. One may note from this form that the kinetic mixing matrix is analogous to the matrices found in mass- and neutrino flavour mixing.

In general $\left(\psi^\dagger O \varphi\right)^\dagger = \varphi^\dagger O^\dagger \psi$ for matrices φ, O and ψ, thus $\left(\varphi^\dagger O \varphi\right)^\dagger = \varphi^\dagger O^\dagger \varphi$. Consequently, if O is anti-Hermitian then $\left(\varphi^\dagger O \varphi\right)^\dagger = -\varphi^\dagger O \varphi$, hence if $\varphi^\dagger O \varphi \in \mathbb{R}$ then any anti-Hermitian contribution is zero and one can thus demand symmetry from O a priori without loss of generality. Therefore, one can symmetrise the kinetic mixing matrix by writing the off-diagonal coupling parameters as $\chi_{12} = \chi_{21} = \chi$.

(a) Feynman diagram of messenger particle exchange at high energy scales, $\Lambda \ll m_\Phi, m_{\Phi'}$.

(b) Feynman diagram of messenger particle exchange at low energy scales, $\Lambda \gg m_\Phi, m_{\Phi'}$; messenger particles only exist as virtual particles.
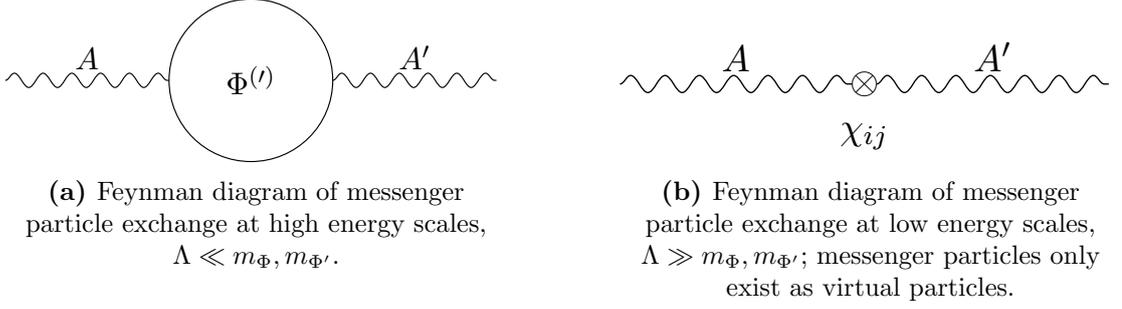
Figure 2.6: Feynman diagrams demonstrating equivalent messenger particle exchanges between a photon A, and dark photon, A', in high and low energy scales.

The Ward-Takahashi identity demonstrates that, without loss of generality, one is able to renormalise theories which are invariant under single $\mathrm{U}\,(1)$ gauges through a redefinition of the gauge coupling and rescaling of the field, i.e. for a field A_μ and coupling e

$$A_\mu \mapsto Z^{\frac{1}{2}} A_\mu \qquad\qquad e \mapsto Z^{-\frac{1}{2}} e,$$

where Z is a renormalisation coefficient containing the divergences of the theory [106–108]. This may be extended to theories incorporating multiple $\mathrm{U}\,(1)$ gauges [109, 110], allowing one to scale both gauge fields of this model:

$$F_{\mu\nu} \mapsto (1+\chi_{11})^{\frac{1}{2}} F_{\mu\nu} \qquad\qquad g_1 \mapsto (1+\chi_{11})^{-\frac{1}{2}} g_1$$

$$B_{\mu\nu} \mapsto (1+\chi_{22})^{\frac{1}{2}} B_{\mu\nu} \qquad\qquad g_2 \mapsto (1+\chi_{22})^{-\frac{1}{2}} g_2,$$

where $g_{1,2}$ are respectively the gauge couplings of the visible and dark sectors. Similarly, the kinetic mixing parameter scales as $\chi = (1+\chi_{11})^{-\frac{1}{2}} (1+\chi_{22})^{-\frac{1}{2}} \chi$ which remains unchanged to leading order, i.e. $\chi \underset{\sim}{\mapsto} \chi$, such that the effective Lagrangian can be written

$$\mathscr{L}_{\text{eff}} = -\frac{1}{4} \begin{pmatrix} F_{\mu\nu} & B_{\mu\nu} \end{pmatrix} \begin{pmatrix} 1 & \chi \\ \chi & 1 \end{pmatrix} \begin{pmatrix} F^{\mu\nu} \\ B^{\mu\nu} \end{pmatrix}.$$

Furthermore, because the energy scale is a priori unknown, the dark photon may be massless like its standard model counterpart, or it may gain a mass through the Stueckelberg or Higgs mechanisms [111–113]. The inclusion of these provides additional massive term to the effective Lagrangian, which finally becomes:

$$\mathscr{L}_{\text{eff}} = -\frac{1}{4} \begin{pmatrix} F_{\mu\nu} & B_{\mu\nu} \end{pmatrix} \begin{pmatrix} 1 & \chi \\ \chi & 1 \end{pmatrix} \begin{pmatrix} F^{\mu\nu} \\ B^{\mu\nu} \end{pmatrix} + \frac{m_{\gamma'}^2}{2} A'_\mu A'^\mu$$

$$= -\frac{1}{4} F_{\mu\nu} F^{\mu\nu} - \frac{1}{4} B_{\mu\nu} B^{\mu\nu} - \frac{1}{2} \chi F_{\mu\nu} B^{\mu\nu} + \frac{1}{2} m_{\gamma'}^2 A'_\mu A'^\mu, \qquad (2.5)$$

where $m_{\gamma'}$ is the dark photon mass. Consequently, the fundamental unknowns in dark photon models are its mass and the kinetic mixing strength parameter. String compactification models estimate this kinetic mixing parameter value in the region $10^{-12} \lesssim \chi \lesssim 10^{-3}$ [114].

The equations of motion governing the gauge fields in this effective theory may be derived using the Euler-Lagrange equation,

$$\frac{\partial \mathscr{L}}{\partial \phi} - \partial_\mu \left(\frac{\partial \mathscr{L}}{\partial (\partial_\mu \phi)} \right) = 0,$$

where ϕ is the field with respect to which the Lagrangian is varied, to be

$$\partial_\mu \left(F^{\mu\nu} + \chi B^{\mu\nu} \right) = 0$$

$$\partial_\mu B^{\mu\nu} + m_{\gamma'}^2 A'^\nu = -\chi m_{\gamma'}^2 \partial_\mu F^{\mu\nu}.$$

Under the change of basis $A_\mu \mapsto \tilde{A}_\mu - \chi A'_\mu$, the first equation takes on a homogeneous Maxwellian form, namely $\partial_\mu \tilde{F}^{\mu\nu} = 0$. However, one may recognise the second equation as the inhomogeneous *Proca equation*, which will be further discussed in Section 2.5.

The $F_{\mu\nu} B^{\mu\nu}$ term in Equation (2.5) is responsible for the kinetic coupling between photons and dark photons, which can be made explicit by diagonalising the term through the change of basis $A'^\mu \mapsto \tilde{A}'^\mu - \chi A^\mu$:

$$\mathscr{L}_{\text{eff}} = -\frac{1}{4} \left(1 - \chi^2 \right) F_{\mu\nu} F^{\mu\nu} - \frac{1}{4} \tilde{B}_{\mu\nu} \tilde{B}^{\mu\nu} + \frac{1}{2} m_{\gamma'}^2 \left(\tilde{A}'_\mu \tilde{A}'^\mu - 2\chi \tilde{A}'_\mu A^\mu + \chi^2 A_\mu A^\mu \right).$$

The Euler-Lagrange equations of motion for this system are given by

$$\left(\left(1 - \chi^2 \right) \partial_\mu \partial^\mu + \chi^2 m_{\gamma'}^2 \right) A^\nu = \chi m_{\gamma'}^2 \tilde{A}'^\nu$$

$$\left(\partial_\mu \partial^\mu + m_{\gamma'}^2 \right) \tilde{A}'^\nu = \chi m_{\gamma'}^2 A^\nu, \tag{2.6}$$

the latter of which will be used in later analysis.

As a consequence of this result, one is able to see that visible photons act as sources for dark photons and vice versa. In Section 2.5, it will be discussed how the equation of motion for dark photons can be solved as four simultaneous Klein-Gordon equations.

2.5   The Proca Equation

Initially derived in 1936 by the Romanian physicist Alexandru Proca as a means of generalising Maxwell's equations, the eponymous Proca equation is the equation of motion

for massive vector bosons [115]. For an arbitrary field B with mass m, it is canonically written

$$\partial_\mu \left(\partial^\mu B^\nu - \partial^\nu B^\mu \right) + m^2 B^\nu = 0.$$

By substitution of the field B^μ for the electromagnetic four-potential, A^μ, one can show that Maxwell's equations are special cases of the Proca equation, in which $m = 0$. Furthermore, one is able to show that the Proca equation is equivalent to a set of four Klein-Gordon equations in theories which conserve four-current, as demonstrated in Appendix B, so can be solved as such.

2.6   Conclusion

In this chapter, several dark matter candidates were introduced, namely axion-like particles, dilaton-like particles and dark photons. Their theoretical underpinnings have been detailed and their couplings to ordinary matter demonstrated. Additionally, the equations of motion dictating the kinematics of these particles were presented and discussed.

Chapter 3

Theory: Laser Wake Field Acceleration

> *"[I]n theory, theory and practice are the same. In practice, they are not."*
>
> — Benjamin Brewster,
> *Yale Literary Magazine [116]*

3.1 Laser Wake Field Acceleration

A plasma is a quasi-neutral state of matter, comprised of positively-charged ions and negatively charged electrons. When subjected to an electromagnetically-interacting driving beam that is not too powerful, the plasma electrons undergo oscillations which generate a sinusoidally-varying electric field. The parameters underlying the scheme of laser wake field acceleration are numerous and stand in delicate balance with one another. In this section a number of these parameters will be discussed.

3.1.1 Plasma Perturbations and Plasma Frequency

Arguably the most important quantity in all schemes of plasma wake field acceleration is the plasma (angular) frequency, ω_p, which denotes the cyclic rate at which plasma electrons oscillate. A derivation of the expression for this frequency will now be presented using electrodynamical perturbation theory.

Maxwell's equations for a system comprised of an arbitrary number of particle species,

s, are as follows:

$$\nabla \cdot (\epsilon_0 \mathbf{E}) = \sum_s q_s n_s \tag{3.1}$$

$$\nabla \cdot \mathbf{B} = 0$$

$$\nabla \times \mathbf{E} = -\partial_t \mathbf{B} \tag{3.2}$$

$$\nabla \times \left(\frac{1}{\mu_0} \mathbf{B} \right) = \partial_t \left(\epsilon_0 \mathbf{E} \right) + \sum_s q_s n_s \mathbf{u}_s,$$

where q_s, n_s and $\mathbf{u}_s$ are respectively the charge, number density and velocity of a species s and $\mathbf{E}$ and $\mathbf{B}$ are the electric and magnetic fields. Additionally, the equation of motion for a species of effective mass m_s^* under the influence of electromagnetic fields is given by the Lorentz-Maxwell force equation:

$$m_s^* n_s \left(\partial_t \mathbf{u}_s + (\mathbf{u}_s \cdot \nabla) \mathbf{u}_s \right) = q_s n_s \left(\mathbf{E} + \mathbf{u}_s \times \mathbf{B} \right). \tag{3.3}$$

To approximately model the motion of each species within a plasma, one is able to write each parameter as a perturbation series, i.e.

$$\mathbf{E}_s \left(t, \mathbf{x} \right) = \mathbf{E}_{0s} \left(t, \mathbf{x} \right) + \mathbf{E}_{1s} \left(t, \mathbf{x} \right) + \dots$$

$$\mathbf{B}_s \left(t, \mathbf{x} \right) = \mathbf{B}_{0s} \left(t, \mathbf{x} \right) + \mathbf{B}_{1s} \left(t, \mathbf{x} \right) + \dots$$

$$\mathbf{u}_s \left(t, \mathbf{x} \right) = \mathbf{u}_{0s} \left(t, \mathbf{x} \right) + \mathbf{u}_{1s} \left(t, \mathbf{x} \right) + \dots$$

$$n_s = n_{0s} + n_{1s} + \dots,$$

where zeroth order terms are assumed to be constant, i.e.

$$\left\{ \mathbf{E}_{0s} \left(t, \mathbf{x} \right), \mathbf{B}_{0s} \left(t, \mathbf{x} \right), \mathbf{u}_{0s} \left(t, \mathbf{x} \right) \right\} = \left\{ \mathbf{E}_{0s}, \mathbf{B}_{0s}, \mathbf{u}_{0s} \right\}.$$

Additionally, one truncates the series to first order by assuming that each successive order of perturbation is sufficiently small to be neglected, i.e. for a parameter A then $A_p \gg A_q$ for perturbation orders $p < q$. Under these constraints, by assuming that the system is comprised of only electrons and ions, Equation (3.1) to zeroth order is written

$$\nabla \cdot (\epsilon_0 \mathbf{E}_0) = q_e n_{0e} + q_i n_{0i},$$

but since $\mathbf{E}_0$ is constant its derivatives evaluate to zero, thus one derives

$$n_{0e} = -\frac{q_i}{q_e} n_{0i}.$$

Typical plasmas are considered *quasi-neutral*, meaning that they are macroscopically neutral but microscopically their constituents may exhibit different regional distributions. As such, by assuming that $q_e = -q_i$, one is able to define a constant ambient

number density of both the electrons and ions which comprise the plasma:

$$n_{0e} = n_{0i} \equiv n_0.$$

One may now linearise the Lorentz-Maxwell and Maxwell equations, limiting total perturbation orders to zeroth and first, as follows:

$$m_s^* n_0 \left(\partial_t \mathbf{u}_{1s} + (\mathbf{u}_{0s} \cdot \boldsymbol{\nabla}) \mathbf{u}_{1s} \right) = q_s n_0 \left(\mathbf{E}_1 + \mathbf{u}_{0s} \times \mathbf{B}_1 + \mathbf{u}_{1s} \times \mathbf{B}_0 \right) \tag{3.4}$$

$$\begin{cases} \displaystyle \sum_s q_s n_0 = 0 \\ \boldsymbol{\nabla} \cdot (\epsilon_0 \mathbf{E}_1) = \displaystyle \sum_s q_s n_{1s} \end{cases} \tag{3.5}$$

$$\begin{cases} \boldsymbol{\nabla} \cdot \mathbf{B}_0 = 0 \\ \boldsymbol{\nabla} \cdot \mathbf{B}_1 = 0 \end{cases}$$

$$\begin{cases} \boldsymbol{\nabla} \times \mathbf{E}_0 = -\partial_t \mathbf{B}_0 = 0 \\ \boldsymbol{\nabla} \times \mathbf{E}_1 = -\partial_t \mathbf{B}_1 \end{cases}$$

$$\begin{cases} \dfrac{1}{\mu_0} \boldsymbol{\nabla} \times \mathbf{B}_0 = \epsilon_0 \partial_t \mathbf{E}_0 + \displaystyle \sum_s q_s n_0 \mathbf{u}_{0s} \\ \dfrac{1}{\mu_0} \boldsymbol{\nabla} \times \mathbf{B}_1 = \epsilon_0 \partial_t \mathbf{E}_1 + \displaystyle \sum_s q_s \left(n_{1s} \mathbf{u}_{0s} + n_0 \mathbf{u}_{1s} \right). \end{cases} \tag{3.6}$$

Taking the divergence of Equation (3.6) and using the identity $\boldsymbol{\nabla} \cdot (\boldsymbol{\nabla} \times \mathbf{A}) = 0$ for an arbitrary vector $\mathbf{A}$ with Equation (3.5), then one derives the linearisation of the charged fluid continuity equation:

$$\sum_s q_s \partial_t n_{1s} + q_s \boldsymbol{\nabla} \cdot (n_0 \mathbf{u}_{1s}) = 0. \tag{3.7}$$

Setting $\mathbf{B}_0 = \mathbf{u}_{0s} = \mathbf{0}$ and taking the time derivative of the continuity equation and substituting Equation (3.4), then

$$\sum_s \partial_t^2 n_{1s} + \frac{q_s n_0}{m_s^*} (\boldsymbol{\nabla} \cdot \mathbf{E}_1) = 0.$$

From this, one can use Equations (3.5) and (3.7) to derive

$$\sum_s \partial_t^2 n_{1s} + \frac{q_s^2 n_0}{m_s^* \epsilon_0} n_{1s} = 0.$$

Assuming that all species are decoupled from one another, i.e. there is no further ionisation or recombination within the plasma, one then notes that each constituent species undergoes simple harmonic motion with characteristic angular frequency

$$\omega_s = \sqrt{\frac{q^2 n_0}{m_s^* \epsilon_0}}.$$

One sees that the oscillation frequency for a species is inversely proportional to its mass, hence the dominant behaviours of plasmas are derived from its electrons since $\omega_e \gg \omega_{\text{ion}}$. In practice, the relativistic mass increase in the ions due to the driving pulse must be included in the calculation. As such, substituting the average effective mass $m_s^* = \langle \gamma \rangle m_s$, where m_s is the rest energy of the species and $\langle \gamma \rangle$ the laser cycle-averaged Lorentz factor, the characteristic frequency governing a plasma is thus defined as

$$\omega_p := \sqrt{\frac{e^2 n_0}{\langle \gamma \rangle m_e \epsilon_0}}.$$

One also notes that this is independent of the particle oscillation wavelength, resulting in a group velocity of zero, i.e. $\dfrac{\partial \omega}{\partial k} = 0$, hence the driving force establishes a stationary plasma wave.

3.1.2   Refractive Index

The refractive index, η, experienced by electromagnetic radiation is defined as being the ratio of the speed of light in vacuo, c, to the radiation phase velocity through a medium, v_p, i.e.

$$\eta := \frac{c}{v_p},$$

where the phase velocity is defined as being the ratio of the radiation angular frequency, ω, to its wavenumber, k, i.e. $v_p \equiv \frac{\omega}{k}$.

The dispersion relation for an electromagnetic wave propagating in a cold, collisionless unmagnetised plasma is given by

$$\omega^2 = \omega_p^2 + k^2 c^2.$$

From the above definitions of phase velocity and refractive index, one concludes

$$\eta = \sqrt{1 - \left(\frac{\omega_p}{\omega}\right)^2}.$$

This equation serves as an accurate representation of the refractive index under the given caveats, however a more extensive description which incorporates collisions and an

external magnetic field assumes the form of the Appleton-Hartree equation:

$$\eta^2 = 1 - \frac{X}{1 - iZ - \frac{\frac{1}{2}Y_T^2}{1 - X - iZ} \pm \frac{1}{1 - X - iZ}\sqrt{\frac{1}{4}Y_T^4 + Y_L^2\left(1 - X - iZ\right)^2}},$$

where the terms are defined as follows:

- $X = \frac{\omega_p^2}{\omega^2}$

- $Y = \frac{\omega_B}{\omega} = \sqrt{Y_L^2 + Y_T^2}$

- $Y_L = \frac{\omega_L}{\omega}$

- $Y_T = \frac{\omega_T}{\omega}$

- $Z = \frac{\nu}{\omega}$

- ω = electromagnetic wave angular frequency

- $\omega_p \equiv \sqrt{\frac{n_e e^2}{\langle\gamma\rangle m_e \epsilon_0}}$ = plasma frequency

- $\omega_B = \frac{B_0|e|}{m_e}$ = electron gyro-frequency

- $\omega_L = \omega_B \cos\left(\theta\right)$

- $\omega_T = \omega_B \sin\left(\theta\right)$

- ν = electron-ion collisional frequency

- B_0 = ambient external magnetic field strength

- θ = angle between the ambient magnetic field vector and direction of electromagnetic propagation.

A derivation of this can be found in John Ratcliffe's *The Magneto-Ionic Theory & Its Applications to the Ionosphere* [117, §2]. One notes that under the constraints of a collisionless unmagnetised plasma this reduces to the aforementioned form.

3.1.3   Underdense and Overdense Plasmas

The physics of interactions between a laser and plasmas of varying densities can be broadly generalising into two regimes: those of *underdense* and *overdense*.

When the characteristic timescale of the incoming electromagnetic wave is less than that of the plasma, the laser pulse is able to propagate through the plasma, i.e. $\omega_{\text{laser}} > \omega_p \Rightarrow \eta \in \mathbb{R}$; this is the *underdense regime*. Per contra, when this is inverted and the characteristic timescale of the laser is greater than that of the plasma, the waves become evanescent and the medium is able to absorb or reflect the incoming pulse, akin to an object bouncing off of a wall, i.e. $\omega_{\text{laser}} < \omega_p \Rightarrow \eta \in \mathbb{C}$; this is the *overdense regime*.

The critical density, n_c, denotes the boundary between the underdense and overdense regimes and is defined as being the density corresponding to when the laser and plasma frequencies are equal, i.e. $\omega_{\text{laser}} = \omega_p$. As such, it can be shown that the critical density

is given by

$$n_c = \frac{4\pi^2 \epsilon_0 m_e c^2}{e^2} \frac{1}{\lambda_{\text{laser}}^2},$$

where λ_{laser} is the laser wavelength. Consequently, for efficient electron acceleration in gaseous plasmas, one wishes to tune the density of the plasma such that the laser pulse is able to excite a wake, i.e. $n_0 < n_c$.

3.1.4   Normalised Laser Amplitude

When discussing the propagation of electromagnetic radiation through underdense plasmas, one should first examine the external fields used to excite the wake. Consider the Lorentz-Maxwell force equation

$$\frac{\mathrm{d}\mathbf{p}}{\mathrm{d}t} = q\left(\mathbf{E} + \mathbf{v}\times\mathbf{B}\right), \tag{3.8}$$

where $\mathbf{p} \equiv \gamma m\mathbf{v}$ is the three-momentum of a particle of charge q and mass m travelling with a velocity $\mathbf{v}$ under the influence of an electric field $\mathbf{E}$ and magnetic field $\mathbf{B}$, $\gamma \equiv \left(1 - \beta^2\right)^{-\frac{1}{2}}$ is the Lorentz factor, and $\beta \equiv \frac{v}{c}$ the normalised velocity.

One can ansatz a monochromatic plane wave solution propagating along the z-axis for the electromagnetic fields, i.e. $\mathbf{E} = E_0 \cos\left(k_z z - \omega t\right)\hat{\mathbf{e}}_x$. In this formulation, from Equation (3.2), one calculates the corresponding magnetic field to be $\mathbf{B} = \frac{E_0}{c}\cos\left(k_z z - \omega t\right)\hat{\mathbf{e}}_y$, i.e. $\|\mathbf{B}\| = \frac{\|\mathbf{E}\|}{c}$. By introducing the notation to denote the components of a quantity $\mathbf{u}$ transverse to the direction of propagation as $\mathbf{u}_\perp = \mathbf{u} - \left(\mathbf{u}\cdot\hat{\mathbf{e}}_z\right)\hat{\mathbf{e}}_z$, one is then able to write $\left(\frac{\mathrm{d}\mathbf{p}}{\mathrm{d}t}\right)_\perp = \frac{\mathrm{d}\mathbf{p}_\perp}{\mathrm{d}t}$ since $\frac{\mathrm{d}\hat{\mathbf{e}}_z}{\mathrm{d}t} = 0$. Further, since $\mathbf{B} = \mathbf{B}_\perp$, then the second parenthesised term in Equation (3.8) can be written $\left(\mathbf{v}\times\mathbf{B}\right)_\perp = v_z \mathbf{e}_z \times \mathbf{B}_\perp$. As such, the Lorentz-Maxwell equation transverse to the direction of propagation is given by

$$\frac{\mathrm{d}}{\mathrm{d}t}\mathbf{p}_\perp = q\left(\mathbf{E}_\perp + v_z \frac{\mathbf{E}_\perp}{c}\right) = q\left(1 - \beta_z\right)\mathbf{E}_\perp.$$

Since $v_z = \frac{\mathrm{d}z}{\mathrm{d}t}$, one can rewrite this

$$\frac{\mathrm{d}}{\mathrm{d}t}\mathbf{p}_\perp = \frac{\mathrm{d}}{\mathrm{d}t}\left(-\frac{qE_0}{\omega}\sin\left(kz - \omega t\right)\hat{\mathbf{e}}_y\right),$$

thus

$$\mathbf{p}_\perp = -\frac{qE_0}{\omega}\sin\left(kz - \omega t\right)\hat{\mathbf{e}}_y$$

is one possible solution. Consequently, the transverse motion for an electron acting under the influence of a laser pulse has normalised transverse momentum

$$\gamma\beta_\perp = -\frac{eE_0}{m_e c\omega}\sin\left(kz - \omega t\right),$$

which defines the *normalised laser amplitude* $a_0 := \frac{eE_0}{m_e c \omega}$. This is the peak amplitude of the normalised electric field associated with the laser. In other texts this is instead called the *normalised vector potential* and written $a_0 = \frac{e\|\mathbf{A}\|}{m_e c}$, where $\mathbf{A}$ is the magnetic vector potential, which for a plane electromagnetic wave solution has amplitude $\|\mathbf{A}\| = \frac{\|\mathbf{E}\|}{\omega}$. Alternatively, writing $\beta = \left\|\frac{\mathbf{p}}{\gamma m c}\right\|$, one sees that when $a_0 > 1$ then $p > \gamma m c$, introducing a third moniker for a_0: the *normalised momentum*. A consequence of this formulation is that electrons initially at rest become relativistic with velocities proportional to the field strength.

3.1.5   Laser Intensity

The cycle-averaged field energy density $\langle \mathscr{U} \rangle$ of a monochromatic electromagnetic plane wave with peak amplitude E_0 inside a medium of refractive index η is given by [118, §9.3]

$$\langle \mathscr{U} \rangle = \frac{1}{2}\eta^2 \epsilon_0 E_0^2. \tag{3.9}$$

The intensity of an electromagnetic wave traversing the medium is given by

$$I = v_p \langle \mathscr{U} \rangle,$$

where $v_p = \frac{c}{\eta}$ is the phase velocity of the wave through the medium. Consequently, using this with the definition for the normalised laser amplitude one is able to write the intensity as a function of only a_0 and the laser wavelength λ_{laser}:

$$I = \frac{2\pi^2 \epsilon_0 m_e^2 c^5}{e^2}\left(\frac{a_0}{\lambda_{\text{laser}}}\right)^2.$$

3.1.6   Ponderomotive Force

The ponderomotive force, from the Latin "pondus" *weight* and "motivum" *moving cause*, is the force responsible for the setting in motion of massive particles within a plasma. The formal definition of the ponderomotive force is a contentious issue and a rigorous derivation of this quantity is beyond the scope of this thesis. However, it is possible to provide a heuristic derivation based on more detailed analyses. Rigorous contemporary derivations utilise techniques of Lagrangian and Hamiltonian averaging, thus one is justified in formulating the ponderomotive force using energetic quantity averages [119–123]. Additionally, as the pondermotive force induces motion of particles within a plasma, one expects it to vary with the properties of the plasma. Combining these factors, one is able to exposit the ponderomotive force as the down-gradient of the laser cycle-averaged energy gain per particle. As the energy gain per particle is the ratio of the energy density

to the number density of the system prior to excitation, then the simplest dimensionally correct form of the pondermotive force in terms of these quantities is

$$\mathbf{F}_{\text{pond}} = -\boldsymbol{\nabla}\left\langle \frac{\mathscr{U}}{n_0} \right\rangle = -\frac{1}{n_0}\boldsymbol{\nabla}\langle \mathscr{U}\rangle,$$

where $\mathbf{F}_{\text{pond}}$ denotes the ponderomotive force, $\mathscr{U}$ is the energy density of the electromagnetic field and n_0 is the ambient number density of the plasma. From the formulation of the laser energy field density found in Equation (3.9), one can write the ponderomotive force resulting from a **frequency-matched** laser pulse in a plasma as

$$\mathbf{F}_{\text{pond}} = -\frac{1}{2}\frac{\epsilon_0}{n_0}\boldsymbol{\nabla}E_0^2.$$

Hence, from the definitions of the plasma frequency and normalised laser amplitude, one derives

$$\mathbf{F}_{\text{pond}} = -\frac{e^2}{2\langle\gamma\rangle m_e \omega_p^2}\boldsymbol{\nabla}E_0^2 = -\frac{m_e c^2}{2\langle\gamma\rangle}\boldsymbol{\nabla}a_0^2.$$

From this one sees that electromagnetically-interacting particles are pushed away from regions of highest laser intensity, thus the ponderomotive force can be seen as the radiation pressure of the laser pulse.

One notes that heavier particles are accelerated less than their lighter counterparts, resulting in their relatively slow motion, as exhibited in the characteristic frequencies earlier derived. This difference in mass between the ions and electrons establishes the space charge separation, thus establishing the wake field. Additionally, because the ponderomotive force is second-order in the normalised laser amplitude, i.e. $F_{\text{pond}} \propto |a_0|^2$, low intensity lasers provide very little acceleration since $a_0 \ll 1 \Rightarrow a_0^2 \ll 1$, however high intensity lasers provide extremely large acceleration gradients because $a_0 \gg 1 \Rightarrow a_0^2 \gg 1$. Consequently, high intensity lasers are ideal for driving plasma wake fields.

3.1.7   Acceleration Gradient

Core to the purpose of laser wake field acceleration is the ability to accelerate particles. This is achieved through the establishment of an electric field, also known as the acceleration gradient, through the driving of a plasma electron stationary wave.

From the definition of the normalised laser amplitude, a_0, one is able to derive an approximate relation for the resultant peak acceleration gradient of a laser-driven plasma as

$$E_0 \sim \frac{m_e c \omega_p}{e}\sqrt{a_0} \propto \sqrt{n_e}.$$

As a consequence of this form, one notes that greater intensity lasers result in greater electric fields. Additionally, greater density plasmas are able to support higher electric fields. From these, one sees a clear desire for intense lasers and dense plasmas in the acceleration of a beam of electrons.

3.1.8   Dephasing Length

One of the main limitations to the length of a plasma in LWFA is a phase mismatch between the accelerated electrons and the wake.

Recall that the dispersion relation for an electromagnetic wave in a cold plasma is given by

$$\omega^2 = \omega_p^2 + c^2 k^2.$$

From this one is able to calculate the laser's phase velocity

$$v_p \equiv \frac{\omega}{k} = \sqrt{c^2 + \frac{\omega_p^2}{k^2}}$$

and group velocity

$$v_g \equiv \frac{\partial \omega}{\partial k} = \frac{c^2}{\sqrt{c^2 + \frac{\omega_p^2}{k^2}}} = \frac{c^2}{v_p}.$$

The phase velocity of a plasma wave driven by a laser pulse is equal to the laser's group velocity if the evolution of the pulse during propagation is insignificant [124]. Consequently, the normalised wake velocity is

$$\beta_p^{\text{wake}} \equiv \frac{v_p^{\text{wake}}}{c} = \frac{v_g}{c} = \frac{c}{v_p}.$$

Using the earlier derived expression for the laser phase velocity with the definitions of the plasma and critical frequencies, it follows from $\frac{v_g}{c} = \sqrt{1 - \left(\frac{\omega_p}{\omega}\right)^2}$ that

$$\beta_p^{\text{wake}} = \sqrt{1 - \left(\frac{n_e}{n_c}\right)}. \tag{3.10}$$

Since the trapped plasma electrons are accelerated to ultra-relativistic energies, the normalised velocity tends to unity, i.e.

$$\beta_e \sim 1. \tag{3.11}$$

One sees from Equations (3.10) and (3.11) that the electron velocity is slightly, but significantly, greater than that of the plasma wave, with the difference becoming more

pronounced at higher plasma densities. As such, accelerated electrons are able to outpace the wake, thus placing a fundamental limit on the maximum length of plasma for a driven plasma at a given density, known as the *dephasing length*, which will be denoted L_{dph}.

Electrons are able to gain energy while in the acceleration phase of the wake field, situated in the latter half of a plasma wavelength. Assuming the plasma electrons get trapped at the start of the wake's acceleration phase, they can be accelerated until caught up by a half plasma wavelength. The dephasing time, t_{dph}, is the time required for these electrons to travel a distance $d = \frac{\lambda_p}{2}$ relative to the wake, i.e.

$$t_{\text{dph}} = \frac{d}{\Delta v} = \frac{\lambda_p}{2c \left(\beta_e - \beta_p^{\text{wake}} \right)}.$$

From this and Equations (3.10) and (3.11) one sees that the dephasing length $L_{\text{dph}} = ct_{\text{dph}}$ is calculated to be

$$L_{\text{dph}} \approx \frac{n_c}{n_e} \lambda_p \propto n_e^{-\frac{3}{2}}.$$

As a result of this, one concludes that the length of a laser-driven plasma accelerator is limited by electron dephasing, which is inversely proportional to the plasma density. Consequently, one must balance the plasma accelerator length with its density.

3.2   Conclusion

This chapter explored the theory underpinning laser wake field acceleration, a novel method of particle acceleration which is capable of producing extremely powerful electric fields. However, efficient application of this methodology requires careful consideration of how several system parameters must be balanced.

Chapter 4

Theory: Microwave Resonant Cavities and Photonic Bandgap Lattices

"My friend, Jack Hughes, just got a job as a prosecutor in France..."

— Anonymous

4.1 Microwave Resonant Cavities

4.1.1 Exposition

Resonant cavities belong to a class of closed metal structures called *waveguides* which are used to confine electromagnetic fields. The composition internal to these cavities are typically free space or a dielectric medium. By appropriately pairing the dimensions of the structure with the frequencies of the electromagnetic fields inside the cavity, these resonance structures are able to support and reinforce specific bandwidths. For practical reasons, these cavities typically operate at microwave frequencies, i.e. $300\,\mathrm{MHz}$ to $30\,\mathrm{GHz}$, where the wavelengths are of order $1\,\mathrm{mm}$ to $1\,\mathrm{m}$. However, the geometry of the cavities allow them to support multidimensional electromagnetic modes. These modes are categorised into three classes: Transverse Electric (TE) modes, in which the electric field is transverse to the direction of propagation, Transverse Magnetic (TM) modes, in which the magnetic field is transverse to the direction of propagation, and Transverse ElectroMagnetic (TEM) modes, in which both electric and magnetic fields are transverse to the direction of propagation. The modes of concern in this thesis are

those in which the magnetic field is transverse to the cavity's primary axis, namely TM modes.

4.1.2   Resonant Frequencies

Maxwell's equations in a medium of permittivity ϵ and permeability μ are given by the following:

$$\boldsymbol{\nabla} \cdot \mathbf{E} = \frac{\rho}{\epsilon} \tag{4.1}$$

$$\boldsymbol{\nabla} \cdot \mathbf{B} = 0 \tag{4.2}$$

$$\boldsymbol{\nabla} \times \mathbf{E} = -\partial_t \mathbf{B} \tag{4.3}$$

$$\boldsymbol{\nabla} \times \mathbf{B} = \mu\epsilon\partial_t \mathbf{E} + \mu\mathbf{j}, \tag{4.4}$$

where $\mathbf{E}$ is the electric field, $\mathbf{B}$ is the magnetic field and $\mathbf{j}$ is the current associated with a charge density ρ.

By taking the curl of Equation (4.3) and substituting Equation (4.1), one receives a wave equation for the electric field:

$$\left(\nabla^2 - \mu\epsilon\partial_t^2\right)\mathbf{E} = \boldsymbol{\nabla}\left(\frac{\rho}{\epsilon}\right) + \partial_t\mathbf{j}. \tag{4.5}$$

Similarly, taking the curl of Equation (4.4) and substituting Equations (4.2) and (4.3), one derives a wave equation for the magnetic field:

$$\left(\nabla^2 - \mu\epsilon\partial_t^2\right)\mathbf{B} = -\mu\boldsymbol{\nabla} \times \mathbf{j}. \tag{4.6}$$

It will be assumed that there exist no free charges within the cavity and that the cavity walls are composed of a perfect conductor. Ohm's law, which relates the electromagnetic current density and electric field within a material, is given by $\mathbf{j} = \sigma\mathbf{E}$, where σ is the material conductivity. Charge carriers within perfect conductors are able to traverse the medium unabated, otherwise stated that the conductivity tends to infinity, thus there exists no electric field within the bulk of the cavity walls, i.e. $\lim_{\sigma \to \infty} \mathbf{E} = \frac{\mathbf{j}}{\sigma} = \mathbf{0}$. By Faraday's law (Equation (4.3)), one sees that the magnetic field inside the medium is static, i.e. $\partial_t\mathbf{B} = \mathbf{0}$. With the bulk behaviours concluded, one can now turn attention to the surface.

At the interstice between two dielectric media, one is able to show by field continuity across the boundary that the components transverse ($\perp$) and parallel ($\parallel$) to the surface

satisfy

$$\epsilon_1 E_{1_\perp} - \epsilon_2 E_{2_\perp} = \Sigma$$

$$\mathbf{E}_{1_\parallel} - \mathbf{E}_{2_\parallel} = \mathbf{0}$$

$$B_{1_\perp} - B_{2_\perp} = 0$$

$$\frac{1}{\mu_1}\mathbf{B}_{1_\parallel} - \frac{1}{\mu_2}\mathbf{B}_{2_\parallel} = \mathbf{K} \times \hat{\mathbf{n}},$$

where Σ is the surface charge density, $\mathbf{K}$ is the surface current density and $\hat{\mathbf{n}}$ is the unit vector normal to the surface. Consequently, there are no tangential electric fields or parallel magnetic fields at the inner wall boundaries, i.e. $\mathbf{E}_\parallel = \mathbf{0}$ and $\mathbf{B} = \mathbf{0}$. As such, the conditions at the inner wall boundaries of the resonant cavity can be chosen to be

$$\mathbf{E}_\parallel = \mathbf{0} \tag{4.7}$$

$$\mathbf{B}_\perp = \mathbf{0}, \tag{4.8}$$

where the Equation (4.8) denotes the definition of *transverse magnetic* (TM) propagation.

For notational brevity, one may combine the set of separate electric and magnetic fields into a single entity $\mathbf{\Psi} = \{\mathbf{E}, \mathbf{B}\}$ such that Equations (4.5) and (4.6) can be collectively written

$$\left(\nabla^2 - \mu\epsilon\partial_t^2\right)\mathbf{\Psi} = \mathbf{0}.$$

One notes that this a wave equation with phase velocity $v_p = \frac{1}{\sqrt{\mu\epsilon}}$, which has a plane wave solution

$$\mathbf{\Psi} = \left[C_1 \sin\left(\mathbf{k}\cdot\mathbf{x} \pm \omega t\right) + C_2 \cos\left(\mathbf{k}\cdot\mathbf{x} \pm \omega t\right)\right]\hat{\mathbf{\Psi}},$$

where $\mathbf{k}$ is the wavevector, ω the wave angular frequency, $\hat{\mathbf{\Psi}}$ the wave unit vector and $C_{1,2}$ are arbitrary constant amplitudes. The wave equation then becomes

$$\left(\nabla^2 + \mu\epsilon\omega^2\right)\mathbf{\Psi} = \mathbf{0}.$$

Writing $k^2 \equiv \frac{\omega^2}{v_p^2} = \mu\epsilon\omega^2$, then

$$\left(\nabla^2 + k^2\right)\mathbf{\Psi} = \mathbf{0}.$$

In general there are no limitations on the shape of a resonant cavity, however for mathematical simplicity it will be assumed to have a cylindrical geometry, i.e. a circular-faced prism of internal radius r and length L running parallel to the z axis with plates sealing either end, as shown in Figure 4.1.
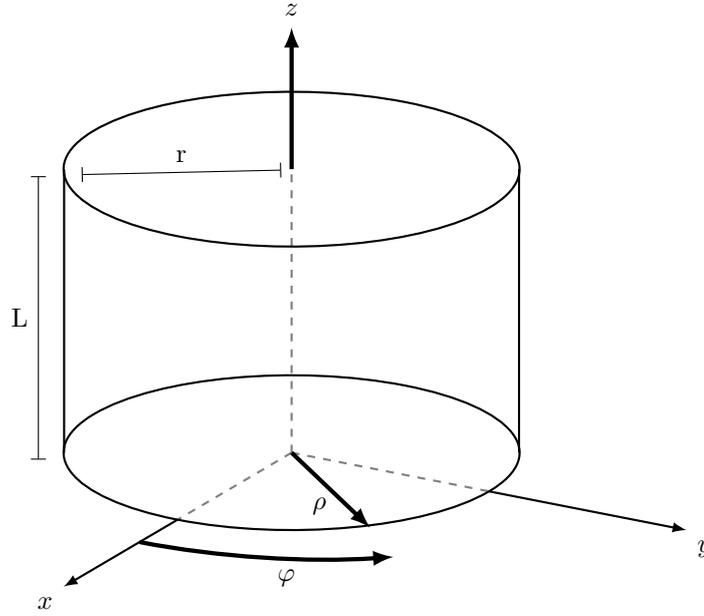
Figure 4.1: Microwave resonance cavity with a cylindrical geometry.

In cylindrical coordinates (ρ, φ, z) the Laplacian operator is given by [105, p. 360]:

$$\nabla^2 = \frac{1}{\rho} \frac{\partial}{\partial \rho} \left(\rho \frac{\partial}{\partial \rho} \right) + \frac{1}{\rho^2} \frac{\partial^2}{\partial \varphi^2} + \frac{\partial^2}{\partial z^2} \, .$$

Assuming the primary axis of the cavity, and hence wave propagation direction, runs parallel to the z-axis, then one is able to separate the fields into their constituent variable components, i.e.

$$\mathbf{\Psi}\left(\rho, \varphi, z\right) = R\left(\rho\right) \Phi\left(\varphi\right) Z\left(z\right). \tag{4.9}$$

In this form the partial differential wave equation becomes an ordinary differential equation:

$$\frac{1}{\rho R} \frac{\mathrm{d}}{\mathrm{d}\rho} \left(\rho \frac{\mathrm{d}R}{\mathrm{d}\rho} \right) + \frac{1}{\rho^2 \Phi} \frac{\mathrm{d}^2 \Phi}{\mathrm{d}\varphi^2} + k^2 = -\frac{1}{Z} \frac{\mathrm{d}^2 Z}{\mathrm{d}z^2} \, .$$

Since the left- and right-hand sides are independent of one another, but are always equal, they must both also be equal to some constant, which will be denoted h^2:

$$\begin{cases} \dfrac{\mathrm{d}^2 Z}{\mathrm{d}z^2} = -h^2 Z \\ \dfrac{1}{\rho R} \dfrac{\mathrm{d}}{\mathrm{d}\rho} \left(\rho \dfrac{\mathrm{d}R}{\mathrm{d}\rho} \right) + \dfrac{1}{\rho^2 \Phi} \dfrac{\mathrm{d}^2 \Phi}{\mathrm{d}\varphi^2} + k^2 = h^2. \end{cases}$$

Furthermore, by introducing a temporary variable $\ell^2 = k^2 - h^2$ one is able to write the remaining multi-variate equation

$$\frac{\rho}{R} \frac{\mathrm{d}}{\mathrm{d}\rho} \left(\rho \frac{\mathrm{d}R}{\mathrm{d}\rho} \right) + \ell^2 \rho = -\frac{1}{\Phi} \frac{\mathrm{d}^2 \Phi}{\mathrm{d}\varphi^2} \, .$$

As before, the sides are equal but independent, thus one may introduce a second separation variable $-n^2$, where the minus sign has been chosen to reflect the expected oscillatory behaviour. Consequently, the total set of equations governing the wave equation are

$$
\begin{cases}
\dfrac{\mathrm{d}^2 Z}{\mathrm{d}z^2} = -h^2 Z & (4.10) \\[2mm]
\dfrac{\mathrm{d}^2 \Phi}{\mathrm{d}\varphi^2} = -n^2 \Phi & (4.11) \\[2mm]
\rho \dfrac{\mathrm{d}}{\mathrm{d}\rho}\left(\rho \dfrac{\mathrm{d}R}{\mathrm{d}\rho}\right) + \left(\ell^2 \rho^2 - n^2\right) R = 0. & (4.12)
\end{cases}
$$

The general solution to Equation (4.10) is

$$
Z = A \sin(hz) + B \cos(hz),
$$

where A and B are arbitrary constant amplitudes. From boundary condition (4.7), one sees that at the ends of the cylinder the transverse electric fields vanish, hence $\dfrac{\mathrm{d}E_x}{\mathrm{d}x} = \dfrac{\mathrm{d}E_y}{\mathrm{d}y} = 0$ and thus, using $\boldsymbol{\nabla} \cdot \mathbf{E} = 0$, then $\dfrac{\mathrm{d}E_z}{\mathrm{d}z} \overset{!}{=} 0$ at boundaries $z \in \{0, L\}$. Substituting the lower bound, one concludes that $A = 0$, and so by substituting the upper bound one gets $\dfrac{\mathrm{d}Z}{\mathrm{d}z}(z = L) = -Bh \sin(hL)$, hence $h = \frac{m\pi}{L}$, where $m \in \mathbb{Z}$, thus

$$
Z = B \cos\left(\frac{m\pi}{L} z\right). \tag{4.13}
$$

Turning now to the angular components in Equation (4.11), the general solution is

$$
\Phi = A' e^{in\varphi} + B' e^{-in\varphi}. \tag{4.14}
$$

This component remains a priori unconstrained, however one may impose a 2π periodicity in φ, i.e. $\varphi \equiv 0 \pmod{2\pi}$, hence one concludes that $n \in \mathbb{Z}$.

Using the newly derived parametrised solutions, the radial Equation (4.12) can be written

$$
\rho^2 \frac{\mathrm{d}^2 R}{\mathrm{d}\rho^2} + \rho \frac{\mathrm{d}R}{\mathrm{d}\rho} + \left(\left(k^2 - \left(\frac{m\pi}{L}\right)^2\right)\rho^2 - n^2\right) R = 0,
$$

which assumes the form of the Bessel ordinary differential equation [125, §9.1]. Because one expects the radial function to be regular, i.e. analytic and single-valued, at $\rho = 0$, one chooses the solution of a Bessel function of the first kind, J_n, with argument $\sqrt{k^2 - \left(\frac{m\pi}{L}\right)^2}\,\rho$, i.e.

$$
R(\rho) = J_n\left(\sqrt{k^2 - \left(\frac{m\pi}{L}\right)^2}\,\rho\right). \tag{4.15}
$$

Combining Equations (4.13), (4.14) and (4.15), then Equation (4.9) becomes

$$\boldsymbol{\Psi}\left(\rho,\varphi,z\right) = J_n\left(\sqrt{k^2 - \left(\frac{m\pi}{L}\right)^2}\,\rho\right)\left[A'e^{in\varphi} + B'e^{-in\varphi}\right]\left[B\cos\left(\frac{m\pi}{L}z\right)\right]\hat{\mathbf{z}}.$$

One is able to amalgamate the parametrised amplitudes into an overall field amplitude Ψ_0, giving an overall general solution

$$\boldsymbol{\Psi}\left(\rho,\varphi,z\right) = \Psi_0 J_n\left(\sqrt{k^2 - \left(\frac{m\pi}{L}\right)^2}\,\rho\right)\cos\left(\frac{m\pi}{L}z\right)\left[c_1 e^{in\varphi} + c_2 e^{-in\varphi}\right]\hat{\mathbf{z}}.$$

Owing to the condition in Equation (4.7), the longitudinal electric field vanishes at the radial boundaries, i.e. $E_z = 0$ at $\rho = r$, thus

$$J_n\left(\sqrt{k^2 - \left(\frac{m\pi}{L}\right)^2}\,r\right) = 0.$$

Let α_{np} denote the p$^{\text{th}}$ positive zero of Bessel function J_n, then

$$k^2 = \left(\frac{\alpha_{np}}{r}\right)^2 + \left(\frac{m\pi}{L}\right)^2.$$

However, $k^2 \equiv \frac{\omega^2}{v_p^2}$, hence

$$\omega_{npm} = \frac{1}{\sqrt{\mu\epsilon}}\sqrt{\left(\frac{\alpha_{np}}{r}\right)^2 + \left(\frac{m\pi}{L}\right)^2}, \tag{4.16}$$

where $m, n \in \mathbb{Z}$ and $p \in \mathbb{N}$. As such, only particular frequency eigenmodes can form standing waves within the cavity, the values of which being determined by the cavity dimensions and internal material composition.

4.2   Photonic Band Gap Structures

Photonic band gap (PBG) structures, also known as photonic crystals, are periodic crystal-like systems comprised of dielectric media which are capable of controlling the flow of electromagnetic radiation. By drawing analogies with solid state physics, one is able to derive a variety of behaviours exhibited by photons within such a lattice.

4.2.1   Preliminaries

Lattices, being periodic structures, have discrete translational symmetries, thus it becomes beneficial to introduce a set of *primitive lattice vectors* $\mathbf{a}_i$ which define the characteristic lattice periodicity. As such, any shift of integer combinations of these primitive vectors, i.e. $\mathbf{a} = \sum_{i=1}^{3} n_i \mathbf{a}_i$, where $n_i \in \mathbb{Z}$, results in a return to the initial conditions.

Similarly, one benefits from introducing *primitive reciprocal lattice vectors* $\mathbf{b}_j$, which have units of inverse lengths, and are defined such that

$$\mathbf{a}_i \cdot \mathbf{b}_j = 2\pi\delta_{ij}.$$

4.2.2   Electromagnetism as an Eigenvalue Problem

Consider a system comprised of macroscopic, isotropic, non-dispersive dielectric media of permittivity $\epsilon\left(\mathbf{r}\right) = \epsilon_0\epsilon_r$, where ϵ_0 is the permittivity in vacua and $\epsilon_r \equiv \epsilon_r\left(\mathbf{r}\right)$ is the relative permittivity, and permeability $\mu\left(\mathbf{r}\right) = \mu_0\mu_r$, where μ_0 is the permeability in vacuo and $\mu_r \equiv \mu_r\left(\mathbf{r}\right)$ is the relative permeability. Additionally, the media will be assumed transparent, i.e. $\mu, \epsilon \in \mathbb{R}^+$. Maxwell's equations for such a system are written

$$\boldsymbol{\nabla} \cdot \mathbf{E} = \frac{\rho}{\epsilon}$$

$$\boldsymbol{\nabla} \cdot \mathbf{B} = 0$$

$$\boldsymbol{\nabla} \times \mathbf{E} = -\partial_t\mathbf{B} \tag{4.17}$$

$$\boldsymbol{\nabla} \times \mathbf{B} = \partial_t\left(\mu\epsilon\mathbf{E}\right) + \mu\mathbf{j}, \tag{4.18}$$

where ρ and $\mathbf{j}$ are the free charge and current densities.

In general, the electromagnetic fields may take elaborate forms which would make the following section needlessly complicated. As such, for the sake of simplicity, the real fields will be replaced by their complex equivalents and expanded into sets of harmonic modes of the forms

$$\mathbf{E}\left(t, \mathbf{r}\right) = \mathbf{E}\left(\mathbf{r}\right)e^{-i\omega t}$$

$$\mathbf{B}\left(t, \mathbf{r}\right) = \mathbf{B}\left(\mathbf{r}\right)e^{-i\omega t},$$

where ω is the angular frequency of a given mode.

Assuming that there are no electromagnetic sources or sinks within the system, i.e. $\rho = \mathbf{j} = 0$, then by dividing Equation (4.18) by $\mu\epsilon$ and taking the curl of the result, one obtains

$$\boldsymbol{\nabla} \times \left(\frac{1}{\mu\epsilon}\boldsymbol{\nabla} \times \mathbf{B}\right) = -i\omega\boldsymbol{\nabla} \times \mathbf{E}.$$

Substituting Equation (4.17) to remove the curl term on the right-hand side and using the relation for the speed of light $c = \frac{1}{\sqrt{\mu_0\epsilon_0}}$, then one receives an equation for the magnetic field, fully decoupled from the electric field:

$$\boldsymbol{\nabla} \times \left(\frac{1}{\mu_r\epsilon_r}\boldsymbol{\nabla} \times \mathbf{B}\right) = \frac{\omega^2}{c^2}\mathbf{B}. \tag{4.19}$$

By a similar methodology, taking the curl of Equation (4.17) and substituting Equation (4.18), one obtains

$$\frac{1}{\mu_r \epsilon_r} \boldsymbol{\nabla} \times (\boldsymbol{\nabla} \times \mathbf{E}) = \frac{\omega^2}{c^2} \mathbf{E}. \tag{4.20}$$

One may note that Equations (4.19) and (4.20) are of the characteristic form for an eigenvalue problem [105, §8.13], viz. one can define linear eigen-operators $\hat{\Theta}_{\mathbf{B}} = \boldsymbol{\nabla} \times \frac{1}{\mu_r \epsilon_r} \boldsymbol{\nabla} \times$ and $\hat{\Theta}_{\mathbf{E}} = \frac{1}{\mu_r \epsilon_r} \boldsymbol{\nabla} \times \boldsymbol{\nabla} \times$ acting on respective eigenfunctions $\mathbf{B}/\mathbf{E}$ to produce an eigenvalue $\frac{\omega^2}{c^2}$. In this formulation, one is able to deduce a number of properties of these fields.

Owing to the linearity of $\hat{\Theta}$, any linear combination of solutions is itself a solution. Additionally, because the permittivity and permeability are real by construction, this eigen-operator is Hermitian, hence all eigenvalues are real (and hence also positive) and all modes are mutually orthogonal, i.e. $(\mathbf{B}_i, \mathbf{B}_j) = (\mathbf{E}_i, \mathbf{E}_j) = 0 \quad \forall i \neq j$, where $(\cdot, \cdot)$ denotes the inner product of two fields. These properties are stated without proof because they are thoroughly covered in numerous undergraduate textbooks [105, 126, 127].

4.2.3   Bloch's Theorem

Bloch's theorem is an early result of quantum theory in the context of solid state physics. In brief, the theorem states that the wavefunction of an electron, $\psi_{j,\mathbf{k}}$, in a perfectly periodic structure may be written as the product of a periodic function, $u_j(\mathbf{r})$, with a plane wave (cumulatively termed a *Bloch wave*), i.e.

$$\psi_{j,\mathbf{k}}(\mathbf{r}) = u_j(\mathbf{r}) e^{i\mathbf{k}\cdot\mathbf{r}},$$

where $\mathbf{k}$ is the wavevector. However, the same theory holds for photons in regular photonic crystals, the proof of which follows.

The Fourier integral of an eigenfunction of the electric field may be written

$$\mathbf{E}(\mathbf{r}) = \int d\mathbf{k}\, \mathbf{E}(\mathbf{k}) e^{i\mathbf{k}\cdot\mathbf{r}}, \tag{4.21}$$

where $\mathbf{E}(\mathbf{k})$ is the electric field in Fourier space. Writing Equation (4.20) as

$$\boldsymbol{\nabla} \times (\boldsymbol{\nabla} \times \mathbf{E}) = \frac{\omega^2}{c^2} \mu_r \epsilon_r \mathbf{E}, \tag{4.22}$$

one can expand the permittivity as a Fourier series:

$$\epsilon_r(\mathbf{r}) = \sum_{\mathbf{G}} \epsilon_r(\mathbf{G}) e^{i\mathbf{G}\cdot\mathbf{r}}, \tag{4.23}$$

where $\mathbf{G} = \sum_{j=1}^{3} \ell_j \mathbf{b}_j$, with $\ell_j \in \mathbb{Z}$, is a vector in reciprocal space. Substituting the Fourier Equations (4.21) and (4.23) into (4.22), one receives

$$\int d\mathbf{k} \left[\mathbf{k} \times \left(\mathbf{k} \times \mathbf{E}\left(\mathbf{k}\right) \right) + \frac{\omega^2}{c^2} \mu_r \sum_{\mathbf{G}} \epsilon_r \left(\mathbf{G} \right) \mathbf{E} \left(\mathbf{k} - \mathbf{G} \right) \right] e^{i\mathbf{k}\cdot\mathbf{r}} = 0.$$

Since this must hold for all real space $\mathbf{r}$, the integrand must evaluate to zero:

$$\mathbf{k} \times \left(\mathbf{k} \times \mathbf{E}\left(\mathbf{k}\right) \right) + \frac{\omega^2}{c^2} \mu_r \sum_{\mathbf{G}} \epsilon_r \left(\mathbf{G} \right) \mathbf{E} \left(\mathbf{k} - \mathbf{G} \right) = 0. \qquad (4.24)$$

One notes from this that the initial eigenvalue problem is composed only of those Fourier components that are related by the reciprocal lattice vectors, hence only these components are necessary for expressing the eigenfunctions, i.e.

$$\mathbf{E_k}\left(\mathbf{r}\right) = \sum_{\mathbf{G}} \mathbf{E}\left(\mathbf{k} - \mathbf{G}\right) e^{i(\mathbf{k}-\mathbf{G})\cdot\mathbf{r}}.$$

Noting that in general Equation (4.24) has an infinite number of eigenvalues and eigenfunctions, which can be differentiated by a subscript n, then by defining a periodic function $\mathbf{u_k}\left(\mathbf{r}\right) = \sum_{\mathbf{G}} \mathbf{E}\left(\mathbf{k} - \mathbf{G}\right) e^{-i\mathbf{G}\cdot\mathbf{r}}$:

$$\mathbf{E_{k}}_n\left(\mathbf{r}\right) = \mathbf{u_{k}}_n\left(\mathbf{r}\right) e^{i\mathbf{k}_n\cdot\mathbf{r}}.$$

A similar analysis can be conducted for the magnetic field eigenvalue equation, then by denoting the period function $\mathbf{v_{k}}_n\left(\mathbf{r}\right)$ the magnetic field can be written

$$\mathbf{B_{k}}_n\left(\mathbf{r}\right) = \mathbf{v_{k}}_n\left(\mathbf{r}\right) e^{i\mathbf{k}_n\cdot\mathbf{r}}.$$

Consequently, one is able to validly formulate electromagnetic eigenfunctions as Bloch waves.

4.2.4   Photonic Band Gaps

The systems hitherto considered have been general, however it will now be assumed that $\mu_r \sim 1$ since the purpose of this section revolves around the propagation of electric fields within a lattice. Additionally, for simplicity the system will be considered one-dimensional.

The wave equation for the electric field in a dielectric medium is calculated using Equations (4.17) and (4.18) with the vector calculus identity $\boldsymbol{\nabla} \times \left(\boldsymbol{\nabla} \times \mathbf{E} \right) = \boldsymbol{\nabla}\left(\boldsymbol{\nabla} \cdot \mathbf{E} \right) - \nabla^2 \mathbf{E}$:

$$\frac{c^2}{\epsilon_r} \nabla^2 E - \partial_t^2 E = 0.$$

As was shown in Subsection 4.2.3, the electric field can justly be modelled as a Bloch wave, i.e. for an eigenmode n

$$E_{kn}(t,r) = u_{kn}(r) e^{i(k_n r - \omega_n t)}, \tag{4.25}$$

where u_{kn} is a periodic function, and k_n and ω_n are the wavevector and angular frequency of the eigenmode. Owing to its lattice periodicity, the periodic function can be expanded in a similar manner:

$$u_k(r) = \sum_{m=-\infty}^{\infty} E_m \exp\left(i\frac{2\pi m}{a}r\right),$$

where $\mathbf{E}_m$ are Fourier coefficients. Using this then Equation (4.25) can be written

$$E_{kn}(t,r) = \sum_{m=-\infty}^{\infty} E_m(r) \exp\left(i\left(k_n + \frac{2\pi m}{a}\right)r - i\omega_n t\right). \tag{4.26}$$

The relative permittivity of a lattice is periodic in real space, i.e. $\epsilon_r(\mathbf{r}+\mathbf{a}) = \epsilon_r(\mathbf{r})$, hence its inverse is also periodic and can be Fourier expanded as

$$\epsilon_r^{-1}(\mathbf{r}) = \sum_{m=-\infty}^{\infty} \kappa_m \exp\left(i\frac{2\pi m}{a}r\right), \tag{4.27}$$

where $\{\kappa_m\}$ are the Fourier coefficients, which are dictated by the geometry of the dielectric media, and $m \in \mathbb{Z}$. Assuming that the nearest neighbouring lattice distances dominate in this expansion, i.e. $m = 0, \pm 1$, then

$$\epsilon_r^{-1}(\mathbf{r}) \approx \kappa_0 + \kappa_1 \exp\left(i\frac{2\pi}{a}r\right) + \kappa_{-1} \exp\left(-i\frac{2\pi}{a}r\right). \tag{4.28}$$

Substituting Equations (4.26) and (4.28) into the wave equation, one obtains

$$\kappa_1 \left(k + \frac{2\pi(m-1)}{a}\right)^2 E_{m-1} + \kappa_{-1}\left(k + \frac{2\pi(m+1)}{a}\right)^2 E_{m+1}$$
$$\approx \left(\frac{\omega_n^2}{c^2} - \kappa_0\left(k + \frac{2\pi(m+1)}{a}\right)^2\right) E_m.$$

The electric field at a central lattice coordinate, $m = 0$, is

$$E_0 \approx \frac{c^2}{\omega_m^2 - \kappa_0 c^2 k^2}\left(\kappa_1\left(k - \frac{2\pi}{a}\right)^2 E_{-1} + \kappa_{-1}\left(k + \frac{2\pi}{a}\right)^2 E_1\right)$$

and at the preceding lattice point, $m = -1$;

$$E_{-1} \approx \frac{c^2}{\omega_m^2 - \kappa_0 c^2\left(k - \frac{2\pi}{a}\right)^2}\left(\kappa_1\left(k - \frac{4\pi}{a}\right)^2 E_{-2} + \kappa_{-1}k^2 E_0\right).$$

If $\omega_m^2 \sim \kappa_0 c^2 k^2$ then E_0 is a dominant contribution to the electric field expansion. Similarly, if $k \sim \frac{\pi}{a}$ then E_{-1} is an additional dominant contribution. Using these in the

expansion Equation (4.26) and neglected all other terms, then one obtains a set of two coupled linear equations:

$$\begin{pmatrix} \omega^2 - \kappa_0 c^2 k^2 & -\kappa_1 c^2 \left(k - \frac{2\pi}{a}\right)^2 \\ -\kappa_{-1} c^2 k^2 & \omega^2 - \kappa_0 c^2 \left(k - \frac{2\pi}{a}\right)^2 \end{pmatrix} \begin{pmatrix} E_0 \\ E_{-1} \end{pmatrix} = \begin{pmatrix} 0 \\ 0 \end{pmatrix}.$$

The non-trivial solutions to this become apparent when the determinant of the preceding matrix is zero, i.e.

$$\begin{vmatrix} \omega^2 - \kappa_0 c^2 k^2 & -\kappa_1 c^2 \left(k - \frac{2\pi}{a}\right)^2 \\ -\kappa_{-1} c^2 k^2 & \omega^2 - \kappa_0 c^2 \left(k - \frac{2\pi}{a}\right)^2 \end{vmatrix} = 0.$$

Solving this for the angular frequency, one obtains the dispersion relation

$$\omega_\pm \approx \frac{\pi c}{a} \sqrt{\kappa_0 \pm |\kappa_1|} \pm \frac{ac}{\pi |\kappa_1| \sqrt{\kappa_0}} \left(\kappa_0^2 - \frac{|\kappa_1|^2}{4}\right) \left(k - \frac{\pi}{a}\right)^2,$$

consequently when $k \ll \frac{\pi}{a}$ no modes exist within the interval

$$\frac{\pi c}{a} \sqrt{\kappa_0 - |\kappa_1|} < \omega < \frac{\pi c}{a} \sqrt{\kappa_0 + |\kappa_1|}. \tag{4.29}$$

This region of disallowed frequencies within the lattice is the *photonic band gap*. A diagrammatic representation of this band gap in ω-k space is shown in Figure 4.2.
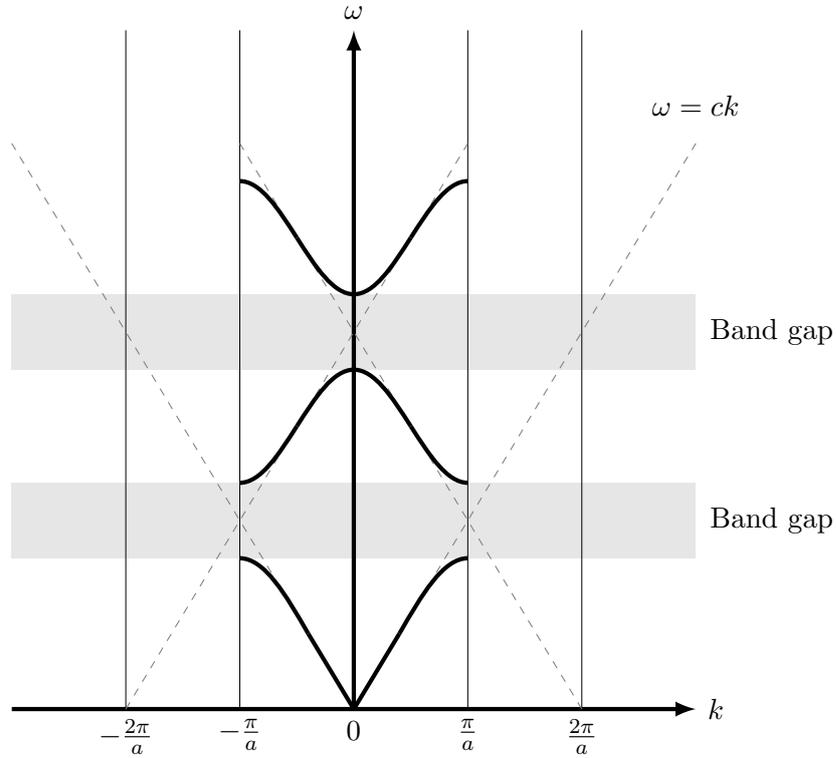
Figure 4.2: Dispersion relation for a one-dimensional photonic lattice with characteristic length a. Disallowed frequencies are indicated by horizontal grey bands.

4.2.5   Calculating Dielectric Fourier Coefficients

With the band gap calculated, one notes that the geometrical Fourier coefficients of the dielectric remain unknown. Reiterating Equation (4.27):

$$\epsilon_r^{-1}\left(\mathbf{r}\right) = \sum_{m=-\infty}^{\infty} \kappa_m \exp\left(i\frac{2\pi m}{a}r\right),$$

then by inverse Fourier transform one is able to write the coefficients

$$\kappa\left(\mathbf{G}\right) = \frac{1}{V_0} \int_{V_0} d\mathbf{r}\, \epsilon_r^{-1} \exp\left(-i\mathbf{G}\cdot\mathbf{r}\right),$$

where V_0 is the volume of the unit lattice cell.

The lattice will be assumed to be comprised of infinite length dielectric rods. For such a system, the volume element becomes infinite, resulting in all coefficients diverging, thus one assumes a priori that $G_z = 0$ such that the lattice reduces to a planar system transverse to the rods. Denoting the two-dimensionality (2) and transversality $\perp$, then under this regime the coefficients become

$$\kappa\left(\mathbf{G}\right) = \frac{1}{V_0^{(2)}} \int_{V_0^{(2)}} d\mathbf{r}_\perp\, \epsilon_{r\perp}^{-1} \exp\left(-i\mathbf{G}_\perp \cdot \mathbf{r}_\perp\right). \tag{4.30}$$

Denoting the rod radius r_a, rod relative permittivity ϵ_a and background permittivity ϵ_b, then the permittivity for a unit lattice cell containing a circular dielectric rod is

$$\frac{1}{\epsilon_r} = \frac{1}{\epsilon_b} + \left(\frac{1}{\epsilon_a} - \frac{1}{\epsilon_b}\right)\Theta\left(r_a - |\mathbf{r}_\perp|\right).$$

Substituting this in Equation (4.30), then

$$\kappa\left(\mathbf{G}\right) = \frac{1}{\epsilon_b}\delta_{\mathbf{G}_\perp,0} + \frac{1}{V_0^{(2)}}\left(\frac{1}{\epsilon_a} - \frac{1}{\epsilon_b}\right)\int_{V_0^{(2)}} \exp\left(iGr\sin\left(\theta - \frac{\pi}{2}\right)\right)\Theta\left(r_a - |\mathbf{r}_\perp|\right)r\,dr\,d\theta,$$

where $r \in [0, \infty)$ and $\theta \in [0, 2\pi)$. Using the identities [125, §9.1]

$$\cos\left(z\sin\left(\theta\right)\right) = J_0\left(z\right) + 2\sum_{k=1}^{\infty} J_{2k}\left(z\right)\cos\left(2k\theta\right)$$

$$\sin\left(z\sin\left(\theta\right)\right) = 2\sum_{k=0}^{\infty} J_{2k+1}\left(z\right)\sin\left(\left(2k+1\right)\theta\right)$$

and [128, §8.511]

$$\exp\left(\pm iz\sin\left(\phi\right)\right) = J_0\left(z\right) + 2\sum_{k=1}^{\infty} J_{2k}\left(z\right)\cos\left(2k\phi\right) \pm 2i\sum_{k=0}^{\infty} J_{2k+1}\left(z\right)\sin\left(2k+1\right)\phi,$$

then

$$\kappa\left(\mathbf{G}\right) = \frac{1}{\epsilon_b}\delta_{\mathbf{G}_\perp,0} + \frac{2\pi}{V_0^{(2)}}\left(\frac{1}{\epsilon_a} - \frac{1}{\epsilon_b}\right)\int_0^{r_a} r J_0\left(Gr\right)\,dr.$$

Finally, using the derivative $\frac{\mathrm{d}}{\mathrm{d}z}\left(zJ_1\left(z\right)\right) = zJ_0\left(z\right)$ then one concludes

$$\kappa\left(\mathbf{G}\right) = \frac{1}{\epsilon_b}\delta_{\mathbf{G}_\perp,0} + 2f\left(\frac{1}{\epsilon_a} - \frac{1}{\epsilon_b}\right)\frac{J_1\left(Gr_a\right)}{Gr_a},$$

where $f = \frac{\pi r_a^2}{V_0^{(2)}}$ is the fraction of the unit cell filled by the dielectric. Using this, one derives the coefficients for a lattice of a-separated circular dielectric rods to be

$$\kappa_0 = \frac{f}{\epsilon_a} + \frac{1-f}{\epsilon_b}$$

$$\kappa_{-1} = 2f\left(\frac{1}{\epsilon_a} - \frac{1}{\epsilon_b}\right)\frac{J_1\left(2\pi\frac{r_a}{a}\right)}{2\pi\frac{r_a}{a}}.$$

4.2.6   Localising Modes

With the existence of the photonic band gap and its relation to the structure of the lattice in which it is located established, one may now consider applications of the phenomenon. One such use is in the altering of the dispersion relation in localised regions through the introduction of defects within a lattice.

Consider the removal of dielectric scatterers from a periodic structure to form a local defect. Whilst the band gap structure deriving from the ensemble inhibits the transmission of electric fields over particular frequency ranges, the lattice spacing in the region of the defect has been adjusted. Accordingly, the defect is able to support otherwise forbidden electric field frequencies, with the surrounding lattice acting as a mirror to confine the radiation. The application of this phenomenon in relation to the measurement of DMCs become apparent when combined with the aforementioned microwave resonance cavity. By applying an electric field to a localised defect within a dielectric lattice at a frequency disallowed by the photonic band gap and measuring the electric field at a sufficiently shielded distance from the source. An unexpectedly high field strength would infer the existence of a weakly-interacting intermediary particle which was able to traverse the lattice, such as ALPs and HSPs.

Chapter 5

Theory: Computation

"Lone and discarded one! divorced by fate
Far from thy wished-for fellows–whither art flown
Where lingerest thou in bereaved estate
Like some lost star, or buried meteor stone?"
— James Joseph Sylvester,
Excerpt from *To a Missing Member of a Family*
Group of Terms in an Algebraic Formula

5.1   Finite Difference Methodology

Finite difference methodologies are used to solve ordinary differential equations by approximating differential operators as difference quotients, allowing one to solve these differential equations numerically, i.e.

$$\frac{\mathrm{d}f(x)}{\mathrm{d}x} \approx \frac{f(x+h) - f(x)}{h}.$$

5.1.1   Derivation

Consider a general function $f(x)$. The value of this function at a difference h away from an initial value x_0 is given by the Taylor series expansion

$$f(x_0 + h) = \sum_{k=0}^{\infty} \frac{f^{(k)}(x_0)}{k!} h^k,$$

where $f^{(k)}(x_0)$ denotes the k$^{\text{th}}$ derivative of the function evaluated at point x_0. Since one cannot numerically compute an infinite series, one instead truncates the series after n terms, encompassing all further terms inside a remainder term R_n, i.e.

$$f(x_0 + h) = \sum_{k=0}^{n} \frac{f^{(k)}(x_0)}{k!} h^k + R_n(x). \tag{5.1}$$

Truncating this to derivatives of first order, one receives

$$f(x_0 + h) = f(x_0) + f'(x_0) h + R_1(x),$$

which can be rearranged as

$$f'(x_0) = \frac{f(x_0 + h) - f(x_0)}{h} - \frac{R_1(x)}{h}.$$

Assuming that $\frac{R_1(x)}{h}$ is negligibly small, one thus approximates the first derivative of the function as

$$f'(x_0) \approx \frac{f(x_0 + h) - f(x_0)}{h}.$$

One notes that this is similar to the definition of the derivative of a smooth function,

$$f'(x_0) = \lim_{h \to 0} \frac{f(x_0 + h) - f(x_0)}{h},$$

excepting that h is now finite, giving the methodology its namesake. This method can be extended to higher order derivatives which may be computed recursively, i.e. retaining only the leading order terms

$$f^{(n)}(x_0) = \frac{f^{(n-1)}(x_0 + h) - f^{(n-1)}(x_0)}{h} - \frac{R_n(x)}{h}. \tag{5.2}$$

5.1.2   Accuracy

The remainder term earlier introduced, more formally known as the *truncation error*, is the deviation from the exact solution that the quantity being calculated takes in the limit $h \to 0$, assuming no other errors. One is able to see from Equation (5.1) that this truncation error is given by

$$R_n(x) = \sum_{k=n+1}^{\infty} \frac{f^{(k)}(x_0)}{k!} h^k.$$

Because h is small by construction, i.e. $h^p \gg h^q$ for $p < q$, when calculating this truncation error one need only consider the lowest order term in h, i.e.

$$R_n(x) \approx \frac{f^{(n+1)}(x_0)}{(n+1)!} h^{n+1}.$$

From recursively applying the relationship from Equation (5.2), one sees that

$$R_n(x) = \mathcal{O}\left(h^{n+1}\right),$$

viz. the error associated with a truncation to first order is proportional to h. Consequently, the truncation error is proportional to h^n, hence becomes negligible at all orders in the limit $h \to 0$.

5.1.3   Strengths and Limitations

Perhaps the most obvious strength to the finite difference methodology is the ease with which it may be understood, given a relatively basic background knowledge of calculus. Additionally, one can see that this method asymptotically approaches a full description of a system in the limit of the finite difference to zero.

Despite its clear strengths, finite difference techniques are not perfect. Owing to its pointwise approximations, the finite difference method cannot accurately handle complex system geometries, such as those with curved boundaries. Additionally, a vanilla finite difference analysis encounters issues at boundaries since there are no adjacent cells with which to calculate differences. Perhaps most detrimentally, because of the manner in which the methodology computes the local differences, the finite difference methodology struggles greatly with unstructured domains, i.e. those with irregular or non-orthogonal meshes.

Regardless of the technique's weaknesses, finite difference methods are often favoured for calculations in which one can assume a priori that the system does not have a complex geometry. Additionally, more exotic finite difference schemes are able to circumvent a number of the drawbacks, such as by adding an padding layer external to the data domain, thus allowing the calculation at boundary surfaces.

5.2   Particle-in-Cell Methodology

Particle-in-cell (PIC) methodology was developed during the mid 1950s by Frank Harlow and Martha Evans for use in simulating hydrodynamical systems [129, 130]. The basis of this technique pivots around the interplay between particles and fields; whereas fields dictate how particles move, particles influence local field strengths. This reciprocal behaviour can be applied algorithmically, facilitating the numeric simulation of non-linear systems involving the co-interactions of particles and fields. The following subsections outline the PIC methodology in the context of plasma physics simulations, in which the particles of interest are the constituent elements of a plasma – namely electrons and ions – and the fields of concern are those of electromagnetism.

5.2.1   Motivation

PIC codes are heavily utilised for the simulation of systems which have coupled equations between particles and fields. Consider an electromagnetohydrodynamical system comprised of charged particles acting under the influence of electromagnetic fields; its equation of motion is the Lorentz-Maxwell equation:

$$m\mathbf{a} = q\left(\mathbf{E} + \mathbf{v} \times \mathbf{B}\right),$$

where m and q are respectively the particle mass and charge, $\mathbf{a}$ is the acceleration experienced by the particle which is moving at a velocity $\mathbf{v}$, and $\mathbf{E}$ and $\mathbf{B}$ are the electric and magnetic fields. By the continuity equation, one sees that shifts in the charged particle number density, ρ, induces a current:

$$\partial_t \rho + \boldsymbol{\nabla} \cdot \mathbf{j} = 0. \tag{5.3}$$

This induced current affects the electric and magnetic fields through the Maxwell-Ampére law

$$\boldsymbol{\nabla} \times \mathbf{B} = \epsilon\mu\partial_t\mathbf{E} + \mu\mathbf{j},$$

where ϵ and μ are the permittivity and permeability of the medium, respectively. However, the opposite processes are also valid assessments of the system. In reverse, changes in electromagnetic fields result in a vector current which shifts the charged particle density through the continuity equation, resulting in the particles experiencing an external force subject to the Lorentz equation. Accordingly, when simulating magnetohydrodynamical systems one wishes to iteratively continue this interplay loop between particles and fields.

5.2.2   System Initialisation

In PIC codes, the computational domain is divided into cells which run parallel to the coordinate axes, collectively forming what is known as a grid or a mesh. The lines which separate these cells are known as grid or mesh lines with their intersections being termed grid or mesh points. Particles are situated inside these cells, giving the methodology its namesake, with associated momenta – thus inhabiting a six-dimensional $(\mathbf{x}, \mathbf{p})$ phase space – whereas the fields of the system reside along the vertices in a staggered Yee grid configuration, as shown in Figure 5.1 [131].

Prior to performing any calculations, PIC codes instantiate the grid along with all particles of the system and assign their corresponding positions and momenta. Fur-
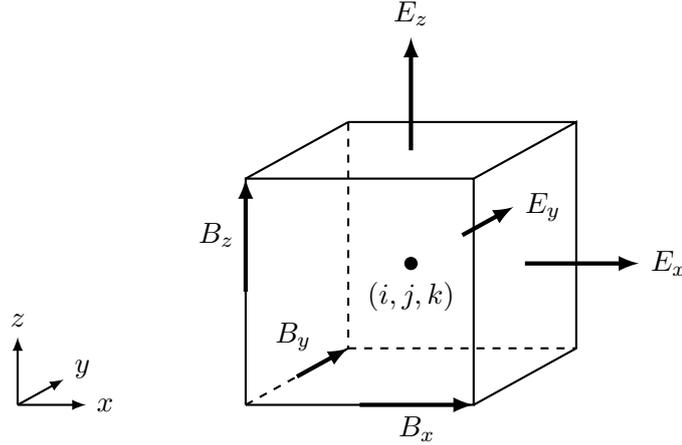
Figure 5.1: Diagram of a Yee cell. Particles are located within
cells encompassed by faces on which electric fields are defined
and vertices on which magnetic fields are defined.

thermore, PIC codes must ensure initial quasi-neutrality; this is typically conducted by assuming an initially unperturbed plasma, thus requiring the solving of the Poisson equation, i.e.

$$\nabla^2\varphi = \frac{\rho}{\epsilon},$$

where φ is the field potential, ρ is the local charge density and ϵ is the permittivity of the medium. The local charge density is calculated as being the number of particles contained within a cell divided by the volume of that cell.

5.2.3   Particle Pusher

Charged particles move under the influence of electromagnetic fields, thus the advancement of particles requires the solving of the Lorentz force equation. This equation of motion for a particle of charge q and mass m travelling at an initial speed $\mathbf{v} = \dfrac{\mathrm{d}\mathbf{x}}{\mathrm{d}t}$ under the influence of an electric field $\mathbf{E}$ and magnetic field $\mathbf{B}$ may be written

$$\frac{\mathrm{d}\mathbf{p}}{\mathrm{d}t} = q\left(\mathbf{E} + \mathbf{v}\times\mathbf{B}\right),$$

where $\mathbf{p} = \gamma m\mathbf{v}$ is the relativistic 3-momentum. PIC codes typically solve this equation using finite difference methods. However, the de facto method for propagating a charged particle is the Boris pusher algorithm, which benefits from conserving phase space volume [132, 133]. This result is an equivalent formulation of Liouville's theorem, thus the total number of systems within the ensemble remains constant.

5.2.4   Charge Distributions

Owing to the charge continuity exhibited in Equation (5.3), when particles enter or leave a cell they alter the cell's charge density, thus inducing a instantaneous current. The magnitude of this current is determined by the number and sizes of particles which traverse the boundaries, while the direction is dictated by the cell face through which the particle(s) pass.

5.2.5   Field Solver

The newly induced current $\mathbf{j}$ alters the time-evolution of the electric fields through Equation (4.4). As such, the result of particle motion is an influence on the local field strengths. Most commonly these new fields are calculated through a finite-difference method.

5.2.6   Field Interpolation

Having calculated the electromagnetic fields within the system, these are interpolated to locations of the particles situated within the cell bounded by the field's point of origin.

5.2.7   Macroparticles

Macroscopic systems may be comprised of upwards of 10^{20} particles, each interacting with one another through a variety of mechanisms. Consequently, it rapidly becomes infeasible to model exact behaviours of every particle in its entirety, thus one must find a means of minimising the complexity without relinquishing details of the overall collective behaviours. The solution to this is to instead model bunches of many real particles, known as *super-particles* or *macroparticles*. Since the equation of motion for the particles can be written in terms of the mass-to-charge ratio, the macroparticle trajectory is equivalent to that of the real particles. Additionally, the removal of point-like particles through modelling macroparticles one is able to circumvent singularities deriving from Coulombic interactions.

5.2.8   Algorithmic Overview

PIC methodology can be briefly summarised as a cycle of four processes which iterate at time steps of Δt:

1. Integration of equations of motion (particle pusher)

2. Calculate charge distribution at grid points; include losses and gains, e.g. emission and absorption

3. Integration of field equations on grid (field solver)

4. Interpolation of fields at particle positions

Figure 5.2 shows a brief overview of the PIC methodology.
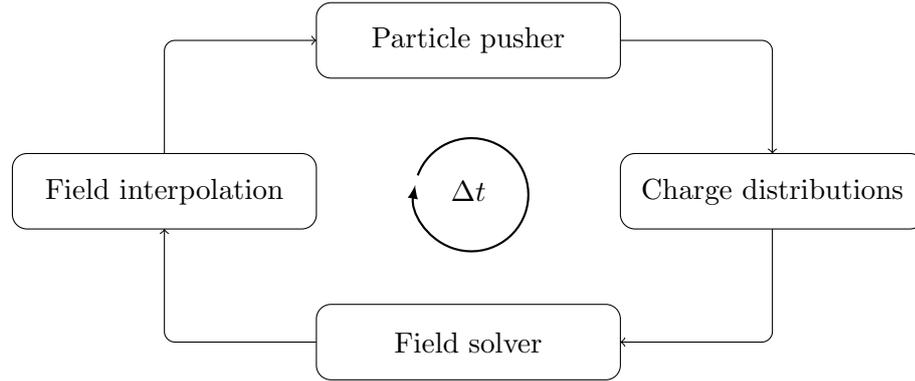
Figure 5.2: Overview of particle-in-cell methodology.

5.2.9   EPOCH

An example of a modern particle-in-cell implementation is EPOCH (Extendable PIC Open Collaboration) [134]. EPOCH is developed by a team of computational plasma physicists headed by Prof. Tony Arber at the University of Warwick and builds upon an earlier code, Project Plasma Simulation Code (PSC), which was written by Prof. Hartmut Ruhl of Ludwig-Maximilians-Universität München [135]. EPOCH is written in Fortran and parallelised using MPI and incorporates such behaviours as collisions, ionisation and quantum electrodynamical effects.

5.3   Green's Function Methodology

5.3.1   Background Theory

Green's functions are a method of solving linear differential equations, i.e. those of the form

$$\hat{L}u\left(\mathbf{x}\right) = f\left(\mathbf{x}\right), \tag{5.4}$$

where $\hat{L}$ is a linear differential operator which acts only upon the arguments of the solution $u\left(\mathbf{x}\right)$, which satisfies boundary conditions on a topological space Ω, and $f\left(\mathbf{x}\right)$

is the source term. The defining equation for the Green's function G of $\hat{L}$ is the unique solution to

$$\hat{L}G\left(\mathbf{x}, \mathbf{x}'\right) = \delta\left(\mathbf{x} - \mathbf{x}'\right). \tag{5.5}$$

From this, one is able to derive the integral equation for the function. Using the sifting property of the Dirac delta distribution, a general function $f\left(\mathbf{x}\right) : \mathbf{x} \in \Omega$ can be written

$$f\left(\mathbf{x}\right) = \int_{\Omega} \delta\left(\mathbf{x} - \mathbf{x}'\right) f\left(\mathbf{x}'\right) \, \mathrm{d}\Omega_{\mathbf{x}'}.$$

Replacing the delta distribution through the defining Equation (5.5), this function can be rewritten

$$f\left(\mathbf{x}\right) = \hat{L}\int_{\Omega} G\left(\mathbf{x}, \mathbf{x}'\right) f\left(\mathbf{x}'\right) \, \mathrm{d}\Omega_{\mathbf{x}'}.$$

Consequently, one can always write the solution $u\left(\mathbf{x}\right)$ from Equation (5.4) as an integral of the form

$$u\left(\mathbf{x}\right) = \int_{\Omega} G\left(\mathbf{x}, \mathbf{x}'\right) f\left(\mathbf{x}'\right) \, \mathrm{d}\Omega_{\mathbf{x}'}. \tag{5.6}$$

5.3.2   Computation

When calculating the solution for systems in which an analytical expression cannot be readily obtained, such as those for which the source exhibits non-linear behaviours, one is able to discretise Equation (5.6) and numerically evaluate the solution through summation.

This methodology has found application in many systems with boundary condition problems, systems with complex geometries, and systems built around dispersion. A select few of these applications will now be presented and discussed.

5.3.2.1   Berger & Lasher (1958)

One of the earliest documented uses of Green's functions in computation can be found in J. M. Berger and G. J. Lasher's 1958 paper [136]. Berger and Lasher outlined how one could practically utilise Green's functions to numerically calculate the solution to the inhomogeneous Poisson's equation in two spatial dimensions, i.e. $\left(\dfrac{\partial^2}{\partial x^2} + \dfrac{\partial^2}{\partial y^2}\right) \varphi\left(x, y\right) = f\left(x, y\right)$, at each time step. To this end, a numeric analysis code was developed and applied on an IBM 704 computer using the Green's function methodology, which was capable of correctly calculating the solution to seven of the eight decimal digits carried by the machine.

In this paper, the authors stated several of the advantages of utilising Green's function method. These included the ability to calculate solutions in systems with multiple different inhomogeneous regions, a guaranteed high degree of accuracy in calculating the solution due to having a "predetermined sequence of arithmetic operations", and the flexibility afforded by being capable of choosing the region(s) in which the solution are calculated.

5.3.2.2   Harwood & Dupère (2012)

A 2012 proceedings by A. Harwood and I. Dupère from the ASME Noise Control and Acoustics Division Conference reported progress in the application of Green's functions in the area of acoustic flows [137]. Hardwood and Dupère identified problems with canonical techniques for simulating acoustics through aerodynamical systems: disparities in length scales, excessive computational expense, and restrictions to simple geometries. In contrast, the authors noted that the application of Green's functions allows efficient and accurate calculation of wave propagation and scattering.

Within their paper, Harwood and Dupère develop an approach to numerically calculate solutions to equations of the form

$$\left(\nabla^2 + k^2\right)\varphi\left(\mathbf{x}, \omega\right) = q\left(\mathbf{x}, \omega\right)$$

on arbitrary geometries, where k is the wavenumber, φ is the velocity potential, $q\left(\mathbf{x}, t\right)$ is the source and it is implied that the temporal component of the solution is harmonic.

5.3.2.3   Mayfield, Gao & Luo (2021)

More contemporaneously, J. Mayfield, Y. Gao and S. Luo's recent pre-proof journal paper describes the application of Green's functions to the numeric simulation of linear scalar wave equations of the form [138]

$$\frac{\partial^2 u\left(t, \mathbf{x}\right)}{\partial t^2} = c^2\left(\mathbf{x}\right)\nabla^2 u\left(t, \mathbf{x}\right) : \left(t, \mathbf{x}\right) \in \mathbb{R}^d \times \left(0, \infty\right).$$

In this paper, the authors split the appropriate Green's function into forward- and backward-propagating components. Following this, the components are approximated by geometrical optics approximations and propagated using the Huygens-Fresnel principle to account for diffraction, reflection &c. The main advantage of the methodology noted by the authors lies in its ability to balance efficiency and accuracy.

Chapter 6

Run:DMC: A Novel Post-Process Numeric Analysis Code

> *"Measure what is measurable, and make measurable what is not so."*
>
> — Antoine-Augustin Cournot
> & Thomas Henri Martin[1]

Note: For brevity this chapter utilises Heaviside-Lorentz units with $\hbar = 1$ except where explicitly otherwise stated.

6.1 The Code

6.1.1 Overview

Run:DMC (a neologism combining the software invocation command "Run:" with an acronym for Dark Matter Candidates) is a post-process analysis software package capable of calculating the strengths of hypothetical fields from simulation output data according to associated coupling parameters. It achieves this through the application of Green's function methodology to numerically solve the inhomogeneous Klein-Gordon equation, namely $\left(\Box + m^2\right)\Psi = \varrho\left(t, \mathbf{x}\right)$. This method facilitates efficient and accurate calculations in systems for which direct calculation is not possible, i.e. those containing arbitrarily complex geometries and/or multiple different inhomogeneous source regions. **Run:DMC** is written in the julia programming language with additional Python elements for data reading. It is currently able to utilise output data from the particle-in-cell

---

[1]This quote is often misattributed to Galileo Galilei [139].

85

(PIC) code EPOCH and the finite difference time domain (FDTD) code MEEP. The ultimate objective of **Run:DMC** is to approach an accurate description of hypothetical fields for any given system in the asymptotic limit of discrete to continuous spaces, i.e. through a marked increase in resolution.

This chapter outlines the inner workings of the code, from design decisions through to the core algorithm and any additional non-standard components. For later reference, a minimal graphical representation of **Run:DMC**'s methodology is shown in Figure 6.1. Each of the process blocks will be expanded upon in following subsections.
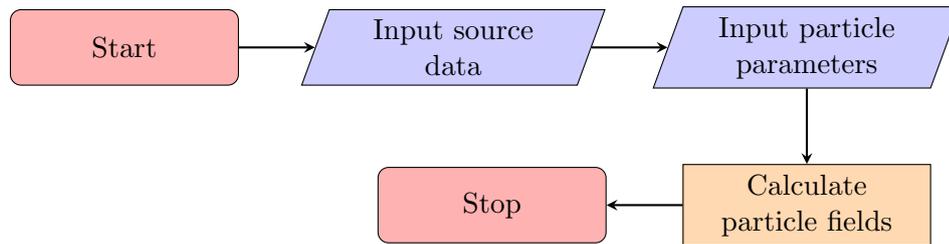
Figure 6.1: Basic overview of **Run:DMC**.

6.1.2   Input Source Data

Prior to the undertaking of any calculations, **Run:DMC** must first be provided the data pertaining to the system, such as spacetime coordinates as well as any relevant fields. These data are stored within a dictionary, which indexes through the implementation of a hash table.

Some behaviours of a given system do not manifest during simulation unless it is run at a sufficiently high resolution, e.g. those deriving from rapid variations in space or time. Often the result of these high resolution simulations are the outputs of extremely large datasets, which would take unreasonable computational resources to analyse. As such, one cannot expect users to always have manageable sizes of data, thus **Run:DMC** has been written with the functionality to reduce the size of the dataset by manually specified scaling factors.

Furthermore, simulation software may save output data in any number of manners, whether it be a single large file or multiple small files, SI vs. CGS vs. dimensionless units, any one of a plethora of file extensions &c. Consequently, one needs to read and store the data such that analysis of the simulation data is consistent; therefore, **Run:DMC** requires that each simulation code has its own particular reader. Each reader must hence be able to access and downsample simulation output data, as well as normalising

its units to SI.

Finally, it would be counter-productive to downsample and normalise units of the source data every time one wished to analyse a simulation's output. Instead, it is significantly more efficient to process the source data once and save it to file, to be read again in potential later analyses. **Run:DMC** utilises julia's `Serialization` package to serialise processed data to disk.

Accounting for the requirements discussed herein, the "Input source data" stage of Figure 6.1 can be expanded as shown in Figure 6.2.
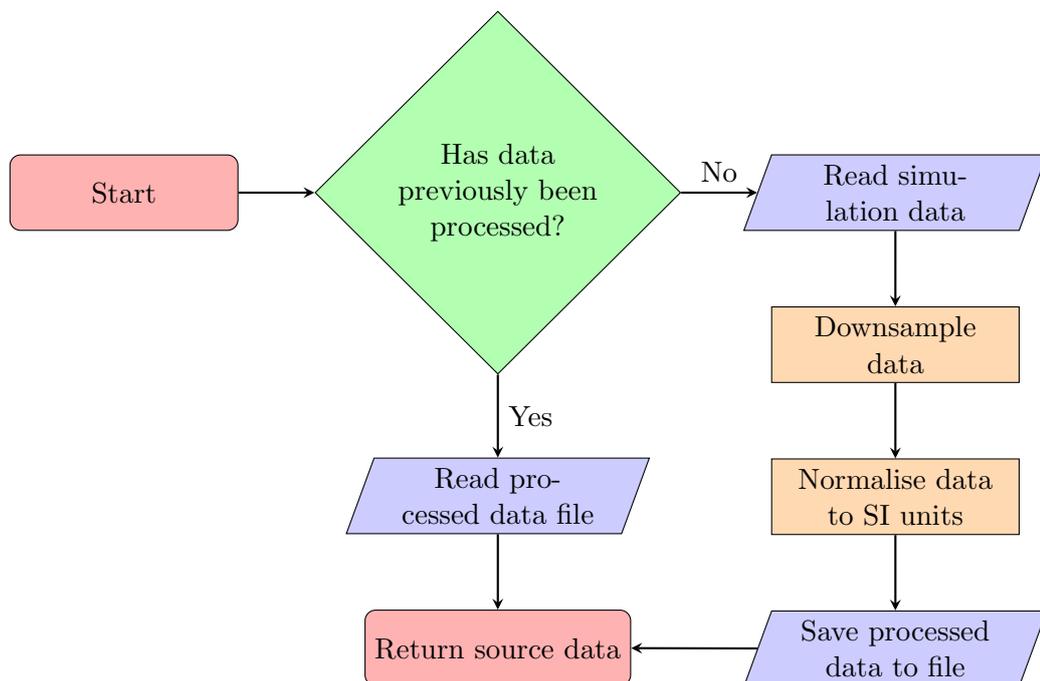
Figure 6.2: Flowchart of **Run:DMC** source data input.

6.1.3   Input Particle Parameters

In physics, every particle has a set of characteristic properties which are afforded to it by a collection of intrinsic parameter values. The input of these is therefore fundamental to a code which calculates the corresponding fields of those particles.

Run:DMC parses associated variables of each particle from a configuration file named "particles", with the input of properties for each particle being delimited by `begin particle` and `end particle` demarcations. Parameters are defined through an infix syntax, e.g. `variable = value`, with a limit of one variable per line. The current necessary parameters for functionality are the designated particle name and its mass, which is measured in eV. Additionally, any variable can be input through this method

– even those not necessary for calculation – allowing one to make notes further to those required.

Furthermore, one may desire to comment the input file without it being interpreted by the particle parser. These comments are denoted by a hash (`#`) character, in line with that found in BASH, Python, julia &c. **Run:DMC**'s particle input files are also whitespace agnostic, allowing for arbitrary spacing and indentation, befitting many user styles.

A basic example of a valid particle input file is as follows:

```
# This is a comment
begin particle
    name = axion     # This is also a comment
    mass = 1e-3
    note = Hello, world
end particle
```

6.1.4   Calculate Particle Fields

The capabilities of **Run:DMC** for the reading of simulation data and loading particle parameters have been hitherto discussed. However, the most important component of a numeric analysis code is clearly the numeric analysis. This subsection now considers the "Calculate particle fields" step of Figure 6.1.

6.1.4.1   Discretisation of the Klein-Gordon Solution

The Klein-Gordon equation solution derived in Equation (2.4) was defined on a smooth manifold, however, numerical analyses are performed on discrete spaces. As such, the desired solution for **Run:DMC** is the equivalent discretised form.

Topological spaces can be classed as discrete or continuous, depending on whether the coordinate system is countable or uncountable, respectively. This section strives to justly translate Equation (2.4) from a continuous space to a discrete one for computational numeric analysis. However, prior to any mathematical trickery, one should immediately note an issue with direct translation to discrete space for the purpose of computational numerics: the limits would require an infinite space to be analysed - a process not afforded by any current technology. If instead one were to assume a priori that the support, i.e.

the domain on which the field is non-zero, is closed and bounded, then without loss of generality one can substitute the infinite domain for the support Ω, outside of which the field is zero, i.e.

$$\Psi\left(t_f,\mathbf{x}_f\right)=\int_\Omega \mathrm{d}^4 x_s\left(\frac{\Theta\left(T\right)\delta\left(T-X\right)}{4\pi X}-\frac{\Theta\left(T-X\right)}{4\pi\sqrt{T^2-X^2}}mJ_1\left(m\sqrt{T^2-X^2}\right)\right)\varrho\left(t_s,\mathbf{x}_s\right).$$

The discrete analogue for integrals in continuous space are sums which span the same domain. Using the common notation that permits specifying limits under the Sigma for an arbitrary numbers of points, and the infinitesimal becoming a unit element of the discrete space, then a direct translation of integration to summation is written

$$\Psi\left(t_f,\mathbf{x}_f\right)=\sum_{t_s,\mathbf{x}_s}\left(\frac{\Theta\left(T\right)\delta\left(T-X\right)}{4\pi X}-\frac{m}{4\pi}\frac{\Theta\left(T-X\right)}{\sqrt{T^2-X^2}}J_1\left(m\sqrt{T^2-X^2}\right)\right)\varrho\left(t_s,\mathbf{x}_s\right)\Delta t\,\Delta V.$$

One can directly substitute the continuous variables for their discrete counterparts because the discrete space is comprised of a subset of the continuous space. However, another problem now arises in that the Dirac delta function is a Schwartzian distribution which is only properly defined on a continuous topological space. As such, it is necessary to translate the Dirac delta to its discrete analogue – the Kronecker delta. This translation is performed in Appendix A, the result of which is the absorption of the temporal measure by the delta distribution, i.e. $\dfrac{\delta_{\mathrm{Kronecker}}}{\Delta t}=\delta_{\mathrm{Dirac}}$, finally culminating in the full discretised equation for the field point:

$$\Psi\left(t_f,\mathbf{x}_f\right)=\sum_{t_s,\mathbf{x}_s}\left(\frac{\Theta\left(T\right)}{4\pi X}\frac{\delta\left(T-X\right)}{\Delta t}\right.$$
$$\left.-\frac{m}{4\pi}\frac{\Theta\left(T-X\right)}{\sqrt{T^2-X^2}}J_1\left(m\sqrt{T^2-X^2}\right)\right)\varrho\left(t_s,\mathbf{x}_s\right)\Delta t\,\Delta V, \quad (6.1)$$

where it is to be understood that $\delta\left(x\right)=1$ if $x=0$ and $\delta\left(x\right)=0$ if $x\neq0$.

6.1.4.2   Unit Elements

Due to the nature of discretisation, **Run:DMC**'s core algorithm requires regular use of unit elements of the system coordinates. These include spatiotemporal elements $\delta\{t,x,y,z\}=\{t,x,y,z\}_{n+1}-\{t,x,y,z\}_n$ and the volume element $\delta V=\delta x\times\delta y\times\delta z$. The simulation software packages employed in this thesis use regularly-spaced spatiotemporal coordinates, thus these elements need only be calculated once and passed by reference thenceforth, making their repeated calculation unnecessary. However, it would be a trivial addition to include the calculation of these elements in situ to accommodate non-linear coordinate systems, such as those found in some fluid codes, at the cost of computational efficiency.

6.1.4.3 Dimensionality

Run:DMC utilises a three-dimensional Green's function to solve the inhomogeneous Klein-Gordon equation. In order to apply this methodology in a coherent and valid manner, one must therefore also have three-dimensional data. However, this is often not the case in simulations, which may instead model lower-dimensional systems. To circumvent this issue, the code ensures that the data is of an appropriate dimensionality, adding dimensions to the data where necessary; this is analogous to considering an infinitesimally thin rod or sheet existing in a three-dimensional topological space.

In circumstances when the simulation data is less than three-dimensional, the code compensates for the missing length scales by falling back to those present in lower dimensions. For example, if the simulation data is two-dimensional and lacks a z-dimension then **Run:DMC** defines the unit element in z as being the lesser of the unit elements in x or y, i.e. $\delta z = \min(\delta x, \delta y)$. Similarly, if the simulation is one-dimensional and also lacks a y-dimension then **Run:DMC** defines the elements in y and z equal to that for x, i.e. $\delta z = \delta y = \delta x$. Consequently, **Run:DMC** is capable of calculating three-dimensional particle fields from one-, two- and three-dimensional simulation data.

6.1.4.4 The Calculation Algorithm

With the source data of the correct dimensionality and corresponding unit elements determined, **Run:DMC** is able calculate the particle fields. Fundamentally the algorithm is required to numerically solve the inhomogeneous Klein-Gordon equation via the earlier derived integral:

$$\Psi\left(t_f, \mathbf{x}_f\right) = \int_{-\infty}^{\infty} \mathrm{d}^4 x_s \left(\frac{\Theta\left(T\right)\delta\left(T-X\right)}{4\pi X} - \frac{m}{4\pi}\frac{\Theta\left(T-X\right)}{\sqrt{T^2-X^2}}J_1\left(m\sqrt{T^2-X^2}\right)\right)\varrho\left(t_s, \mathbf{x}_s\right),$$

where ϱ denotes the source density, and $T = t_f - t_s$ and $X = \|\mathbf{x}_f - \mathbf{x}_s\|$ are respctively the temporal and spatial distances between the field and source points. To accomplish this, **Run:DMC** iterates over all field points, $\left(t_f, \mathbf{x}_f\right)$, seeking all causally-connected source points, $\left(t_s, \mathbf{x}_s\right)$, i.e. those for which $\left(t_f - t_s\right) - \|\mathbf{x}_f - \mathbf{x}_s\| \geq 0$, as shown in the past lightcone of Figure 6.3.

"Massless" and "massive" contributions to the Green's functions are calculated for each causally-connected field point-source point pairing by

$$G_{m=0}\left(t_f, \mathbf{x}_f \,|\, t_s, \mathbf{x}_s\right) = \frac{\Theta\left(t_f - t_s\right)\delta\left(\left(t_f - t_s\right) - \|\mathbf{x}_f - \mathbf{x}_s\|\right)}{4\pi\|\mathbf{x}_f - \mathbf{x}_s\|} \tag{6.2}$$
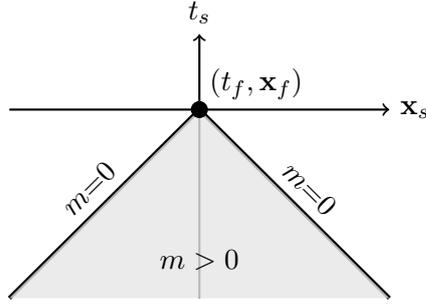
Figure 6.3: Spacetime diagram indicating source points in the
past lightcone of a field point situated at $(t_f, \mathbf{x}_f)$.

$$G_{m \neq 0}\left(t_f, \mathbf{x}_f \,|\, t_s, \mathbf{x}_s\right) = -\frac{m}{4\pi} \frac{\Theta\left(\left(t_f - t_s\right) - \left\|\mathbf{x}_f - \mathbf{x}_s\right\|\right)}{\sqrt{\left(t_f - t_s\right)^2 - \left\|\mathbf{x}_f - \mathbf{x}_s\right\|^2}} J_1\left(m\sqrt{\left(t_f - t_s\right)^2 - \left\|\mathbf{x}_f - \mathbf{x}_s\right\|^2}\right),$$

(6.3)

where the delta function is of the discretised form discussed in Section 6.1.4.1, along
with the source density as defined by corresponding couplings at that location, e.g. for
axions $\varrho\left(t_s, \mathbf{x}_s\right) = g_{a\gamma\gamma}\mathbf{E}\left(t_s, \mathbf{x}_s\right) \cdot \mathbf{B}\left(t_s, \mathbf{x}_s\right)$. The total contribution from a single source
point to a single field point is then calculated as being the product of these components,
i.e. $\Psi\left(t_f, \mathbf{x}_f\right) = G\left(t_f, \mathbf{x}_f \,|\, t_s, \mathbf{x}_s\right) \varrho\left(t_s, \mathbf{x}_s\right)$ with additional multiplicative element factors
for the spatiotemporal grid of the source, as per Equation (6.1). The total field strength
at this field point is then the sum of all contributions from all causally-connected source
points, i.e. $\Psi\left(t_f, \mathbf{x}_f\right) = \sum_{t_s, \mathbf{x}_s} G\left(t_f, \mathbf{x}_f \,|\, t_s, \mathbf{x}_s\right) \varrho\left(t_s, \mathbf{x}_s\right)$. The code then iterates over all
field points, performing the same calculations, in order to build a description of the
entire field.

6.1.5   Additional Algorithmic Components

6.1.5.1   Singularities

When performing calculations involving reciprocals of system variables, one must be
wary of the possibility for infinities to arise. These singularities typically appear when
either a parameter or difference between parameter elements take a value of zero. Since
the calculation being performed by **Run:DMC** involves inverse temporal and spatial
differences, i.e. $\frac{1}{\left\|\mathbf{x}_f - \mathbf{x}_s\right\|}$ and $\frac{1}{\sqrt{\left(t_f - t_s\right)^2 - \left\|\mathbf{x}_f - \mathbf{x}_s\right\|^2}}$, these are the potential sources for
infinities.

Due to the massless contributions having a strong dependence on the spatial differ-
ence between source and field points, there is a clear requirement for these gaps to always
be non-zero. There are a number of ways in which this can be achieved, e.g. catching

spatial differences of zero and substituting for a small constant. The method of resolving singularities implemented in **Run:DMC** involves locating the source and field points on different grids that are staggered by a half source grid length in each dimension, as illustrated in Figure 6.4. This offset has the advantage of being characteristic of the system coordinates, thus is scale-invariant. This also allows for arbitrarily high resolutions in which the offset can become negligible, thus converging on the true value in the approach to continuum. Some computational physics methodologies, such as PIC codes, require interpolation to provide accurate results, however, this has not been implemented into **Run:DMC**. This was chosen to balance computational efficiency with result accuracy: by construction, the source points are evenly spaced from the field points, thus calculated field strengths will be correctly distributed with a constant difference from the "true" value, which vanishes at high resolutions without the need for additional interpolation processes.
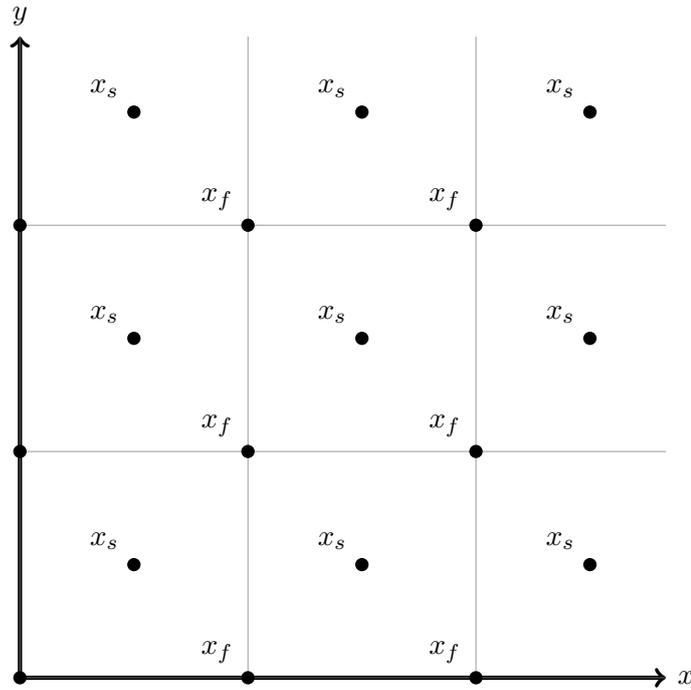
Figure 6.4: Two-dimensional graphical representation of the offset grid between source points, x_s, and field points, x_f. Field points are located on the coordinate grid output by simulation, whereas source points are located in the centre of each grid cell.

Additionally, the massive contributions involve the combination of spatial and temporal differences. However, since the spatial differences can no longer evaluate to zero, one need not concern oneself with temporal differences of zero, thus resolving all singularities.

6.1.5.2 Contributing Source Points

In addition to the core workings of the numeric algorithm outlined in the previous segments, during development it was found that additional functionalities were required to provide results which fit closer to exact analytic solutions. These additional functionalities will now be discussed.

First and foremost, an issue arose in the computation of contributing points in discretised space. Consider the time-dependent 2-sphere, S, which is defined on Minkowski spacetime for a given x_0 as being the set $S = \left\{ x \in \mathbb{R}^3 \; : \; x_i^2 = x_0^2 \right\}$. This is physically manifested as an infinitesimally thin four-dimensional surface on which every point is equidistant in spacetime from a central origin. On a continuous topological space this 2-sphere is comprised of an uncountable set of coordinate values, guaranteeing that for every temporal coordinate there exists an infinite set of spatial coordinates which lie on the surface, and vice versa. However, for discrete topological spaces, on which spatial and temporal coordinates may only take specific values, one cannot make the same claim; as such, one cannot completely describe the 2-sphere on discrete topological spaces. However, in the limit to continuum this coordinate set becomes dense, thus approaching an increasingly well-approximated representation. Since the discrete time coordinates are a subset of those in continuous time, without loss of generality one is able to directly compare the spatial coordinates between discrete and continuous spaces at time slices in discrete space.

To illustrate this, consider a field point located at some arbitrary point in Minkowski spacetime $\left(t_f, \mathbf{x}_f \right)$. The past lightcone of this point at three consecutive time slices, t_0, t_1 and t_2, with $t_0 = t_f > t_1 > t_2$, is shown in Figure 6.5a. At each of these time slices, t_n, the 2-sphere is the surface of radius $r = \sqrt{x^2 + y^2 + z^2} = \sqrt{t_n^2}$, as shown in Figure 6.5b.

From this, one notes a stark contrast between the set of coordinates representing the 2-sphere on continuous and discrete spaces. One may even note that it is possible for the 2-sphere in a time slice to miss all discrete grid points, resulting in a complete absence of causally-connected source points from that time slice. A naïve but effective solution to this problem is to posit that the surface (contour lines in Figure 6.5b) is no longer infinitesimally thin but it instead assumes a thickness, Δ. The requirements of this thickness are that it takes a quantity of length that is characteristic and meaningful in the context of the coordinate system and scale, as well as being a length which

(a) Spacetime diagram indicating three consecutive time slices $t_0 = t_f > t_1 > t_2$ along the past lightcone of a field point. Source points lying along the diagonals contribute masslessly to the field point at $(t_f, \mathbf{x}_f)$ whereas those residing inside the shaded region contribute massively.

(b) x-y plane projection of a 2-sphere in Minkowski spacetime at three consecutive time steps, $t_0 = t_f > t_1 > t_2$. Solid contour lines indicate the constant radius of the 2-sphere on a continuous topological space. Small square nodes signify the locations of the 2-sphere on a discrete topological space, which only occur at the coincidence of the surface with exact grid cell centres. In the time slices chosen, the only contributing source points are those in t_1.

Figure 6.5: Diagrammatic representations of causally-connected source points to individual field point.

vanishes in the spatial limit to continuum. To this end, it was decided that the surface thickness would take the value of the unit cell diagonal, i.e. $\Delta = \sqrt{\delta x^2 + \delta y^2 + \delta z^2}$. Figure 6.6a illustrates how this manifests itself in the context of a spacetime diagram while Figure 6.6b demonstrates how this increases the number of points used to represent the 2-sphere.

Despite the success of this method in better approximating the discrete 2-sphere to continuous behaviour and avoiding time slices altogether lacking contributing points, it raises a further issue. Each discrete grid point contained within the surface thickness represents a source term which contributes equally to all other source points to the total field, for a given spacetime interval, resulting in an over-abundance of source contribution, e.g. four contributing points at equal-time $t_0 = t_f$. The solution to this implemented in **Run:DMC** was to scale the contributions according to the grid point's proximity to the true surface location. This thickness is required to fall off with distance from the lightsphere surface in order to ensure that field points rely less on more distant source points. The choice of this scaling is ultimately an arbitrary detail, provided it

(a) Spacetime diagram indicating three consecutive time slices $t_0 = t_f > t_1 > t_2$ along the past lightcone of a field point. Source points lying within the lightcone thickness along the diagonals contribute masslessly to the field point at $(t_f, \mathbf{x}_f)$ whereas those residing inside the shaded region contribute massively.

(b) x-y plane projection of a 2-sphere with surface thickness $\Delta = \sqrt{\delta x^2 + \delta y^2}$ at consecutive time steps, $t_0 = t_f > t_1 > t_2$. All grid cell centres contained within the cyan regions contribute to the discrete representation of the 2-sphere surface.

Figure 6.6: Diagrammatic representations of causally-connected source points to individual field point with lightcone thickness.

falls off with distance and approximately sums to the same total contribution as in continuous, however for simplicity it was decided to be a linear fall off with distance as the ratio of the surface thickness with a boundary at the extremities of the surface width. Mathematically this scaling factor, δ, was formulated as

$$\delta = \left| \frac{\Delta t - \|\Delta x\| - \Delta}{\Delta} \right|, \tag{6.4}$$

where Δt and Δx respectively denote the temporal and spatial differences in discretised spacetime. Figure 6.7 graphically represents how this manifests itself.

A flowchart of the core algorithm implemented in **Run:DMC** is shown in Figure 6.8. Each process block will be briefly expanded upon following the chart.

Calculate elements of source data

To facilitate more efficient calculation, the elements of the system are precalculated and utilised throughout. The time element, δt, is calculated as being the temporal difference between the first and second time steps in the system data, i.e. $\delta t = t_2 - t_1$. Spatially, the x-axis denotes the primary axis of the simulation data, thus it is assumed that there are at least two elements in this direction; it is calculated by $\delta x = x_2 - x_1$. In order to handle 1D data, the y element – which is taken to be the secondary axis – is given
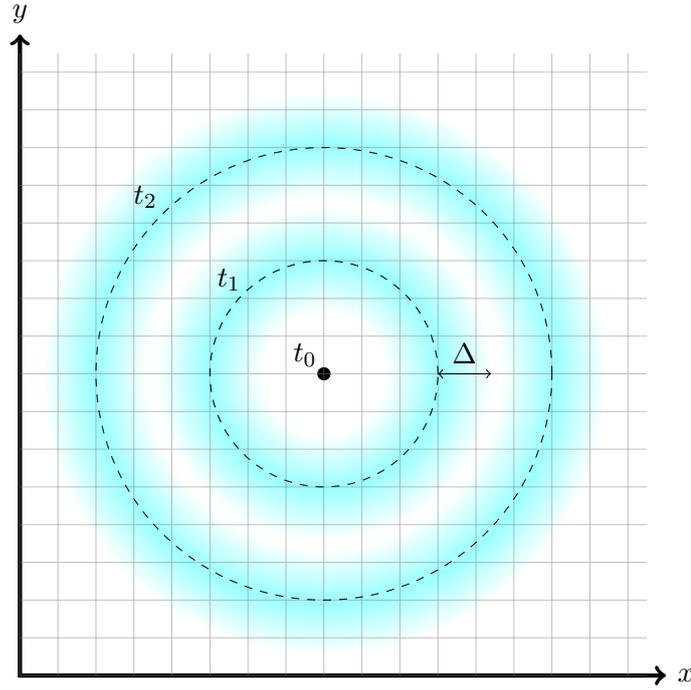
Figure 6.7: x-y plane projection of a 2-sphere with surface thickness $\Delta = \sqrt{\delta x^2 + \delta y^2}$ and scaling factor $\delta = \left| \frac{\Delta t - \|\Delta x\| - \Delta}{\Delta} \right|$ at consecutive time steps, $t_0 > t_1 > t_2$.
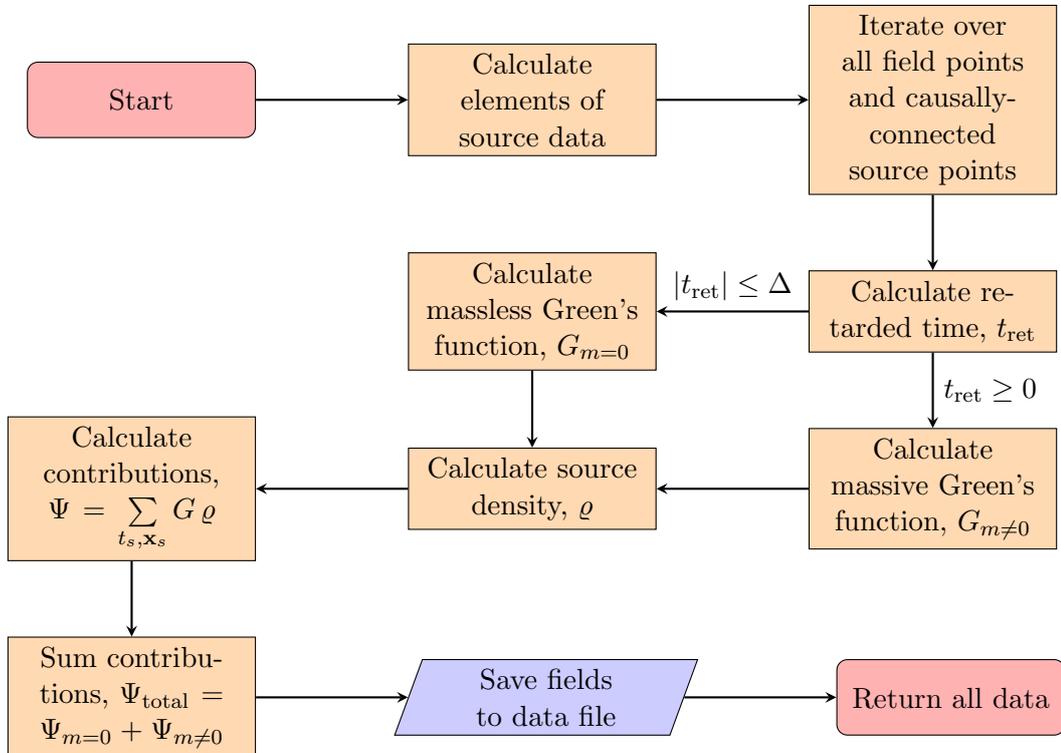
Figure 6.8: Flowchart of **Run:DMC** core algorithm.

by $\delta y = \delta x$ if it is only one element in size and $\delta y = y_2 - y_1$ otherwise. Similarly, $\delta z = \min(\delta x, \delta y)$ if the length of z is unitary and $\delta z = z_2 - z_1$ otherwise. Using these, the volume element and lightcone thickness are calculated by $\delta V = \delta x \times \delta y \times \delta z$ and $\Delta = \sqrt{\delta x^2 + \delta y^2 + \delta z^2}$, respectively.

Iterate over all field points and causally-connected source points

In its current incarnation, **Run:DMC** enforces causality by iterating over all data time steps preceding the time at which a field point is observed.

Calculate retarded time, $t_{\mathbf{ret}}$

The retarded time for each field point-source point pairing is calculated from the spatiotemporal coordinates by $t_{\mathrm{ret}} = (t_f - t_s) - \|\mathbf{x}_f - \mathbf{x}_s\|$, where t_f and t_s are the field and source time coordinates, and $\mathbf{x}_f$ and $\mathbf{x}_s$ are the corresponding spatial coordinates.

Calculate massless Green's function, $G_{m=0}$

If the retarded time is calculated to be within the lightcone thickness of zero, i.e. $\|t_{\mathrm{ret}}\| \leq \Delta$, then the interval is lightlike and the massless Green's function is calculated by Equation (6.2) as

$$G_{m=0}\left(t_f, \mathbf{x}_f \,|\, t_s, \mathbf{x}_s\right) = \frac{\Theta\left(t_f - t_s\right) \delta\left(\left(t_f - t_s\right) - \|\mathbf{x}_f - \mathbf{x}_s\|\right)}{4\pi \|\mathbf{x}_f - \mathbf{x}_s\|}.$$

This is then scaled by the distance per Equation (6.4) as $\delta = \left| \frac{\Delta t - \|\Delta x\| - \Delta}{\Delta} \right|,.$

Calculate massive Green's function, $G_{m \neq 0}$

If the retarded time is calculated to be less than or equal to zero then the interval is timelike and the massive Green's function is calculated by Equation (6.3) as

$$G_{m \neq 0}\left(t_f, \mathbf{x}_f \,|\, t_s, \mathbf{x}_s\right) = -\frac{m}{4\pi} \frac{\Theta\left(\left(t_f - t_s\right) - \|\mathbf{x}_f - \mathbf{x}_s\|\right)}{\sqrt{\left(t_f - t_s\right)^2 - \|\mathbf{x}_f - \mathbf{x}_s\|^2}} J_1\left(m \sqrt{\left(t_f - t_s\right)^2 - \|\mathbf{x}_f - \mathbf{x}_s\|^2}\right).$$

Calculate source density, ϱ

The source density of a particle is calculated from its coupling to ordinary matter. For ALPs, $\varrho\left(t_s, \mathbf{x}_s\right) = \mathbf{E}\left(t_s, \mathbf{x}_s\right) \cdot \mathbf{B}\left(t_s, \mathbf{x}_s\right)$, for DLPs $\varrho\left(t_s, \mathbf{x}_s\right) = \mathbf{E}^2\left(t_s, \mathbf{x}_s\right) - \mathbf{B}^2\left(t_s, \mathbf{x}_s\right)$ and HSPs $\varrho\left(t_s, \mathbf{x}_s\right) = \mathbf{E}\left(t_s, \mathbf{x}_s\right)$.

Calculate contributions, $\Psi = \sum_{t_s, \mathbf{x}_s} G\varrho$

For each field point, the field strength contributions due to massless and massive components are calculated separately as being the inner product of the respective Green's

functions and source density, along with multiplicative factors of the spatiotemporal unit elements.

Sum contributions, $\Psi_{\mathbf{total}} = \Psi_{m=0} + \Psi_{m\neq 0}$

The overall field strength at a given spacetime location is calculated as being the sum of the massless and massive contributions.

Save fields to data file

Julia's `Serialization` package is utilised to serialise the processed data to disk.

6.2   Case Testing

Prior to taking any results from **Run:DMC** as given, it must first prove itself capable of correctly calculating the resultant fields of analytically calculable systems. As previously calculated in Equation (2.4), the value of a field Ψ at a spacetime coordinate $(t_f, \mathbf{x}_f)$ is calculated from its source density ϱ by

$$\Psi\left(t_f, \mathbf{x}_f\right) = \int_{-\infty}^{\infty} \mathrm{d}^4 x_s \left(\frac{\Theta\left(T\right)\delta\left(T-X\right)}{4\pi X} - \frac{m}{4\pi}\frac{\Theta\left(T-X\right)}{\sqrt{T^2-X^2}}J_1\left(m\sqrt{T^2-X^2}\right)\right)\varrho\left(t_s, \mathbf{x}_s\right),$$

where $T = t_f - t_s$ and $X = \left\|\mathbf{x}_f - \mathbf{x}_s\right\|$.

Within the following subsections, test cases will be outlined, corresponding fields analytically calculated, physical interpretations discussed and numeric results compared with those expected. Owing to the Bessel function, the massive contributions are significantly harder to analytically calculate than their massless counterparts and will only be considered in the final case test, where the solution is readily calculable and comparable with numeric outcome.

It was found during development that results from systems with disparate time and length scales were highly inaccurate or inefficient. When initially conducting the test cases presented later, results for systems in which the temporal elements were much larger than the grid separations, the calculated fields exhibited large discontinuities. In contraposition, the results when the temporal spacing was significantly smaller than that of the spatial were unable to be run to completion due to excessive forecasted duration. The heuristic explanation for these behaviours is as follows. If steps in time, δt, are sufficiently large relative to steps in space, δx, i.e. $\delta t \gg \delta x$, then between time steps the lightsphere surface extends beyond multiple cell lengths, thus reducing the number of source points that are able to contribute to each field point and hence resulting in

a severe reduction in calculated field strength. However, in cases to the counter, i.e. $\delta t \ll \delta x$, it requires multiple time steps for the signal to reach adjacent cells; whilst this does not negatively affect the computed field strength, each additional time step takes longer than its predecessor due to calculating the contributions from all source points in all preceding time steps. As such, the calculation becomes increasing inefficient with a large number of time steps. On balance, it was decided that the ideal configuration for computation was that the time and length scales of all test cases must be commensurate with the propagation speed of light in vacuo, i.e.

$$\frac{\delta x}{\delta t} \sim c,$$

a result reminiscent of, but unrelated to, the Courant-Friedrichs-Lewy condition. It should be noted that this may not be entirely optimal and potentially warrants further investigation.

Each test case was performed at a multitude of resolutions in order to illustrate the asymptotic behaviour in the approach to continuum. These resolutions are designated "low", "medium" and "high", with the corresponding number of grid points $(t \times x \times y \times z)$ as follows:

Low resolution:	$16 \times 16 \times 16 \times 1$
Medium resolution:	$64 \times 64 \times 64 \times 1$
High resolution:	$512 \times 512 \times 512 \times 1.$

Note 1: All massless test cases were generated as two-dimensional data on a $100\,\mu\text{m} \times 100\,\mu\text{m}$ square mesh. This was chosen to mimic the source sizes within the systems which will be later investigated, e.g. the plasma wavelength for a plasma of density $n_0 = 10^{24}\,\text{m}^{-3}$ is $\lambda_p \sim 30\,\mu\text{m}$.

Note 2: All massless test cases use sources of unitary density, i.e. $\varrho\left(t_s, \mathbf{s}\right) = \frac{1}{\delta V}$.

Note 3: For notational brevity, the component intervals between source creation $(t_0, \mathbf{x}_0)$ and field observation $(t_f, \mathbf{x}_f)$ are denoted $\Delta t = t_f - t_0$ and $\|\Delta \mathbf{x}\| = \|\mathbf{x}_f - \mathbf{x}_0\|$.

6.2.1   Transient Stationary Point Source

From an analytical perspective, the simplest case for which to calculate the resultant field is that of a source which exists at a single point in spacetime, namely a stationary point source that comes into existence for an infinitesimal instance, whereupon it vanishes.

The density for a point-like source located at a single spacetime coordinate $(t_0, \mathbf{x}_0)$ is given by

$$\varrho\left(t_s, \mathbf{x}_s\right) = \delta\left(t_s - t_0\right) \delta^{(3)}\left(\mathbf{x}_s - \mathbf{x}_0\right).$$

From this, one is able to evaluate the integrals with ease, simply carrying over the points for which $t_s = t_0$ and $\mathbf{x}_s = \mathbf{x}_0$, giving

$$\Psi_{m=0}\left(t_f, \mathbf{x}_f\right) = \frac{\Theta\left(\Delta t\right) \delta\left(\Delta t - \|\Delta\mathbf{x}\|\right)}{4\pi \|\Delta\mathbf{x}\|}.$$

Physically, this massless contribution manifests itself as a 2-sphere propagating outward from the source point at the speed of light, falling off linearly with Euclidian distance between the source creation and field observation. The numerically calculated field for such a system is shown in Figure 6.9.
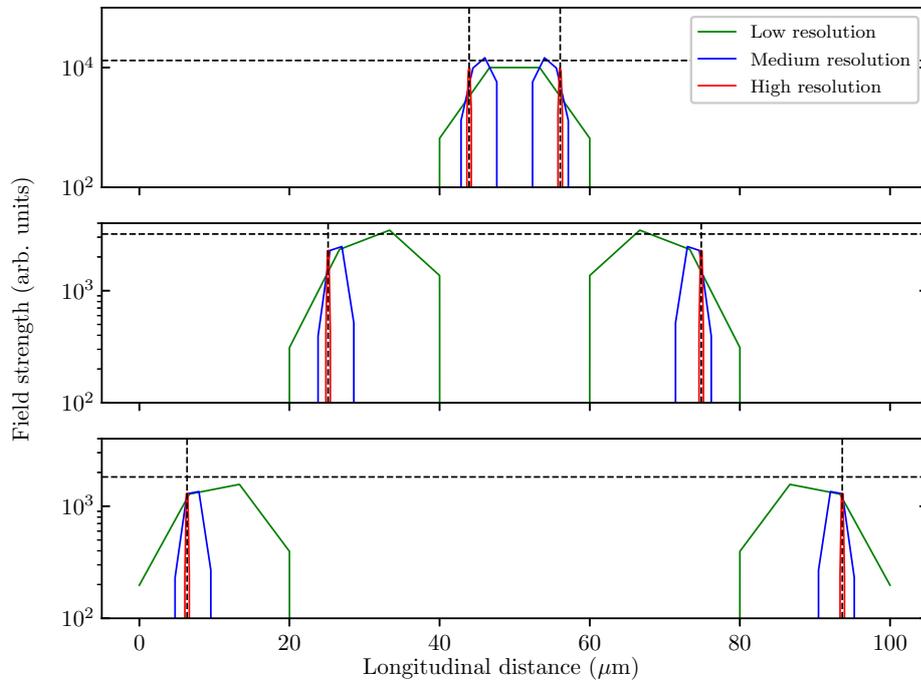
Figure 6.9: Field strength of an $m = 0$ transient stationary point source located in the centre of the domain ($x = 50\,\mu\text{m}$). Vertical black lines indicate the delta distributions propagating at the speed of light away from the central position at given time steps. Horizontal black line indicates expected peak value as
$$\frac{1}{4\pi c(t_1 - t_0)}.$$
Time steps: 21.2 fs (top), 79.4 fs (middle), 143 fs (bottom).

From Figure 6.9 it can be seen that the overall field distribution is comprised of two equal distributions which separate and retreat from the point of origin in opposite directions at the speed of light, as expected. Regardless of resolution, these distributions are composed of the same number of points, the ensemble width of which decreases with

increased resolution. Additionally, the calculated value remains approximately correct, albeit underestimated, for all resolutions.

Combining these observations, one may justly conclude that the computed distribution approaches that calculated analytically, i.e. resembling two radially-diminishing delta distributions departing the source point at the speed of light. Consequently, **Run:DMC** has demonstrated its capabilities in numerically analysing systems which may be modelled as a set of massless transient point sources.

6.2.2   Persistent Stationary Point Source

Perhaps the most prevalent of the point-like source systems taught during undergraduate studies is that of an eternal stationary source. This system is used in solving such problems as Laplace's equation of electrostatics, i.e. $\nabla^2 \Psi = 0$, the $\mathbb{R}^3$ solution to which is given by $\Psi(t, \mathbf{x}) = \frac{1}{4\pi \|\mathbf{x}\|}$. However, the following test case concerns situations in which the requirement of eternal existence is not assumed, instead dealing with sources coming into existence.

The density for a stationary point-like source located at spatial coordinate $\mathbf{x}_0$ which comes into existence at time t_0 and persists thenceforth is written

$$\varrho(t_s, \mathbf{x}_s) = \Theta(t_s - t_0)\, \delta(\mathbf{x}_s - \mathbf{x}_0).$$

Integrating over x_s in order to remove the source delta gives

$$\Psi_{m=0}(t_f, \mathbf{x}_f) = \int_{-\infty}^{\infty} \mathrm{d}t_s \left(\frac{\Theta(T)\, \Theta(t_s - t_0)\, \delta(T - \|\Delta\mathbf{x}\|)}{4\pi \|\Delta\mathbf{x}\|} \right),$$

where $\Delta\mathbf{x} = \mathbf{x}_f - \mathbf{x}_0$.

Prior to undertaking the remaining integral, one must first calculate the roots of the delta, t_n, such that it can be written in the form

$$\delta(f(t_s)) = \sum_n \frac{\delta(t_s - t_n)}{\left| f'(t_s)\big|_{t_s = t_n} \right|},$$

where $f'(t_s) = \dfrac{\mathrm{d}}{\mathrm{d}t_s} f(t_s)$ [105, §13.1.3]. These roots can be shown to be $t_n = t_f \pm \|\Delta\mathbf{x}\|$, however one notes that just one of these roots is valid since $t_f - t_n - \|\Delta\mathbf{x}\| = 0$ only holds for the root inclusive of the negative sign, i.e.

$$t_n = t_f - \|\Delta\mathbf{x}\|.$$

Since $\|\Delta\mathbf{x}\| \geq 0 \ \forall \Delta\mathbf{x}$, one calculates the massless field contributions to be

$$\Psi_{m=0}\left(t_f, \mathbf{x}_f\right) = \frac{\Theta\left(\Delta t - \|\Delta\mathbf{x}\|\right)}{4\pi\|\Delta\mathbf{x}\|}, \tag{6.5}$$

where $\Delta t = t_f - t_0$. This is physically interpreted as a steady radially-diminishing contribution which permeates the hypervolume of the lightsphere centred on source point $(t_0, \mathbf{x}_0)$. One may note that as the time between the source creation and field observation approaches infinity, the step function tends to unity, i.e. $\lim_{\Delta t \to \infty} \Theta\left(\Delta t - \|\Delta\mathbf{x}\|\right) \to 1$, resulting in a solution convergence to the expected Coulombic behaviour from the solution to Laplace's equation:

$$\Psi_{m=0}\left(t_f, \mathbf{x}_f\right) = \frac{1}{4\pi\|\Delta\mathbf{x}\|}. \tag{6.6}$$
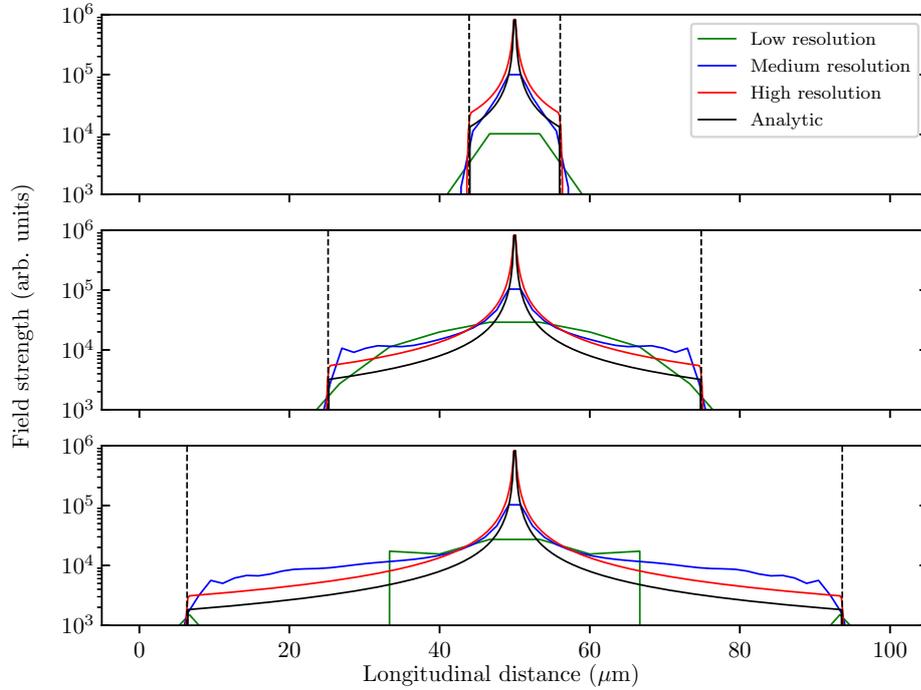
Figure 6.10: Field strength of an $m = 0$ persistent stationary point source located in the centre of the domain. Analytical solution given by Equation (6.6). Vertical black dashed lines indicate the lightcone surface propagation away from central source position at given time steps.
Time steps: 21.2 fs (top), 79.4 fs (middle), 143 fs (bottom).

The solid black line of Figure 6.10 demonstrates a finitely peaked distribution of the result calculated in Equation (6.5). One is able to see clearly that the numerically calculated behaviours very closely match those expected from analytic analysis across all resolutions, for example, the calculated field values are approximately confined by the speed of light propagating away from the source in vacuo, as indicated by the vertical dashed lines. Additionally, the distribution of the numeric results closely resembles that

of the analytic result, with a calculation overestimation in values between the two results being of order 1% relative to the peak, i.e. $\sim \frac{10^4}{10^6}$. Furthermore, one notes that the peak value increases with resolution, a result deriving from the decreased cell size; in the limit to continuum this value should asymptotically approach infinity.

As a consequence of this test case, it is the author's wish that the reader should be convinced as to the efficacy of **Run:DMC** in analysing systems comprised of static sources which survive longer than single instances of time, in particular that distributions are correct and calculated values are close to those expected.

6.2.3   Moving Point Source

Hitherto only stationary point-like sources have been considered, however the nature of some systems is such that sources within the domain may be moving. As such, this test case considers a moving point source at a relativistic speed.

The density of a source which comes into existence at $(t_0, \mathbf{x}_0)$ moving at a constant speed $\mathbf{v}$ is written

$$\varrho\left(t_s, \mathbf{x}_s\right) = \Theta\left(t_s - t_0\right) \delta^{(3)}\left(\mathbf{x}_s - \left(\mathbf{x}_0 + \mathbf{v}\left(t_s - t_0\right)\right)\right).$$

Initially integrating over $\mathbf{x}_s$ to remove the source delta, one gets

$$\Psi_{m=0}\left(t_f, \mathbf{x}_f\right) = \int_{-\infty}^{\infty} \mathrm{d}t_s \left(\frac{\Theta\left(T\right)\Theta\left(t_s - t_0\right)\delta\left(T - \left\|\Delta\mathbf{x} - \mathbf{v}\left(t_s - t_0\right)\right\|\right)}{4\pi\left\|\Delta\mathbf{x} - \mathbf{v}\left(t_s - t_0\right)\right\|}\right).$$

As with the persistent stationary source test case (6.2.2), one must first calculate the roots of the delta, t_n, prior to undertaking the final integral, in order to write the delta as

$$\delta\left(f\left(t_s\right)\right) = \sum_n \frac{\delta\left(t_s - t_n\right)}{\left|f'\left(t_s\right)\big|_{t_s=t_n}\right|},$$

which one computes to be

$$t_n = \gamma^2\left(t_f - \left(\Delta\mathbf{x} + \mathbf{v}t_0\right)\cdot\mathbf{v}\right) \pm \sqrt{\gamma^4\left(t_f - \left(\Delta\mathbf{x} + \mathbf{v}t_0\right)\cdot\mathbf{v}\right)^2 - \gamma^2\left(t_f^2 - \left(\Delta\mathbf{x} + \mathbf{v}t_0\right)^2\right)},$$

where $\gamma \equiv \left(1 - v^2\right)^{-\frac{1}{2}}$. However, by definition of the delta root, $t_f - t_n - \left\|\Delta\mathbf{x} - \mathbf{v}\left(t_n - t_0\right)\right\| = 0 \ \forall\Delta\mathbf{v}$ thus, by considering the case in which $\mathbf{v} = \mathbf{0}$, one concludes that the only valid root is that with the negative sign.

Using $f\left(t_s\right) = t_f - t_s - \left\|\Delta\mathbf{x} - \mathbf{v}\Delta t'\right\|$, one is able to show that

$$\left|\frac{\mathrm{d}}{\mathrm{d}t_s}\left(f\left(t_s\right)\right)\Big|_{t_s=t_n}\right| = \frac{\left\|\mathbf{v}\left(t_n - t_0\right) - \Delta\mathbf{x}\right\| + \left(\mathbf{v}\left(t_n - t_0\right) - \Delta\mathbf{x}\right)\cdot\mathbf{v}}{\left\|\mathbf{v}\left(t_n - t_0\right) - \Delta\mathbf{x}\right\|}.$$

103

By introducing a unit vector $\hat{\boldsymbol{\xi}}$ such that $\mathbf{v}\left(t_n - t_0\right) - \Delta\mathbf{x} = \left\|\mathbf{v}\left(t_n - t_0\right) - \Delta\mathbf{x}\right\|\hat{\boldsymbol{\xi}}$, one can then write the delta as

$$\delta\left(T - \left\|\Delta\mathbf{x} - \mathbf{v}\left(t_s - t_0\right)\right\|\right) = \frac{1}{1 + \hat{\boldsymbol{\xi}} \cdot \mathbf{v}}\delta\left(t_s - t_n\right).$$

Finally, one may carry out the remaining integral and hence conclude the massless field contributions to be

$$\Psi_{m=0}\left(t_f, \mathbf{x}_f\right) = \frac{1}{1 + \hat{\boldsymbol{\xi}} \cdot \mathbf{v}}\frac{1}{4\pi}\frac{\Theta\left(t_f - t_n\right)\Theta\left(t_n - t_0\right)}{\left\|\mathbf{v}\left(t_n - t_0\right) - \Delta\mathbf{x}\right\|}. \tag{6.7}$$

Physically this manifests itself as a singularity moving at a speed $\mathbf{v}$, whose field strength diminishes radially with distance from the source as $\frac{1}{\|\mathbf{v}\Delta t - \Delta\mathbf{x}\|}$. One may note that in the limit of $\mathbf{v} \to 0$ this solution tends to that of the persistent static source, i.e. Equation (6.5). Figure 6.11 illustrates the numeric analysis of a point-like source moving at a constant relativistic speed $v = 0.9c$, instantiated at $x = 0\,\mu\text{m}$ and moving in the positive x-direction toward $x = 100\,\mu\text{m}$. The black line models the analytic expression derived in Equation (6.7). From this, one sees that the field propagation ahead of the source is limited by the speed of light, which results in an asymmetric tail either side of the source, compressing on the side of propagation direction and stretching behind.

From Figure 6.11 one observes the asymptotic behaviour approaching that expected from the analytic result. The dominant behavioural shifts observed with increased resolutions reside in the peak value growing as the distribution becomes increasingly keen, a result afforded by the smaller cell sizes. Additionally, small peaks become increasingly prevalent along the distribution tail with increased resolution, suggesting a numeric artefact which likely results the encapsulation-interpolation methodology earlier described. One notes that the distribution is always underestimated versus the analytic expectation. This test case highlights **Run:DMC**'s ability to calculate fields derived from moving point sources, as well as its incorporation of relativistic behaviours.

6.2.4   Persistent Time-Varying Stationary Source

The cases considered heretofore have been used to demonstrate the efficacy of **Run:DMC** in calculating massless contributions for a multitude of systems. Despite this, there are no clear methods of calculating the massive contributions in most of these systems. A final test case therefore considers a system in which it is possible to exactly calculate the massive contributions for a sufficiently long time; that of a point-like source whose density varies with time.
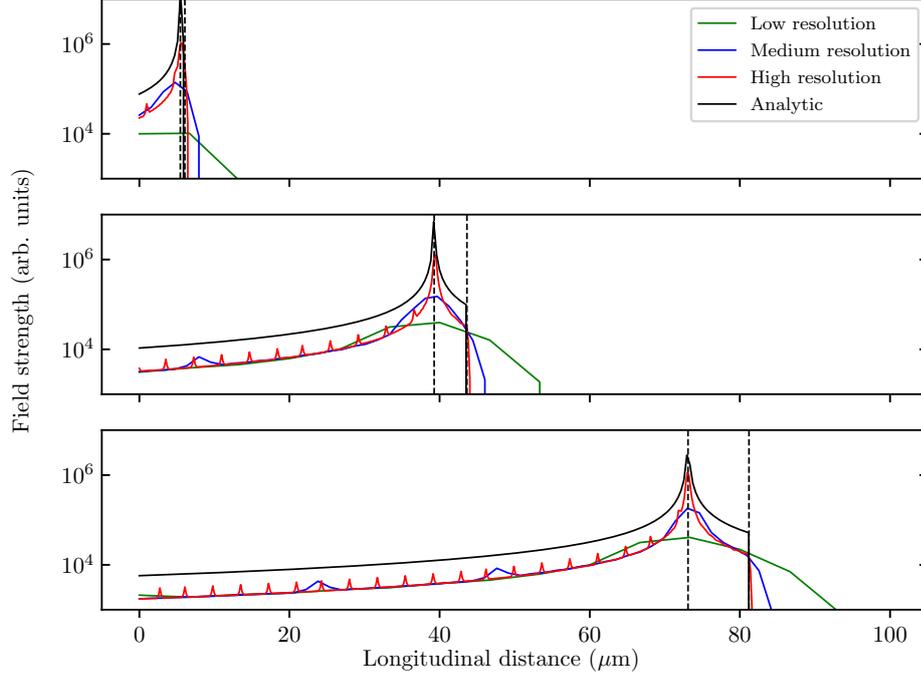
Figure 6.11: Field strength of an $m = 0$ moving point source
initially located in the left side of the domain and moving at a
constant speed $v = 0.9c$ along the positive longitudinal direction.
Analytical solution given by Equation (6.7). The right-most
vertical black dashed line indicates the propagation of light from
the initial source position at given time steps and the left-most
line indicates the source location.
Time steps: 21.2 fs (top), 159 fs (middle), 276 fs (bottom).

The density for a point source located at $\mathbf{x}_0$ whose density oscillates sinusoidally with
angular frequency ω and amplitude b for which the value at initial time t_0 is a is given
by

$$\varrho\left(t_s, \mathbf{x}_s\right) = \Theta\left(t_s - t_0\right) \delta^{(3)}\left(\mathbf{x}_s - \mathbf{x}_0\right)\left(a + b\sin\left(\omega\left(t_s - t_0\right)\right)\right).$$

Initially integrating over x_s to remove the source delta gives the massless contribution

$$\Psi_{m=0}\left(t_f, \mathbf{x}_f\right) = \int_{-\infty}^{\infty} dt_s \frac{\Theta\left(T\right)\Theta\left(t_s - t_0\right)\delta\left(T - \|\Delta\mathbf{x}\|\right)}{4\pi\|\Delta\mathbf{x}\|}\left(a + b\sin\left(\omega\left(t_s - t_0\right)\right)\right).$$

As in previous cases, the only valid root of the delta can be calculated to be $t_n = t_f - \|\Delta\mathbf{x}\|$, hence the massless contributions are

$$\Psi_{m=0}\left(t_f, \mathbf{x}_f\right) = \frac{\Theta\left(\Delta t - \|\Delta\mathbf{x}\|\right)}{4\pi\|\Delta\mathbf{x}\|}\left(a + b\sin\left(\omega\left(\Delta t - \|\Delta\mathbf{x}\|\right)\right)\right), \qquad (6.8)$$

where the Heaviside function $\Theta\left(\Delta t + \|\Delta\mathbf{x}\|\right)$ has been excluded due to it vanishing only
in regions where the second Heaviside function also vanishes.

105

In a similar manner to evaluating other test cases, one initially integrates over x_s, giving the massive contributions as

$$\Psi_{m\neq0}\left(t_f, \mathbf{x}_f\right) = \frac{1}{4\pi} \int_{t_0}^{t_f - \|\Delta\mathbf{x}\|} dt_s \; \frac{-m}{\sqrt{T^2 - \|\Delta\mathbf{x}\|^2}}$$
$$\times J_1\left(m\sqrt{T^2 - \|\Delta\mathbf{x}\|^2}\right)\left(a + b\sin\left(\omega\left(t_s - t_0\right)\right)\right). \quad (6.9)$$

Introducing a new variable $\xi = m\sqrt{T^2 - \|\Delta\mathbf{x}\|^2}$ allows one to rewrite this integral as

$$\Psi_{m\neq0}\left(t_f, \mathbf{x}_f\right) = -\frac{1}{4\pi} \int_{t_0}^{m\sqrt{\Delta t^2 - \|\Delta\mathbf{x}\|^2}} d\xi \; \frac{m J_1\left(\xi\right)}{\sqrt{\xi^2 + m\|\Delta\mathbf{x}\|^2}}$$
$$\times \left(a + b\sin\left(\omega\left(\Delta t - \frac{1}{m}\sqrt{\xi^2 + m^2\|\Delta\mathbf{x}\|^2}\right)\right)\right).$$

By considering the behaviour at a sufficiently long time, i.e. $t \gg \|\Delta\mathbf{x}\|$, one is able to approximate the following:

$$\begin{cases} \Delta t^2 - \|\Delta\mathbf{x}\|^2 \sim \Delta t^2 \\ \xi^2 + m^2\|\Delta\mathbf{x}\|^2 \sim \xi^2. \end{cases}$$

Furthermore, by using the trigonometric identity $\sin\left(\alpha \pm \beta\right) = \sin\left(\alpha\right)\cos\left(\beta\right) \pm \cos\left(\alpha\right)\sin\left(\beta\right)$, the massive contributions may now be written

$$\Psi_{m\neq0}\left(t_f, \mathbf{x}_f\right) = -\frac{ma}{4\pi}\int_0^{m\Delta t} d\xi \; \frac{J_1\left(\xi\right)}{\xi} - \frac{mb}{4\pi}\left[\sin\left(\omega\Delta t\right)\int_0^{m\Delta t} d\xi \; \frac{J_1\left(\xi\right)}{\xi}\cos\left(\frac{\omega}{m}\xi\right)\right.$$
$$\left. - \cos\left(\omega\Delta t\right)\int_0^{m\Delta t} d\xi \; \frac{J_1\left(\xi\right)}{\xi}\sin\left(\frac{\omega}{m}\xi\right)\right].$$

Using the following identities [128, §6.693]:

$$\int_0^\infty \frac{J_\nu\left(\alpha x\right)}{x}\sin\left(\beta x\right)\,dx = \begin{cases} \frac{1}{\nu}\sin\left(\nu\arcsin\left(\frac{\beta}{\alpha}\right)\right) & \beta \leq \alpha \\ \frac{\alpha^\nu\sin\left(\frac{\nu\pi}{2}\right)}{\nu\left(\beta + \sqrt{\beta^2 - \alpha^2}\right)^\nu} & \beta \geq \alpha \end{cases}$$

$$\int_0^\infty \frac{J_\nu\left(\alpha x\right)}{x}\cos\left(\beta x\right)\,dx = \begin{cases} \frac{1}{\nu}\cos\left(\nu\arcsin\left(\frac{\beta}{\alpha}\right)\right) & \beta \leq \alpha \\ \frac{\alpha^\nu\cos\left(\frac{\nu\pi}{2}\right)}{\nu\left(\beta + \sqrt{\beta^2 - \alpha^2}\right)^\nu} & \beta \geq \alpha \end{cases}$$

one is then able to calculate the massive contributions to be

$$\lim_{t \to \infty} \Psi_{m \neq 0}\left(t_f, \mathbf{x}_f\right) = -\frac{ma}{4\pi}$$
$$- \frac{b}{4\pi}\left[\sin\left(\omega\Delta t\right)\mathrm{Re}\left(\sqrt{m^2 - \omega^2}\right) - \cos\left(\omega\Delta t\right)\mathrm{Re}\left(\omega - \sqrt{\omega^2 - m^2}\right)\right]. \quad (6.10)$$

The analytic expression in Equation (6.10) effectively trisects the behaviours of the field according to oscillation frequency relative to the mass, i.e. $\omega \lesseqqgtr m$. It was found during testing that, regardless of overall behaviours, within fifteen oscillation periods of the source under all mass-frequency ratios the value of this long-time approximation was not reached, making the continued analysis unreasonable. This was explained as being analogous to calculating the temperature distribution in the region of an oscillatory heat source and comparing the result to the heat death of the Universe.

Despite this, the massive results of **Run:DMC** can still be compared to an expected behaviour through the numeric evaluation of Equation (6.9). Because this additional analysis to be conducted is of a significantly different – and notably simpler – nature, it serves as a valid benchmark when examining **Run:DMC**'s capabilities in resolving massive contributions.

Figure 6.12 illustrates the capability of **Run:DMC** in calculating the massless contributions of time-varying sources. As can be seen, the numeric results closely follow the expected behaviours according to the analytic expression derived in Equation (6.10). Despite having well-matched peak values and distributions, discrepancies between analytic expectation and numeric result become increasingly prominent at higher frequencies. These differences are likely the consequence of the inability of **Run:DMC** to resolve extremely high frequency oscillations at the given resolution.

(a) $\omega = m$
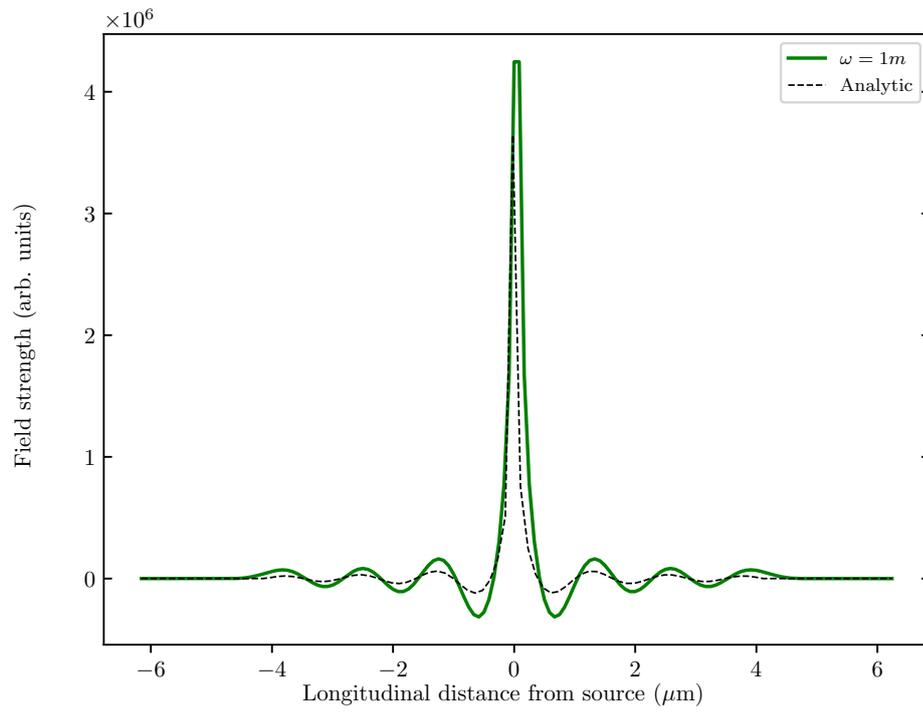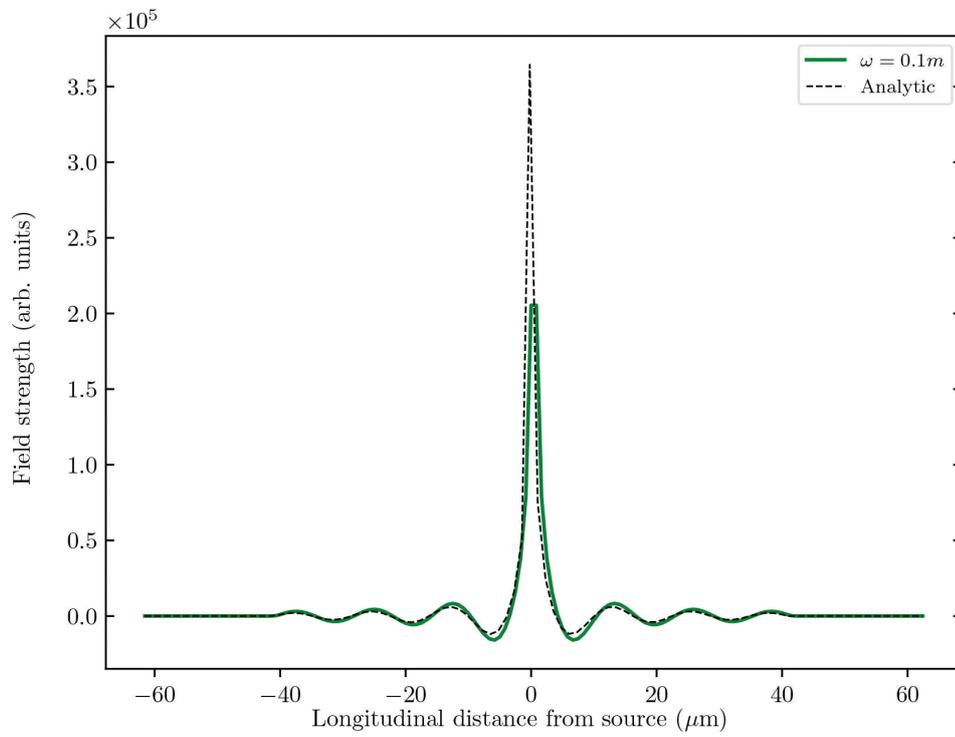
(b) $\omega = 0.1m$
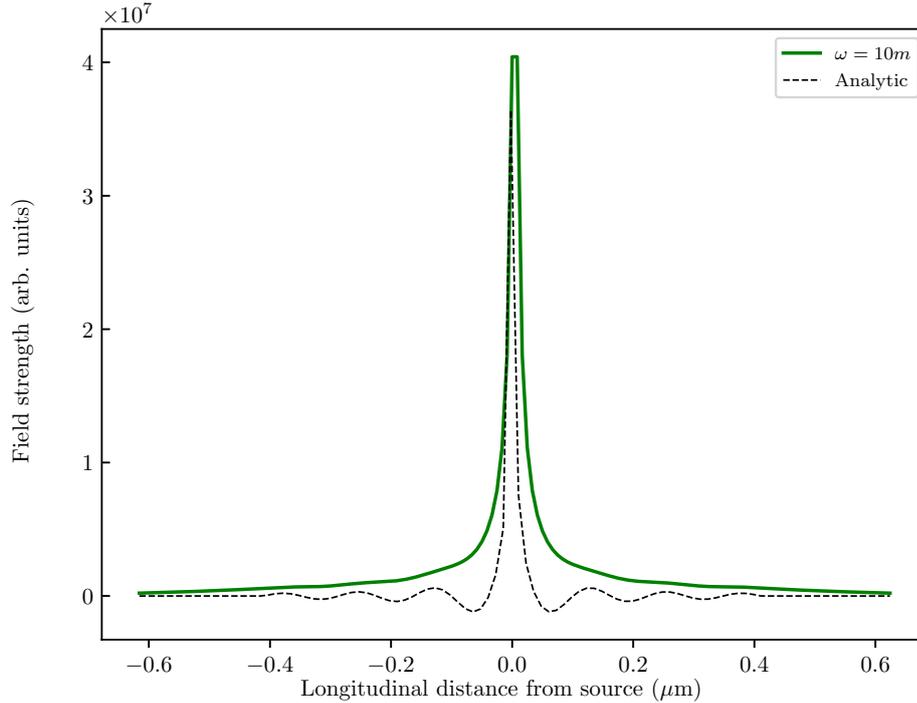
(c) $\omega = 10m$

Figure 6.12: Field strength of an $m = 0$ persistent time-varying stationary point source. Black dashed lines indicates expected behaviours according to Equation (6.8). The source initial value is given by $a = 0$, the oscillation amplitude $b = 1$ and oscillation angular frequency is defined as a proportion of the oscillations of the particle mass, which is $m = 1\,\text{eV}$.

Figure 6.13 demonstrates **Run:DMC**'s capabilities in calculating massive field contributions across the regimes $\omega \lesseqqgtr m$. As is evident from these, **Run:DMC** is able to approximately calculate the behaviours across the spectrum of oscillation-mass ratios, as well as order of magnitude values, provided the oscillations are sufficiently low for the resolution. Whilst one can analytically calculate $\lim_{x\to0} \frac{J_1(x)}{x} = 1$ through l'Hôpital's rule, numerically this would diverge. Consequently, one should not pay too much heed to the "analytic" numeric result in the central regions of source location.

From Figures 6.12 and 6.13, it has been demonstrated that **Run:DMC** is able to calculate values of the correct order for massive contributions in the regimes $\omega \leq m$, however it cannot resolve the field structure for oscillation frequencies significantly smaller than that corresponding to the particle mass. Additionally, it is apparent that the code struggles with calculating massive contributions beyond providing rough order of magnitude estimates.

(a) $\omega = m$
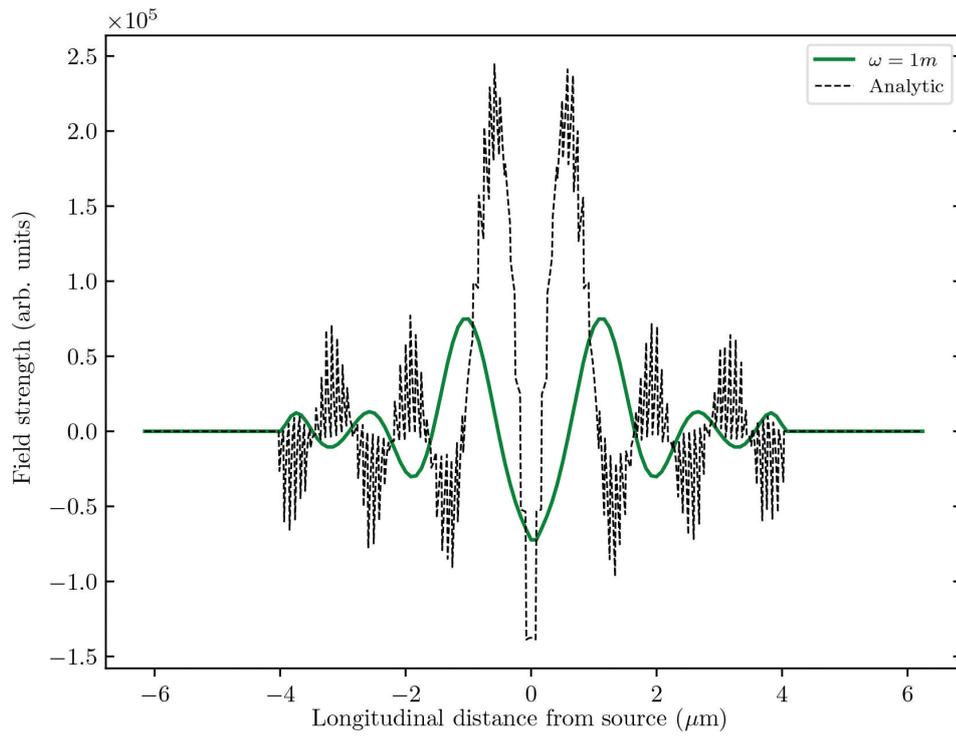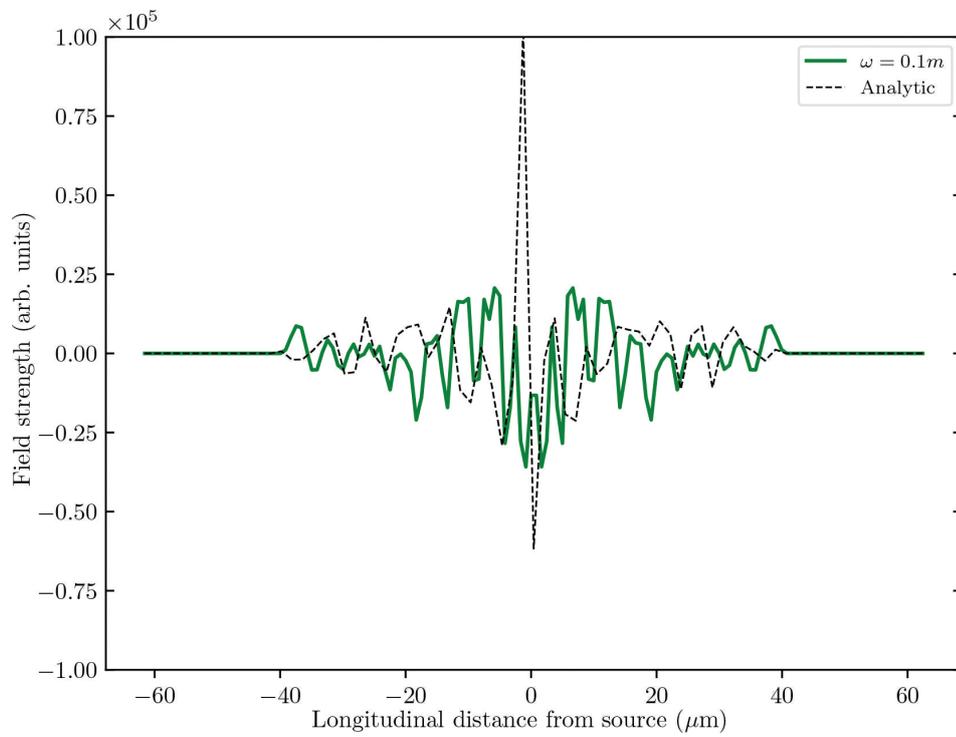
(b) $\omega = 0.1m$

(c) $\omega = 10m$
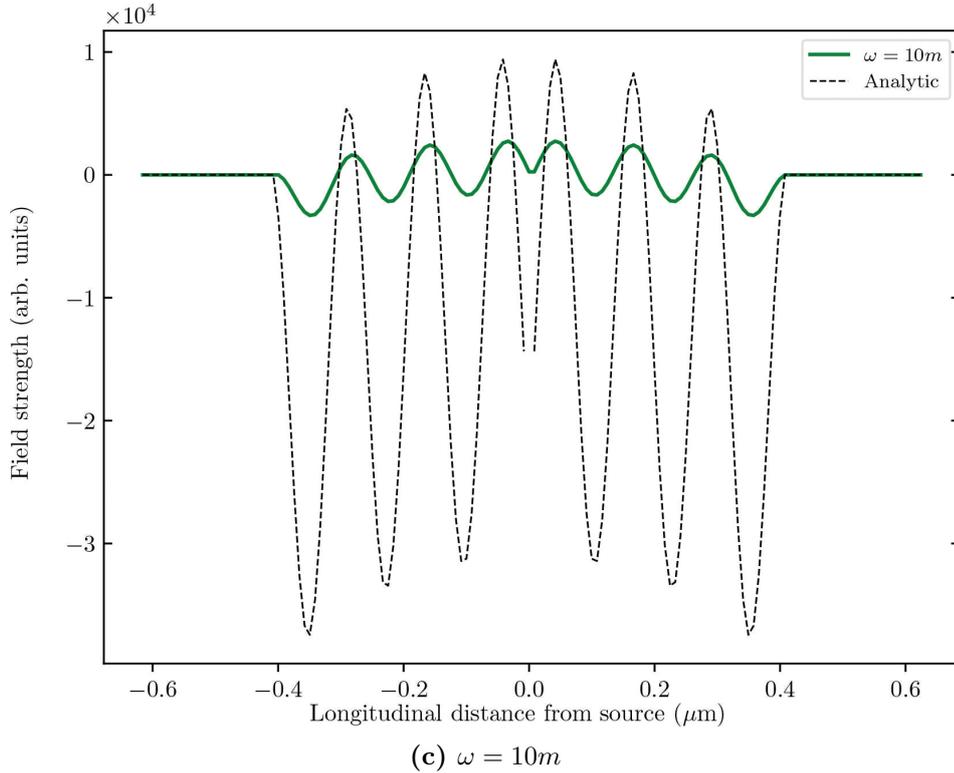
Figure 6.13: Field strength of an $m = 1\,\mathrm{eV}$ persistent time-varying stationary point source. The source initial value is given by $a = 0$, the oscillation amplitude $b = 1$ and oscillation angular frequency is defined as a proportion of the oscillations of the particle mass, which is $m = 1\,\mathrm{eV}$. Black dashed lines indicate numerically integrated values.

6.2.5   Conclusions

With the final test case concluded, the author's intention to have thoroughly convinced readers as to the efficacy of **Run:DMC** in calculating the fields corresponding to systems comprised of point-like sources exhibiting a multitude of behaviours can be summarised as a partial success.

By analytically calculating exact expressions for these systems, it has been shown that **Run:DMC** is capable of calculating massless contributions with relative accuracy and seeming convergence to the analytic expressions in the limit to continuous spacetime. As such, it is able to provide order of magnitude estimates with overall accurate shape, albeit often with artefacts, but would be unsuitable for exact calculations in its current state. Further, **Run:DMC** can calculate massive contributions to within an order of magnitude of their true values for $\omega \leq m$, but the exact structure requires additional work. From the results earlier discussed, one sees that the strengths of **Run:DMC** lie in evaluating fields for which massive contributions are negligible, in particular those

produced within spatially static systems.

With its strengths and weaknesses in mind, it can be argued that **Run:DMC** is a suitable tool for calculating approximate field strengths of particles with small masses, including those of ALPs, DLPs and HSPs. Additionally, the systems in which **Run:DMC** excels are static, non-transient, and those in which the dominant contributions are massless, i.e. the primary source and field co-propagate ultrarelativistically. As will later be seen, this makes **Run:DMC** a suitable tool for investigating the proposed methods of dark matter production in this thesis.

6.3   Queries of Methodology

With the capabilities and inner workings of **Run:DMC** covered, one may begin to query a number of decisions made in the development of **Run:DMC**. This section addresses all questions foreseen by the author.

Perhaps the most obvious question regards the foundation of the project: Why employ numerical analysis techniques for approximate outcomes instead of striving for exact analytical results? The answer to this is simple: most real systems are not analytically calculable. Of those that are not exactly computable, an approximation is considered sufficiently close if it approaches the true value with increased computational resources, as demonstrated by **Run:DMC**.

A clear follow-up question is then, Why would one create a new numerical analysis code in lieu of implementing additional functionality to an existing simulation software, such as EPOCH or MEEP? Consider the further development of an existing codebase; any amendments made would be specific to, and tailored for, that software. As such, should one wish to use or compare results with another simulation software they would find themselves in need of designing, developing and testing the same functionality within the context of a second codebase. In contrast, **Run:DMC** strives for versatility and reusability, obeying the time-honoured maxim of avoiding the reinvention of the wheel. It is capable of analysing the output of any simulation software, with the only requirement for which being an appropriate data reader.

From this, a new question likely spawns: Why has **Run:DMC** been written using integration over Green's functions instead of utilising any other method of solving the inhomogeneous Klein-Gordon equation? First and foremost, the method employed is

theoretically capable of solving any linear partial differential equation (PDE) by reformulating it in terms of integrals, with the resulting integral equation being an exact solution to the governing PDE. Whereas methods that rely on approximations of derivatives between adjacent grid points – such as finite difference – suffer from issues calculating boundary terms, the Green's function methodology is impervious to this since it is directly and exactly calculated between particular source and field points. Further to this, in the limit of discrete to continuous spaces, i.e. with greater resolution, the Green's function method asymptotically approaches the true value. Because the value for each source-field point pairing is calculated, the methodology is capable of handling an arbitrary number of source and field points with the only cost being computational resources. Furthermore, the field point locations can be extended beyond the simulational domain, allowing for a wider use case than every other method which requires their being contained within the domain.

A final foreseeable question is that of limitations: Under what circumstances can **Run:DMC** not be trusted to correctly calculate the field? Since the methodology utilised reformulates the PDE in terms of Green's functions, an obvious restriction of **Run:DMC** is the requirement for the governing PDE to be linear, otherwise Green's functions are inapplicable. Furthermore, the recruited Green's function is that for freespace, making the explicit assumption that the field is non-interacting with the simulation media – a just assumption when considering DMC fields but restrictive with canonical Standard Model fields.

6.4   Future Development

In the interest of full disclosure, the shortcomings of **Run:DMC**, along with their intended solutions, will be considered in this section. It is the author's intent to address the following points in coming years with potential collaborators.

6.4.1   Speed and Efficiency Improvements

Despite the code being developed with speed and efficiency in mind, there remain improvements yet to be implemented.

Further speed gains may be achieved by substituting the containers in which the data is stored. Currently data is stored in a dictionary, which is constructed internally as mutable hash tables which access data in amortised complexity $\mathcal{O}(1)$, i.e. constant

regardless of data size. The dominant reasons for this choice of composite data type were (a) familiarity and (b) the initial ease of writing. However, by establishing necessary data fields, heretofore unknown, **Run:DMC** may be rewritten instead using immutable structs, which also have access complexity $\mathcal{O}(1)$. Whilst on a cursory glance this rewrite appears to be of little benefit, due to the nature of complexity calculations there are additional hidden constants that render structs more efficient. Whereas dictionaries require hashes to access intended data, structs are contiguous blocks of physical memory that allow for different data variables to be accessed through a single pointer – a more efficient process than hashing and searching for matches. Consequently, one can expect marginal speed differences between the data structures, however on the scale of several million data points being accessed multiple times, there would be measurable speed increases.

On a final note, the author recognises possible (read highly likely) algorithmic shortcomings and corresponding changes to be made. For instance, there may be a more efficient method of establishing contributing source points for each field point; if this were the case then one could expect significant speed boosts following its implementation.

6.4.2   Additional Functionality

Beyond aspects of performance, **Run:DMC** would benefit from supplementary functionality which would enhance its capabilities as a numeric analysis tool for the calculation of particle fields.

The first addition to be considered would be to allow the input of system parameters via a secondary configuration file. This would meet the needs of a larger set of users by alleviating the current necessity for user-added code to specify the appropriate data reader, simulation variables to be read &c. In a similar vein, a desirable functionality to be added to the particle input file would be the ability to specify a coupling/kinetic mixing in terms of variables specified in the system input file – this could be achieved by the evaluation of these expressions.

Currently **Run:DMC** has the ability to numerically calculate fields which obey the Klein-Gordon equation, i.e. those of spin-0; this is clearly a subset of a much larger set of potential applications. Consequently, an advantageous generalisation to the code would be to include the ability to solve for an arbitrary spin. In all likelihood, the most

general solution would be numerically inefficient, so the implementation would be to code the additional Green's function for other major relativistic wave equations, e.g. Dirac (spin-1/2), Proca (spin-1), Rarita-Schwinger (spin-3/2) &c, only resorting to the general solution if none of those are the use case. The benefit of this methodology is that there would be no appreciable difference in runtime versus a tailored code since it would be identical once the use case is established.

Some theoretical frameworks, such as Kaluza-Klein theory and string theory, rely upon different dimensionality to the 3+1 found in **Run:DMC**. The existence of a second configuration file for specifying system parameters, as suggested above, could contain a flag denoting the number of dimensions, which would allow for the existence of additional extents.

A further generalisation that could be made is the handling of particles of greater rank (dimensionality/spacetime degrees of freedom) than scalar (rank-0). This could be achieved by recursively adding to the structure of the particle until reaching the desired dimensionality. Each component of the particle's field may then be calculated iteratively, with any sensible compiler optimising out this unnecessity for cases of scalar particles.

A limitation of **Run:DMC** comes in the shape of the language(s) used. The julia programming language in which **Run:DMC** has been written was developed around the philosophy that developers should have readily available interoperability with other languages through the utilisation of shared libraries. This functionality has already been employed in **Run:DMC** for the reading of data from the EPOCH simulation code which, at the time of writing, lacks a native julia reader for the output data files. However, a reader for the Python programming language exists, which has allowed the reading of EPOCH outputs into julia for analysis. Despite its strengths, julia is a relatively new programming language, thus currently lacks the wide adoption of more mature mathematical programming languages such as FORTRAN and C/C++, hence finding additional collaborators for further development may prove challenging.

6.4.3   Public Release

It is the author's intent to further develop the **Run:DMC** code by addressing the improvements and additional functionalities considered herein and ultimately releasing it under a copyleft publishing licence, i.e. providing recipients the four fundamental freedoms of software with the stipulation that they be reciprocal, namely [140]:

Freedom 0 : The freedom to run the program as you wish, for any purpose;

Freedom 1 : The freedom to study how the program works, and change it so it does your computing as you wish;

Freedom 2 : The freedom to redistribute copies so you can help others;

Freedom 3 : The freedom to distribute copies of your modified versions to others.

Chapter 7

Results: ALPs and DLPs from LWFA

"I'm being quoted to introduce something but I have no idea what it is and I certainly don't endorse it."
— Randall Munroe, *XKCD 1942*

7.1 Recapitulation

This chapter considers the potential of magnetised laser-driven plasma wake field accelerators for the production of specific DMCs, namely axion-like particles and dilaton-like particles, i.e. fields which couple to $-\mathbf{E} \cdot \mathbf{B}$ and $\mathbf{E}^2 - \mathbf{B}^2$, respectively. The hypothesis of this investigation is that these fields can be produced and are capable of escaping the plasma. To this end, a scan of a select parameter space was conducted to ascertain dependences that these DMCs may have on particular system variables.

7.2 Motivation

Axion-like particles are well-motivated hypothetical particles initially theorised to restore charge-parity symmetry in quantum chromodynamics while dilatons are scalar fields resulting from compactification of higher-dimensional theories. However, more recently these hypothetical fields have been noted to exhibit similar properties as dark matter. Despite over forty years of *passive* searches surveilling astrophysical sources such as galactic halos and Sol, ALPs yet remain elusive. However, there has been a recent push for purely laboratory-based ALP searches [141]. In recent years, several papers have suggested the potential for laser-based systems to be utilised for the laboratory-based

detection of ALPs [142–145]. The proposition addressed in this chapter concerns the laboratory-based production of ALPs and dilatons, first theorised by David Burton and Adam Noble in their 2018 publication [84].

In their paper, Burton and Noble analytically investigated the prospect for *active* ALP production from a laser-driven plasma wake field accelerator subject to a strong external magnetic field. Their calculations were restricted to one dimension, ensuring that angular components are ignored, thus guaranteeing the magnetic and wake fields may only be co- or anti-parallel, i.e. $\mathbf{E} \cdot \mathbf{B} = \pm \|\mathbf{E}\| \|\mathbf{B}\|$. Additionally, owing to the highly non-linear nature of the bubble regime in plasma accelerators, Burton and Noble focussed their considerations to the linear regime, however they were also able to infer ALP field behaviours in the bubble regime through scaling laws. Their chosen representative parameter values were: plasma frequency $\omega_p = 2 \times 10^{13} \, \mathrm{rad \, s^{-1}}$, Lorentz factor $\gamma = 100$, magnetic field strength $B = 35 \, \mathrm{T}$, and coupling constant $g = 0.88 \times 10^{10} \, \mathrm{GeV^{-1}}$.

Under the aforementioned considerations, Burton and Noble derived an analytic expression governing the expected ALP energy flux density produced by a magnetised laser-driven plasma-based accelerator. Using this expression, they concluded that the produced flux density of ALPs of mass $m_a \lesssim 10^{-4} \, \mathrm{eV \, c^{-2}}$ would be greater than solar axions at terrestrial detectors[1].

Whilst their paper provided a proof-of-concept and order-of-magnitude estimates, Burton and Noble recognised the requirement for numeric analysis in more detailed investigations. The advantages therein include additional behaviours, such as electron interactions with the magnetic fields, as well as being able to extend the acceleration to the non-linear regime.

Finally, a recent phenomenological paper explored the contributions to the axion field from a laser-plasma interaction [146]. The team concluded that the dominant contributions to ALP fields derive from the laser pulse, not the wake itself. Further, they predicted that regardless of mass, the ALP field strength should grow linearly with distance travelled through the plasma.

---

[1]It should be noted that these particles would be produced in high flux bursts instead of the constant flux from the sun.

7.3   Methodology

The methodology utilised herein employs the particle-in-cell code EPOCH to conduct 2D LWFA simulations in order to generate the electromagnetic fields to be used for calculation [134]. An example input deck for the undertaking of EPOCH simulations can be found in Appendix D. The results of these simulations were post-process numerically analysed by **Run:DMC** in order to calculate the field strengths of ALPs and dilatons at a multitude of masses corresponding with the generated electromagnetic fields. To achieve this, the Python EPOCH file reader was utilised to bring the generated data into memory in an appropriate form for **Run:DMC** to analyse. From the calculated quantities, trends and dependencies were noted and explanations offered. The coupling constant used was $g = 0.88 \times 10^{10}\,\mathrm{GeV}^{-1}$, in line with Burton and Noble's paper.

Readers may question whether the approach of post-processing the generated data would miss important dynamics such as reactionary forces from field production. In response to this, the author notes a recent paper by Mendonça et al. which further investigated the prospect for magnetised plasmas to act as ALP sources [147]. In this paper the authors formalised the conversion process between the magnetised wake field and axions, in the process deriving an axion-plasmon coupling parameter which they concluded to be sufficiently small that the presence of axions contributes negligibly to plasma phenomena. Furthermore, they deduced that magnetised plasmas are able to act as sources for ALPS, thus adding credence to the initial proposal as well as validating the methodology presented in this thesis.

7.4   Parameter Value Selection

The proposed scheme of DMC production focusses on currently available experimental equipment and their capacities, insofar as all utilised parameter values are currently achievable somewhere globally, albeit not necessarily within the same facility. Tables 7.1 to 7.3 illustrate the parameter values or range of values over which will be of concern in this chapter. These will be further discussed in following subsections.

7.4.1   Laser Parameters

The choice of laser parameter values could have been arbitrary, however it is useful to set a baseline as an existing experimental facility. The foundational set of values for the laser parameters have been taken from the Astra Gemini laser system, located at the

Table 7.1: Table of laser parameter values.

Laser Parameter	Value range
Wavelength, λ_L	$800\,\mathrm{nm}$
a_0	3
Transverse spot size	$\frac{\lambda_p}{2} \sim 16.7\,\mathrm{\mu m}$
Pulse duration	$\frac{t_p}{4} \sim 27.8\,\mathrm{fs}$
Profile	Bi-Gaussian

Table 7.2: Table of plasma parameter values.

Plasma Parameter	Value range
Total length	$1\,\mathrm{mm}$
Ramp length	$100\,\mathrm{\mu m}$
Density, n_e	$10^{24}\,\mathrm{m^{-3}}$

Table 7.3: Table of magnet parameter value ranges over which
will be scanned.

Magnet Parameter	Value range
Strength	0 to 1000 T
Angle from longitudinal	0 to $\frac{\pi}{2}$ rad

Central Laser Facility, Rutherford-Appleton Laboratory, United Kingdom [148]. This 500 TW Ti:Sapphire laser is capable of delivering 800 nm light pulses with energies of 15 J and durations of 30 fs.

7.4.2   Plasma Parameters

In addition to those for the laser, the chosen plasma parameter values were decided upon by those achievable and typically implemented experimentally.

7.4.2.1   Peak Density

As demonstrated in Section 3.1, the critical density of a plasma is given by

$$n_c = \frac{4\pi^2 \epsilon_0 m_e c^2}{e^2} \frac{1}{\lambda_L^2}.$$

Using this with the requirement that one wishes to maximise the wake excitation by minimising absorption and reflection, one concludes an upper plasma density limit of $n_e \lesssim 1.7 \times 10^{27}\,\mathrm{m^{-3}}$. This is commensurate with densities utilised in laser-driven wake field acceleration experiments, for which the typical range is 10^{23} to $10^{27}\,\mathrm{m^{-3}}$ [149, §11.2.2, p. 284]. However, due to the limitations of the laser pulse duration, the maximum plasma density for a pulse of duration $\frac{t_p}{4}$, where $t_p = \frac{2\pi}{\omega_p} = 30\,\mathrm{fs}$ is the plasma oscillation period, is approximately $n_e = 10^{24}\,\mathrm{m^{-3}}$.

7.4.2.2   Density Distribution

The plasma density profile indicates the distribution of electron number density along a specified direction. Theoretically these distributions can take forms that are physically unrealisable, hence one must consider experimental limitations when defining the density profile of the plasma.

Naïvely, one may assume the plasma taking a top-hat density profile, i.e. one in which the plasma takes a constant density throughout its length and vacuum elsewhere, however this results in an unrealistic spatial discontinuity in number density. Despite this, experimentalists are able to produce quasi-top-hat density distributions of supersonic gas jets for plasma-based accelerators using de Laval nozzles [150,151]. The result of this is a smooth transition to peak density from either end of the plasma, as shown in Figure 7.1.
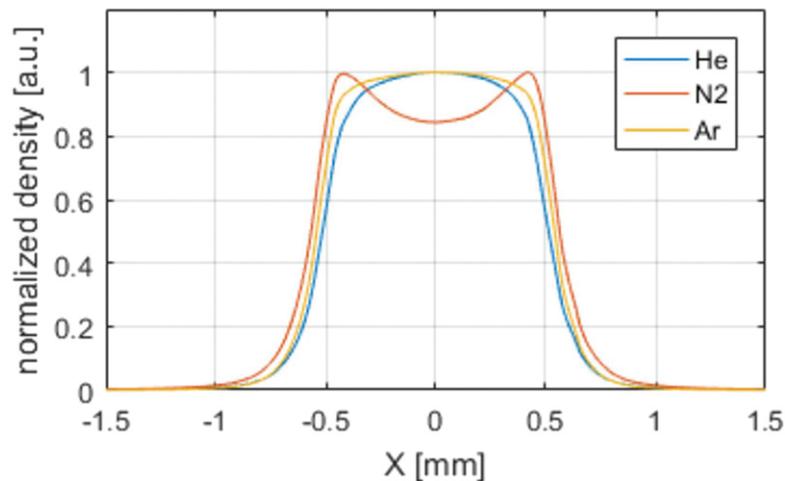
Figure 7.1: Typical plasma density profiles produced by a de Laval gas nozzle along the direction of laser propagation [152].

There is no canonical equation governing this family of distributions thus, without loss of generality, one is able to consider a general distribution which meets a similar profile. As such, the assumed plasma density profile will be piecewise linear, comprising of an up-ramp, a flat peak and a down-ramp, asserting a vacuum ($n_e = 0$) outside of the plasma, i.e. mathematically formulated as

$$
n_e = n_{\text{peak}} \times
\begin{cases}
\left\| \frac{x - x_{\text{start}}}{x_1 - x_{\text{start}}} \right\| & x_{\text{start}} \leq x \leq x_1 \\[2mm]
1 & x_1 \leq x \leq x_2 \\[2mm]
\left\| \frac{x_{\text{end}} - x}{x_{\text{end}} - x_2} \right\| & x_2 \leq x \leq x_{\text{end}} \\[2mm]
0 & \text{otherwise,}
\end{cases}
$$

where x_{start}, x_1, x_2 and x_{end} respectively denoted the plasma start, end of up ramp, end of down ramp and end of plasma, which can be represented graphically as shown in Figure 7.2.
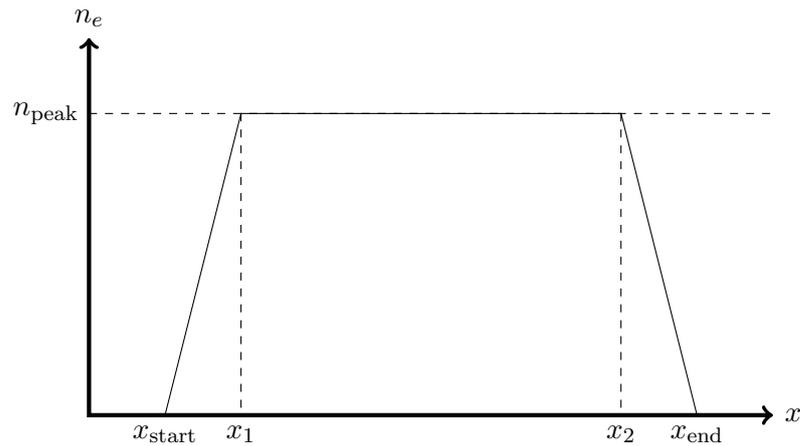
Figure 7.2: Piecewise linear plasma density profile along the direction of laser propagation.

Additionally, one must consider the length of the plasma channel. The dominant consideration of plasma accelerators is over what distance one is capable of accelerating electrons before they close in on the driving beam. This distance is known as the dephasing length, which was given in Section 3.1.8 as

$$
L_{\text{dph}} \approx \frac{n_c}{n_e} \lambda_p \propto n_e^{-\frac{3}{2}}.
$$

For a representative parameter set of $\lambda_L = 800\,\text{nm}$ and $n_e = 10^{25}\,\text{m}^{-3}$, one calculates a dephasing length of $L_{\text{dph}} \sim 1\,\text{mm}$, which is a typical plasma length for LWFA experiments [153]. The density distribution generated by the PIC code EPOCH is shown in Figure 7.3.
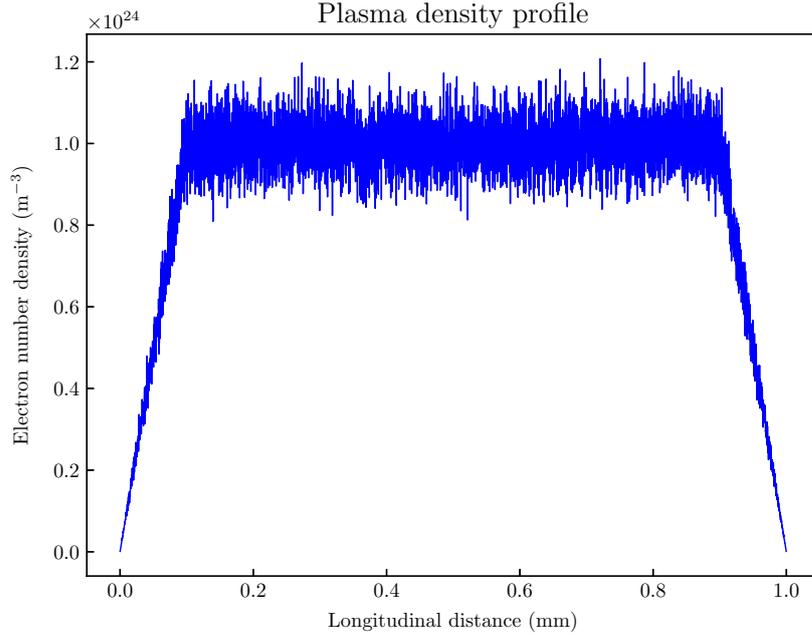
Figure 7.3: Electron plasma density profile generated by
EPOCH.

7.4.3   High Magnetic Field

The magnetic field strength employed in simulations herein will range from $0\,\mathrm{T}$ to $1000\,\mathrm{T}$.
One might initially consider $1000\,\mathrm{T}$ to be unattainable in a laboratory setting, however
its feasibility is less distant than might be expected.

Sufficiently high fields have already been achieved in laboratories, albeit destructively. In 2018 a team from the University of Tokyo, Japan, used the technique of
electromagnetic flux-compression to produce a magnetic field of $1200\,\mathrm{T}$, which destroyed
their laboratory [154]. Aside, the current record for highest non-destructive field is held
by the National High Magnetic Field Laboratory in Florida, USA, for their achievement
of over $100\,\mathrm{T}$ in 2012 [155].

One must also assess the necessary duration of the external magnetic field for the
application. According to the Appleton-Hartree equation [156, p. 23], the refractive index experienced by an electromagnetic wave propagating along the z-direction through a
cold collisionless magnetised plasma at a density of $n_e = 10^{24}\,\mathrm{m}^{-3}$ subjected to external
magnetic field $B = 10^3\,\mathrm{T}$ is $\eta = 0.999$. As such, the propagation duration over a distance $\ell = 10\,\mathrm{mm}$ is $t = \frac{\ell\eta}{c} \sim 3.3\,\mathrm{ps}$, which one concludes to be the minimum necessary
duration of the magnetic field for the proposed experiment. The relevance of this becomes apparent when considering a recent experimental technique of generating strong

quasi-static magnetic fields via capacitative coils for short periods of time [157]. Furthermore, proposed next-generation strong magnetic field production schemes indicate that strengths of 10^4 T should be achievable for durations on the order of nanoseconds – a sufficient duration for the purpose of the schemes proposed herein [158,159].

In light of the above points, it should become clear that exposing a laser wake field accelerator to a 1000 T magnetic for its full duration is not far removed from the realms of already achievable field strengths, and realistically attainable within the next generation.

7.5   Results

Several theoretically-derived features of ALP fields produced within magnetised laser wakefield accelerators were investigated. The magnetic field in the simulated system was directed along the direction of laser propagation with a strength of 1 T.

7.5.1   Field Structure

Burton and Noble's initial proposition of ALP production in magnetised LWFA considered the plasma wake as the source of the dark matter candidates. However, the more recent paper from Huang et al. posited that the laser pulse bore the responsibility for the majority of the particle production. Both of these propositions will be considered in this subsection, which presents the ALP and DLP field structures within a laser-driven plasma-based accelerator.

Figure 7.4 illustrates the electric field along the direction of propagation, which is the dominant field in plasma-based accelerators, along with the corresponding fields for ALPs and DLPs.

As can be seen in Figure 7.4, the peak ALP and DLP field values reside in the region of the laser pulse, thus affirming Huang et al.'s conclusion that the dominant contributions derive from the driving beam. The reason for this derives from the laser pulse providing a stronger electric field than the wake itself, which also provides additional behaviours. ALPs couple to $-\mathbf{E}\cdot\mathbf{B}$, whereas the DLPs couple to $\mathbf{E}^2-\mathbf{B}^2$; consequently, the ALP field amplitude is negative while the DLP is positive, with the laser strength also explaining the vast interspecies difference in magnitudes between the field amplitudes. Further, the wake also contributes to the DMC fields, validating Burton and Noble's analysis.
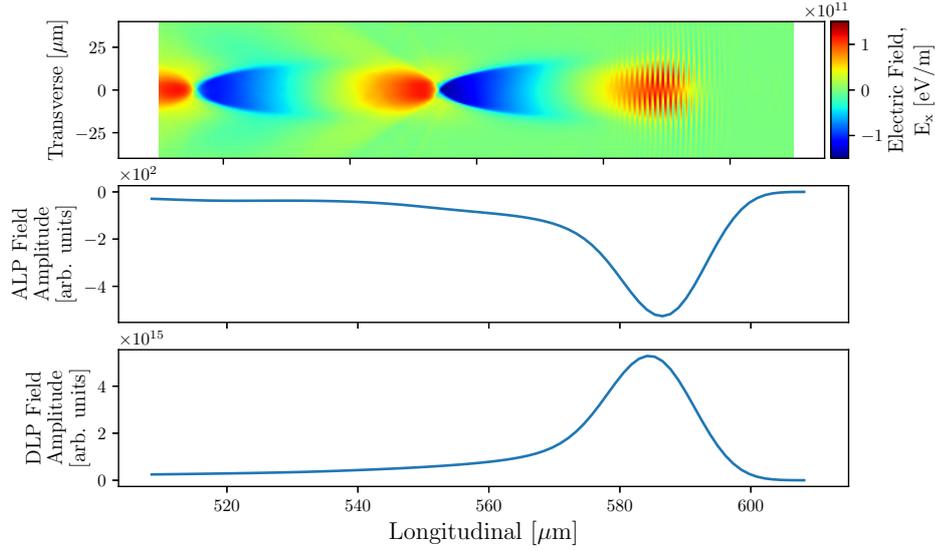
Figure 7.4: Top: Longitudinal electric field. **Middle:** ALP field amplitude. **Bottom:** DLP field amplitude.

7.5.2   Quasistaticity

The energy flux density of a field Ψ, $\mathbf{P}_\Psi$, is given by

$$\mathbf{P}_\Psi = - \left(\partial_t \Psi \right) \left(\boldsymbol{\nabla} \Psi \right).$$

The temporal expectation value of this quantity, $\langle P_\Psi \rangle$, is given by the normalised integral over a period T, i.e.

$$\langle P_\Psi \rangle = \frac{1}{T} \int_0^T P_\Psi \, \mathrm{d}t.$$

However, because the results lie within a moving window, the coordinate system changes every time slice, thus there would be no guarantee that the same coordinate lies within consecutive times. As such, the nature of the results does not lend itself conducive to being integrated over time. Instead, one is able to replace the temporal integral by a spatial integral.

For an arbitrary 1D function $f(x,t)$ the temporal expectation value $\langle f \rangle$ at a coordinate x is given by

$$\langle f \rangle (x) = \frac{1}{t_1 - t_0} \int_{t_0}^{t_1} f(x,t) \, \mathrm{d}t,$$

while its spatial expectation value $\langle\langle f \rangle\rangle$ at a time t is

$$\langle\langle f \rangle\rangle (t) = \frac{1}{x_1(t) - x_0(t)} \int_{x_0(t)}^{x_1(t)} f(x,t) \, \mathrm{d}x.$$

Suppose instead that f depends solely on a single variable $\zeta = x - vt$. Introducing $\mathit{f}(\zeta)$ such that $f(x,t) = \mathit{f}(\zeta)$, it then follows that

$$\langle f \rangle (x) = -\frac{1}{v} \frac{1}{t_1 - t_0} \int_{x-vt_1}^{x-vt_0} \mathit{f}(\zeta) \, \mathrm{d}\zeta$$

and

$$\langle\langle f \rangle\rangle (t) = \frac{1}{x_1 (t) - x_0 (t)} \int_{x_0(t)-vt}^{x_1(t)-vt} \mathcal{f} (\zeta) \, \mathrm{d}\zeta.$$

However, because $x_1 (t_1) - x_0 (t_1) = -v (t_1 - t_0)$, then $\langle f \rangle (x_1 (t_1)) = \langle\langle f \rangle\rangle (t_1)$. Consequently, by assuming that the field structure is static within the moving window (*quasistatic*), i.e. a function of $x - v_{\mathrm{window}}t$, one calculates the spatial expectation value of the moving window to be equivalent to that of the temporal.

In Burton and Noble's paper, the authors assumed a quasistatic ALP field structure, writing "The ALP field is static in the wake frame", however it was previously unknown whether this was truly the case. In order to assess this assumption, $\langle P_\Psi \rangle$ and $\langle\langle P_\Psi \rangle\rangle$ of the ALP field were calculated using $\mathbf{P}_\Psi = - (\partial_t \Psi) (\boldsymbol{\nabla} \Psi)$ and $\mathbf{P}_\Psi = -\left(-v_{\mathrm{window}} \frac{\partial}{\partial x} \Psi \right) (\boldsymbol{\nabla} \Psi)$, respectively; under the assertion of quasistaticity, one expects the two flux densities to coalign. Figure 7.5 illustrates how these formulations compare with one another.
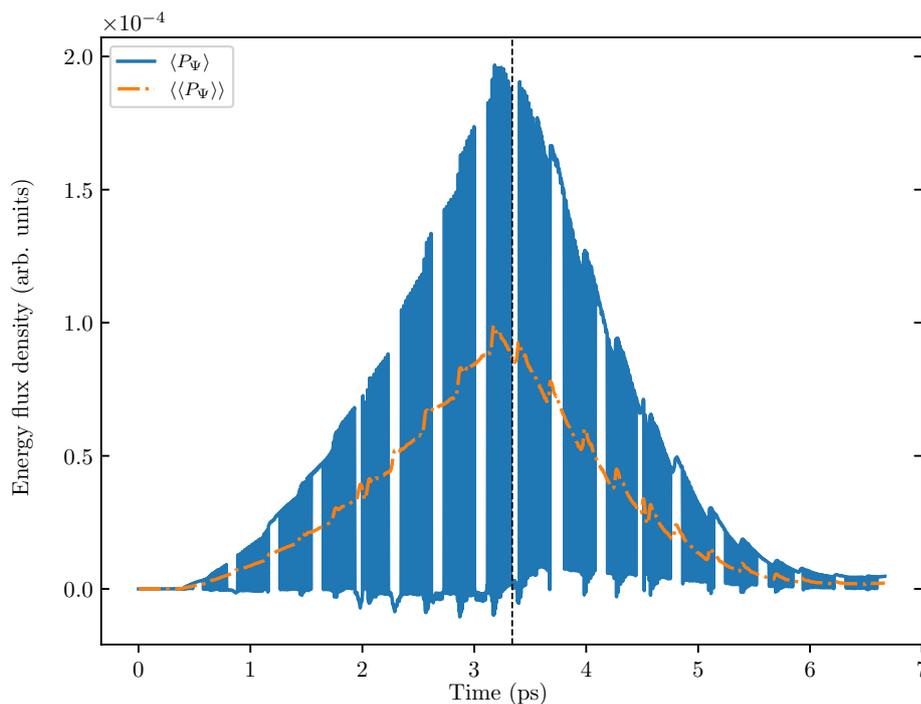
Figure 7.5: Comparison of temporal derivative, $\langle P_\Psi \rangle = \frac{1}{t_1 - t_0} \int_{t_0}^{t_1} f(x, t) \, \mathrm{d}t$, and spatial derivative, $\langle\langle P_\Psi \rangle\rangle = \frac{1}{x_1(t)-x_0(t)} \int_{x_0(t)-vt}^{x_1(t)-vt} \mathcal{f}(\zeta) \, \mathrm{d}\zeta$, when calculating field energy flux densities. Dashed vertical black line indicates end of plasma; additional propagation length is $1\,\mathrm{mm}$.

From Figure 7.5 one sees that, to a reasonable approximation, the ALP and dilaton field structures are quasistatic, albeit with the temporal derivative being approximately

twice the magnitude as spatial derivatives. That being said, the $\langle P_\Psi \rangle$ suffers from regular fluctuations – resulting in blocks of seemingly filled regions – as well as completely nullified regions – diverging from local data trends. These behaviours are likely a result of the aforementioned issues due to discretisation as well as the structure propagation not being perfectly matched with the window speed. Consequently, one is able to replace temporal integrals by appropriately scaled spatial integrals when calculating field energy flux density expectation values, provided one only considers the actual values to be approximate. An addition behaviour worthy of note is the rapid falloff in field strength following the plasma; the reason for this is that in vacuo the electric field – and hence ALP source – is negligible, thus the Klein-Gordon equation becomes homogeneous, i.e. dispersive, and one accordingly expects ALP and DLP field strengths to diminish as the inverse square of distance from the plasma exit.

7.5.3   Magnetic Field Direction

It has so far been demonstrated that the primary contributing factor toward the ALP field derives from the laser pulse as well as one being able to assume quasistaticity in the ALP field during propagation with reasonable confidence.

Burton and Noble assumed that the magnetic field could be either co- or antiparallel to the direction of propagation by conducting their analysis in one spatial dimension. However, this approach is extremely limited as it restricts all additional behaviours to that one dimension, which may be physically unrealistic. For example, the Lorentz force experienced by a plasma electron within an external magnetic field has orthogonal components to the singular dimension available. As such, this subsection investigates the dependence of DMC fields on the relative angles between the external magnetic field and the direction of propagation.

The modelled plasma channel was chosen to be cylindrical such that, owing to the symmetry of the system, it is sufficient to have only one relative angle between the direction of propagation and the external magnetic field. The analysis conducted utilised a $B = 1\,\mathrm{T}$ magnetic field and varied the relative angle at regular intervals over the range $\theta = \left[\frac{\pi}{2}, 0\right]$, where $\theta = \frac{\pi}{2}$ indicates the magnetic field being perpendicular to the direction of propagation and $\theta = 0$ indicates their being co-parallel. Figures 7.7 and 7.9 illustrate the results of these analyses.

One sees from Figure 7.7 that when the external magnetic field is perpendicular to
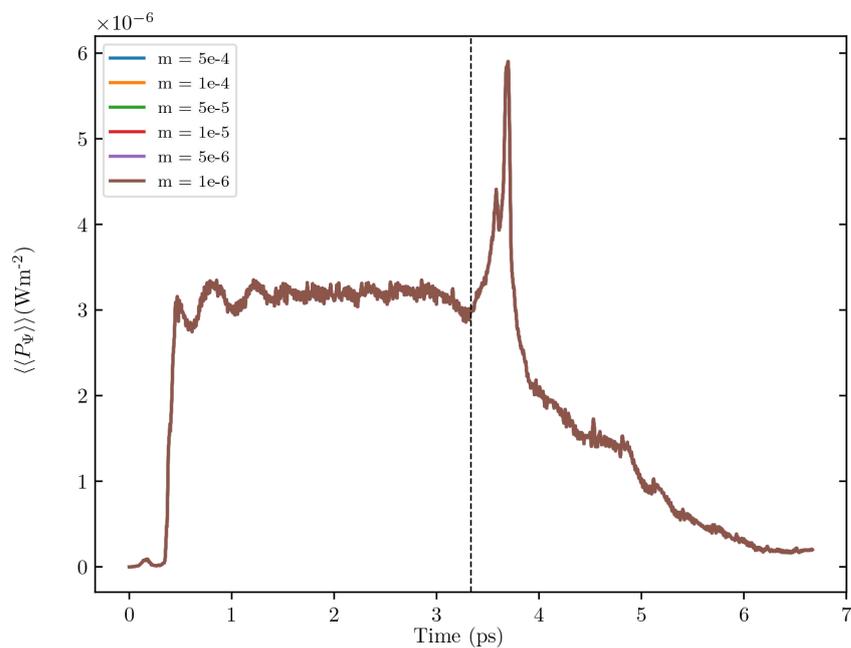
(a) ALP energy flux density at $\theta = \frac{\pi}{2}$.
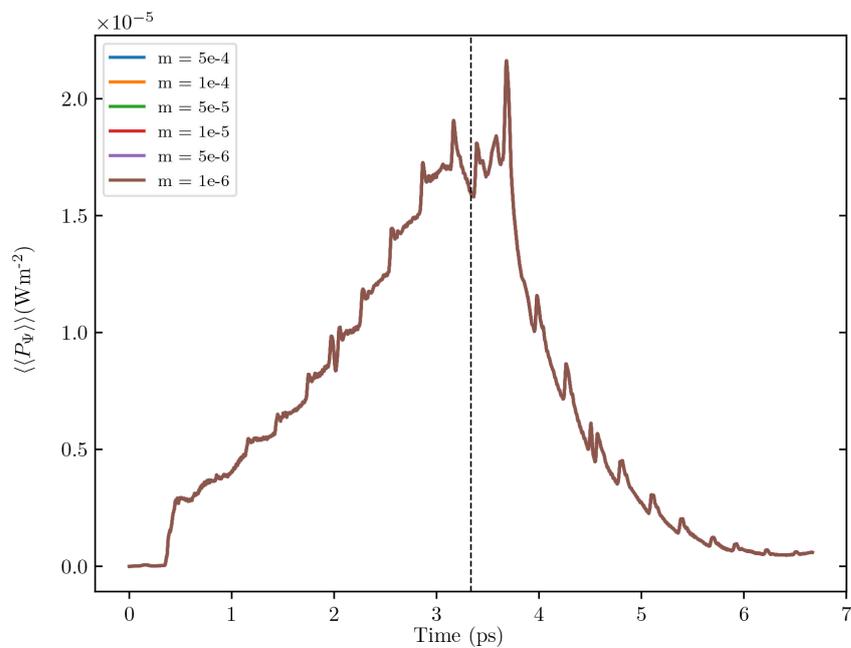
(b) ALP energy flux density at $\theta = \frac{3\pi}{8}$.
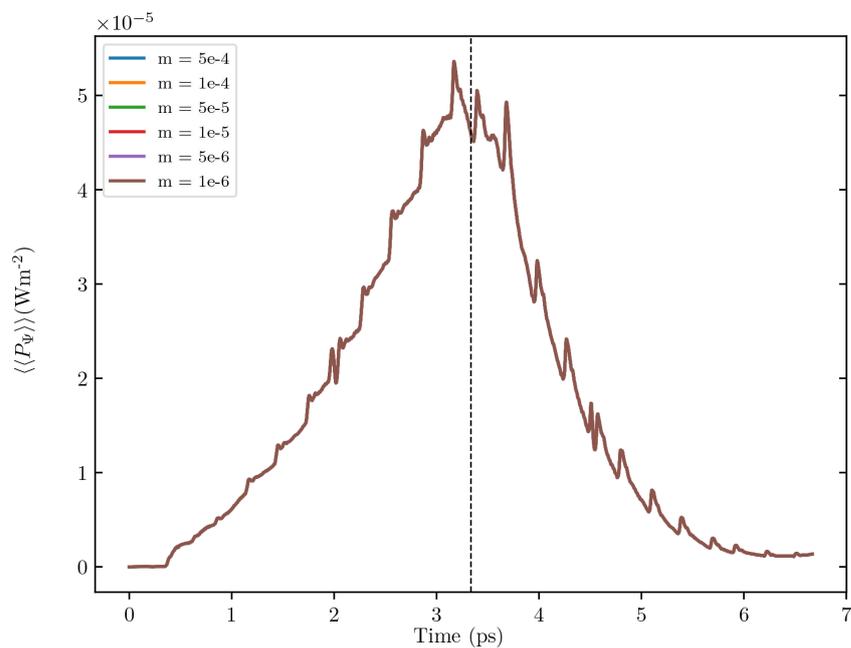
(c) ALP energy flux density at $\theta = \frac{\pi}{4}$.
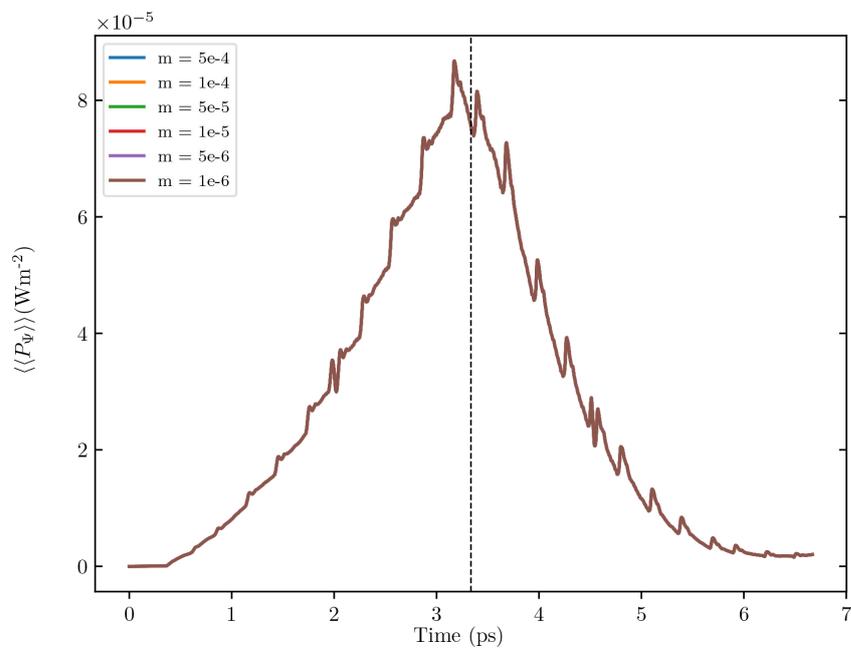
(d) ALP energy flux density at $\theta = \frac{\pi}{8}$.
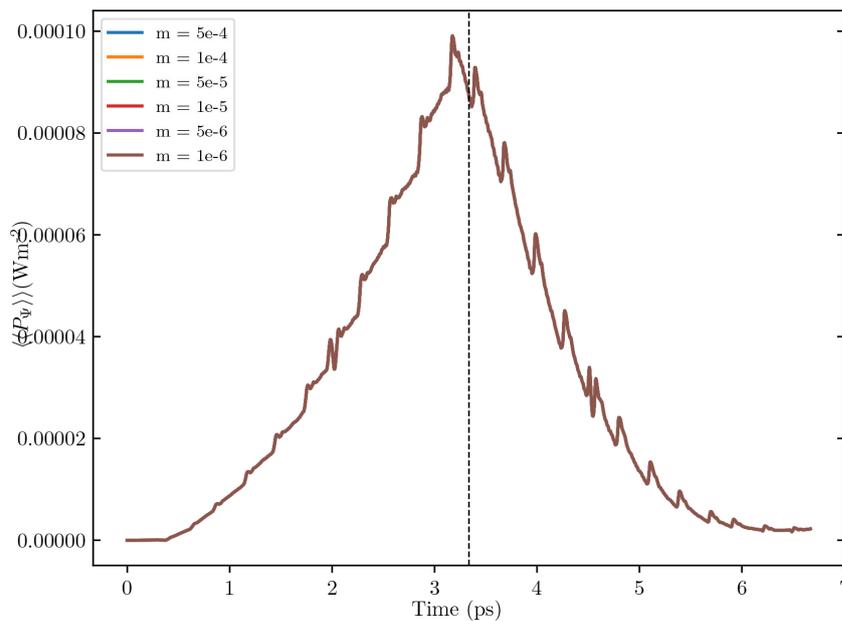
(e) ALP energy flux density at $\theta = 0$.

Figure 7.6: Energy flux density of ALP field for a variety of external magnetic field angles relative to the direction of propagation. Dashed vertical lines indicate end of plasma. Additional propagation length of $1\,\text{mm}$.
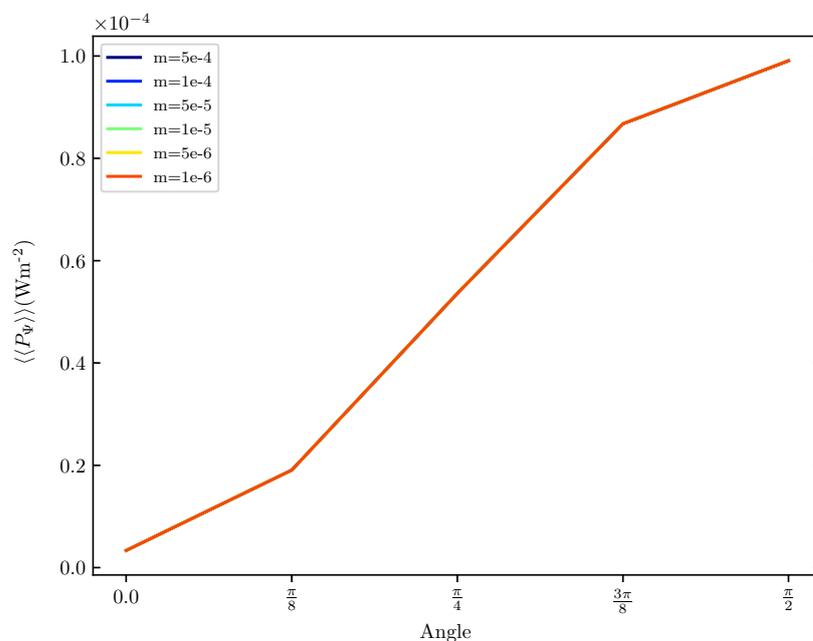
Figure 7.7: Peak energy flux density values of ALP field during plasma propagation across a variety of external magnetic field angles relative to the direction of propagation.
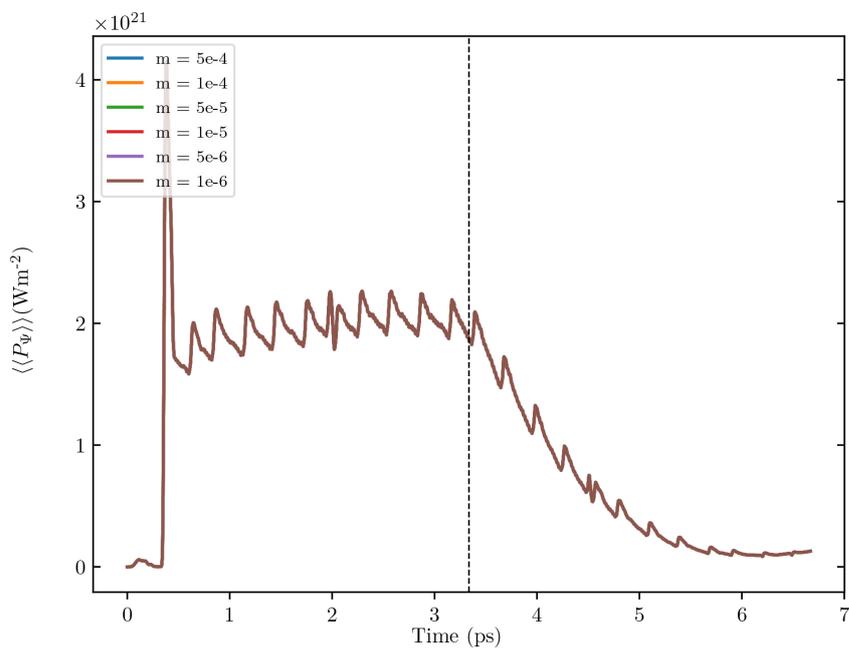
(a) DLP energy flux density at $\theta = \frac{\pi}{2}$.
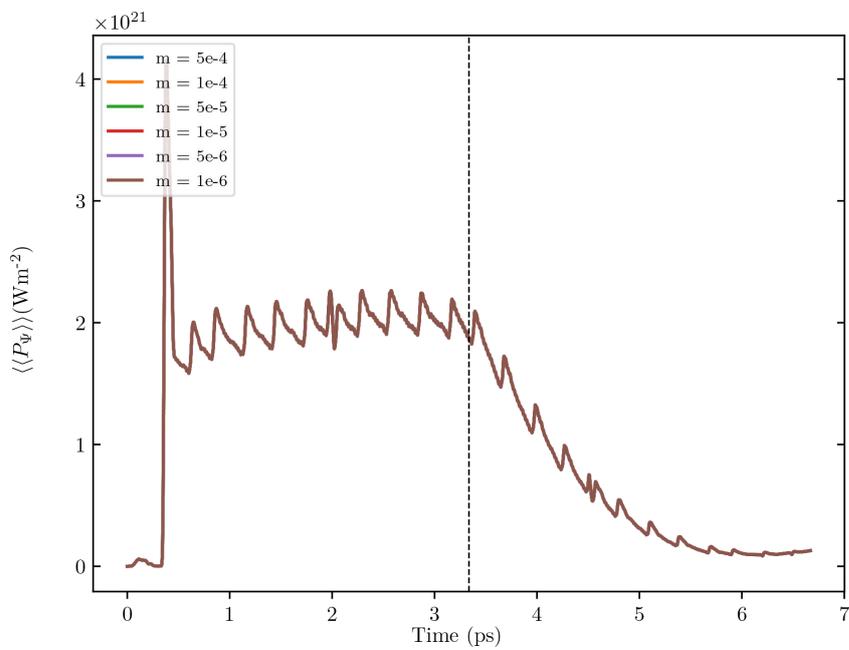
(b) DLP energy flux density at $\theta = \frac{3\pi}{8}$.
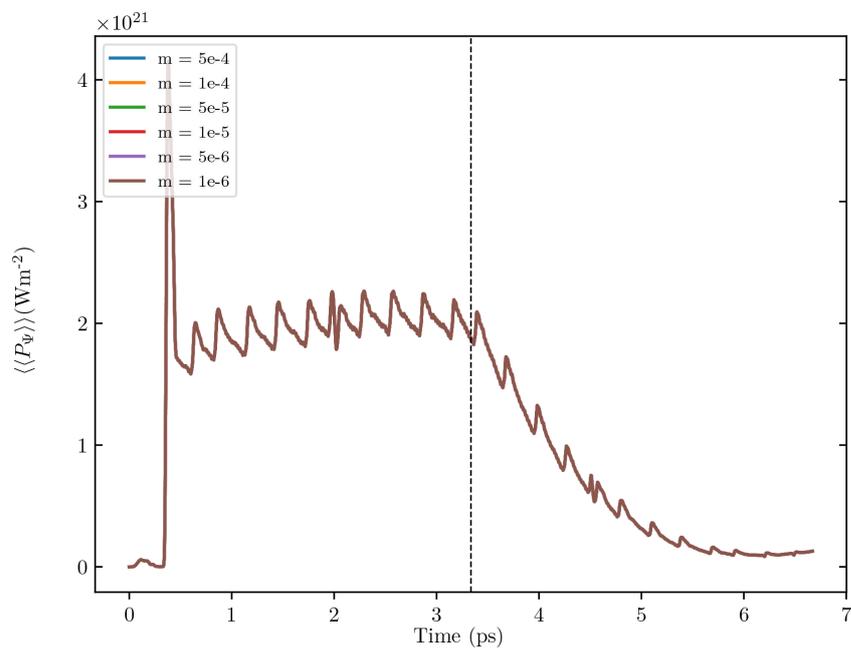
(c) DLP energy flux density at $\theta = \frac{\pi}{4}$.
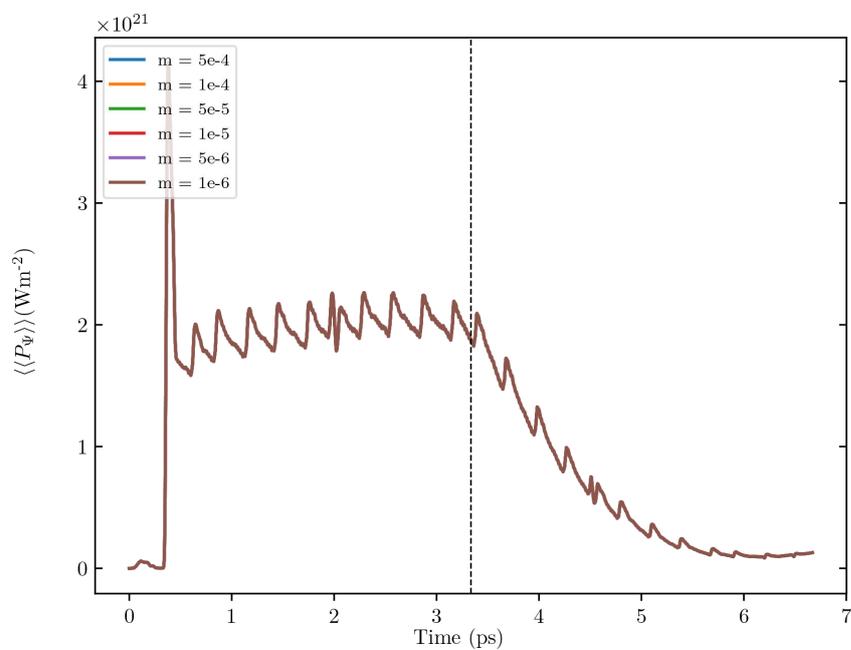
(d) DLP energy flux density at $\theta = \frac{\pi}{8}$.
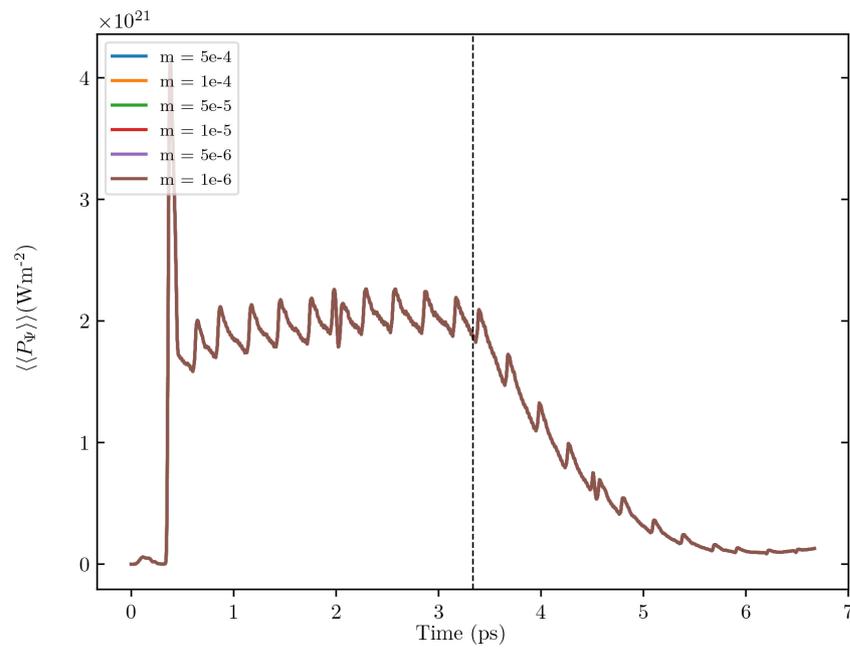
(e) DLP energy flux density at $\theta = 0$.

Figure 7.8: Energy flux density of DLP field for a variety of magnetic field angles relative to the direction of propagation. Dashed vertical lines indicate end of plasma. Additional propagation length of 1 mm.
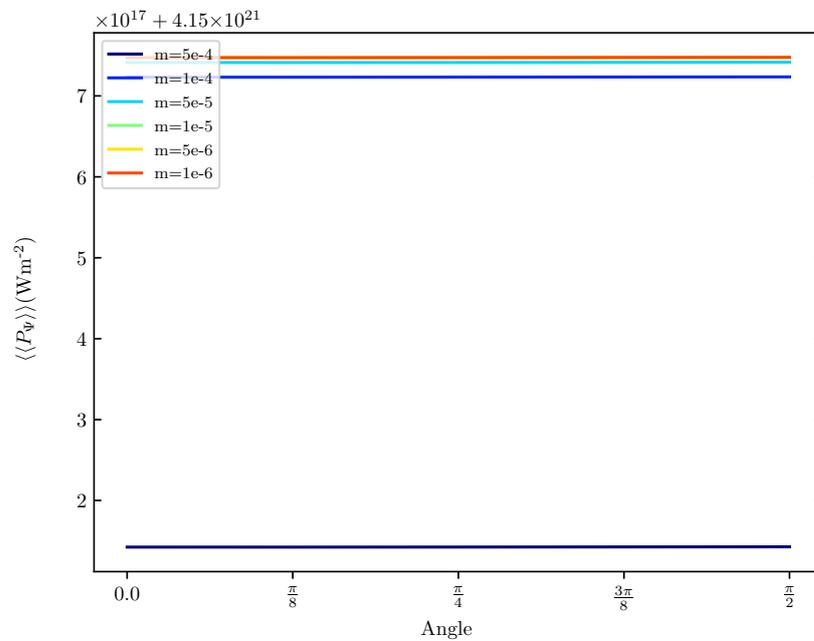
Figure 7.9: Peak energy flux density values of DLP field during plasma propagation across a variety of external magnetic field angles relative to the direction of propagation.

133

the propagation direction, i.e. $\theta = \frac{\pi}{2}$, the ALP field does not undergo growth, instead maintaining an approximately constant value. This is due to the transverse electric field not co-propagating with the window, instead only providing transitory contributions. Additionally, one finds that the rate of ALP field growth is greatest when the magnetic field is co-parallel with the propagation direction, i.e. $\theta = 0$. An interesting, but unsurprising, result is that the DLP field appears to be independent of θ. DLPs, being scalar fields, are invariant under parity transformations and so one expects this lack of angular dependence. A particularly interesting observation is that, irrespective of mass in the range considered, all ALP fields have equal energy flux densities, as do all dilaton fields, thus the massive contributions to the solution are inconsequential. The reason for this lies with the fact that massive contributions for these particles scale as $\Psi_{m \neq 0} \propto m J_1(m)$, thus with their relatively low masses, this term is negligible when not near resonance, e.g. the Compton wavelength for ALPs of mass $m = 10^{-3}\,\mathrm{eV}$ is $\lambda \sim 1\,\mathrm{mm}$, significantly larger than the current simulation. A further behaviour of interest is the formation of regular peaks in field strength over time. Between the results displayed here and later, one is able to see that the magnetic field does not affect the frequency of these peaks, however, the frequency for DLPs is twice that as for ALPs. Consequently, one can tentatively conclude that the peaks derive from the electric field, where their regularity signifies a periodic electric structure, thus the author concludes that the peaks are a result of the wake.

7.5.4   Magnetic Field Strength

It has so far been demonstrated that the optimal relative angle between the external magnetic field and direction of propagation is $\theta = 0$. This subsection presents investigations into the dependence of the ALP and DLP fields upon the strength of the magnetic field. During these investigations the magnetic field strength was varied over the range 0 to $1000\,\mathrm{T}$ with the value of the relative angle set to $\theta = 0$. Figures 7.11 and 7.13 demonstrate the energy flux density of the DMC fields at a variety of magnetic field strengths.

First and foremost, as earlier observed, the field energy flux densities are quasi-independent of mass – a result unerred by significantly stronger magnetic fields. Additionally, from Figure 7.11 one is able to verify that the rate of growth of ALP fields is approximately linear. The combination of these observations are in agreement with the conclusions of Huang et al [146].
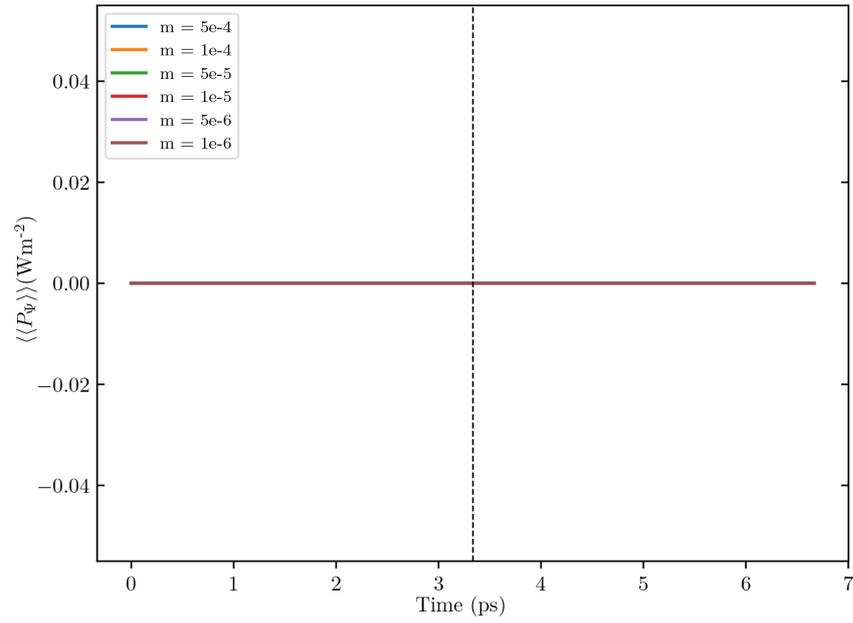
(a) ALP energy flux density at $\|\mathbf{B}_x\| = 0\,\mathrm{T}$.
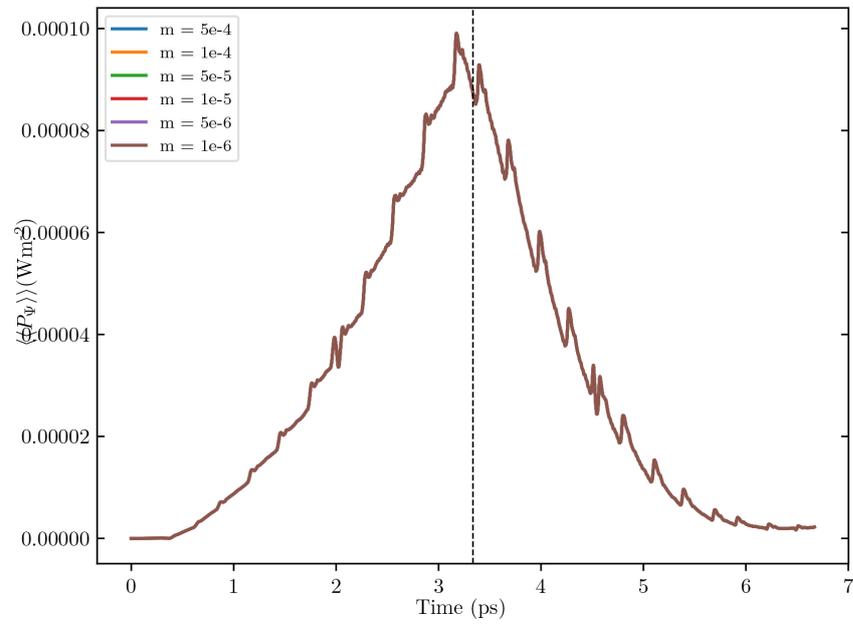
(b) ALP energy flux density at $\|\mathbf{B}_x\| = 1\,\mathrm{T}$.
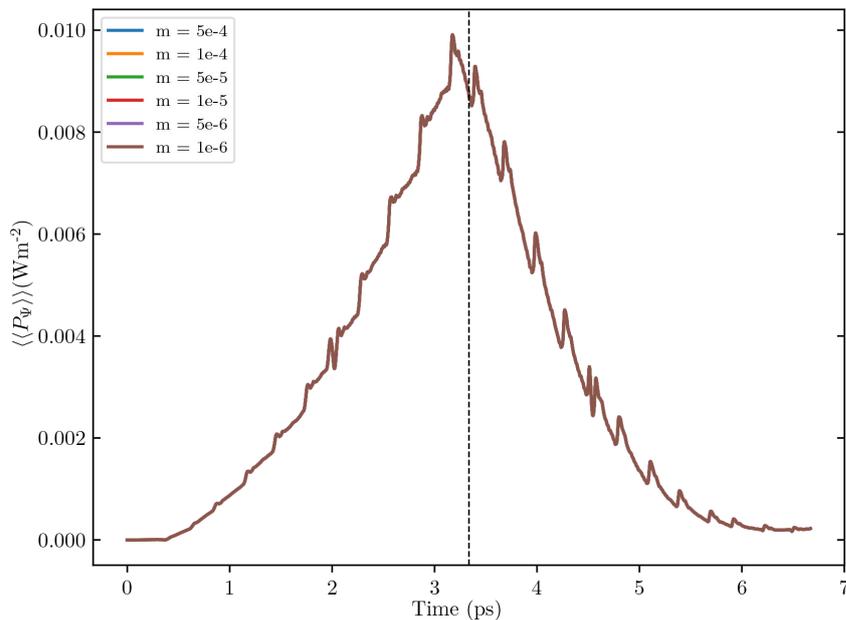
(c) ALP energy flux density at $\|\mathbf{B}_x\| = 10\,\mathrm{T}$.
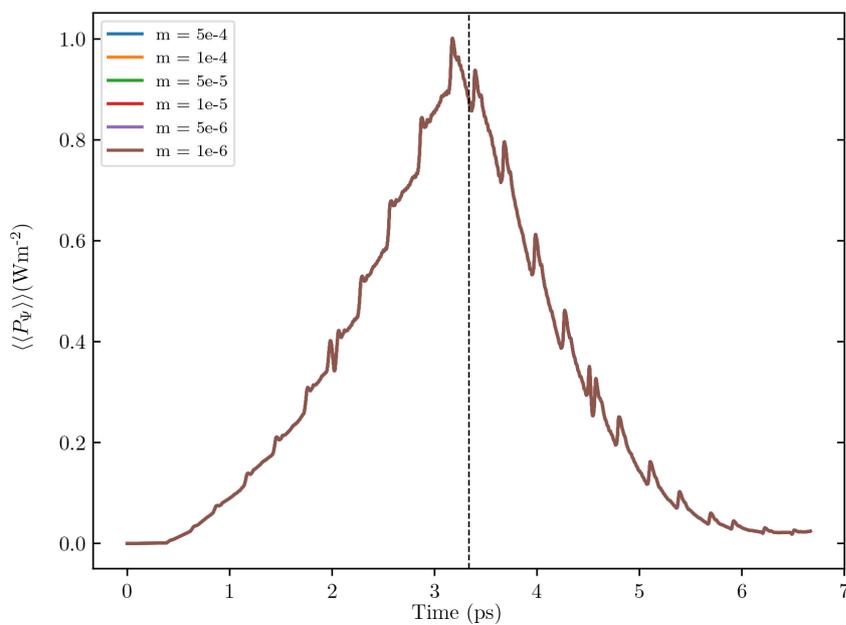
(d) ALP energy flux density at $\|\mathbf{B}_x\| = 100\,\mathrm{T}$.
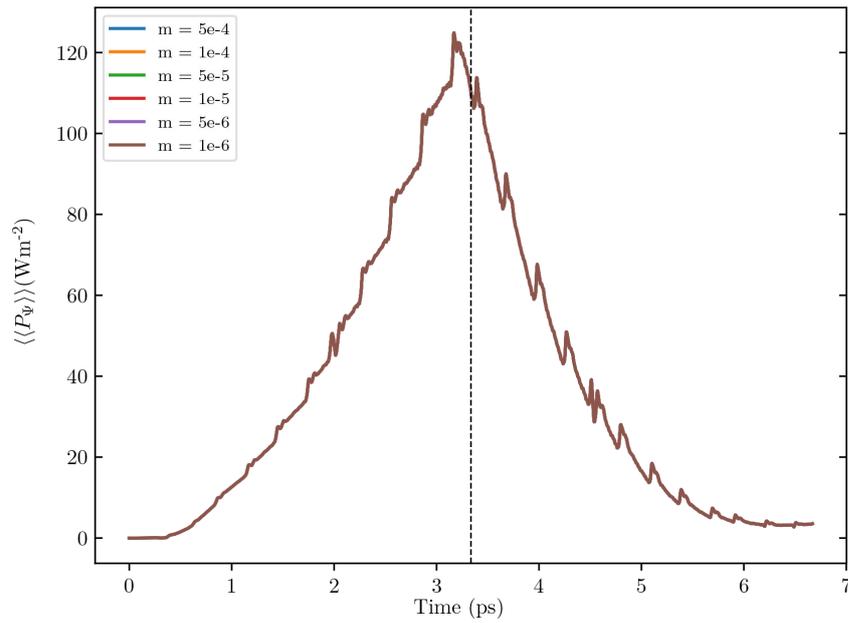
(e) ALP energy flux density at $\|\mathbf{B}_x\| = 1000\,\mathrm{T}$.

Figure 7.10: Energy flux density of ALP field across a variety of magnetic field strengths. Dashed vertical lines indicate end of plasma. Additional propagation length of $1\,\mathrm{mm}$.
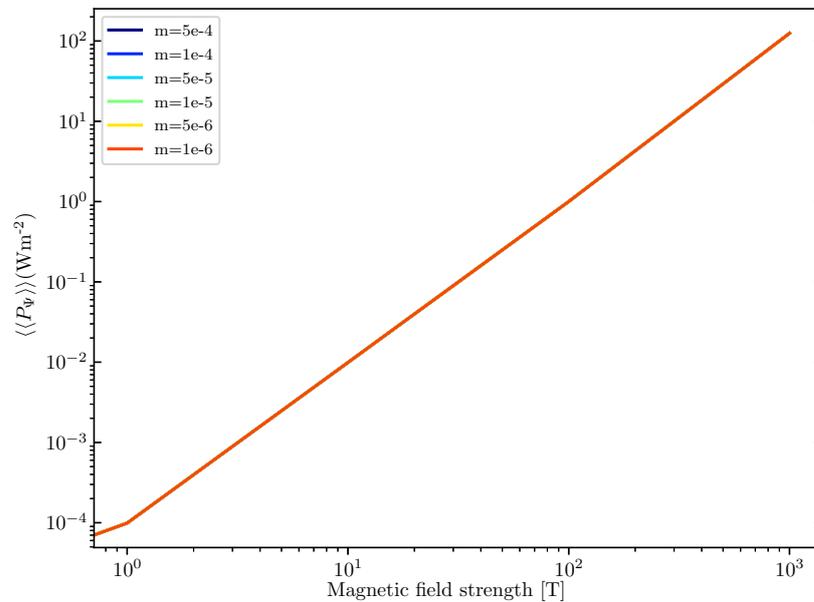
Figure 7.11: Peak energy flux density values of DLP field during plasma propagation across a variety of external magnetic field angles relative to the direction of propagation.

137
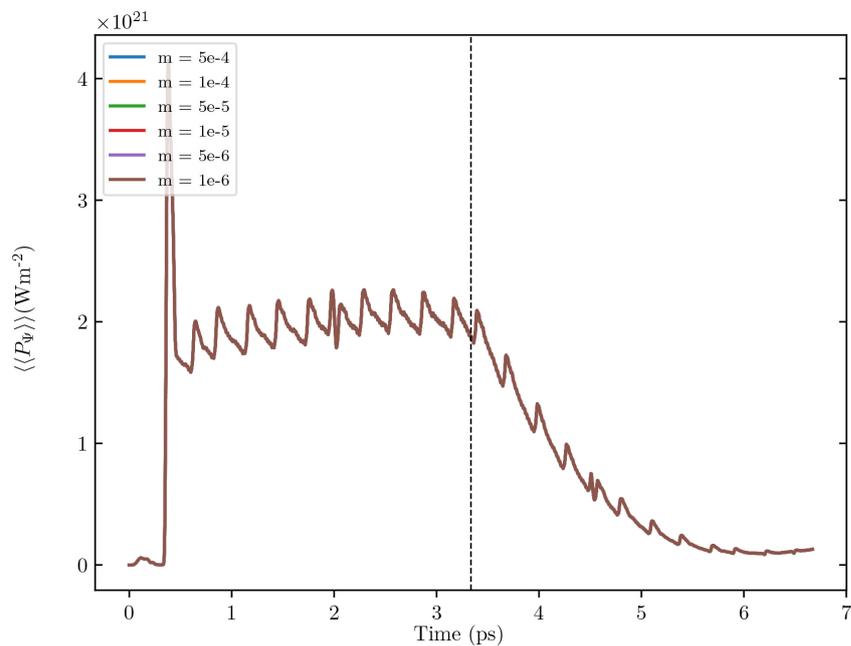
(a) DLP energy flux density at $\|\mathbf{B}_x\| = 0\,\mathrm{T}$.
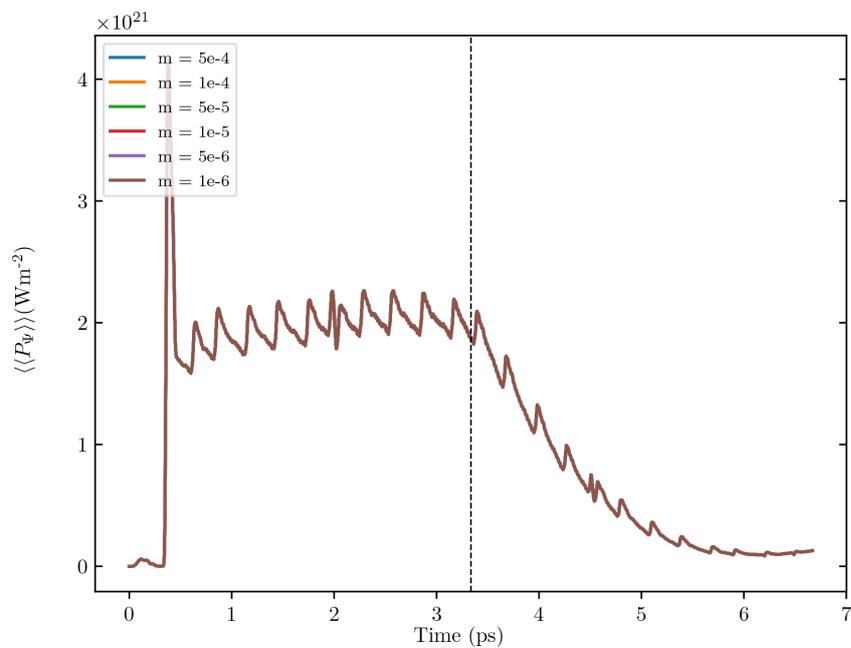
(b) DLP energy flux density at $\|\mathbf{B}_x\| = 1\,\mathrm{T}$.
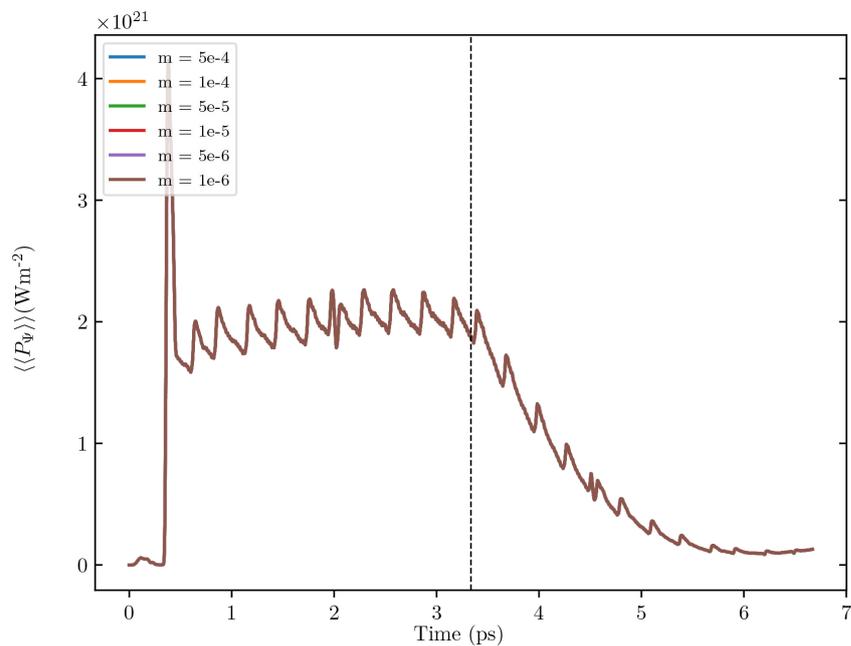
(c) DLP energy flux density at $\|\mathbf{B}_x\| = 10\,\mathrm{T}$.
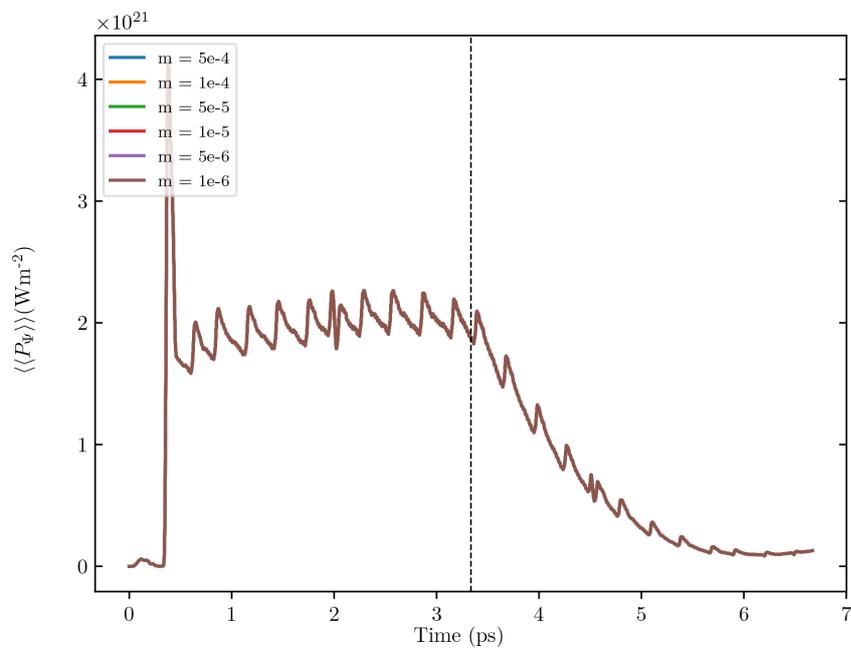
(d) DLP energy flux density at $\|\mathbf{B}_x\| = 100\,\mathrm{T}$.
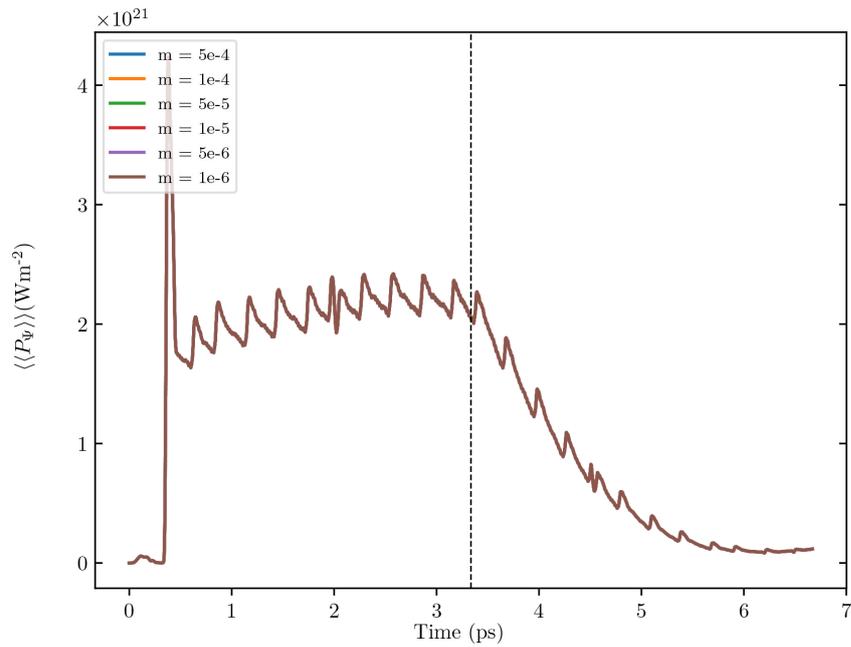
(e) DLP energy flux density at $\|\mathbf{B}_x\| = 1000\,\mathrm{T}$.

Figure 7.12: Energy flux density of DLP field across a variety of magnetic field strengths. Dashed vertical lines indicate end of plasma. Additional propagation length of 1 mm.
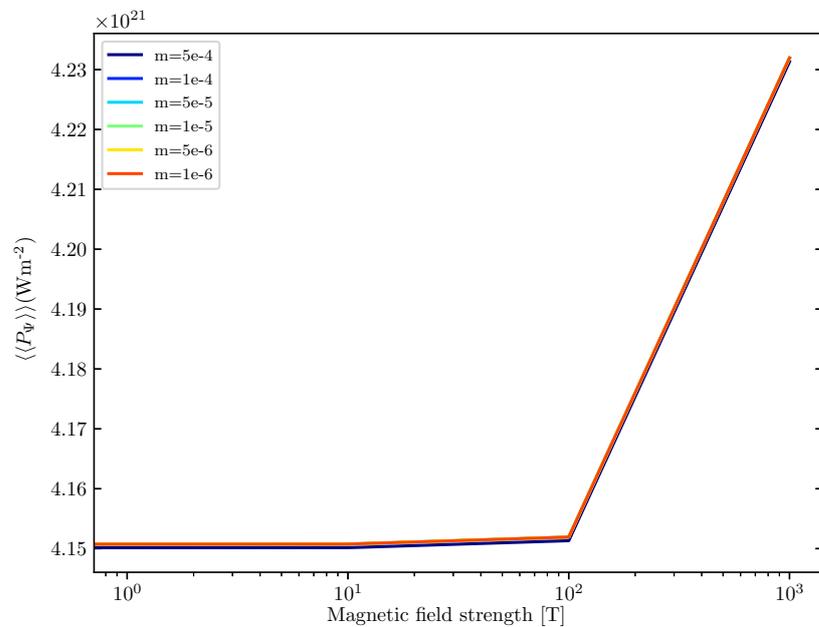
Figure 7.13: Energy flux density of DLP field for a variety of magnetic field strengths. Dashed vertical lines indicate end of plasma. Additional propagation length of 1 mm.

One is able to compare ALP field strengths across the range of magnetic field strengths. Because the energy flux density $\mathbf{P}_\Psi$ is proportional to the field energy E, which is itself proportional to the square of the field strength Ψ, which is proportional to the magnetic field $\mathbf{B}$, i.e. $\mathbf{P}_\Psi \propto E \propto \Psi^2 \propto \mathbf{B}^2$, then one expects P_Ψ to increase two orders of magnitude for every order of magnitude increase of $\|\mathbf{B}\|$ – a prediction of Burton and Noble's substantiated by Figure 7.11.

Considering now the DLP field energy flux densities shown in Figure 7.13, one notes that, as with the results for the ALP fields, there is exceedingly little variation across masses. Perhaps most notably, the field values change very little over the full range of examined magnetic field strengths. This is a result deriving from the large electric fields present in plasma-based accelerators, resulting in $\|\mathbf{E}\| \gg \|\mathbf{B}\|$; consequently, the DLP energy flux densities are relatively unaffected.

7.6   Discussion

The post-process numeric analysis code **Run:DMC** was applied to data generated by the particle-in-cell plasma simulation code EPOCH in order to calculate the field strengths of dark matter candidates, including axion-like particles and dilaton-like particles. The results affirmed theoretically-predicted behaviours, as well as discovering previously untheorised trends.

The first noteworthy results of the analysis is the verification of Burton and Noble's assumption of quasistaticity, while identifying the dominant ALP and DLP source as the laser pulse, in agreement with Huang et al. Further, it has been demonstrated that the optimal angle for ALP field growth is when the external magnetic field is co-parallel with the direction of laser propagation and that the rate of growth of the ALP field is proportional to the square of the magnetic field strength. Unsurprisingly, being scalar, the DLP field was unaffected by the relative angle between the external magnetic field and propagation direction. Additionally, the DLP field does not benefit from the presence of external magnetic fields and it is the author's conjecture that external magnetic fields instead hinder DLP production in LWFA.

Prior to drawing final and full conclusions regarding field strengths, additional work is required. A shortcoming of the aforementioned results lies in the one-dimensionality of the field calculated; because the field is a central lineout, off-central-axis field strengths

could not be considered. Additionally, the energy flux density drop-offs following emergence from the plasma remain inconclusive.

Whilst it has been shown that magnetised laser-driven plasma-based accelerators can act as sources of ALPs and dilatons, it may not be the best source. For example, laser-driven wake field accelerators are the shortest of plasma-based accelerator schemes, however the ALP fields produced would benefit from increased length. Huang et al. noted that there was a compromise in plasma accelerator length and sustainable rate of ALP field growth; as such particle-driven wake field accelerators may surpass the final ALP flux density at the end of the plasma vs LWFA. In contrast, there is no advantage for dilatons of any mass to have this additional duration due to the field strengths not developing in the same manner as ALPs. Instead, dilatons benefit from high electric fields and low magnetic fields; as such the author's recommendation for laboratory-based dilaton production would be to utilise extremely short laser-driven plasma accelerators with a train of laser pulses.

Chapter 8

Results: Dark Photons and ALPs from PBG Lattice

> *"Be thine own palace, or the world's thy jail."*
>
> — John Donne, *To Sir Henry Wotton*

8.1 Motivation

The premise of this project was the utilisation of photonic band gap lattices for the confinement of electric fields generated within magnetic resonant cavities, potentially allowing the production and detection of dark photons (HSPs) and axion-like particles. This builds upon previous work by Rebecca Seviour, Ian Bailey, Nathan Woollett and Peter Williams [160]. In their 2014 paper, the group investigated the capacity for a spatially defective triangular dielectric lattice structure to localise the electric fields situated within a microwave resonance cavity, as shown in Figure 8.1.

The team simulated the transmission of an electric field through a two-dimensional multi-defect triangular lattice, where the dielectric structure was comprised of sapphire rods with relative permittivity $\epsilon_r = 9$. It was found that this arrangement is capable of approximately confining the electric field photons to within several characteristic lattice lengths. Through so doing, it was found that at a distance of ten lattice lengths from a source, the electric field strength dropped by a factor of 10^7, effectively decoupling the regions, as indicated in Figure 8.2.

As a consequence of this analysis, the authors were able to conclude that the electric field at a sufficiently displaced region would be effectively negligible. As such, if one
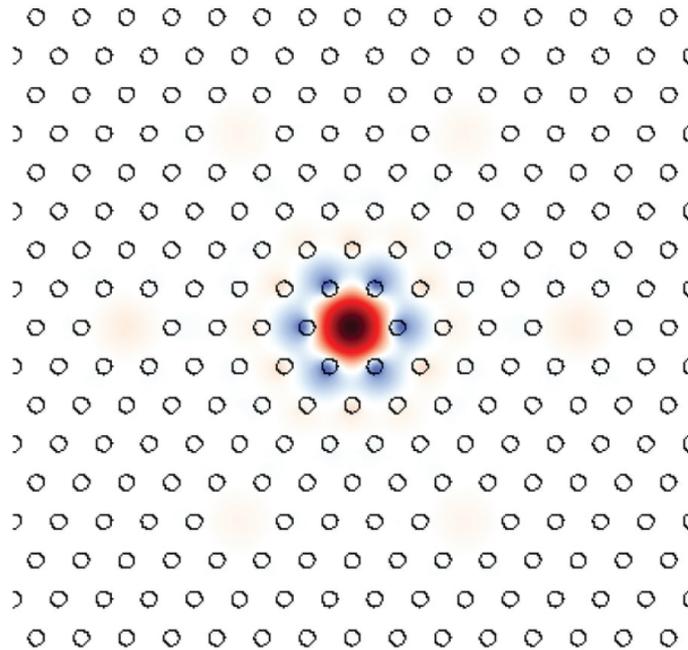
Figure 8.1: Electric field strength over distance in a triangular
lattice with source located in a central defect [160]. Red indicates
electric field strength in the negative z-direction, with blue
indicating the same field in the positive z-direction.
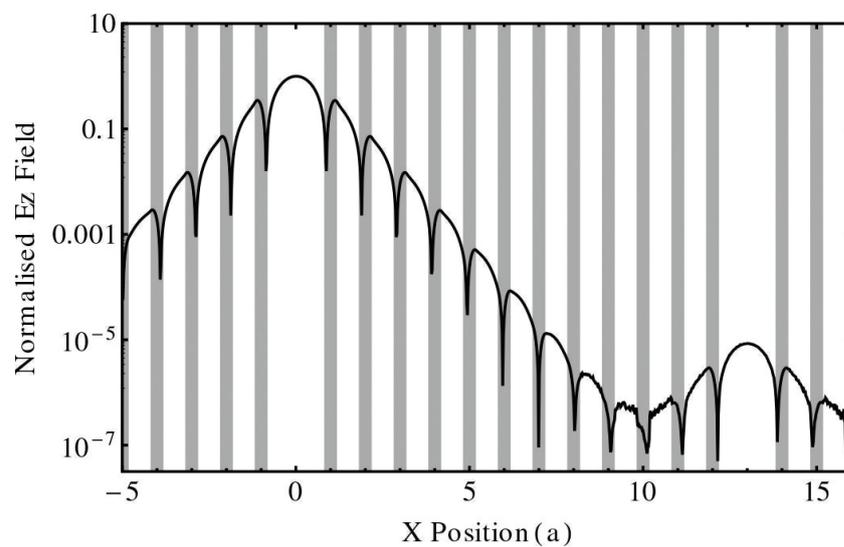
Figure 8.2: Normalised electric field strength as a function of
distance from source ($x = 0$), measured in lattice constants, a.
Vertical bars indicate dielectric rods responsible for the band gap
structure [160].

144

were to measure an unexpectedly large electric field in one of these spatially separated defect regions, one would infer the existence of a feebly-interacting intermediary particle. Through kinetic mixing with the standard model photon, dark photons are a prime candidate for such an experiment. However, the lattice may also be immersed in a magnetic field in order to facilitate the generation of axion-like particles, which would also be capable of traversing the dielectric media unhindered.

The proposed experimental setup is to create a photonic bandgap lattice comprised of sapphire rods inside a microwave resonant cavity. Two defects would be introduced to the system in sufficiently separated regions by removing rods from the lattice. The entire system would then be immersed inside of a uniform magnetic field and an electric field would be applied to one of the defects at a frequency which would be localised. A straight wire cathode will be installed within the non-electrified defect in order to measure the electric field. If the observed electric field strength is greater than expected then one would infer the existence of intermediary electromagnetically-interacting particles, namely ALPs and HSPs.

8.2   Methodology

As with Chapter 7, the methodology for this project involved conducting simulations of an existing experimental system and performing post-process analysis of the output. The chosen experiment for analysis was the CERN Resonant WISP Search (CROWS) and the simulation code utilised herein was the MIT Electromagnetic Equation Propagator (MEEP) [161]. Following the generation of the electromagnetic fields, **Run:DMC** was used to calculate the field strengths of ALPs and HSPs.

8.2.1   The MEEP Code

MEEP is a software package for simulating the time-evolution of electromagnetic radiation via Maxwell's equations. It utilises a finite-difference algorithm (outlined in Section 5.1) in the time-domain on a uniformly spaced grid in space and time. It uses normalised units to facilitate scale-invariant calculations and supports the inclusion of nearly arbitrary materials and a variety of boundary conditions.

8.2.2   MEEP Units

Whilst MEEP benefits from scale-invariance by using dimensionless quantities, its application in relation to **Run:DMC**'s numeric analysis is problematic. **Run:DMC** utilises SI units, thus when calculating fields in the context of a proposed experimental undertaking, the MEEP output data requires scaling by appropriate factors prior to analysis. To this end, there are four degrees of freedom between the two systems: length $[\ell]$, time $[t]$, current $[I]$ and mass $[m]$, which may all be calibrated through choices of values for physical parameters.

The simplest degree of freedom is that of the length scale, which in the context of a lattice is canonically denoted a. As such, one defines the length scale by defining the lattice constant as

$$[\ell] = a. \tag{8.1}$$

Through dimensional analysis, one sees that units of time are equivalent to those of a length-to-speed ratio. Consequently, by defining a characteristic physically significant constant speed, e.g. the speed of light through a medium c, one is able to use the length scale to define the time scale as

$$[t] = \frac{a}{c}. \tag{8.2}$$

Noting that the speed of light is given by $c = \frac{1}{\sqrt{\mu\epsilon}}$, where μ and ϵ are respectively the permeability and permittivity of the medium, then one need only define one of μ or ϵ as the other is forced to take a value such that c takes the earlier defined value. As the system being considered in this chapter focusses on phenomena relating to electric fields, the defined parameter was chosen to be the permittivity ϵ, which has units

$$[\epsilon] = \frac{t^4 I^2}{m\ell^3},$$

where I is current and m is mass. Substituting Equations (8.1) and (8.2) into this permittivity dimension equation one then obtains a current-mass ratio of

$$\left[\frac{I}{m}\right] = \frac{\epsilon c^4}{a}. \tag{8.3}$$

Equation (8.3) is a linear equation with two unknown variables, thus leaving a single degree of freedom. One may hence make an arbitrary choice of definition

$$[I] = I_0 \tag{8.4}$$

such that one derives the mass definition

$$[m] = \frac{I_0^2 a}{\epsilon c^4}.$$ (8.5)

Consequently, using Equations (8.2), (8.4) and (8.5) with the permittivity, one is able to translate from MEEP units to an arbitrary unit system through the definitions of a set of four fundamental quantities: a, c, ϵ and I_0.

8.2.3   Scalar Representation of Vector Bosons

The addition of a dark sector $\text{U}(1)$ symmetry to the standard model introduces a new mediating gauge boson, the dark photon. As a gauge boson, the dark photon is a vector boson and hence is theorised to have multi-dimensional components, viz. x, y and z. In its current state of development, **Run:DMC** is only capable of handling scalar fields, thus the simulated electric field was restricted to the z-direction, i.e. $\mathbf{E} = (0, 0, E_z)$, through which one is able to treat the dark photon as a scalar boson, thus facilitating the calculation.

8.2.4   ALP Production

The localisation of electric field within a photonic band gap lattice not only aids in the detection of dark photons via kinetic mixing, but can also serve as a means of detecting axion-like particles. By applying a constant and uniform background magnetic field to the cavity, it is possible for ALPs to be produced within a electromagnetised PBG lattice defect and detected in another, sufficiently separated, region. Because the DMCs are known a priori to have weak coupling to ordinary matter fields, the addition of this background magnetic field will not significantly affect the DMC dynamics.

8.2.5   Previous Investigations

Previous explorations into this proposed experimental scheme involved the simulation of electric field propagation throughout a lattice of dielectric rods [160]. The authors quantified the expected electric field strength at some detector region due to a source through a definition of the so-called geometric factor of the lattice. Through this they were able to estimate the relative electric field strength at a spatially separated region from the source.

Additionally, in his PhD thesis, Michael Betz outlined an equation to be calculated for a DMC field Ψ at a point $\mathbf{x}$ due to a source ϱ at point $\mathbf{x}'$ as effectively

$$\Psi\left(t, \mathbf{x}\right) = \int_{\Omega} \mathrm{d}^3 \mathbf{x}' \frac{e^{-ik\|\mathbf{x}-\mathbf{x}'\|}}{4\pi \|\mathbf{x} - \mathbf{x}'\|} \varrho\left(t, \mathbf{x}'\right) \tag{8.6}$$

where Ω denotes the support of the source and $k = \sqrt{\omega^2 - m_\Psi^2}$ is the wavenumber associated with a DMC of mass m_Ψ oscillating at a frequency ω [162]. The source term for ALPs is $\varrho = -g_{a\gamma\gamma}\mathbf{E} \cdot \mathbf{B}$, whereas for HSPs $\varrho = \chi m_{\gamma'}^2 E_z$, from Equation (2.6). One may note that Equation (8.6) is the Fourier transform of Equation (2.4), thus is a limited use case of its **Run:DMC** counterpart in that it assumes a harmonic behaviour, i.e. the DMC oscillates sinusoidally in time at a single frequency. Consequently, when **Run:DMC** calculates the production of DMCs at each step in time, it is evaluating the above equation with additional details which were previously excluded.

8.3   CROWS

CROWS was an experiment probing the existence of sub-eV weakly-interacting slim particles (WISPs), the primary focus of which are axion-like particles and dark photons. The experiment involves the utilisation of a microwave cavity with LSW methodology in an effort to infer the existence of these hypothetical particles. The inner dimensions of the CROWS microwave cavity are illustrated in Figure 8.3.

CROWS ran at a frequency of several GHz within a $3\,\mathrm{T}$ superconducting magnet. Contrary to the proposed experiment, CROWS did not utilise a PBG lattice, instead utilising a second cavity – running in synchronicity to the generating cavity – for detection, using external electromagnetic shielding as the walls through which light may shine. However, the system under investigation proposes a single cavity which houses a PBG lattice, into which an electric field is applied.

8.4   Results

The same input file used in the generation of the system shown in Figures 8.1 and 8.2 was used to perform the MEEP simulation for this project. This MEEP simulation produces multiple HDF5 data files containing grid coordinates and field data. These data were read by **Run:DMC** into an appropriate format and used to calculate the corresponding DMC fields.
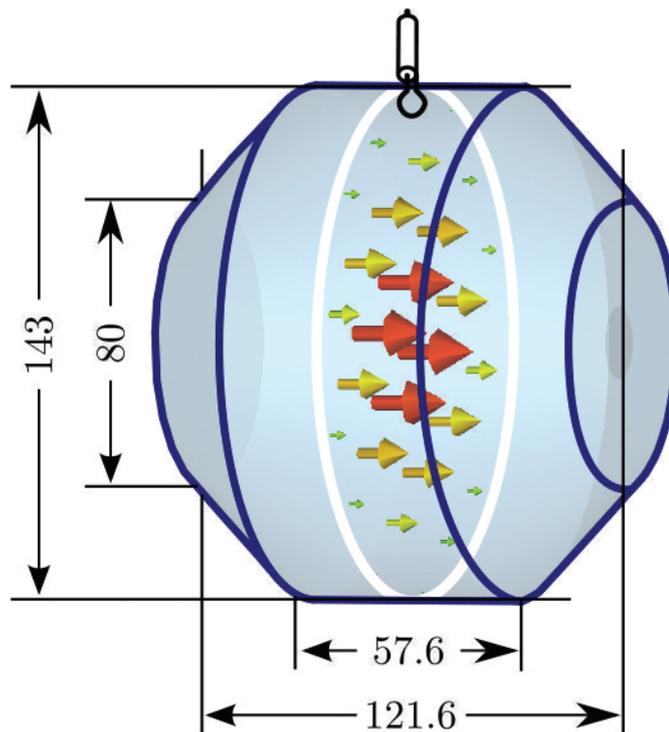
Figure 8.3: Inner dimensions of CROWS microwave cavity
(mm). Image adapted from Reference [163].

8.4.1   Unit Scaling

As earlier noted, the definitions of four system constants to MEEP's dimensionless parameters bring them into physically meaningful quantities. Since **Run:DMC** is written using SI units and the system of concern for this chapter has relative permittivity of unitary order, the following definitions were made in the reading of simulation data output from MEEP:

$$c = 299\,792\,458\,\mathrm{m\,s^{-1}} \qquad (8.7)$$

$$\epsilon = 8.854\,187 \times 10^{-12}\,\mathrm{F\,m^{-1}}$$

$$I_0 = 1\,\mathrm{A},$$

leaving the lattice spacing a yet unconstrained. As this length scale is a free parameter, it was chosen in such a manner as to localise photons of a given frequency using the dimensional quantities of the CROWS cavity shown in Figure 8.3.

Assuming the interior medium of the cavity to have permittivity and permeability of order those for free space, then by using Equation (4.29) with the cavity dimensions, one derives the available range of angular frequencies in the TM010 mode as being between $5 \times 10^9\,\mathrm{rad\,s^{-1}}$ and $9 \times 10^9\,\mathrm{rad\,s^{-1}}$. Since $a = \frac{c}{f} = \frac{2\pi c}{\omega}$, one obtains a range of length scales of 33 mm to 50 mm. Choosing the lower bound of these with the set of parameters

149

in Equation (8.7), then by renormalisation one obtains a maximum simulation electric field value of approximately $7\,\mathrm{MV\,m^{-1}}$, which is readily achievable with modern microwave cavities. Additionally, the rods were calculated to be of radius $6.6\,\mathrm{mm}$, within the capabilities of modern sapphire fabrication methods [164].

8.4.2   Free Parameters

The DMC masses of interest in this microwave cavity experiment are $10^{-4.5}$ to $10^{-3.5}\,\mathrm{eV\,c^{-2}}$ [160]. Consequently, the dark photon and ALP masses for which the fields were calculated spanned this range in half-integer orders of magnitude.

As earlier mentioned, a constant and uniform background magnetic field is necessary for the production of ALPs. This was chosen to be $\|\mathbf{B}\| = 1\,\mathrm{T}$ as this is currently readily achievable in many experimental facilities globally. Assuming that the external magnetic field permeates the entire cavity shown in Figure 8.3, the required magnetised volume is approximately $1550\,\mathrm{cm^3}$.

8.4.3   Results: DMC Field Structure

Arguably the most important aspect of dark matter candidate production in static systems is the manner in which the respective fields are spatially distributed. Figure 8.4 indicates the spatial distribution of $m = 10^{-3.5}\,\mathrm{eV}$ ALP fields across a number of time steps while Figure 8.5 indicates the distribution of $m = 10^{-3.5}\,\mathrm{eV}$ dark photon fields across the same time steps.

One observes from Figures 8.4 and 8.5 that the fields for both ALPs and HSPs are distributed radially with a central region of high intensity. Furthermore, the DMC fields can be seen to oscillate in conjunction with the electric field. Additionally, as will be demonstrated shortly, the fields follow the same trends across the mass spectrum, albeit at different magnitudes. Finally, one is able to note that the magnitudes of the ALP and HSP for equal masses are equal; this is a result of the electric and magnetic fields being limited to one dimension, i.e. $\Psi_{\mathrm{HSP}} \sim \|\mathbf{E}\| = \|E_z\|$ and $\Psi_{\mathrm{ALP}} \sim \mathbf{E} \cdot \mathbf{B} = E_z B_z$, consequently because $B_z = 1\,\mathrm{T}$ then $\Psi_{\mathrm{HSP}} \sim \Psi_{\mathrm{ALP}}$, excluding scaling factors such as particle masses and coupling constants.
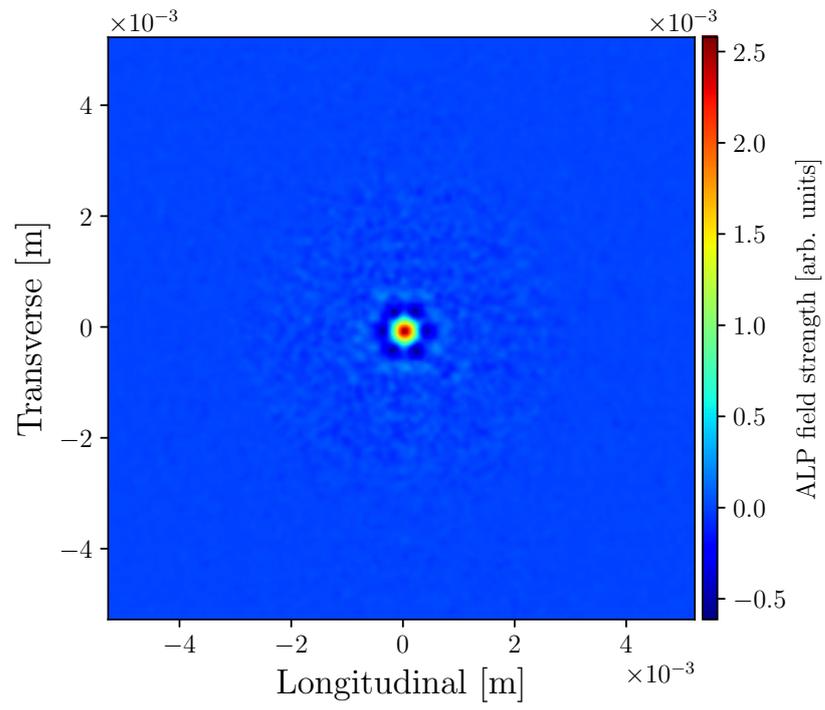
(a) $t = 0.00\,\text{ps}$
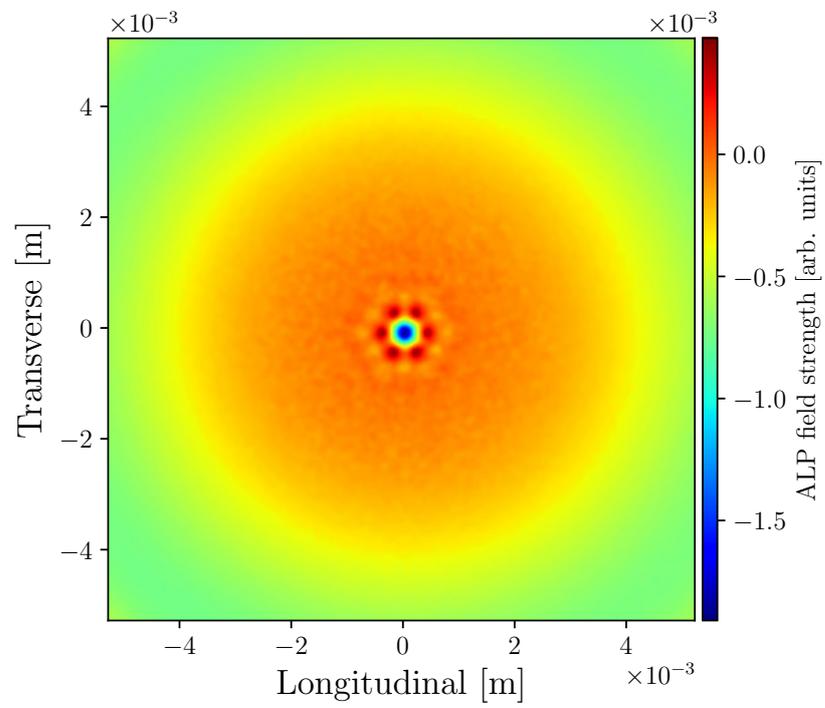
(b) $t = 275\,\text{ps}$
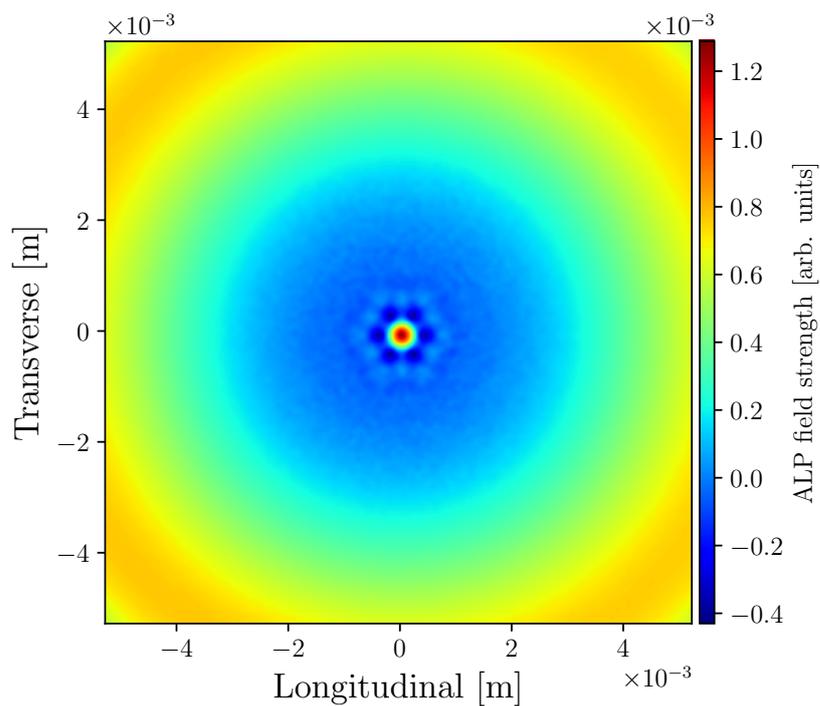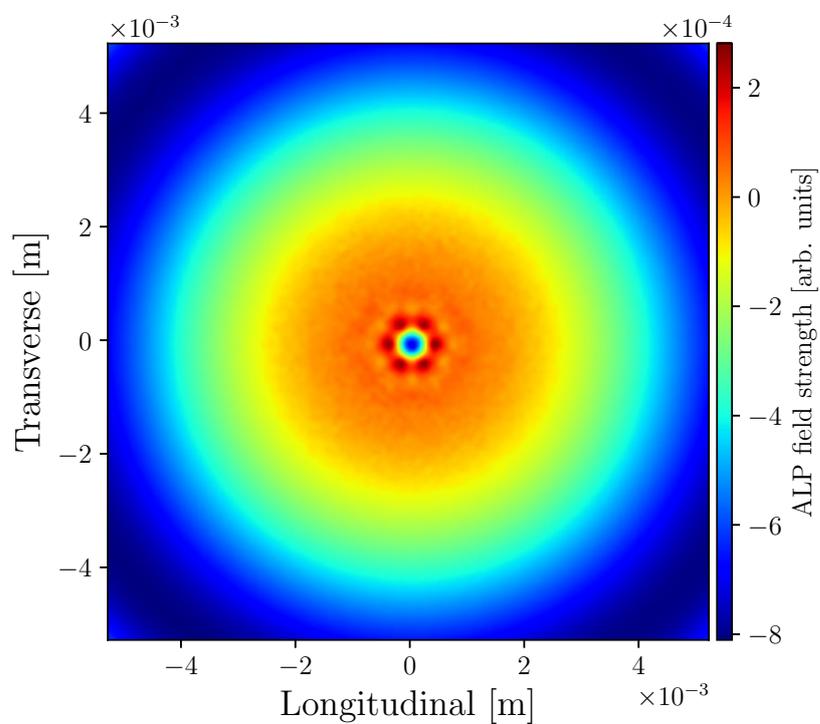
(c) $t = 550\,\mathrm{ps}$

(d) $t = 826\,\mathrm{ps}$

Figure 8.4: Axion-like particle fields of mass $m = 10^{-3.5}\,\mathrm{eV}$ at different time steps in photonic bandgap lattice.
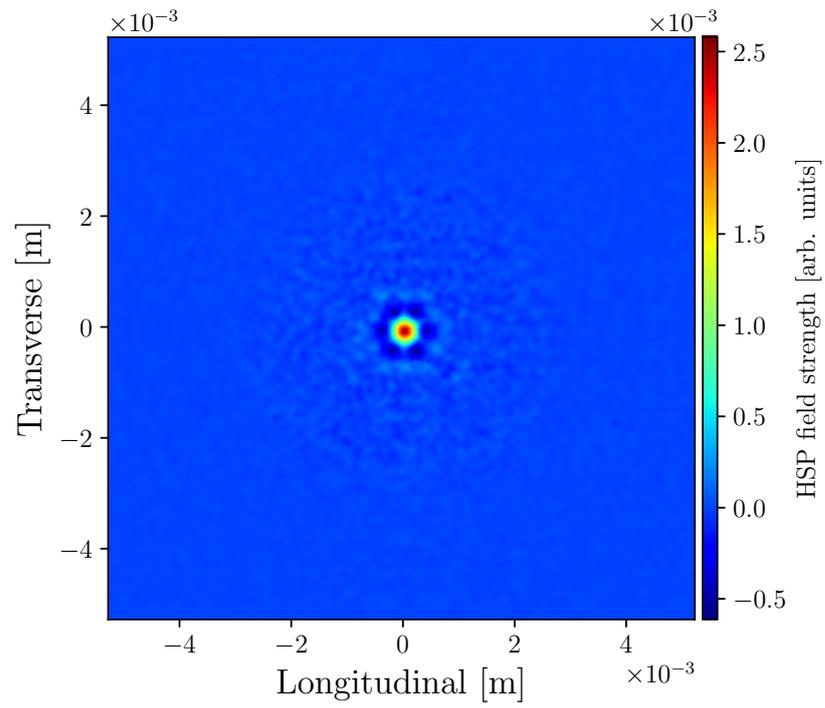
(a) $t = 0.00\,\mathrm{ps}$
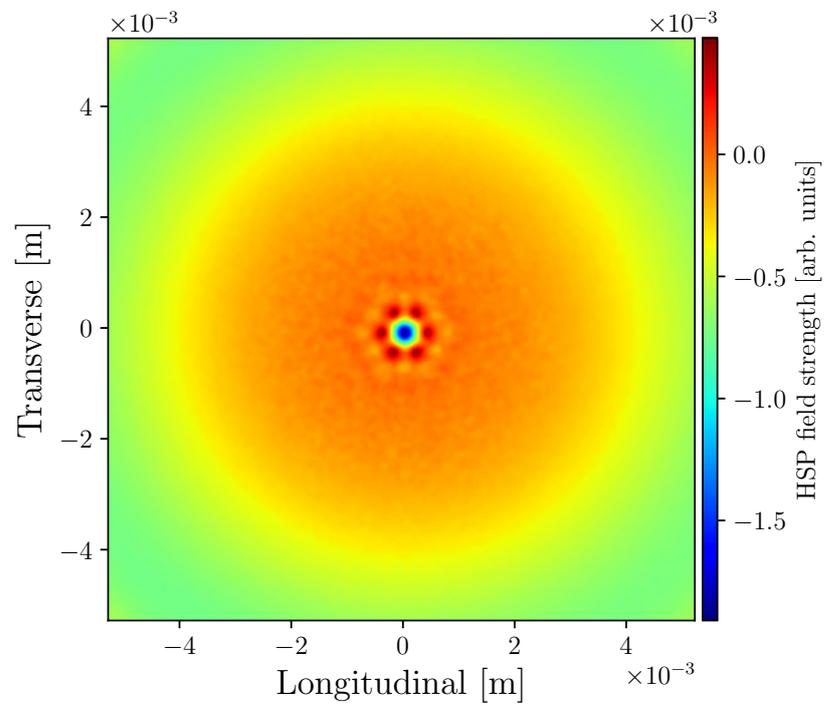
(b) $t = 275\,\mathrm{ps}$
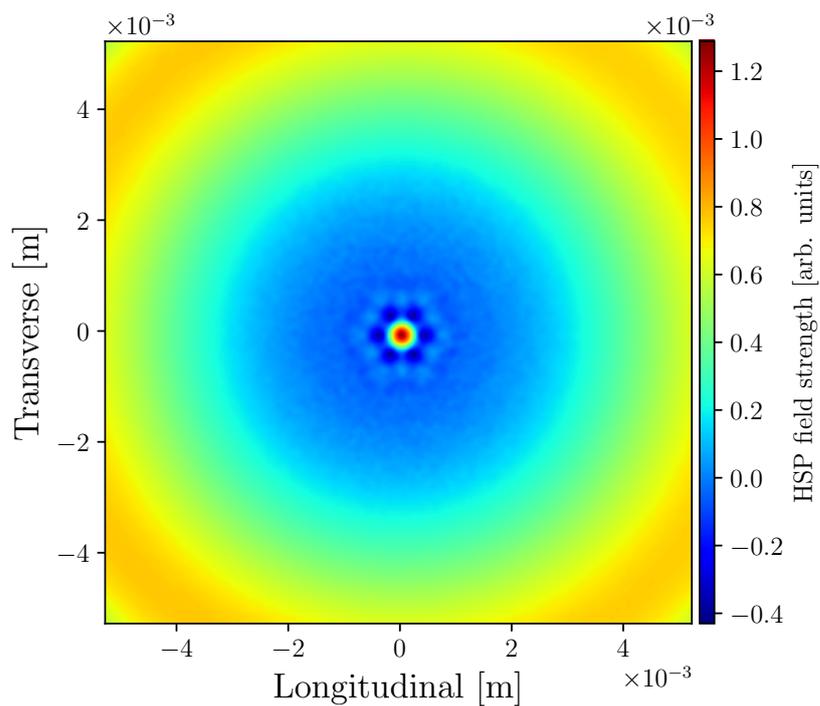
(c) $t = 550\,\text{ps}$
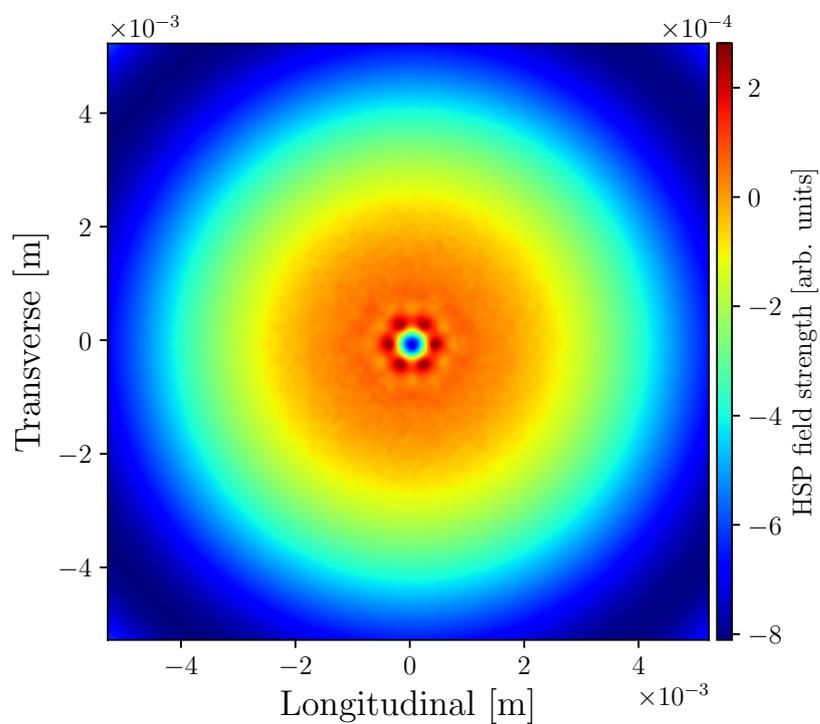
(d) $t = 826\,\text{ps}$

Figure 8.5: Dark photon fields of mass $m = 10^{-3.5}\,\text{eV}$ at different time steps in photonic bandgap lattice.

8.4.4   Results: Mass Spectrum Variations

As earlier mentioned, the distributions of the dark matter candidate fields are approximately the same across the mass spectra of interest. Whilst the analyses were conducted in two dimensions, these surface plots do not lend themselves useful to comparing multiple datasets. Instead, one-dimensional profile across the central axis provide clearer comparisons across mass spectra. Figure 8.6 demonstrates the field strengths across mass for ALPs while Figure 8.6 indicates those for HSPs.
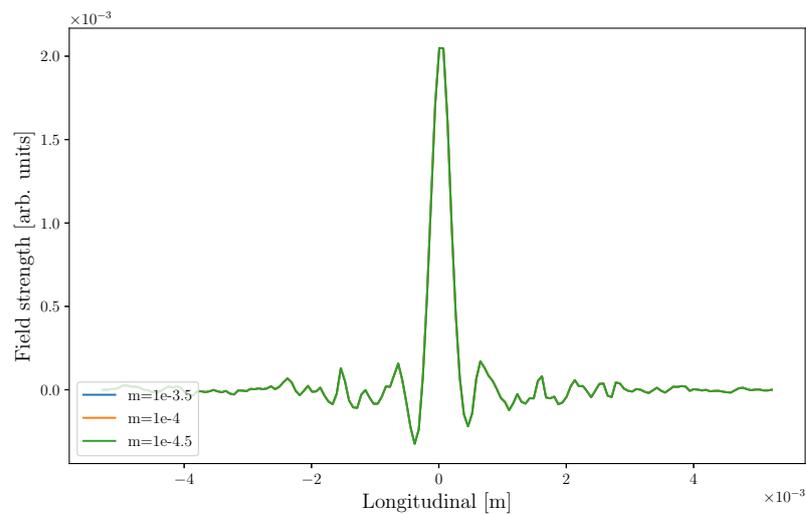
(a) $t = 0.00\,\mathrm{ps}$
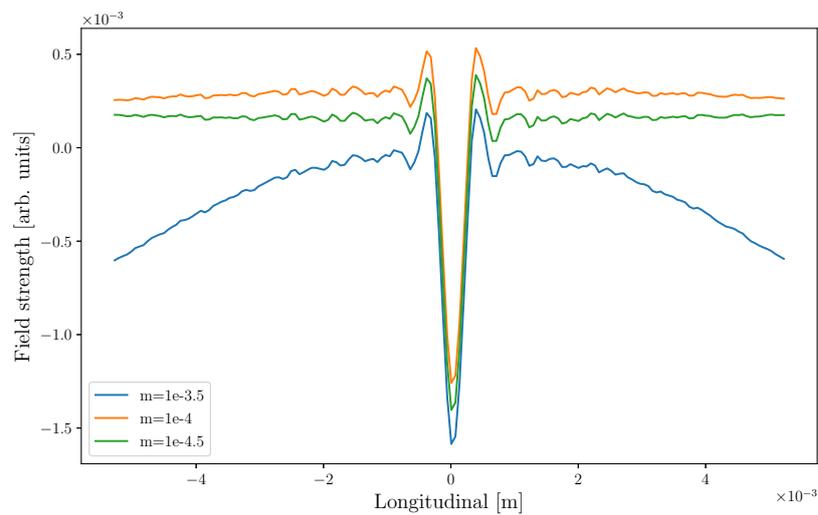
(b) $t = 275\,\mathrm{ps}$
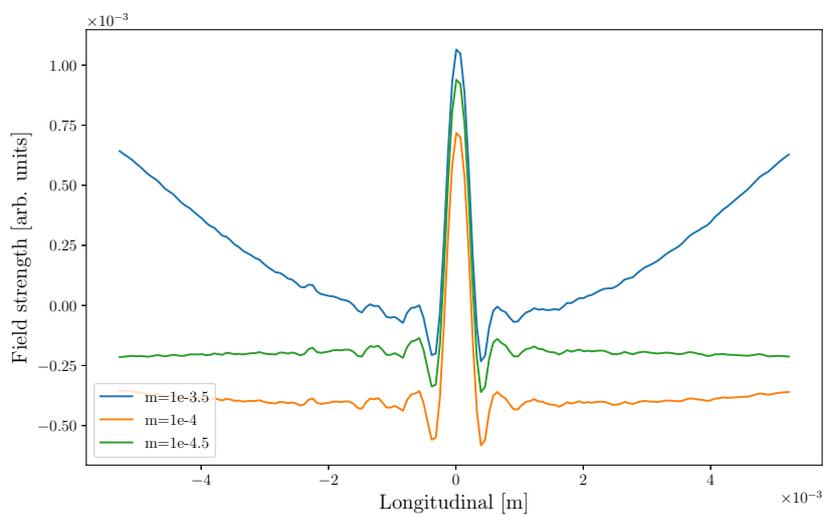
(c) $t = 550\,\mathrm{ps}$
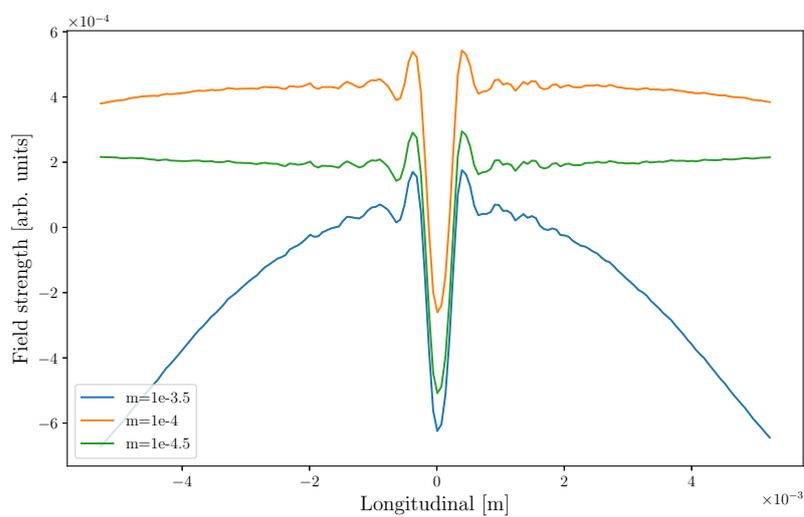
(d) $t = 826\,\mathrm{ps}$

Figure 8.6: Central lineout of axion-like particle fields at different time steps in photonic bandgap lattice.
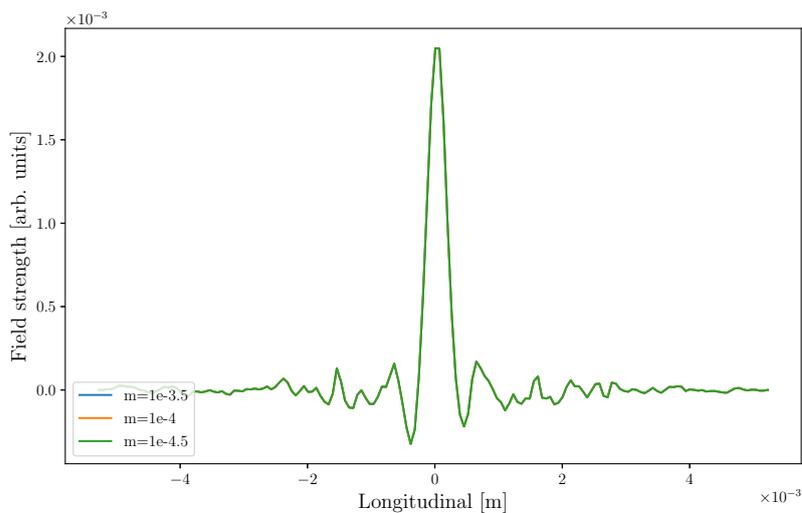
(a) $t = 0.00\,\text{ps}$
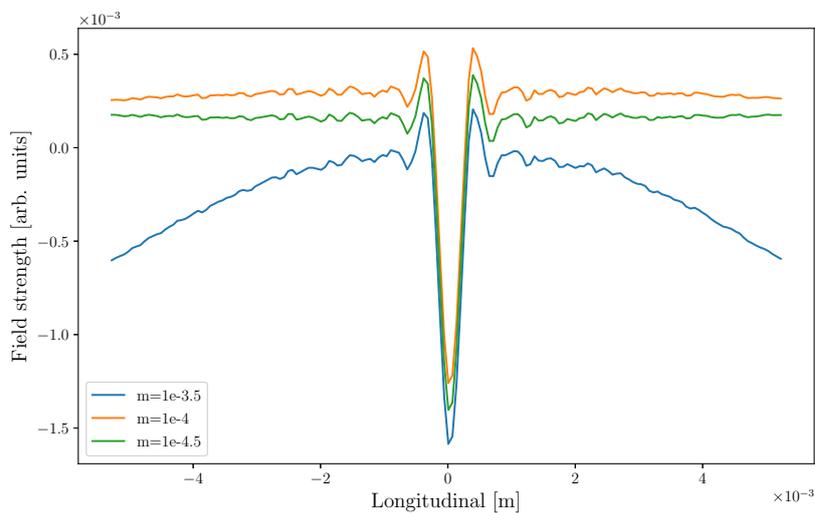
(b) $t = 275\,\text{ps}$

First and foremost, Figures 8.6 and 8.7 more clearly demonstrate the agreement between ALP and HSP fields when the magnetic field is unitary. This is an expected result Additionally, one sees that field behaviours are similar across the mass spectrum, albeit at different scales. The more massive fields exhibit more uniform distributions than those of lower mass fields.

8.4.5   Results: Field Saturation

The production of progressively stronger dark matter fields cannot continue ad infinitum. The taking of the limit of time to infinity from Equation (2.4) shows that a theoretical field strength plateau is inevitable. As such, it is of interest to investigate how rapidly
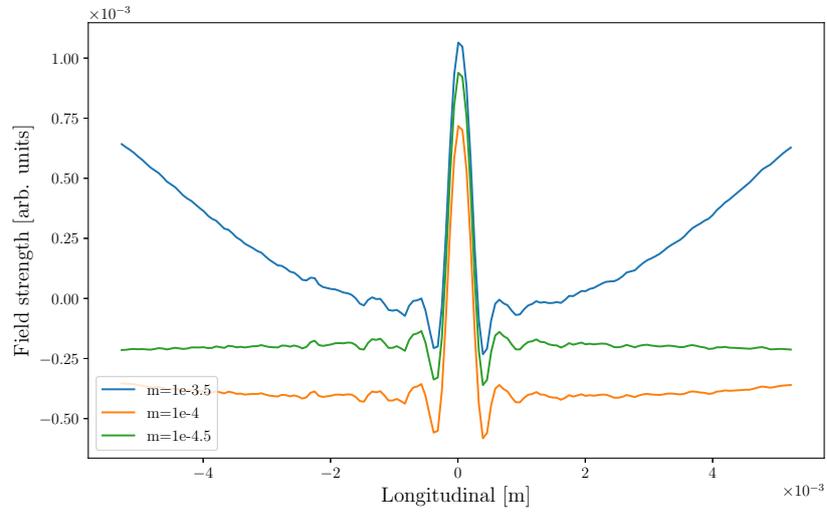
(c) $t = 550\,\mathrm{ps}$
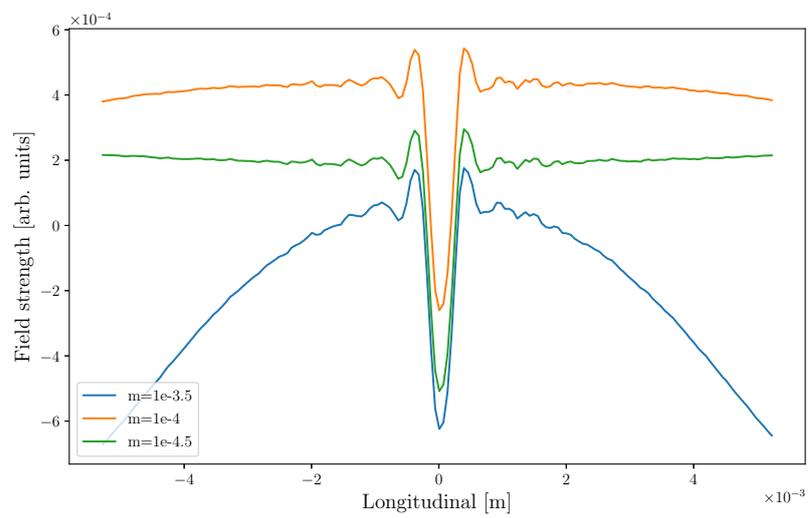
(d) $t = 826\,\mathrm{ps}$

Figure 8.7: Central lineout of dark photon fields at different time steps in photonic bandgap lattice.

the fields reach saturation. This is readily calculable in microwave cavity simulations owing to the static nature of the setup; for this reason it was not possible in the earlier LWFA analysis.

To evaluate the field saturation, **Run:DMC** was used to conduct numeric analysis following an initial period in which the electric field propagated throughout the lattice. The time evolution of the DMC field strength at a distance of ten lattice spacings from the electromagnetic source was then calculated. Due to technical limitations, it was not possible to obtain results at regular enough intervals to infer smooth trends, thus would require additional work before being used in application for experimental undertaking. With that noted, it was found that that all fields evolve in approximately the same manner, with oscillations occurring at a rate which scales weakly with their masses, i.e. smaller masses have a greater number of oscillations per unit time. Additionally, the investigation established that the fields saturated rapidly as no further growth was demonstrated. Consequently, one need only operate the microwave cavity for short durations in order to maximise the DMC fields prior to observation.

8.5   Further Work

Despite the success in calculating the DMC fields, there yet remains improvements to be made and further analyses to conduct.

The Green's function utilised by **Run:DMC** assumes a free space solution, devoid of interactions with ordinary matter. However, it has previously been shown that ALPs are produced at the interface between substances with significantly disparate dielectric properties, such as those found in this investigation [165]. As such, one would expect marginally greater quantites of ALPs. This behaviour is unlikely to be implemented into **Run:DMC** in the near future, and further investigations would benefit from this phenomenon being implemented in the simulation code itself.

Chapter 9

Conclusion

> *"No one can be a great thinker who does not recognise, that as a thinker it is his first duty to follow his intellect to whatever conclusions it may lead."*
>
> — John Stuart Mill, *On Liberty*

9.1 Overview

The purpose of this doctoral programme was the further exploration of two recently proposed experimental schemes of laboratory-based production and detection of dark matter candidates. Both approaches utilise electromagnetic radiation for production and light-shining-through-wall methodology for detection. These investigations have culminated in the development of a numeric analysis code, **Run:DMC**, the algorithmic components of which have been presented in this thesis.

The first proposed experimental scheme utilises a laser wake field accelerator situated within a powerful external magnetic field. Owing to their couplings to these electromagnetic fields, it was previously theorised that this arrangement would be ideal for the production of axion-like and dilaton-like particles. These particles were predicted to be produced with momentum co-parallel with the accelerator, thus allowing them to propagate after the plasma. Due to their weak couplings with ordinary matter, these axion-like particles and dilaton-like particles may then traverse an absorber medium, whereupon they may be stimulated to decay into detectable photons through the reverse Primakoff effect.

The second scheme proposed the usage of a microwave resonant cavity in applying

a localised electric field within a defect of a photonic band gap lattice. This dielectric lattice serves to approximately confine photons to a lattice defect, making detection of supernumerary electric fields at displacements of several characteristics lattice lengths indicative of dark photon intermediaries.

9.2   Axion-like particles and dilaton-like particles from laser wake field acceleration

Previous theoretical analysis had involved 1D analytic calculations of a laser wake field accelerator subjected to a strong external magnetic field. The results of this found that ALPs could be produced with energy flux densities comparable to those reaching Earth from the Sun, with greater values achievable for masses $m_a \lesssim 10^4\,\mathrm{eV\,c^{-2}}$, albeit only for the duration of the burst.

The further exploration of this scheme involved the simulation of a laser-driven plasma accelerator using the PIC code EPOCH and subsequent analysis using **Run:DMC**. The representative parameter values used were taken from existing facilities, including the Astra Gemini laser at the Central Laser Facility in Rutherford Appleton Laboratory. The parameters under consideration for these investigations were the magnetic field strength as well as the angle between the magnetic and wake fields.

The first noteworthy result of this investigation was the definitive exclusion of ALPs being produced in unmagnetised laser-driven plasmas. Whilst this outcome likely further extends to general unmagnetised plasmas, the author wishes to avoid making overgeneralisations. Additionally, it was found that the ALP field resulting from a magnetised plasma is proportional to the external magnetic field strength to which it is subjected. This is in line with theoretical expectations as the axionic minimal-coupling to electromagnetic fields is linear in both.

The second line of enquiry in this project investigated the dependence of the ALP fields upon the angle of the magnetic field relative to the wake. It was found that the field growth is maximal when the magnetic field is co-parallel with the direction of laser propagation in the plasma channel, in line with assumptions made in previous works. Whilst this was not unexpected, confirmation of such is an important milestone in the possible development of a laboratory-based search for these dark matter candidates. Additionally, it was uncertain how ALP fields would behave at non-co-parallel angles.

The earlier presented results indicate that non-longitudinal components are capable of producing ALP fields, however the field growth rate is severely limited when considering orthogonal fields.

9.3   Axion-like particles and dark photons from photonic band gap lattices

Previous works on this proposition have involved the simulation of the propagation of an electric field within a photonic band gap lattice. The conclusions of this work were that it was possible to effectively localise electric fields to regions of lattice defects. It was hypothesised that this localisation could be used to detect dark photons and axion-like particles via light-shining-through-wall methodology.

The analysis presented herein concluded that it is possible to produce dark matter candidate fields within a microwave cavity resonator. During initialisation these fields oscillate with the electric field source, however it was also possible to calculate the field saturation strength.

9.4   Final Thoughts and Further Development

The two experimental schemes investigated throughout this PhD programme proved theoretically promising as candidates for laboratory-based dark matter production. The results presented herein support earlier hypotheses as well as elucidating upon well-reasoned assumptions. Additionally, the same methodologies may also prove useful in the development of low energy particle physics, an area of research relatively untouched by particle accelerators. On a final note, the author draws readers' attentions to Chapter 6, in which it was found that resolution and numeric error almost always served to calculate values as being smaller than theoretical prediction. As such, the values presented in this thesis pertaining to dark matter fields should be taken to be smaller than those that be would physically manifest during experimental operation, albeit to within reasonable agreement.

As mentioned in Chapter 6, the author intends to publish **Run:DMC** as a free and open source software under a copyleft licence. Prior to public release, there are adjustments and additions to be made to the codebase. Such additions include the capacity to parallelise analyses across multiple nodes, which will likely be achieved through the

inclusion of MPI (Message Passing Interface). This addition would allow the utilisation of greater computational resources within a given runtime, which would in turn provide more accurate results. Additionally, the author intends to generalise the means by which one uses **Run:DMC** to calculate fields corresponding with input data. Through so doing, it is the author's goal to provide users the capability of also calculating directly observable fields resulting from DMC decay, e.g. $a \rightarrow \gamma\gamma$.

Further works on the projects investigated through this thesis are possible. A rigorous quantum field theory treatment of dark matter candidate production would provide more accurate theoretical predictions of an idealised system to which simulations could be compared; this would not be limited to either experimental proposal. Additionally, one may wish to investigate related experimental schemes such as particle-driven plasma wake field acceleration, which offer significantly longer acceleration lengths and hence longer durations of dark matter field growth.

It is the author's hope that as a result of the research presented within this thesis the wider scientific community is encouraged to further pursue investigations into methods of laboratory-based dark matter production and detection.

Appendix A

Dirac and Kronecker Deltas

Whereas Dirac deltas are used in continuous systems, its discrete counterpart, the Kronecker delta, is required for numeric calculations. One must thus be able to interchange them in order to translate between continuous analytic expressions and discrete numeric calculations.

The Dirac delta $\delta(x)$ is a distribution which is mathematically defined on a topological space X as satisfying

$$\int_X f(x)\,\delta(x-y)\;\mathrm{d}x = \begin{cases} f(y) & y \in X \\ 0 & y \notin X. \end{cases} \tag{A.1}$$

Conversely, the Kronecker delta δ_{ij} is a function which takes the value 1 when its indices are equal and 0 when they are not, i.e.

$$\sum_{x_i \in X} f(x_i)\,\delta_{ij} = \begin{cases} f(x_j) & x_j \in X \\ 0 & x_j \notin X. \end{cases} \tag{A.2}$$

Consequently, the Kronecker delta acts similarly to the Dirac delta, in that when multiplied by a test function and integrated over, the result is the test function at a specific point. However, translating between them is not a simple matter of notation.

Heuristically, the following relations hold:

Directly substituting components for their discrete counterparts, Equation (A.1) reads

$$\sum_{x_i \in X} f(x_i)\,\delta(x_i - x_j)\,\Delta x_i = \begin{cases} f(x_j) & x_j \in X \\ 0 & x_j \notin X. \end{cases}$$

	Continuous		**Discrete**
Coordinates	x	$\mapsto$	x_i
	y	$\mapsto$	x_j
Element	$\mathrm{d}x$	$\mapsto$	Δx_i
Domain	$\int_X$	$\mapsto$	$\sum_{x_i \in X}$

However, in order for this to exactly duplicate Equation (A.2), one thus derives the relation between the Dirac and Kronecker deltas to be

$$\delta\left(x_i - x_j\right) = \frac{\delta_{ij}}{\Delta x_i}.$$

Additional support is lent to this relationship when performing dimensional analysis on the two deltas;

$$\left[\delta_{ij}\right] = 1$$
$$\left[\delta\left(x - y\right)\right] = x^{-1},$$

as well as the limit to continuum:

$$\lim_{\Delta x_i \to 0} \frac{\delta_{ij}}{\Delta x_i} = \begin{cases} \infty & x_i = x_j \\ 0 & \text{otherwise} \end{cases} = \delta\left(x_i - x_j\right) = \delta\left(x - y\right)$$

Appendix B

Justifying $\partial_\mu A^\mu = 0$ in the Proca Equation

Consider the Lagrangian of a massive vector boson given by

$$\mathscr{L} = -\frac{1}{4}F_{\mu\nu}F^{\mu\nu} + \frac{1}{2}m^2 A_\nu A^\nu - A_\nu j^\nu, \qquad (B.1)$$

where A^ν is the electromagnetic four-potential and $F^{\mu\nu}$ is the electromagnetic field tensor which is defined by $F^{\mu\nu} := \partial^\mu A^\nu - \partial^\nu A^\mu$. The Euler-Lagrange equation of motion of this is

$$\Box A^\nu - \partial^\nu\left(\partial_\mu A^\mu\right) + m^2 A^\nu = j^\nu,$$

which is the eponymous *Proca equation*. It can be seen that this cancels down to the inhomogeneous Klein-Gordon equation if $\partial_\mu A^\mu = 0$, which is the generalised Lorenz gauge condition. It is in justifying this condition that motivates this appendix.

Consider the Maxwellian action on a manifold M:

$$\mathscr{S}[A] = \int_M -\frac{1}{4}F_{\mu\nu}F^{\mu\nu} - j_\mu A^\mu \, \mathrm{d}^4 x. \qquad (B.2)$$

For the action to be considered gauge invariant, it must not change under a gauge transformation $A^\mu \mapsto A'^\mu = A^\mu + \partial^\mu f$, where f is an arbitrary function, i.e. $\mathscr{S}[A] \overset{!}{=} \mathscr{S}[A']$. Since ∂^μ and ∂^ν act upon the same coordinate system, the electromagnetic tensor terms can be shown to be gauge invariant:

$$F'^{\mu\nu} = \partial^\mu A'^\nu - \partial^\nu A'^\mu$$

$$= \partial^\mu A^\nu - \partial^\nu A^\mu + \underbrace{\partial^\mu\partial^\nu f - \partial^\nu\partial^\mu f}_{\text{cancel}}$$

$$\equiv F^{\mu\nu}.$$

By expanding the second term of the integrand in Equation (B.2) following gauge transformation, one sees that the action is gauge invariant up to a term, i.e. $\mathcal{S}\left[A'\right] = \mathcal{S}\left[A\right] + \delta\mathcal{S}$, where

$$\delta\mathcal{S} = -\int_M j_\mu \partial^\mu f \, \mathrm{d}^4 x.$$

By Stokes' theorem;

$$\int_M j_\mu \partial^\mu f \, \mathrm{d}^4 x = \int_{\partial M} \hat{n}^\mu j_\mu f \, \mathrm{d}S - \int_M \partial^\mu j_\mu f \, \mathrm{d}^4 x,$$

where ∂M denotes the boundary beyond which the action variation integrand takes a value of zero and $\hat{n}^\mu$ is the four-vector of unit norms for the boundary. Assuming that $\delta\mathcal{S}$ has compact support, i.e. is bounded and has closure, then by definition the surface terms are zero and hence

$$\delta\mathcal{S} = \int_M \partial^\mu j_\mu f \, \mathrm{d}^4 x \overset{!}{=} 0.$$

For this to hold for all functions f, one deduces that $\partial^\mu j_\mu = 0$. This is a sensible conclusion since it takes a physical interpretation of conserving four-current on a universal scale.

Taking the derivative ∂_ν of Equation (B.1) and cancelling the first two terms, one is left with

$$m^2 \partial_\nu A^\nu = \partial_\nu j^\nu.$$

Therefore, by building a theory in which four-current is universally conserved, as found in Maxwell's equations, then when $m \neq 0$ one derives

$$\partial_\nu A^\nu = 0,$$

which may be called a generalised Lorenz gauge condition. Consequently, the Proca equation becomes

$$\Box A^\nu + m^2 A^\nu = j^\nu,$$

i.e. in theories that conserve four-current the Proca equation is equivalent to four simultaneous Klein-Gordon equations.

Appendix C

Solving the Driven Simple Harmonic Oscillator Equation

The equation for a driven undamped simple harmonic oscillator is written

$$\ddot{u} + \omega^2 u = f,$$

where $u = u(t)$ is the solution, ω is the angular frequency and $f = f(t)$ is the source. Since the left side of this equation can be written as a linear operator acting on the solution, one sees that it is possible to obtain the solution using the method of Green's functions, i.e.

$$u(t) = \int G(t, t') f(t') \, \mathrm{d}t' \tag{C.1}$$

for a Green's function G which satisfies

$$\left[\partial_t^2 + \omega^2 \right] G(t, t') = \delta(t - t'). \tag{C.2}$$

Since $G(t, t')$ is defined across the entire domain of $t \in (-\infty, \infty)$, it may be written as the sum of contributions over separate subdomains;

$$G(t, t') = \Theta(t - t') G_>(t, t') + \Theta(t' - t) G_<(t, t') + \delta(t - t') G_=(t, t'), \tag{C.3}$$

where the subscript (in)equalities indicate the relations of t to t', i.e. $G_>$ is the value that G takes for $t > t'$. In this form, it becomes apparent that G undergoes simple harmonic motion on either side of the delta, i.e. $\left[\partial_t^2 + \omega^2 \right] G_{\gtrless}(t, t') = 0$, the general solution to which is $G_{\gtrless}(t, t') = a_{\gtrless}(t') \sin(\omega t) + b_{\gtrless}(t') \cos(\omega t)$. For notational brevity, henceforth in this appendix the argumental parentheses will be dropped, unless their inclusions improve clarity.

Choosing a smooth test function with compact support $g(t)$, then

$$\int_{-\infty}^{\infty} g\ddot{G}\,\mathrm{d}t = \int_{-\infty}^{\infty} \ddot{g}G\,\mathrm{d}t$$

with additional boundary terms which disappear by construction. Consequently, multiplying Equation (C.2) by the test function and integrating over all t gives

$$\int_{-\infty}^{\infty} \left(\ddot{g} + \omega^2 g\right) G\,\mathrm{d}t = g\left(t'\right), \tag{C.4}$$

thus by substituting Equation (C.3) into Equation (C.4) one receives

$$\int_{t'}^{\infty} \left(\ddot{g} + \omega^2 g\right) G_> \,\mathrm{d}t + \int_{-\infty}^{t'} \left(\ddot{g} + \omega^2 g\right) G_< \,\mathrm{d}t + \left.\left(\ddot{g} + \omega^2 g\right) G_=\right|_{t=t'} = g\left(t'\right).$$

Evaluating the above integrals by parts, using the earlier noted fact of simple harmonic motion in $G_{\gtrless}$, and discarding terms within the limits $t \to \pm\infty$ owing to g's compact support, then Equation (C.4) becomes

$$-\dot{g}\left(G_> - G_<\right)\big|_{t=t'} - g\partial_t\left(G_> - G_<\right)\big|_{t=t'} + \left.\left(\ddot{g} + \omega^2 g\right) G_=\right|_{t=t'} = g\left(t'\right).$$

Since g is an arbitrary smooth function, the above must hold $\forall g$. Furthermore, whatever value t' takes, there is always a function that can meet any set of values at each derivative. Therefore, each order of derivative can be treated as being linearly independent, hence by equating coefficients of $\ddot{g}$ one obtains that $G_= = 0 \;\forall g$, leaving $\dot{g}$ and g to give a set of two junction conditions;

$$\begin{cases} \left(G_> - G_<\right)\big|_{t=t'} = 0, \\ \partial_t\left(G_> - G_<\right)\big|_{t=t'} = 1, \end{cases}$$

the first of which indicates continuity of G across the delta.

Imposing the condition that the solution is zero prior to any non-zero source, i.e. $u(t) = 0$ if $f\left(t'\right) = 0 \;\forall t < t'$, then $G_<\left(t, t'\right) = 0$ and hence $a_< = b_< = 0$ since $\sin\left(\omega t\right)$ and $\cos\left(\omega t\right)$ are linearly independent. This gives a new set of junction conditions with two underlying unknowns, $a_>$ and $b_>$;

$$\begin{cases} G_>\big|_{t=t'} = 0, & \text{(C.6a)} \\ \partial_t G_>\big|_{t=t'} = 1. & \text{(C.6b)} \end{cases}$$

Substituting the general simple harmonic solution into Equations (C.6a) and (C.6b) gives a system of linear equations which can be written

$$\begin{pmatrix} \sin\left(\omega t'\right) & \cos\left(\omega t'\right) \\ \omega\cos\left(\omega t'\right) & -\omega\sin\left(\omega t'\right) \end{pmatrix} \begin{pmatrix} a_>\left(t'\right) \\ b_>\left(t'\right) \end{pmatrix} = \begin{pmatrix} 0 \\ 1 \end{pmatrix}.$$

Inverting the preceding matrix gives the parameters as

$$\begin{pmatrix} a_> \left(t'\right) \\ b_> \left(t'\right) \end{pmatrix} = \frac{1}{\omega} \begin{pmatrix} \cos\left(\omega t'\right) \\ -\sin\left(\omega t'\right) \end{pmatrix},$$

thus by substitution into the solution for $G_>$, one obtains

$$G_> \left(t, t'\right) = \frac{1}{\omega} \sin\left(\omega\left(t - t'\right)\right),$$

where the trigonometric identity $\sin\left(\alpha \pm \beta\right) = \sin\left(\alpha\right)\cos\left(\beta\right) \pm \cos\left(\alpha\right)\sin\left(\beta\right)$ has been used to eliminate cosine terms. Finally, the solution u from Equation (C.1) is calculated to be

$$\begin{aligned} u\left(t\right) &= \int_{-\infty}^{\infty} G\left(t, t'\right) f\left(t'\right) \, \mathrm{d}t' \\ &= \int_{-\infty}^{t} \frac{1}{\omega} \sin\left(\omega\left(t - t'\right)\right) f\left(t'\right) \, \mathrm{d}t'. \end{aligned}$$

Appendix D

EPOCH Input Deck

The following is the EPOCH input deck used for simulating a plasma of peak density $1 \times 10^{24}\,\mathrm{m}^{-3}$, length $1\,\mathrm{mm}$, up- and down-ramp lengths $100\,\mathrm{\mu m}$ which is driven by a bi-Gaussian $800\,\mathrm{nm}$ laser pulse with $a_0 = 3$. For readability, long lines have been automatically broken at text width, however they are not split within the input deck itself.

```
begin:constant
    # General constants
    amu = 1836.15   # atomic mass units [electron masses]


    # Plasma parameters
    dens = 1e24 # [m^-3]
    plasma_length = 0.001
    ramp_length = 0.0001
    plasma_start = 0.0
    plasma_end = plasma_start + plasma_length
    plasma1 = plasma_start + ramp_length     # end of up-ramp
    plasma2 = plasma_end - ramp_length       # beginning of
        down-ramp
    plasma_density3 = if((x gt plasma2) and (x lt plasma_end
        ), dens * abs((plasma_end-x)/(plasma_end-plasma2)),
        0.0)
    plasma_density2 = if((x gt plasma1) and (x lt plasma2),
        dens, plasma_density3)
```

```
    plasma_density = if((x gt plasma_start) and (x lt
       plasma1), dens * abs((x - plasma_start)/(plasma1 -
       plasma_start)), plasma_density2)
    omega_p = sqrt((dens * qe^2) / (me * epsilon0))
    lambda_p = 2*pi*c / omega_p
    period_p = 2*pi / omega_p


    # Laser parameters
    wavelength = 800 * nano # [m]
    a0 = 3
    intens = 1.368e6 * (a0/wavelength)^2
    laser_omega = 2.0*pi*c/wavelength
    laser_vg = c * sqrt(1-(omega_p/laser_omega)^2)
    duration = period_p / 4


    # duration is FWHM, need to choose a time for the
       profile to peak at.
    # If centre the gaussian at t = 0, then you miss the
       rising ramp.
    laser_t_peak = 1.5*duration


    x_length = 3*lambda_p # full length (x-direction)
    yh = 40*micron # half width (y-direction)


    delta_x = wavelength/20
    delta_y = delta_x*pi*exp(1)
end:constant


begin:control
    # Global number of gridpoints
    nx = nint(x_length/delta_x)
    ny = nint(2*yh/delta_y)


    # Simulation duration [s]
```

```
    t_end = 2 * plasma_length / c


    # Size of domain (window) [m]

    x_min = 0

    x_max = x_length

    y_min = -yh

    y_max = yh


    dlb_threshold = 0.6

    stdout_frequency = 100


    smooth_currents = T

    maxwell_solver = cowan
end:control


begin:boundaries

    bc_x_min = simple_laser

    bc_x_max = simple_outflow

    bc_y_min = simple_outflow

    bc_y_max = simple_outflow
end:boundaries


begin:laser

    boundary = x_min

    intensity_w_cm2 = intens

    lambda = wavelength


    # Laser profiles

    t_profile = gauss(time, laser_t_peak, duration)

    profile = gauss(y, 0, 0.5*lambda_p)
end:laser


begin:fields

    bx = 0.0
```

```
end:fields


begin:window
    move_window = T
    # wait for leading edge of the laser (not the peak) to
        get 90% through box
    window_start_time = 0.9 * x_length / c
    window_v_x = laser_vg
    bc_x_min_after_move = simple_outflow
    bc_x_max_after_move = simple_outflow
end:window


begin:output
    # Time between file outputs
    dt_snapshot = delta_x / c


    # Grid variables
    grid = always


    # Properties on grid
    ex = always
    ey = always
    bx = always
    by = always
end:output


begin:species
    name = Electron
    charge = -1
    mass = 1.
    npart_per_cell = 16.
    density = plasma_density
end:species
```

Bibliography

[1] J. C. Kapteyn. First Attempt at a Theory of the Arrangement and Motion of the Sidereal System. *ApJ*, **55**:302, May 1922.

[2] Particle Data Group. Review of Particle Physics. *Phys. Rev. D*, **98**(030001), August 2018.

[3] J. Einasto. Dark Matter. *BALT ASTRON.*, **20**(2):231–240, September 2011.

[4] G. Bertone and D. Hooper. History of dark matter. *Rev. Mod. Phys.*, **90**(4):045002, October 2018.

[5] F. Zwicky. Die Rotverschiebung von extragalaktischen Nebeln. *Helv. Phys. Acta*, **6**:110–127, 1933.

[6] John Johnson Jr. *Zwicky: The Outcast Genius Who Unmasked the Universe.* Harvard University Press, 2019.

[7] NASA/IPAC Extragalactic Database (NED). NED results for object Bullet Cluster. https://ned.ipac.caltech.edu/cgi-bin/nph-objsearch?objname=Bullet+Cluster. Accessed: 2020-03-11.

[8] W. Tucker, P. Blanco, S. Rappoport, L. David, D. Fabricant, E. E. Falco, W. Forman, A. Dressler, and M. Ramella. 1E 0657-56: A Contender for the Hottest Known Cluster of Galaxies. *ApJL*, **496**:L5–L8, March 1998.

[9] M. Markevitch et al. A Textbook Example of a Bow Shock in the Merging Galaxy Cluster 1E 0657-56. *ApJL*, **567**:L27–L31, March 2002.

[10] D. Clowe, A. H. Gonzalez, and M. Markevitch. Weak-Lensing Reconstruction of the Interacting Cluster 1E 0657-558: Direct Evidence for the Existence of Dark Matter. *ApJ*, **604**(2):596–603, April 2004.

[11] M. Markevitch et al. Direct Constraints on the Dark Matter Self-Interaction Cross Section from the Merging Galaxy Cluster 1E 0657-56. *ApJ*, **606**:819–824, May 2004.

[12] D. Clowe, M. Bradač, A. H. Gonzalez, M. Markevitch, S. W. Randall, C. Jones, and D. Zaritsky. A Direct Empirical Proof of the Existence of Dark Matter. *ApJL*, **648**:L109–L113, September 2006.

[13] M. Bradač, S. W. Allen, T. Treu, H. Ebeling, R. Massey, R. G. Morris, A. von der Linden, and D. Applegate. Revealing the Properties of Dark Matter in the Merging Cluster MACS J0025.4-1222. *ApJ*, **687**:959–967, November 2008.

[14] Horace W. Babcock. The rotation of the Andromeda Nebula. *Lick Obs. Bull.*, **498**:41–51, January 1939.

[15] V. C. Rubin and W. K. Ford Jr. Rotation of the Andromeda nebula from a spectroscopic survey of emission regions. *ApJ*, **159**, February 1970.

[16] V. C. Rubin, W. K. Ford Jr., and N. Thonnard. Rotational properties of 21 Sc galaxies with a large range of luminosities and radii from NGC 4605 ($R = 4\,\text{kpc}$) to UGC 2885 ($R = 122\,\text{kpc}$). *ApJ*, **238**:471–490, June 1980.

[17] K. C. Freeman. In the disks of spirals and S0 galaxies. *ApJ*, **160**, June 1970.

[18] T. S. van Albada, J. N. Bahcall, K. Begeman, and R. Sanscisi. Distribution of Dark Matter in the Spiral Galaxy NGC 3198. *ApJ*, **295**:305–313, August 1985.

[19] S. Danieli, P. van Dokkum, C. Conroy, R. Abraham, and A. J. Romanowsky. Still Missing Dark Matter: KCWI High-resolution Stellar Kinematics of NGC1052-DF2. *ApJ*, **874**(2):L12, March 2019.

[20] WMAP Timeline. https://map.gsfc.nasa.gov/news/events.html. Accessed: 2019-12-23.

[21] C. L. Bennett et al. Nine-year Wilkinson Microwave Anisotropy Probe (WMAP) Observations: Final Maps and Results. *ApJ Supp.*, **208**(2), September 2013.

[22] Discovery Science. First Second of the Big Bang. How The Universe Works 3, 2014.

[23] G. Lüders. ON THE EQUIVALENCE OF INVARIANCE UNDER TIME RE-VERSAL AND UNDER PARTICLE-ANTIPARTICLE CONJUGATION FOR RELATIVISTIC FIELD THEORIES. *Dan. Mat. Fys. Medd.*, **28**(5), 1954.

[24] W. Pauli. *Niels Bohr and the Development of Physics.* Pergamon Press, 1955.

[25] R. Jost. Eine Bemerkung zum CTP-Theorem. *Helv. Phys. Acta*, **30**:409–416, 1957.

[26] Jost R. *Theoretical physics in the twentieth century: a memorial volume to Wolfgang Pauli.* New York: Interscience Publishers, 1960.

[27] C. Abel et al. Measurement of the Permanent Electric Dipole Moment of the Neutron. *Phys. Rev. Lett.*, **124**:081803, February 2020.

[28] R. D. Peccei and H. R. Quinn. CP Conservation in the Presence of Pseudoparticles. *Phys. Rev. Lett.*, **38**(25):1440–1443, March 1977.

[29] R. D. Peccei and H. R. Quinn. Constraints imposed by CP conservation in the presence of pseudoparticles. *Phys. Rev. D*, **16**(6):1791–1797, September 1977.

[30] S. Weinberg. A New Light Boson? *Phys. Rev. Lett.*, **40**(4):223–226, January 1978.

[31] F. Wilczek. Problem of Strong P and T Invariance in the Presence of Instantons. *Phys. Rev. Lett.*, **40**(5):279–282, January 1978.

[32] F. A. Wilczek. Asymptotic Freedom: From Paradox to Paradigm. https://www.nobelprize.org/uploads/2018/06/wilczek-lecture.pdf, December 2004. Nobel Lecture at Aula Magna, Stockholm University. Transcript accessible at https://www.nobelprize.org/uploads/2018/06/wilczek-lecture.pdf.

[33] J. Kandaswamy, P. Salomonson, and J. Schechter. Does the Decay Mode $K^+ \to \pi^+ +$ axion Already Rule Out the Axion? *Phys. Lett.*, **74B**(4,5):377–380, April 1978.

[34] F. P. Calaprice, R. W. Dunford, R. T. Kouzes, M. Miller, A. Hallin, M. Schneider, and D. Schreiber. Search for axion emission in the decay of excited states of ^{12}C. *Phys. Rev. D*, **20**(11):2708–2713, December 1979.

[35] P. F. Jacques, M. Kalelkar, Miller P. A., R. J. Plano, P. Stamer, E. B. Brucker, E. L. Koller, S. Taylor, C. Baltay, H. French, M. Hibbs, R. Hylton, K. Shastri, and A. Vogel. Search for prompt neutrinos and penetrating neutral particles in

a beam-dump experiment at Brookhaven National Laboratory. *Phys. Rev. D*, **21**(5):1206–1208, March 1980.

[36] A. Barroso and N. Mukhopadhyay. Nuclear axion decay. *Phys. Rev. C*, **24**(5):2382–2385, November 1981.

[37] C. Edwards et al. Upper Limit for $J/\psi \rightarrow \gamma +$Axion. *Phys. Rev. Lett.*, **48**(14):903–906, April 1982.

[38] J. E. Kim. Weak-Interaction Singlet and Strong CP Invariance. *Phys. Rev. Lett.*, **43**(2):103–107, July 1979.

[39] M. A. Shifman, A. I. Vainshtein, and V. I. Zakharov. Can confinement ensure natural CP invariance of strong interactions? *Nucl. Phys. B*, **166**:493–506, April 1980.

[40] A. R. Zhitnitsky. On Possible Suppression of the Axion Hadron Interactions (In Russian). *Sov. J. Nucl. Phys.*, **31**:260, 1980.

[41] M. Dine, W. Fischler, and M. Srednicki. A Simple Solution to the Strong CP Problem with a Harmless Axion. *Phys. Lett.*, **104B**(3):199–202, August 1981.

[42] P.A. Zyla et al. Review of Particle Physics. *PTEP*, 2020(8):083C01, 2020.

[43] J. Preskill, M. B. Wise, and F. Wilczek. Cosmology of the Invisible Axion. *Phys. Lett.*, **120B**(1, 2, 3):127–132, January 1983.

[44] J. Ipser and P. Sikivie. Can Galactic Halos Be Made of Axions? *Phys. Rev. Lett.*, **50**(12):925–927, March 1983.

[45] M. S. Turner. Windows in the axion. *Phys. Rep.*, **197**:67–97, December 1990.

[46] L. D. Duffy and K. van Bibber. Axions as dark matter particles. *New Journal of Physics*, **11**(105008), October 2009.

[47] P. Sikivie. Experimental Tests of the "Invisible" Axion. *Phys. Rev. Lett.*, **51**(16):1415–1417, October 1983.

[48] C. Hagmann, D. Kinion, W. Stoeffl, K. van Bibber, E. Daw, J. McBride, H. Peng, L. J. Rosenberg, H. Xin, J. Laveigne, P. Sikivie, N. S. Sullivan, D. B. Tanner, D. Moltz, F. Nezrick, M. S. Turner, N. Golubev, and L. Kravchuk. First results from a second generation galactic axion experiment. *Nucl. Phys. Proc. Suppl. B*, **51**(2):209–212, November 1996.

[49] ADMX announces breakthrough in axion dark matter detection technology. https://news.fnal.gov/2018/04/admx-announces-breakthrough-in-axion-dark-matter-detection-technology/. Accessed: 2020-03-08.

[50] K. Zioutas et al. First Results from the CERN Axion Solar Telescope. *Phys. Rev. Lett.*, **94**:121301, April 2005.

[51] S. Andriamonje et al. An improved limit on the axion–photon coupling from the CAST experiment. *JCAP*, **2007**(04):010, April 2007.

[52] CAST Collaboration. New CAST limit on the axion-photon interaction. *Nat. Phys.*, **13**:584–590, May 2017.

[53] G. Cantatore, F. Della Valle, E. Milotti, L. Dabrowski, and C. Rizzo. Proposed measurement of the vacuum birefringence induced by a magnetic field on high energy photons. *Phys. Lett. B*, **265**:418–424, August 1991.

[54] E. Zavattini et al. Experimental Observation of Optical Rotation Generated in Vacuum by a Magnetic Field. *Phys. Rev. Lett.*, **96**(11):110406, March 2006.

[55] E. Zavattini et al. New PVLAS results and limits on magnetically induced optical rotation and ellipticity in vacuum. *Phys. Rev. D*, **77**:032006, February 2008.

[56] B. Bellazzini, C. Csáki, J. Hubisz, J. Serra, and J Terning. A higgs-like dilaton. *Eur. Phys. J C*, **73**:2333, February 2013.

[57] A. Efrati, E. Kuflik, S. Nussinov, Y. Soreq, and T. Volansky. Constraining the Higgs-dilaton with LHC and dark matter searches. *Phys. Rev. D*, **91**:055034, March 2015.

[58] A. Arvanitaki, J. Huang, and K. V. Tilburg. Searching for dilaton dark matter with atomic clocks. *Phys. Rev. D*, **91**:015015, January 2015.

[59] L. di Lella and C. Rubbia. The Discovery of the W and Z Particles. *Advanced Series on Directions in High Energy Physics*, **23**:137–163, November 2015.

[60] R. Holdom. Two U(1)'s and ϵ charge shifts. *Phys. Lett.*, **166B**(2):196–198, January 1986.

[61] P. Galison and A. Manohar. Two Z's or not two Z's? *Phys. Lett.*, **136B**(4):279–283, March 1984.

[62] R. Essig et al. Dark Sectors and New, Light, Weakly-Coupled Particles. October 2013. https://arxiv.org/abs/1311.0029.

[63] J. D. Bjorken, R. Essig, P. Schuster, and N. Toro. New Fixed-Target Experiments to Search for Dark Gauge Forces. *Phys. Rev. D*, **80**(075018), October 2009.

[64] E. Rrapaj and S. Reddy. An Overview of Recent Progress in Laser Wakefield Acceleration Experiments. *Proceedings of the CAS-CERN Accelerator School: Plasma Wake Acceleration*, October 2016.

[65] S. Andreas, C. Niebuhr, and A. Ringwald. New limits on hidden photons from past electron beam dumps. *Phys. Rev. D*, **86**:095019, November 2012.

[66] P. F. Harrison. An introduction to the BABAR experiment. *Nucl. Instrum. Meth. A*, **368**:81–89, December 1995.

[67] J. P. Lees et al. Search for Invisible Decays of a Dark Photon Produced in e^+e^- Collisions at BABAR. *PRL*, **119**, September 2017.

[68] R. Essig et al. Search for a New Vector Boson A' Decaying to e^+e^-. January 2010. A New Proposal to Jefferson Lab PAC35.

[69] G. B. Franklin et al. Searching for the vector boson A' decaying to e^+e^-. *EPJ Web of Conferences*, **142**, April 2017.

[70] J. Redondo and A. Ringwald. Light shining through walls. *Cont. Phys.*, **52**(3):211–236, April 2011.

[71] H. Primakoff. Photo-Production of Neutral Mesons in Nuclear Electric Fields and the Mean Life of the Neutral Meson. *Phys. Rev.*, **81**:899, January 1951.

[72] T. Tajima and J. M. Dawson. Laser Electron Accelerator. *Phys. Rev. Lett.*, **43**(4):267–270, July 1979.

[73] V. I. Veksler. Coherent Principle of Acceleration of Charged Particles. *Proc. CERN Symp. 1*, 1956.

[74] I. Langmuir and L. Tonks. Oscillations in Ionized Gases. *Phys. Rev.*, **33**:195–210, February 1929.

[75] Y. B. Faǐnberg. Acceleration of particles in a plasma. *Sov. J. At. Energ.*, **6**:297–309, November 1960.

[76] C. M. Soukoulis. *Photonic Band Gaps and Localization.* Plenum Publishing Corporation, Spring Street, New York 10013, 1993.

[77] J. W. Strutt (Lord Rayleigh). *The Philosophical Magazine*, **24**:145–159, August 1887.

[78] E. Yablonovitch. Inhibited Spontaneous Emission in Solid-State Physics and Electronics. *Phys. Rev. Lett.*, **58**(20):2059–2062, May 1987.

[79] S. John. Strong Localization of Photons in Certain Disordered Dielectric Superlattices. *Phys. Rev. Lett.*, **58**(23):2486–2489, June 1987.

[80] E. Yablonovitch and T. J. Gmitter. Photonic Band Structure: The Face-Centered-Cubic Case. *Phys. Rev. Lett.*, **63**(18):1950–1953, October 1989.

[81] J. D. Joannopoulos et al. *Photonic Crystals: Molding the Flow of Light.* Princeton University Press, 41 William Street, Princeton, NJ 08540, 2008.

[82] P.-S. Laplace. *A Philosophical Essay on Probabilities.* John Wiley & Sons, London: Chapham and Hall, Limited, 1902.

[83] H. J. Poincaré. *The Foundations of Science.* The Science Press, New York and Garrison, NY, USA, 1913.

[84] D. Burton and A. Noble. Plasma-based wakefield accelerators as sources of axion-like particles. *New J. Phys.*, **20**:033022, March 2018.

[85] A. K. Harman, S. Ninomiya, and S. Adachi. Optical constants of sapphire ($\alpha - Al_2O_3$) single crystals. *J. Appl. Phys.*, **76**(12):8032–8036, December 1994.

[86] Quotes selected by Palle Jorgensen. http://homepage.math.uiowa.edu/~jorgen/hadamardquotesource.html. Accessed: 2021-08-08.

[87] J.-P. Kahane. Jacques Hadamard. *Math. Intell.*, **13**(1):23–29, 1991.

[88] S. Weinberg. The U(1) problem. *Phys. Rev. D*, **11**(12):3583–3593, June 1975.

[89] S. A. Adler. Axial-Vector Vertex in Spinor Electrodynamics. *Phys. Rev.*, **177**(5), January 1969.

[90] J. S. Bell and R. Jackiw. A PCAP Puzzle: $\pi^0 \to \gamma\gamma$ in the σ Model. *Il Nuovo Cimento*, **LX A**(1), March 1969.

[91]   W. A. Bardeen. Anomalous Ward Identities in Spinor Field Theories. *Phys. Rev.*, **184**(5), August 1969.

[92]   M. E. Peskin and D. V. Schroeder. *An Introduction to Quantum Field Theory.* Westview Press, 1995.

[93]   M. Kuster, G. Raffelt, and B. Beltrán. *Axions: Theory, Cosmology and Searches.* Springer Press, 2008.

[94]   W. A. Bardeen. Anomalous currents in gauge field theories. *Nucl. Phys. B*, **75**:246–258, June 1974.

[95]   A. A. Belavin et al. Pseudoparticle Solutions of the Yang-Mills Equations. *Phys. Lett. B*, **59**(1):85–87, October 1975.

[96]   G. 't Hooft. Symmetry Breaking through Bell-Jackiw Anomalies. *Phys. Rev. Lett.*, **37**:8–11, July 1976.

[97]   G. 't Hooft. Computation of the quantum effects due to a four-dimensional pseudoparticle. *Phys. Rev. D*, **14**(12):3432–3450, December 1976.

[98]   G. 't Hooft. How instantons solve the U(1) problem. *Phys. Rep.*, **142**:357–387, September 1986.

[99]   C. G. Callan, R. F. Dashen, and D. J. Gross. The Structure of the Gauge Theory Vacuum. *Phys. Lett. B*, **63**:334–, August 1976.

[100]   J. E. Kim and C. Gianpaolo. Axions and the strong CP problem. *Rev. Mod. Phys.*, **82**:557–601, March 2010.

[101]   R. Jackiw and C. Rebbi. Vacuum Periodicity in a Yang-Mills Quantum Theory. *Phys. Rev. Lett.*, **37**:172–175, July 1976.

[102]   M. Kaku. *Quantum Field Theory: A Modern Introduction.* Oxford University Press, Madison Avenue, New York 10016-4314, 1993.

[103]   A. Zee. *Einstein Gravity in a Nutshell.* Princeton University Press, 2013.

[104]   NIST Digital Library of Mathematical Functions. https://dlmf.nist.gov, Release 1.0.24 of 2019-09-15. F. W. J. Olver, A. B. Olde Daalhuis, D. W. Lozier, B. I. Schneider, R. F. Boisvert, C. W. Clark, B. R. Miller, B. V. Saunders, H. S. Cohl, and M. A. McClain, eds.

[105] K. F. Riley, M. P. Hobson, and S. J. Bence. *Mathematical Methods for Physics and Engineering.* Cambridge University Press, The Edinburgh Building, Cambridge, CB2 8RU, UK, 2012.

[106] F. J. Dyson. The S Matrix in Quantum Electrodynamics. *Phys. Rev.*, **75**(11):1736–1755, June 1949.

[107] J. C. Ward. *Phys. Rev.*, **78**:182, April 1950.

[108] Y. Takahashi. On the Generalized Ward Identity. *Il Nuovo Cimento*, **6**(2):371–375, August 1957.

[109] F. Del Aguila, G. D. Coughlan, and M. Quirós. Gauge coupling renormalisation with several U (1) factors. *Nucl. Phys. B*, **307**:633–648, September 1988.

[110] M. Luo and Y. Xiao. Renormalization group equations in gauge theories with multiple U (1) groups. *Phys. Lett. B*, **555**:279–286, March 2003.

[111] E. C. G. Stueckelberg. Die Wechselwirkungskräfte in der Elektrodynamik und in der Feldtheorie der Kernkräfte. *Helv. Phys. Acta*, **11**:225–244, November 1938.

[112] P. W. Higgs. Broken Symmetries and the Masses of Gauge Bosons. *Phys. Rev. Lett.*, **13**(16):508–509, October 1964.

[113] D. Feldman, Z. Liu, and P. Nath. *Phys. Rev. D*, **75**:115001, June 2007.

[114] J. Jaeckel and A. Ringwald. The Low-Energy Frontier of Particle Physics. *Ann. Rev. Nucl. Part. Sci.*, **60**:405–437, 2010.

[115] A. Proca. Sur la théorie ondulatoire des électrons positifs et négatifs. *J. Phys. Radium*, **7**(8):347–353, 1936.

[116] B. Brewster. *The Yale Literary Magazine*, **47**(5):202, February 1882.

[117] J. A. Ratcliffe. *The Magneto-Ionic Theory & Its Applications to the Ionosphere.* Cambridge University Press, Bentley House, 200 Euston Road, London, UK, 1962.

[118] D. J. Griffiths. *Introduction to Electrodynamics.* Cambridge University Press, University Printing House, Cambridge, CB2 8BS, UK, 4 edition, 2019.

[119] J. R. Cary and A. N. Kaufman. Ponderomotive Force and Linear Susceptibility in Vlasov Plasma. *Phys. Rev. Lett.*, **39**:402–403, August 1978.

[120] G. W. Kentwell. An average Lagrangian formulation of ponderomotive forces in Vlasov plasmas. *J. Plasma Phys.*, **34**:289–298, October 1985.

[121] D. Bauer, P. Mulser, and W. H. Steeb. Relativistic Ponderomotive Force, Uphill Acceleration, and Transition to Chaos. *Phys. Rev. Lett.*, **75**:4622–4625, Dec 1995.

[122] I. Y. Dodin and N. J. Fisch. Positive and negative effective mass of classical particles in oscillatory and static fields. *Phys. Rev. E*, **77**:036402, Mar 2008.

[123] D. A. Burton, R. A. Cairns, B. Ersfeld, A. Noble, S. Yoffe, and D. A. Jaroszynski. Observations on the ponderomotive force. In Dino A. Jaroszynski, editor, *Relativistic Plasma Waves and Particle Beams as Coherent and Incoherent Radiation Sources II*, volume 10234, pages 17 – 22. International Society for Optics and Photonics, SPIE, 2017.

[124] Esarey, E. and others. Overview of Plasma-Based Accelerator Concepts. *IEEE Trans. Plasma Science*, **24**(2):252–288, April 1996.

[125] M. Abramowitz and I. A. Stegun. *Handbook of Mathematical Functions With Formulas, Graphs, and Mathematical Tables*. United States Department of Commerce, 1972.

[126] G. B. Arfken, H. J. Weber, and F. E Harris. *Mathematical Methods for Physicists*. Academic Press, 225 Wyman Street, Waltham, MA 02451, USA, 2013.

[127] R. Shankar. *Principles of Quantum Mechanics*. Springer Press, 2nd edition, 2014.

[128] I. S. Gradshteyn and I. M. Ryzhik. *Table of Integrals, Series and Products*. Academic Press, 84 Theobald's Road, London, WC1X 8RR, UK, 7 edition, 2007.

[129] F. H. Harlow. A Machine Calculation Method for Hydrodynamic Problems. *Los Alamos Scientific Laboratory, LAMS-1956*, November 1955.

[130] F. H. Harlow and M. W. Evans. The Particle-in-Cell Method for Hydrodynamic Calculations. *Los Alamos Scientific Laboratory Report, LA-2139*, **13**, November 1957.

[131] K. S. Yee. Numerical Solution of Initial Boundary Value Problems Involving Maxwell's Equations in Isotropic Media. **14**(3):302–307, May 1966.

[132] J. P. Boris. pages 3–67, 1970. Proc. of the Fourth Conference on Numerical Simulation of Plasmas.

[133] H. Qin et al. Why is the Boris algorithm so good? *Phys. Plasmas*, **20**:084503, August 2013.

[134] T. D. Arber, K. Bennett, C. S. Brady, A. Lawrence-Douglas, M. G. Ramsay, N. J. Sircombe, P. Gillies, R. G. Evans, H. Schmitz, A. R. Bell, and C. P. Ridgers. Contemporary particle-in-cell approach to laser-plasma modelling. *Plasma Phys. Contr. F.*, **57**(11):1–26, November 2015.

[135] H. Ruhl. *Introduction to Computational Methods in Many Body Physics.* Rinton Press, 2006.

[136] J. M. Berger and G. J. Lasher. THE USE OF DISCRETE GREEN'S FUNCTIONS IN THE NUMERICAL SOLUTION OF POISSON'S EQUATION. *Illinois J. Math.*, **2**:593–607, November 1958.

[137] A. R. G. Harwood and I. D. J. Dupère. Numerical evaluation of the compact Green's function for the solution of acoustic flows. *Proceedings of the Internoise 2012/ASME NCAD meeting*, August 2012.

[138] J. Mayfield, Y. Gau, and S. Luo. An asymptotic Green's function method for the wave equation. *J. Comp. Phys.*

[139] A. Kleinert. Der messende Luchs: Zwei verbreitete Fehler in der Galilei-Literatur. *NTM Zeitschrift für Geschichte der Wissenschaften, Technik und Medizin*, **17**(2):199–206, May 2009.

[140] Richard M. Stallman. The Free Software Definition. https://www.gnu.org/philosophy/free-sw.html.en. Accessed: 2020-01-14.

[141] J. Jaeckel et al. Need for purely laboratory-based axionlike particle searches. *Phys. Rev. D*, **75**:013004, January 2007.

[142] J. T. Mendonça. Axion excitation by intense laser fields. *EPL*, **79**(2):21001, July 2007.

[143] B. Döbrich and H. Gies. Axion-like-particle search with high-intensity lasers. *JHEP*, **2010**(22), October 2010.

[144] S. Villalba-Chávez and A. Di Piazza. Axion-induced birefringence effects in laser driven nonlinear vacuum interaction. *JHEP*, **2013**(136), November 2013.

[145] S. Villalba-Chávez. Laser-driven search of axion-like particles including vacuum polarization effects. *JHEP*, **881**:391–413, April 2014.

[146] S. Huang et al. Axion-like-particle generation by laser-plasma interaction. May 2020.

[147] J. T. Mendonça et al. Axion production in unstable magnetized plasmas. *Phys. Rev. D*, **101**:051701, March 2020.

[148] C. J. Hooker et al. Commissioning the Astra Gemini Petawatt Ti:Sapphire Laser System. *2008 Conference on Lasers and Electro-Optics and 2008 Conference on Quantum Electronics and Laser Science*, pages 1–2, 2008.

[149] P. McKenna, D. Neely, R. Bingham, and D. A. Jaroszynski. *Laser-Plasma Interactions and Applications*. Springer International Publishing, Switzerland, 2013.

[150] G. Grittani et al. High energy electrons from interaction with a structured gas-jet at FLAME. *Nucl. Instrum. Meth. A*, 740:257–265, March 2014.

[151] C. Aniculaesei. *Experimental Studies of Laser Plasma Wakefield Acceleration*. October 2015. Doctoral Thesis.

[152] S. Lorenz et al. Characterization of supersonic and subsonic gas targets for laser wakefield electron acceleration experiments. *Matter Radiat. at Extremes*, **4**:015401, January 2019.

[153] B. Hidding et al. Plasma Wakefield Accelerator Research 2019 - 2040 : A community-driven UK roadmap compiled by the Plasma Wakefield Accelerator Steering Committee (PWASC). April 2019.

[154] D. Nakamura, A. Ikeda, H. Sawabe, Y. H. Matsuda, and S. Takeyama. Record indoor magnetic field of 1200 t generated by electromagnetic flux-compression. *Review of Scientific Instruments*, **89**(9):095106, 2018.

[155] J. Marcelo, R. Daou, S. A. Crooker, F. Weickert, A. Uchida, A. E. Feiguin, C. D. Batista, H. A. Dabkowska, and B. D. Gaulin. Magnetostriction and magnetic texture to 100.75 Tesla in frustrated $SrCu_2(BO_3)_2$. *PNAS*, **109**(31):12404–12407, July 2012.

[156] R. Helliwell. *Whistlers and Related Ionospheric Phenomena*. Stanford University Press, Stanford, California, U.S.A, 1965.

[157] J. J. Santos et al. Laser-driven platform for generation and characterization of strong quasi-static magnetic fields. *New J. Phys.*, **17**(8):083051, August 2015.

[158] F. Pérez, A. J. Kemp, L. Divol, C. D. Chen, and P. K. Patel. Deflection of MeV Electrons by Self-Generated Magnetic Fields in Intense Laser-Solid Interactions. *Phys. Rev. Lett.*, **111**:245001, December 2013.

[159] Ph. Korneev, E. d'Humières, and V. Tikhonchuk. Gigagauss-scale quasistatic magnetic field generation in a snail-shaped target. *Phys. Rev. E*, **91**:043107, April 2015.

[160] R. Seviour et al. Hidden-sector photon and axion searches using photonic band gap structures. *J. Phys. G: Nucl. Phys.*, **41**(3):035005, March 2014.

[161] A. F. Oskooi, D. Roundy, M. Ibanescu, P. Bermel, J. D. Joannopoulos, and S. G Johnson. MEEP: A flexible free-software package for electromagnetic simulations by the FDTD method. *Comp. Phys. Commun.*, **181**:687–702, 2010.

[162] M. Betz. The CERN Resonant Weakly Interacting Sub-eV ParticleSearch (CROWS). February 2014.

[163] M. Betz et al. First results of the CERN Resonant Weakly Interacting sub-eV Particle Search (CROWS). *Phys. Rev. D*, **88**:075014, October 2013.

[164] D. M. Allen, R. Redondo, and M. Dany. Fabrication methods for the manufacture of sapphire microparts. *Microsyst. Technol.*, **18**:1835–1841, March 2012.

[165] A. N. Ioannisian, N. Kazarian, A. J. Millar, and G. G. Raffelt. Axion-photon conversion caused by dielectric interfaces: quantum field calculation. *Journal of Cosmology and Astroparticle Physics*, 2017:005–005, 2017.